University of Southampton Research Repository

Copyright © and Moral Rights for this thesis and, where applicable, any accompanying data are retained by the author and/or other copyright owners. A copy can be downloaded for personal non-commercial research or study, without prior permission or charge. This thesis and the accompanying data cannot be reproduced or quoted extensively from without first obtaining permission in writing from the copyright holder/s. The content of the thesis and accompanying research data (where applicable) must not be changed in any way or sold commercially in any format or medium without the formal permission of the copyright holder/s.

When referring to this thesis and any accompanying data, full bibliographic details must be given, e.g.

Thesis: Author (Year of Submission) "Full thesis title", University of Southampton, name of the University Faculty or School or Department, PhD Thesis, pagination.

Data: Author (Year) Title. URI [dataset]

UNIVERSITY OF SOUTHAMPTON

FACULTY OF ENGNIEERING AND THE ENVIRONMENT

Energy technology Group

DESIGN OF CERIA SUPPORTED NICKEL-BASED CATALYSTS FOR SELECTIVE HYDROGENATION OF MALEIC ANHYDRIDE

by

XIN LIAO

Thesis for the degree of Doctor of Philosophy

11/2017

UNIVERSITY OF SOUTHAMPTON

ABSTRACT

FACULTY OF ENGINEERING AND THE ENVIRONMENT

Engineering

Thesis for the degree of Doctor of Philosophy

DESIGN OF CERIA SUPPORTED NICKEL-BASED CATALYSTS FOR SELECTIVE HYDROGENATION OF MALEIC ANHYDRIDE

Xin Liao

This thesis presents my efforts in the design and development of novel ceria (CeO_2)-supported Ni-based catalytic materials to realise effective and highly selective liquid phase hydrogenation of maleic anhydride (MA), an important process in producing crucial platform chemicals. In my research, metallic Ni and defective ceria ($CeO_{2-\delta}$) are defined as an efficient metal catalyst and active support, respectively, and tuning the properties of the Ni/$CeO_{2-\delta}$ catalysts through different strategies is verified to be effective in controlling selectivity of succinic anhydride (SA) via preferential hydrogenation of C=C or gamma butyrolactone (GBL) via C=O hydrogenolysis. We made great efforts to correlate the improved performance with various influential properties of the novel catalysts.

A thorough survey of recent advances in MA hydrogenation processes and catalysts (Chapter 1) clarified that MA conversion and selectivity on the catalysts depended on the active metal species and their interaction with support. The well-explored impacts of crystalline and textural structures of catalyst supports are also important. We therefore proposed the Ni/$CeO_{2-\delta}$ catalysts to be novel, low-cost and green catalysts in order to address the great challenges in the industrial MA hydrogenation process. The rational experimental methodologies and the theoretical background were presented and justified in Chapter 2.

Firstly, through the comparative investigation into the liquid phase MA hydrogenation on Ni/$CeO_{2-\delta}$ and Ni/Al_2O_3 catalysts (Chapter 3), the defective ceria ($CeO_{2-\delta}$) support was defined as an active support, which offered desirable oxygen vacancies (Ovac) and interaction with Ni responsible for the promoted activity and selectivity. Meanwhile, the outstanding performance of Ni and its unique interaction with $CeO_{2-\delta}$ were specified via a comparative study of MA hydrogenation

on $CeO_{2-\delta}$-supported transition metals (Chapter 4), where the electronic interaction between Ni and $CeO_{2-\delta}$ was stressed.

The fine-tuning of Ni loading on $CeO_{2-\delta}$ support allowed me not only to optimise the catalysts but also to define the active sites, underlining the contributions of Ovac, metallic Ni species, and the Ni-CeO_2 interface to MA hydrogenation on the xNi/CeO_2 catalysts (Chapter 5). Through quasi-quantitative analyses, we established that Ovac played pivotal roles in SA selectivity, while the Ni species and the Ni-CeO_2 interface dominated the yield of GBL.

The Ni/$CeO_{2-\delta}$ catalysts with 5 wt% Ni loading (in avoidance of the influence of significant surface coverage) were prepared using different-shaped CeO_2 supports which terminated with different percentage of predominant crystal surfaces and possessed different Ovac levels. We found that their catalytic performance of MA hydrogenation was dependent on the specific morphology. Peculiarly, the $CeO_{2-\delta}$ nanorod-supported Ni catalyst showed the highest activity due to the highest Ni dispersion and Ovac concentration (Chapter 6).

In order to further tune the performance of MA hydrogenation, $CeO_{2-\delta}$ supported bimetallic Ni-based catalysts were prepared through the incorporation of a second transition metal, including Fe, Co, Cu and Zn, with a different number of outer shell d electrons (Chapter 7). It was found that only Cu can effectively improve MA conversion and the selectivity to SA. Qualitative and quantitative characterisation revealed that Cu perturbed the valance electronic structure of Ni, thus altering the hydrogenation activation ability. The formation of the Ni-Cu alloy also modulated the metal-support interaction. Thus, the $CeO_{2-\delta}$-supported bimetallic Ni-Cu alloy catalysts displayed enhanced MA hydrogenation performance, particularly SA selectivity.

CeO_2 was applied as a promoter to modify the surface of 15 wt% Ni/SiO_2 catalysts, in order to further validate the roles of CeO_2 (Chapter 8). MA hydrogenation was affected by the coverage of CeO_2, with higher activity and selectivity on the 3CeO_2@15Ni/SiO_2 catalyst with 3 wt% $CeO_{2-\delta}$ loading (versus Ni/SiO_2 weight). The surface CeO_2 species can improve C=O adsorption and activation on the CeO_2-decorated Ni/SiO_2 catalyst, which contributed to the excellent catalytic activity in C=O hydrogenolysis.

Overall, the thesis reports a systematic study of the design and application of $CeO_{2-\delta}$ support, the Ni-$CeO_{2-\delta}$ interaction, and the optimisation of active metal for developing green and robust MA hydrogenation catalysts. The roles of Ovac, the Ni-$CeO_{2-\delta}$ electronic interaction and Ni species in MA hydrogenation have been summarised in Chapter 9. The research will be facilitating the future development of novel and effective catalysts for industrial MA hydrogenation processes.

Table of Contents

Table of Contents i
List of Tables vii
List of Figures ix
List of Accompanying Materials xv
Academic Thesis: Declaration Of Authorship xvii
Acknowledgements xix
Chapter 1 Overview of Maleic Anhydride Hydrogenation Processes and Catalysts 21
1.1 Introduction 21
1.2 The socio-economic importance of MA hydrogenation 24
1.3 Advances of supported catalysts for MA hydrogenation 26
1.3.1 Pd-based catalysts 27
1.3.2 Ru-based catalysts 29
1.3.3 Pt-based catalysts 31
1.3.4 Cu-based catalysts 32
1.3.5 Ni-based catalysts 35
1.3.6 Catalytic challenges 39
1.4 The mechanism of MA hydrogenation 40
1.4.1 MA adsorption on metal surface 41
1.4.2 MA adsorption on oxide surface 43
1.4.3 Mechanism of C=C hydrogenation 44
1.4.4 Mechanism of C=O hydrogenolysis 46
1.5 Strategies for promoting MA hydrogenation catalyst 47
1.5.1 Active support-cerium oxide 47
1.5.2 Modification of surface metal active species 54
1.6 Aims and methodologies of this thesis 56
1.6.1 Objectives 56
1.6.2 Methodologies 56
Chapter 2 Experimental methodologies 59

2.1 Materials 59
2.2 Methodologies 59
2.2.1 Powder X-ray Diffraction 59
2.2.2 Raman spectroscopy 62
2.2.3 X-ray photoelectron spectroscopy 63
2.2.4 Hydrogen temperature programmed reduction/desorption 64
2.3 Auxiliary characterisation 66
2.4 Catalyst evaluation 66
Chapter 3 The comparative studies of 10Ni/$CeO_{2-\delta}$ and 10Ni/Al_2O_3 catalysts on MA hydrogenation **71**
3.1 Introduction 71
3.2 Experimental 72
3.2.1 Catalyst preparation 72
3.2.2 Catalyst characterisation and evaluation 73
3.3 Results and discussion 73
3.3.1 Structure and texture of catalysts 73
3.3.2 Redox properties of the catalysts 77
3.3.3 Surface properties of 10Ni/$CeO_{2-\delta}$ catalyst 78
3.3.4 Hydrogen activation on the catalysts 80
3.3.5 Catalytic performance 82
3.4 Conclusion 84
Chapter 4 MA hydrogenation over $CeO_{2-\delta}$ supported transition metal catalysts **86**
4.1 Introduction 86
4.2 Experimental 87
4.2.1 Preparation of ceria support 87
4.2.2 Preparation of M/$CeO_{2-\delta}$ (M=Co, Ni and Cu) catalysts 87
4.2.3 Catalyst characterisation and evaluation 88
4.3 Results and discussion 88
4.3.1 Structure and morphology 88
4.3.2 Reduction behaviour of the MO_x/CeO_2 precursors 91

4.3.3 Surface structural analysis 92
4.3.4 Hydrogen activation on the M/$CeO_{2-\delta}$ catalysts 94
4.3.5 Catalytic hydrogenation of maleic anhydride 95
4.4 Conclusion 99
Chapter 5 Loading effect of Ni on MA hydrogenation over xNi/$CeO_{2-\delta}$ catalysts 103
5.1 Introduction 103
5.2 Experimental 104
5.2.1 Catalyst preparation 104
5.2.2 Catalyst characterisation and evaluation 105
5.3 Results and discussion 105
5.3.1 Structure evolution of the xNi/$CeO_{2-\delta}$ catalysts 105
5.3.2 The reducibility of xNiO/CeO_2 sample 108
5.3.3 The surface properties of xNi/$CeO_{2-\delta}$ catalysts 110
5.3.4 Catalyst performance 118
5.4 Discussion 119
5.4.1 C=C hydrogenation over xNi/$CeO_{2-\delta}$ catalysts 119
5.4.2 C=O hydrogenolysis over xNi/$CeO_{2-\delta}$ catalysts 123
5.5 Conclusion 126
Chapter 6 The effects of CeO_2 morphology on MA hydrogenation over the Ni/$CeO_{2-\delta}$ catalysts 129
6.1 Introduction 129
6.2 Experimental 130
6.2.1 Preparation of CeO_2 supports with different morphology 130
6.2.2 Preparation of Ni/$CeO_{2-\delta}$ catalysts 131
6.2.3 Catalyst characterisation and evaluation 131
6.3 Results and discussion 132
6.3.1 Morphology and structure of various CeO_2 supports 132
6.3.2 Redox properties of the 5Ni/$CeO_{2-\delta}$ catalyst precursors 136
6.3.3 Structure and morphology of 5Ni/$CeO_{2-\delta}$ catalysts 137

6.3.4 Surface element analysis 139
6.3.5 Hydrogen activation over 5Ni/$CeO_{2-\delta}$ catalysts 142
6.3.6 Catalytic performance 143

6.4 Conclusion 149

Chapter 7 MA hydrogenation over bimetallic Ni-Cu/$CeO_{2-\delta}$ catalysts 151

7.1 Introduction 151
7.2 Experimental 152

7.2.1 Catalyst preparation 152
7.2.2 Catalyst characterisation and evaluation 153

7.3 Results and discussion 153

7.3.1 Structure evolution of bimetallic xNiyCu/$CeO_{2-\delta}$ catalysts 153
7.3.2 Redox properties of xNiyCu/$CeO_{2-\delta}$ catalysts 156
7.3.3 Surface element analysis 157
7.3.4 Hydrogen activation on the xNiyCu/$CeO_{2-\delta}$ catalysts 157
7.3.5 Catalytic performance 162

7.4 Conclusion 167

Chapter 8 Effects of CeO_2 on MA hydrogenation on CeO_2@Ni/SiO_2 catalysts 169

8.1 Introduction 169
8.2 Experimental 170

8.2.1 Preparation of 15Ni/SiO_2 catalysts 170
8.2.2 Preparation of xCeO_2@15Ni/SiO_2 catalysts 170
8.2.3 xCeO_2@15Ni/SiO_2 catalysts characterisation and evaluation 171

8.3 Results and discussion 171

8.3.1 Structure and morphology of xCeO_2@15Ni/SiO_2 catalysts 171
8.3.2 Redox properties of xCeO_2@15Ni/SiO_2 catalysts 173
8.3.3 Surface defects of xCeO_2@15Ni/SiO_2 catalysts 174
8.3.4 Hydrogen activation on the xCeO_2-15Ni/SiO_2 catalysts 175
8.3.5 Catalytic performance 176

8.4 Conclusion 180

Chapter 9 Summary and outlook 182

9.1 Summary 182

9.2 Outlook 186

Appendix A The fundamental theory about characterisation 188

A.1 X-ray diffraction 188

A.2 X-ray photoelectron spectroscopy 189

A.3 Raman spectroscopy 192

A.4 BET theory for surface area determination 193

Appendix B The auxiliary results of MA conversion over Ni/CeO$_{2-\delta}$ catalyst 195

Appendix C Bimetallic Ni-M/CeO$_{2-\delta}$ systems for MA hydrogenation 199

Publications 201

Bibliography 203

List of Tables

Table 1.1 Pd-based catalysts used in the MA&SA hydrogenation 28

Table 1.2 Ru-based catalysts for MA&SA hydrogenation 30

Table 1.3 Comparison of the liquid-phase maleic anhydride hydrogenation over Ni-based catalysts on different supports 37

Table 1.4 Binding energies of MA adsorption on different metal surfaces 42

Table 2.1 Materials for catalyst preparation and evaluation 59

Table 3.1 The structure parameters of the CeO_2 and metallic Ni. 75

Table 3.2 The textual properties of supports and catalysts 76

Table 3.3 Quantitative analyses of the fitted Ce 3d core level XPS peaks 79

Table 3.4 Quantitative analyses of the fitted O 1s core level XPS peaks 80

Table 3.5 H_2 chemisorption capability of the reduced samples 81

Table 4.1 Properties of the MO_x/CeO_2 precursors and corresponding $M/CeO_{2-\delta}$ catalysts 89

Table 4.2 H_2 uptake, metal dispersion and hydrogenation rate constants on $M/CeO_{2-\delta}$ catalysts 94

Table 5.1 Recipe for preparation of $xNi/CeO_{2-\delta}$ catalysts 104

Table 5.2 The surface areas (S_{BET}), Ni loading and the average crystallite sizes of CeO_2, NiO and metallic Ni in the reduced catalysts 106

Table 5.3 XPS analysis of the $xNi/CeO_{2-\delta}$ catalysts 114

Table 6.1 The structure of three low index surfaces of ceria and their Ovac formation energy 130

Table 6.2 Structure and physical parameters of various CeO_2 supports and $5Ni/CeO_{2-\delta}$ catalysts 133

Table 6.3 Quantitative XPS analysis of the $5Ni/CeO_{2-\delta}$ catalysts 141

Table 6.4 H_2 uptake and metal dispersion of the $5Ni/CeO_{2-\delta}$ catalysts 143

Table 7.1 The structure parameters of metallic Ni-Cu alloy, Ni and Cu in the $xNiyCu/CeO_2$ catalysts 155

Table 7.2 H_2 uptake of the $xNiyCu/CeO_{2-\delta}$ catalysts 161

Table 7.3 The structure parameters of fresh and used $6Ni4Cu/CeO_{2-\delta}$ catalysts 166

Table 8.1 The physical parameters of $xCeO_2@15Ni/SiO_2$ catalysts 172

Table 8.2 The quantitative analysis of H_2-TPD profiles of $xCeO_2$-$15Ni/CeO_2$ catalysts 176

List of Figures

Figure 1.1 Potential energy diagram for the catalytic and non-catalytic reactions 22

Figure 1.2 The global market of MA from 2015 to 2024[15] 24

Figure 1.3 Schematic pathways of MA hydrogenation (adapted from Ref.[26]) 25

Figure 1.4 Plausible reaction pathway for selective GBL formation over Pt–Sn/Al_2O_3 catalyst[42] 31

Figure 1.5 Pathway of MA hydrogenation to GBL and BDO over Cu-ZnO catalyst (adapted from Ref.[68]) 32

Figure 1.6 Comparative study of MA hydrogenation over Co/Al_2O_3, Ni/Al_2O_3 and Cu/Al_2O_3 catalysts at 140°C and 0.5 MPa[73] 35

Figure 1.7 The proposed different adsorption modes of MA on metal surface[90] . 41

Figure 1.8 MA adsorption and decomposition on ZnO surface[92] 43

Figure 1.9 DFT-computed reaction energetics for the hydrogenation of maleic anhydride to succinic anhydride on a Pd(111) surface[88] 45

Figure 1.10 Presumed reaction mechanism over the Ru-based complex[34] 46

Figure 1.11 Schematic representation of the activation of the C=O bond in α , β - unsaturated carbonyls on Pd–$M^{\delta +}$[45] 47

Figure 1.12 The perfect fluorite structures of CeO_2[114] and defects on the (111) surface of CeO_2 material (white large balls are on the top O^{2-} layer; grey large ones are on the third O^{2-} layer; yellow and orange ones are on the second Ce cation layers. Yellow indicates a Ce^{4+} cation and orange indicates a Ce^{3+} cation. Black ones are on the forth Ce^{4+} layer).[115] 49

Figure 1.13 Acetone adsorption on the (A) fully oxidised and (B) reduced CeO_2(111) thin film [118] 49

Figure 1.14 Diagram of H adsorption on the surface of CeO_2[121] 50

Figure 1.15 Illustration of H_2 interaction with CeO_2 with the formation of surface OH and Ce–H[126] 51

Figure 1.16 Kinetic data Arrhenius-type plots for CO oxidation over (A) Al_2O_3 and (B) CeO_2 supported catalysts[130] 52

Figure 1.17 The research flow chart for the PhD thesis 56

Figure 2.1 Typical XRD patterns of (A) NiO/CeO_2 precursors and (B) Ni/$CeO_{2-\delta}$ catalysts adapted from Ref.[150] 60

Figure 2.2 Simplified representation of a crystal (A) without and (B) with microstrain[154]..61

Figure 2.3 Raman spectra of Gd-doped CeO_2 samples adapted from Ref.[158]....62

Figure 2.4 The core level XPS spectra of Ni2$p_{3/2}$ in the bimetallic Cu-Ni/SiO_2 catalysts adapted from Ref.[167] 63

Figure 2.5 (A) Illustration and (B) photo of the batch reactor for MA hydrogenation...66

Figure 2.6 Conversion of MA against the stirring rate (A) and particle size of catalysts (B) over 15Ni/$CeO_{2-\delta}$ catalyst. Reaction condition: 4.9 g MA, 0.1 g catalyst, 40 ml THF as solvent, 210°C and 5 MPa for 20 min..67

Figure 2.7 The calibration curves of MA, SA and GBL concentration 68

Figure 3.1 The schematic procedure for preparation of 10Ni/$CeO_{2-\delta}$ catalyst 72

Figure 3.2 XRD patterns of (A) the CeO_2-based samples and (B) the Al_2O_3-based samples: (1) CeO_2, (2) 10NiO/CeO_2, (3) 10Ni/$CeO_{2-\delta}$ and (i) Al_2O_3, (ii) 10NiO/Al_2O_3, (iii) 10Ni/Al_2O_3 73

Figure 3.3 N_2 adsorption–desorption isotherms patterns of 10Ni/$CeO_{2-\delta}$ and 10Ni/Al_2O_3 76

Figure 3.4 The H_2-TPR profiles of (a) NiO, (b) 10NiO/CeO_2 and (c) 10NiO/Al_2O_3 ...77

Figure 3.5 The core-level XPS spectra of the reduced 10Ni/$CeO_{2-\delta}$ catalyst (A) Ce 3d and (B) O1s...78

Figure 3.6 H_2-TPD profiles of (a) the 10Ni/$CeO_{2-\delta}$ and (b) the 10Ni/Al_2O_3 catalysts 80

Figure 3.7 Conversion of MA (A) and yields of SA (B) and GBL over 10Ni/$CeO_{2-\delta}$ and 10Ni/Al_2O_3 catalysts at 210°C under 5 MPa for 8h duration. 82

Figure 4.1 The scheme of catalyst preparation for the Ni/$CeO_{2-\delta}$ catalyst 87

Figure 4.2 XRD pattern of (A) the MO_x/CeO_2 precursors and (B) the M/$CeO_{2-\delta}$ catalysts (M= Co, Ni and Cu, respectively). 89

Figure 4.3 The dependence of metal crystallite sizes on those of metal oxides ..90

Figure 4.4 TEM images of M/$CeO_{2-\delta}$ samples. (A) 10Co/$CeO_{2-\delta}$, (B) 10Ni/$CeO_{2-\delta}$ and (C) 10Cu/$CeO_{2-\delta}$ 90

Figure 4.5 H_2-TPR profiles of MO_x/CeO_2 samples 91

Figure 4.6 Raman spectra of (A) MO_x/CeO_2 precursors and (B) reduced $M/CeO_{2-\delta}$ catalysts 92

Figure 4.7 H_2-TPD profiles of $CeO_{2-\delta}$ and $M/CeO_{2-\delta}$ catalysts 94

Figure 4.8 (A) Conversion of MA over the $M/CeO_{2-\delta}$ catalysts at 210°C and 5 MPa for 8 h and (B) kinetic curves of the $M/CeO_{2-\delta}$ catalysts for MA conversion 95

Figure 4.9 (A) Selectivity of SA and (B) yield of GBL over $M/CeO_{2-\delta}$ catalysts at 210°C and 5 Mpa for 8 h 97

Figure 5.1 (A) XRD patterns of calcined $xNiO/CeO_2$ samples and (B) the enlarged pattern at the range of 26-31° 105

Figure 5.2 XRD patterns of reduced $xNi/CeO_{2-\delta}$ catalysts 107

Figure 5.3 TEM images of typical catalysts (A) $5Ni/CeO_{2-\delta}$; (B) $10Ni/CeO_{2-\delta}$; (C) $17.5Ni/CeO_{2-\delta}$ and (D) $30Ni/CeO_{2-\delta}$ catalysts 107

Figure 5.4 (A H_2-TPR profiles of $xNiO/CeO_2$ precursors and (B) closer observation to the TPR profiles of the $2NiO/CeO_2$, $5NiO/CeO_2$ and CeO_2 108

Figure 5.5 Raman spectra of (A) the $xNiO/CeO_2$ precursors and (B) reduced $xNi/CeO_{2-\delta}$ catalysts: (a) $CeO_{2-\delta}$; (b) $2Ni/CeO_{2-\delta}$; (c) $5Ni/CeO_{2-\delta}$; (d) $10Ni/CeO_{2-\delta}$; (e) $15Ni/CeO_{2-\delta}$; (f) $17.5Ni/CeO_{2-\delta}$; (g) $20Ni/CeO_{2-\delta}$; (h) $30Ni/CeO_{2-\delta}$ 110

Figure 5.6 Ratios of I_D/I_{F2g} for the $xNiO/CeO_2$ precursors and $xNi/CeO_{2-\delta}$ catalysts 111

Figure 5.7 XPS spectra of $Ni2p_{3/2}$ for reduced $xNi/CeO_{2-\delta}$ catalysts 112

Figure 5.8 (A) Ce3d and (B) O1s core-level XPS spectra of the xNi/CeO_2 catalysts (a) $CeO_{2-\delta}$, (b) $5Ni/CeO_{2-\delta}$, (c) $10Ni/CeO_{2-\delta}$, (d) $17.5Ni/CeO_{2-\delta}$ and (e) $30Ni/CeO_{2-\delta}$ ... 113

Figure 5.9 H_2-TPD profiles of (A) the unreduced and reduced CeO_2 and (B) $xNi/CeO_{2-\delta}$ catalysts 115

Figure 5.10 H_2-TPD-MS profiles of (A) unreduced CeO_2 and (B) reduced $CeO_{2-\delta}$ samples 116

Figure 5.11 Total (A) and site-defined (B) hydrogen uptake on the $xNi/CeO_{2-\delta}$ catalysts 117

Figure 5.12 (A) MA conversion over the reduced $xNi/CeO_{2-\delta}$ catalysts in 1h and (B) the specific MA conversion over the $xNi/CeO_{2-\delta}$ catalysts at 30 min 118

Figure 5.13 (A) Selectivity of SA and (B) yield of GBL over the reduced xNi/$CeO_{2-\delta}$ catalysts at 210 °C and 5 MPa for 8 h 119

Figure 5.14 Pathway of MA hydrogenation with low unoccupied molecular orbital, charge and bond length 120

Figure 5.15 (A) Comparison of MA conversion over representative catalysts and (B) nickel loading dependence of $TOF_{MA\rightarrow SA}$ and Ovac-induced hydrogen desorption 121

Figure 5.16 (A) Ni loading dependence of $TOF_{SA\rightarrow GBL}$ against H_2 uptake on nickel species for the xNi/$CeO_{2-\delta}$ catalysts and (B) effect of nickel crystallite size on the $TOF_{MA\rightarrow SA}$ and $TOF_{SA\rightarrow GBL}$ 124

Figure 6.1 TEM, HRTEM and FT images of CeO_2-NP (A, D), CeO_2-NR (B, E) and CeO_2-NC (C, F) supports 132

Figure 6.2 XRD patterns of various CeO_2 supports 134

Figure 6.3 Raman spectra of (A) various CeO_2 support and (B) enlarged the corresponding Raman spectra 135

Figure 6.4 H_2-TPR profiles of 5NiO/CeO_2 precursors 136

Figure 6.5 TEM, HRTEM and FT images of (A, D) 5Ni/$CeO_{2-\delta}$ -NP, (B, E) 5Ni/$CeO_{2-\delta}$ -NR and (C, F) 5Ni/$CeO_{2-\delta}$ -NC supports 137

Figure 6.6 (A) XRD patterns and (B) Raman spectra of various 5Ni/$CeO_{2-\delta}$ catalysts 138

Figure 6.7 XPS spectra of (A) Ce3d and (B) O1s for reduced 5Ni/$CeO_{2-\delta}$ catalysts (a) 5Ni/$CeO_{2-\delta}$ -NP, (b) 5Ni/$CeO_{2-\delta}$ -NR and (c) 5Ni/$CeO_{2-\delta}$ -NC....139

Figure 6.8 Ni2$p_{3/2}$ XPS spectra of reduced 5Ni/$CeO_{2-\delta}$ catalysts (a) 5Ni/$CeO_{2-\delta}$ -NP, (b) 5Ni/$CeO_{2-\delta}$ -NR and (c) 5Ni/$CeO_{2-\delta}$ -NC 141

Figure 6.9 H_2-TPD profiles of 5Ni/$CeO_{2-\delta}$ catalysts 142

Figure 6.10 MA conversion over 5Ni/$CeO_{2-\delta}$ catalysts at 180°C and under 5 MPa of hydrogen pressure 143

Figure 6.11 Arrhenius plots of ln (k) versus 1/T for MA conversion over different shaped 5Ni/$CeO_{2-\delta}$ catalysts....144

Figure 6.12 Yields of GBL over the 5Ni/$CeO_{2-\delta}$ catalysts in the 8 h MA hydrogenation at 210°C and 5 MPa hydrogen pressure 146

Figure 6.13 Stability of 5Ni/$CeO_{2-\delta}$ -NR catalyst in MA hydrogenation at 180°C and 5 MPa of H_2 for 1 h. Reaction condition: 4.9 g MA, 40 ml THF and 0.5 g catalyst. 147

Figure 6.14 (A) TEM and HRTEM images, (B) XRD patterns and (C) Raman spectra of 5Ni/$CeO_{2-\delta}$ -NR catalyst 148

Figure 7.1 (A) XRD pattern for unreduced bimetallic xNiyCu/CeO_2 precursors and CeO_2 support and (B) Enlarged XRD pattern for reduced xNiyCu/$CeO_{2-\delta}$ catalysts 153

Figure 7.2 The lattice parameters of metallic species from both experimental tests and simulated by the Vegard law for the xNiyCu/$CeO_{2-\delta}$ catalysts 154

Figure 7.3 H_2-TPR profiles of bimetallic xNiOyCuO/CeO_2 precursors and pure NiO and CuO 156

Figure 7.4 (A) Ni2$p_{3/2}$ and (B) Cu2$p_{3/2}$ XPS spectra of xNiyCu/$CeO_{2-\delta}$ catalyst reduced at 300°C for 3 h. 157

Figure 7.5 Surface and bulk ratios of Ni/(Ni+Cu) estimated by XPS the bimetallic xNiyCu/$CeO_{2-\delta}$ catalysts 159

Figure 7.6 H_2-TPD profiles of the 10Ni/$CeO_{2-\delta}$, 10Cu/$CeO_{2-\delta}$ and xNiyCu/$CeO_{2-\delta}$ catalysts 160

Figure 7.7 (A) Conversion of MA and (B) yields of SA on xNiyCu/$CeO_{2-\delta}$ catalysts at 210°C and under 5 MPa for 1 h duration 162

Figure 7.8 (A) Conversion of MA and (B) $TOF_{MA\rightarrow SA}$ versus the atomic ratio of Ni/(Ni+Cu) in initial 10 min course of the hydrogenation process 163

Figure 7.9 Selectivity of bimetallic xNiyCu/$CeO_{2-\delta}$, 10Cu/$CeO_{2-\delta}$ and 10Ni/$CeO_{2-\delta}$ catalysts after 8 h 164

Figure 7.10 Stability of the 6Ni4Cu/$CeO_{2-\delta}$ catalyst in cycling MA hydrogenation 165

Figure 7.11 XRD patterns of fresh and used 6Ni4Cu/$CeO_{2-\delta}$ catalysts 166

Figure 8.1 Typical metal–CeO_2 configurations of the CeO_2 –containing catalysts 169

Figure 8.2 XRD patterns of reduced xCeO_2@15Ni/SiO_2 catalysts 171

Figure 8.3 TEM and HRTEM images of reduced 15Ni/SiO_2 (A, C) and 3CeO_2@15Ni/SiO_2 catalysts (B, D) 173

Figure 8.4 (A) H_2-TPR profiles of xCeO_2@15Ni/SiO_2 catalysts and (B) the dependence of hydrogen consumption against the Ce content 173

Figure 8.5 Raman spectra of xCeO_2@15Ni/SiO_2 catalysts 174

Figure 8.6 H_2-TPD profiles of reduced xCeO_2@15Ni/SiO_2 catalysts 175

Figure 8.7 MA conversion over xCeO_2@15Ni/SiO_2 catalysts at 210℃ and 5 MPa 176

Figure 8.8 (A) Selectivity of SA and (B) yield of GBL over xCeO_2@15Ni/SiO_2 catalysts at 210℃ and 5 MPa 177

Figure 8.9 FT-IR spectra for cyclohexanone adsorption on 3CeO_2@15Ni/SiO_2 and 15Ni/SiO_2 catalysts under ambient temperature and 210℃ 179

Figure 8.10 Stability of the 3CeO_2@15Ni/SiO_2 catalyst in cycling MA hydrogenation 180

List of Accompanying Materials

Academic Thesis: Declaration Of Authorship

I, Xin Liao declare that this thesis and the work presented in it are my own and has been generated by me as the result of my own original research, *selective hydrogenation of maleic anhydride on surface engineered Ni-based catalysts*

………

………

I confirm that:

1. This work was done wholly or mainly while in candidature for a research degree at this University;
2. Where any part of this thesis has previously been submitted for a degree or any other qualification at this University or any other institution, this has been clearly stated;
3. Where I have consulted the published work of others, this is always clearly attributed;
4. Where I have quoted from the work of others, the source is always given. With the exception of such quotations, this thesis is entirely my own work;
5. I have acknowledged all main sources of help;
6. Where the thesis is based on work done by myself jointly with others, I have made clear exactly what was done by others and what I have contributed myself;
7. Parts of this work have been published as: *Applied Catalysis A, General*, 2014, 488, 256 and *Catalysts*, 2017, 7(9), 272

Signed:……………………………………………………………………………………………

Date:

Acknowledgements

It would not have been possible to finish my PhD project and write up my thesis without the guidance and help of the kind people around me who offered their valuable and kind help in the span of this study. I would like send my wishes and sincere appreciation to them.

First and foremost, sincere appreciation must go to my supervisor Dr. Zheng Jiang for his kind help and guidance in my research, timely discussions on my questions, invaluable advice and encouragement as well as trust in my abilities. I would like to express my gratitude to my second supervisor Prof. Martyn Hill who put his great efforts on revising my papers and guiding my research and proof-reading my publications. I must sincerely thank Prof. Yong-xiang Zhao, my co-supervisor at Shanxi University, China, who provided generous accesses to experimental facilities and fundamental support when I carried out collaborative research in the labs. I have been extremely lucky to have the supervisors and learned carefulness, focus and patience from them.

Besides my advisors, I would like to thank Dr. Stewart Parker and Prof. Martine Jones from the world-leading Rutherford Appleton Laboratory, STFC, who offered very useful training and discussion in collection and analyses of data from the state-of-the-art neutron scattering spectroscopy. It is memorable and invaluable research experience for me from various perspectives to work with the very kind people in that period.

I am warmly thankful to my colleagues and friends for being awesome and wonderful all the time. Without you guys, the lab life would be lonely and boring.

A special thanks to my family. Any word cannot express how grateful I am to my father and mother for all of the sacrifices that you have made for my benefits.

Chapter 1 Overview of Maleic Anhydride Hydrogenation Processes and Catalysts

1.1 Introduction

Since Paul Sabatier, the Nobel Prize Laureate, discovered the hydrogenation process wherein a small amount of metallic Ni can facilitate the addition of hydrogen to unsaturated compounds in 1897,[1] the knowledge of hydrogenation processes has continuously accumulated. Nowadays, catalytic hydrogenations have been widely applied in the petrochemical industry (hydrodesulphurisation, oil refining, etc.), ammonia synthesis, the conversion of syngas ($CO+H_2$) to liquid fuels, environmental protection (deNO_x, removal of SO_x and CO, etc.), food processing industries (fat hardening), and many more laboratory-scale research and development areas. The scientific and technological fundamentals of hydrogenation have been discussed in several books[2-5] and literature reviews,[6-8] whereas the hydrogenation of compounds containing multiple unsaturated bonds still faces great challenges regarding the product yield, selectivity, operational process and cost. These issues closely relate to catalyst performance (activity, selectivity and stability) and its operational conditions.

In the widespread industrial processes for fine chemicals and valuable pharmaceuticals, the chemo-selective removal of a specific group represents the prominent challenge in the upgrading of organic feedstock, which usually contains multifunctional groups of chemically reactive C=C, C=O, C≡C and C≡N bonds, a cyclic structure or fragments, or heteroatoms, etc.[9, 10] In those hydrogenation processes, indiscriminate hydrogenation is prone to occur, thus generating mixed products, which causes additional cost, energy penalties and environmental concerns with respect to purifying the targeted products. Therefore, it is highly desired to develop an efficient and economic hydrogenation process to achieve the highly efficient conversion of specific chemical bonds rather than multifunctional groups of the raw reactants.

The effective catalytic hydrogenation process primarily relies on the catalyst because the presence of the catalyst can open a different path with lower activation barriers. As the catalytic hydrogenation pathway presented in Figure 1.1 (A), the catalytic route (the blue line) can reduce the activation barrier by adsorbing and coordinating the reactants on the surface of catalysts, thus opening a more energetically favourable route than the non-catalytic reaction route (the red curve), which must overcome a considerably higher energy barrier (E_a). According to the Arrhenius law, the hydrogenation process over the catalyst will be accelerated while lowering the activation energy. Moreover, active sites of the catalyst can precisely control the adsorption and activation of specific groups, which alter activation energies and modify the kinetics of the catalytic system, giving rise to different selectivity in the reaction (Figure 1.1(B)). However, the control of catalytic selectivity has been hampered by both a lack of understanding of the structure and the properties of catalysts that define such selectivity and the limited range of synthetic tools available to prepare catalysts with the required specific properties.

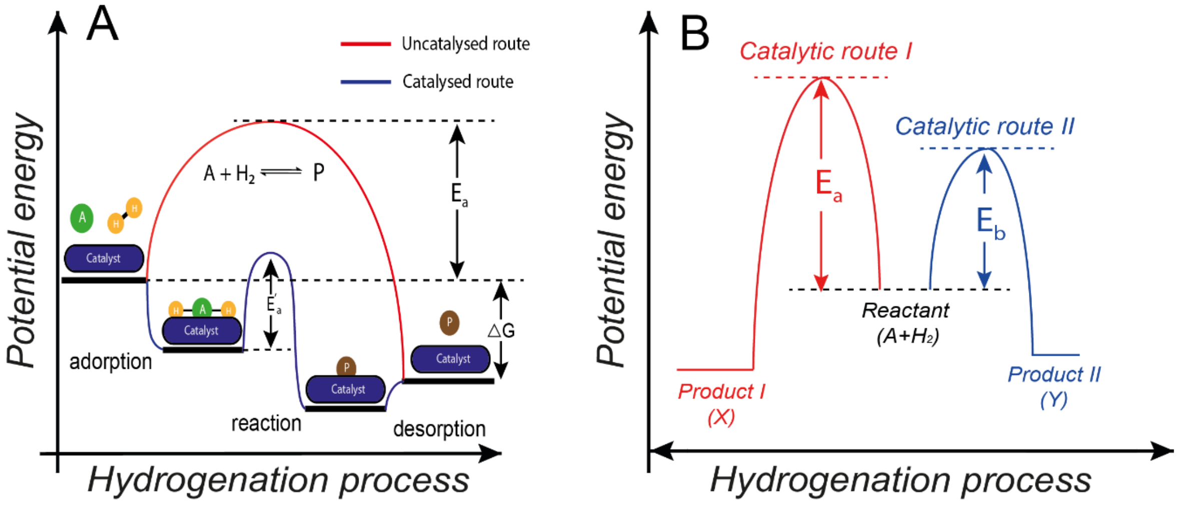
A
Uncatalysed route
Catalysed route
Potential energy
A + H₂ ⇌ P
Eₐ
Eₐ'
ΔG
A
H
H
Catalyst
P
adorption
reaction
desorption
Hydrogenation process
B
Catalytic route I
Catalytic route II
Eₐ
E_b
Reactant
(A+H₂)
Product I
(X)
Product II
(Y)
Potential energy
Hydrogenation process

Figure 1.1 Potential energy diagram for the catalytic and non-catalytic reactions

In general, hydrogenation catalysts can be simply classified into homogeneous catalysts[10] and heterogeneous catalysts[6]. Homogeneous catalysts usually display high activity and selectivity in the hydrogenation reactions because the catalyst and reactants remain in the same phase, thus offering all of the active sites accessible to the reactant. However, the major difficulty in separating the homogeneous catalysts from the reaction mixture restricts their utilisation in industrial practice.[10] Additionally, the organic ligands of the homogeneous catalysts represent serious concerns because they are generally not environmentally friendly. In comparison with homogeneous catalysts, the solid heterogeneous catalysts have many advantages, e.g. being eco-friendly, stable (a long lifespan) and easy to separate and regenerate. Therefore, the heterogeneous catalysts are preferred for large-scale application in industry.

The most common heterogeneous catalysts for hydrogenation are supported catalysts, comprising active metals and supports. The active metals can be costly noble metals (such as Pt, Pd, Ru, etc.) and/or cost-effective non-noble metals (mainly Ni, Cu, Co, etc.), which are dispersed on various supports with a desired surface area and porosity. The support can be oxides (acidic, neutral and basic oxides), carbon materials, zeolites, clays and other mesoporous materials.

For the metal/support catalysts, metal species usually play core roles in determining the catalytic activity and selectivity in hydrogenation reactions. For example, platinum and nickel are extensively used for the addition of hydrogen to olefins, aldehydes and ketones, aromatic compounds and so on, though they generally suffer from low selectivity in the hydrogenation of multifunctional molecules.[11] Pd is very active in C=C hydrogenation but rather weak in the saturation of the C=O group due to the small d bandwidth of Pd that restricts the adsorption of the reactants.[12] The Ru-based catalysts are considered effective catalysts for the selective hydrogenation of benzene to cyclohexene.[13] Copper-based catalysts prefer hydrogenation of C=O in esters to generate corresponding alcohols;[6] Co-based catalysts are more selective to C=O hydrogenolysis than C=C hydrogenation in the α, β-unsaturated carbonyl compounds, but such selectivity is still not high enough to meet the industrial requirements due to their poor activity.[14] Besides monometallic catalysts, bimetallic catalysts are also widely used for hydrogenation processes. Considering intimate contact between the two metals or alloy formation, geometric effects (a change in metal dispersion, decoration of the main metal by the second metals via surface enhancement) and an electronic effect (an electron transfer between the two metals with different electronegativity) are recognised to significantly influence the catalytic behaviour of bimetallic catalysts in hydrogenation reactions.

Besides the choice of metal species, the selectivity of catalysts is also significantly affected by the particle size of the active metal, the support, the metal-support interaction and the presence of promoters.[6, 12] Furthermore, the processes for the preparation and activation of catalysts, the selection of reaction conditions and the operational modes (liquid or gas phase) also play important roles in selective hydrogenation. Taking these complicated factors into account, the development of active and selective catalysts for the hydrogenation of multifunctional molecules remains a challenging task.

In all, because selectivity for the hydrogenation of an organic compound containing multifunctional groups is primarily dependent on the catalyst, the development of a robust and highly selective catalyst requires the consideration of a number of key influential factors, such as the active species, the catalyst structure, the nature of supports and their interaction with active species, etc.

In my PhD research, due to the desirable activity and relatively low cost, Ni-based catalysts are designed and developed for the liquid phase hydrogenation of maleic anhydride, a cyclic molecule containing multifunctional groups of a C=C bond, two C=O bonds and an anhydride group (O=C-O-C=O). Through correlation of their catalytic performance with the structure of catalysts, the active sites for selective C=C and C=O hydrogenation are investigated and defined. The research outcomes are expected to update the state-of-the-art catalysts and fundamentals for industrial MA hydrogenation. We hope the research outcomes may favour the rational design of novel and robust catalysts for various selective hydrogenation of unsaturated aldehydes, ketones and biomass-derived intermediates, which contain C=C and C=O functional groups in their molecules.

1.2 The socioeconomic importance of MA hydrogenation

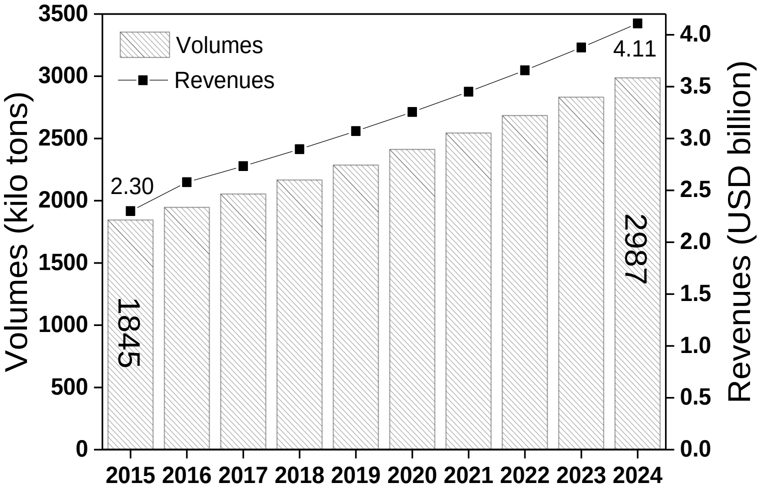

Figure 1.2 The global market of MA from 2015 to 2024[15]

Maleic anhydride is an important feedstock in the chemical industry in fabricating unsaturated polyester resins, fine chemicals, copolymers and additives for lubricating oil.[16] The relevant products are extensively used in the construction, automotive and marine industries.[9, 16] As shown in Figure 1.2, the global demand for maleic anhydride was 1,845.0 kilotonnes in 2015 and is expected to arrive at 2,987.2 kilotonnes by 2024 with a compound annual growth rate (CAGR) of 5.5%.[17] The global MA market was valued at US$2.3 billion in 2015 and is expected to grow to 4.11 billion in 2024 with a CAGR of 10.1% from 2015 to 2024.[17] Besides the huge global marketing demands, the resources of raw materials and the advancement of more efficient technologies also stimulated the massive production of MA. Currently, MA is mainly produced by the partial oxidation of n-butane[18] and benzene[9], both of which are facile and economic routes for the large-scale production of MA. In addition, a new technology that transforms renewable biomass resources to MA has also been developed, for example, the oxidation of furfural and 5-hydroxymethylfurfural[19-21], which can provide sustainable access to MA production.

The breakthrough in the economically massive production of MA offers a vast opportunity to convert MA into highly value-added intermediates in the chemical industry. Indeed, MA is an essential C_4 building block to synthesise a variety of valuable intermediates, such as succinic anhydride (SA), gamma-butyrolactone (GBL), 1,4-butanediol (BDO) and tetrahydrofuran (THF), via a hydrogenation process. Figure 1.3 schematically presents a few key processes relevant to MA hydrogenation. Succinic anhydride, generated via selective hydrogenation of the C=C bond in the MA molecule,[22] is an important industrial intermediate, owing to its wide application in the manufacture of polymeric materials, pharmaceuticals, agrochemicals, dyes, photographic chemicals, flavours, and fragrances.[23] The Energy Department of the USA has described SA as a compound of strategic importance in the future chemical industry.[24] In particular, SA is a critical starting material to produce polybutyrate succinate (PBS), a biodegradable polyester which is expected to grow with a CAGR of 38.9% from 2014 to 2020 because of its potentially high demand in packaging.[25] The market volume of SA in 2015 was about US$346 million and is subject to fast expansion. It is forecasted that the market of SA in 2020 will reach approximately US$1.9 billion with a fast CAGR of 27.8%.[25]

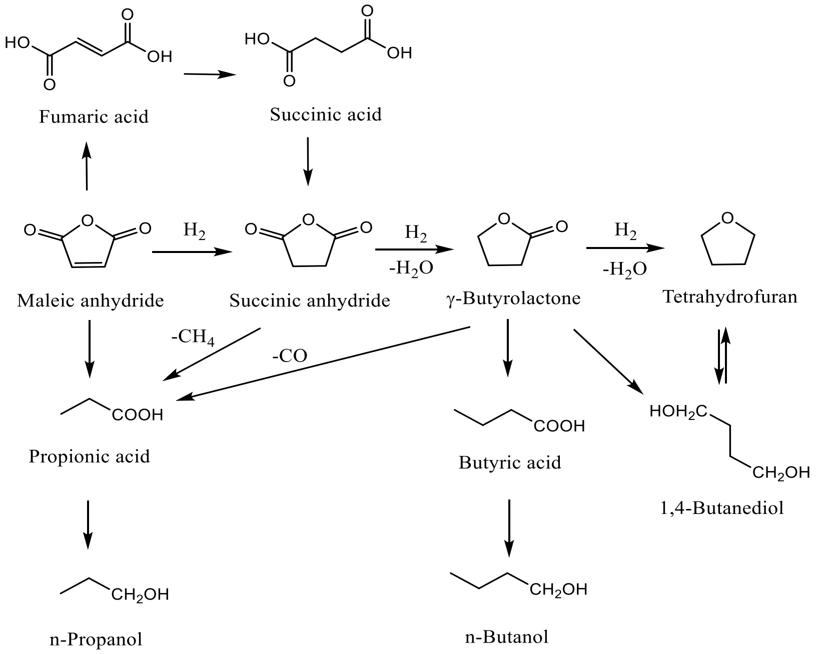
HO
OH
O
Fumaric acid
Succinic acid
Maleic anhydride
H2
Succinic anhydride
-H2O
γ-Butyrolactone
Tetrahydrofuran
-CH4
-CO
COOH
Propionic acid
Butyric acid
HOH2C
CH2OH
1,4-Butanediol
n-Propanol
n-Butanol

Figure 1.3 Schematic pathways of MA hydrogenation (adapted from Ref.[26])

GBL is another widely applied product from the partial hydrogenation of MA without breaking the five-membered ring structure. GBL is an excellent solvent with a high boiling point, which is widely used in polymer and paint industries and can be an eco-friendly alternative to the hazardous trichloroethane solvent. Based on its unique oxygen-containing five-membered ring structure, GBL is also an important intermediate for production of N-methylpyrrolidone[27] and N-vinylpyrrolidone[28]. The present annual marketing volume of pyrrolidones is more than GBP 100 million, mainly arising from their wide utilisation as eco-friendly chemicals and green solvents for water treatment.[25] Moreover, GBL is preferably used as a cell electrolyte in replacing the strongly corrosive acid liquid.[29-31] It is anticipated that the demand for GBL will be blooming due to the fast development of the battery industry.

Besides SA and GBL, further hydrogenation of MA can produce BDO and THF, which also find extensive applications in the chemical and polymer industries.[23] Actually, many important chemical companies have taken MA as a low-cost feedstock to manufacture BDO and THF. For example, the Davy process held in Johnson Matthey provides a flexible way to produce BDO, THF and even GBL from MA, in which the product ratio can be varied easily according to market requirements.[32] In addition, DuPont, Standard Oil, BASF and BP also have also developed their industrial processes to produce GBL, BDO and THF from MA.[33] However, as shown in Figure 1.3, some hydrogenation processes can crack the ring-structure MA into low-value by-products such as propionic acid/alcohol, butyric acid/alcohol, and even greenhouse gas CH_4. Although multifunctional groups in the MA molecule give facile accessibility to different high-value products, it should be made aware that the various products could derive from MA hydrogenation simultaneously, inevitably causing mixture generation. To produce the high-quality product, the subsequent purification requires excessive energy, processes and cost. Therefore, an efficient and effective MA hydrogenation process with high activity and selectivity is highly desirable in the chemical industry for reducing the energy penalty from such purification and hindering the production of chain compounds.

1.3 Advances of supported catalysts for MA hydrogenation

The appropriate choice of catalysts plays pivotal roles in determining the product distribution of MA hydrogenation. Various types of catalysts, such as homogeneous catalysts[34, 35], bare metal catalysts[36, 37] and supported catalysts[6, 18, 26, 32, 33, 38-43], have been extensively reported in open literature. Compared with homogeneous catalysts and bare metal catalysts, supported catalysts are the prevailing choice in MA hydrogenation due to their long lifespan, easy separation, collection and regeneration as well as flexibility in modulating the selectivity of products. This section critically reviewed the supported catalysts for MA hydrogenation in line with the active metallic species.

The metal species applied in hydrogenation include noble metals such as Pd, Pt, and Ru, as well as transition metals such as Ni and Cu. These metals displayed distinct catalytic performance in MA hydrogenation due to their different electronic structures. The intrinsic electronic properties of the metal species were reported to be crucial factors in dominating the activation and dissociation of hydrogen.[44] Moreover, the electronic structure can also affect the adsorption of reactants, which is a prerequisite of any catalytic reaction, and subsequent surface reactions. Besides the intrinsic properties of metal species, geometric structures of metal species, like crystallite size, shape and morphology, as well as surface defects were found to be exerting significant influence on the adsorption phenomenon.[44] This section reviewed catalytic performance of different metal species in MA hydrogenation and addressed their geometric and electronic properties in order to elucidate the effects of metal species on catalytic activity and selectivity as well as to provide clues as to the design of novel robust catalysts.

1.3.1 Pd-based catalysts

Pd-based catalysts are widely applied in the hydrogenation process, especially for C=C and C≡C hydrogenation.[45] However, metallic palladium (Pd^0) is relatively ineffective for C=O hydrogenolysis because of its fully occupied d band ($4d^{10}$) which weakens the adsorption and activation of carbonyls under the reaction conditions.[5,13] As shown in Table 1.1, the monometallic Pd/C catalyst was active for MA hydrogenation to SA, while it displayed low selectivity for GBL production.[46] In contrast, the Pd/TiO_2 catalyst displayed higher activity in GBL production[47], which was supposed to arise from the important roles of TiO_2 support in C=O hydrogenolysis. Infrared spectroscopy evidenced that the partially reduced $Pd\text{-}TiO_x$ interface synergistically enhanced C=O adsorption, thus favouring the reactivity of the C=O group.[48] However, the strong interaction between the $Pd\text{-}TiO_x$ interface and the C=O group may lead to over-hydrogenation. For example, the Pd/TiO_2 catalyst catalysed MA to butyric acid under 240°C and 3 MPa of H_2 pressure, with 100% of MA conversion and a 93.5% yield of butyric acid (BA).[49] Therefore, the suitable strength of C=O adsorption on the catalyst is a crucial factor for MA hydrogenation to GBL.

Besides the support effects on C=O adsorption, adding a second metal is another main strategy to tune C=O adsorption on the surface of Pd-based catalysts. As shown in Table 1.1, the industrial Pd-based catalysts modified with Re and Zr considerably altered the activity in MA hydrogenation and selectivity to GBL, BDO or THF, suggesting that the additional metallic species plays an important role in C=O hydrogenolysis. Nevertheless, only limited information can be acquired on these catalysts reported in patents. To understand the role of Re in Pd-based catalysts, Tapin and co-workers carefully characterised the structure of Pd-Re/TiO_2 catalysts and found that Re species in contact with Pd remained in the oxidation state (Re^{3+}), which synergistically enhanced the capability of Pd in C=O hydrogenolysis.[50]

Table 1.1 Pd-based catalysts used in the MA&SA hydrogenation

Reactions	Catalysts	T (°C)	P (MPa)	S (%)	Ref.
Industrial catalysts					
MA→THF	3%Pd-3%Re/C	190-200	17	90(THF)	[51]
SA→GBL	1%Pd-4%Re/TiO_2	200	3.5	90(GBL)	[50]
SA→BDO	1%Pd-4%Re/TiO_2	200	6.9	90(BDO)	[50]
SA→GBL	5%Pd-5%Zr/C	225	17	92(GBL)	[52]
MA→BDO	3%Pd-3%Ag-6%Re/C	175	9	74(BDO)	[53]
MA→GBL	3%Pd-6%Ag-3%Re/TiO_2 (Rutile)	230-260	5-8	98(GBL)	[54]
Journal reported catalysts					
MA→SA+GBL	1%Pd/SiO_2	240	5	23(GBL)	[46]
	1%Pd/C	240	5	9.7(GBL)	[46]
	1%Pd-0.5%Sn/SiO_2	240	5	33.2(GBL)	[46]
MA→GBL+BA	1%Pd/TiO_2	270	3	93.5(BA)	[49]
SA→GBL	2%Pd/TiO_2	160	15	80(GBL)	[47]

Note: T and P represent the temperature and pressure. S stands for the selectivity. BA is an abbreviation for butyric acid

Jung and co-workers found that the introduction of Sn into the Pd/SiO_2 catalyst can improve MA conversion to GBL under 240°C and 5 MPa of hydrogen pressure in comparison with the Pd/SiO_2 catalyst.[46] They assigned the formation of the Pd-Sn alloy to the enhanced GBL selectivity. Though CO chemical adsorption results suggested that additional Sn masked Pd atoms and decreased the number of Pd atoms exposed on the surface, Sn modified the electronic property of Pd by donating electrons to Pd, as evidenced by x-ray photoelectron spectroscopy (XPS). The Pd-Sn alloy not only enhanced C=O adsorption but also weakened the interaction between Pd and C=C and thus retarded the polymer formation and deposition on the surface of catalysts, which improved stability of the Pd-Sn/SiO_2 catalyst in MA hydrogenation.[55]

Chio and co-workers added Mo, Zn and Zr into Pd-Ni/SiO_2 catalysts in order to enhance MA hydrogenation to GBL.[56] In particular, very high selectivity to GBL (96.4%) was found over Pd-Mo-Ni/SiO_2 catalysts with 98% conversion of MA under 235°C and 9 MPa.[56] These results verify the significant role of dopants in facilitating C=O hydrogenolysis.

Changing the reaction conditions is another way in which to modulate the activity of MA hydrogenation over Pd-based catalysts. In 2002, Pillai and co-workers took advantage of supercritical CO_2 ($scCO_2$) as a reaction medium for MA hydrogenation on Pd/Al_2O_3.[57] They realised 100% MA conversion with more than 80% selectivity to GBL at 200°C and 2.1 MPa H_2 and 12 MPa CO_2. In comparison with a conventional organic solvent, the use of $scCO_2$ as a solvent for hydrogenation can enhance the dissolution of H_2 due to the miscibility of H_2 in $scCO_2$ and decrease the mass transfer resistance for the lower viscosity and higher diffusivity of $scCO_2$[58], thus giving rise to high hydrogenation activity and selectivity. In addition, the authors supposed that under supercritical conditions, the geometry of MA on the surface of Pd via the di-σ mode can be tuned with additional interaction of the C=O groups with the surface.[32] In addition, Wang and co-workers claimed that the small particle size of Pd promoted the reaction rate of MA hydrogenation and facilitated GBL selectivity in $scCO_2$.[59] Although the sustainable supercritical CO_2 solvent is a greener alternative to toxic organic solvents, the extremely high operational pressure would bring about security risks in large-scale application.

1.3.2 Ru-based catalysts

Recently, Ru-based catalysts have attracted great attention for their application in MA hydrogenation due to their high catalytic activity under mild conditions.[60] In some patents, metallic Ru species serve as active components for MA hydrogenation, as summarised and referred to in Table 1.2. It is notable that the metallic Ru species on the carbon nanotube (CNT) displayed 99.2% conversion of MA and approximately 100% selectivity of SA at 150°C and 1.5 MPa of H_2 pressure within 1.5 h.[60] Furthermore, Hong and co-workers prepared different carbon materials so as to support Ru nanoparticles for hydrogenating succinic acid to GBL in the aqueous phase.[61] They correlated the enhanced catalytic performance with the higher surface area of metallic Ru nanoparticles, which were supposed to offer more active sites for SA adsorption and activation.[61] However, it should be noted that metallic Ru catalysts enabled catalysing the hydrogenolysis of SA to propionic acid (PA) due to the intrinsic nature of Ru in the C-C cleavage.[62]

As shown in Table 1.2, the introduction of Re, Sn and Mo into Ru-based catalysts was active for MA and SA hydrogenation to BDO and THF with the removal of two C=O groups in the MA molecules. However, little knowledge on the additives in Ru-based catalysts is able to be obtained from open patents.

Table 1.2 Ru-based catalysts for MA&SA hydrogenation

Reactions	Catalysts	T (°C)	P (MPa)	S (%)	Ref.
Industrial catalysts					
SA→THF	1%Ru-4%Re/C	250	8.3	83 (THF)	[63]
MA→BDO	7%Ru-5%Sn/ZrO_2	225	14	96 (BDO)	[64]
MA→THF	4%Ru-1.3%Mo-1.4%Sn/C	250	13.9	85 (THF)	[65]
Journal reported catalysts					
SA→BDO	1%Ru-3%Re/C	180	8	71 (THF)	[62]
MA→SA	0.2%Ru/CNT	150	1.5	99 (SA)	[60]
SA→GBL	2%Ru/C	240	6	67 (GBL)	[61]

Note: CNT represents carbon nanotube

Di and co-workers systematically investigated the performance of bimetallic Re-Ru/C catalysts in the aqueous hydrogenation of succinic acid in order to shed light on the roles of Re and Ru in the bimetallic catalyst. As characterised by TEM, high-angle annular dark-field STEM (HAADF-STEM), and XPS, the bimetallic Ru-Re/C catalyst exhibited high dispersion of the bimetallic Ru-Re phase and strong Ru-Re interaction, which promoted the activation and adsorption of hydrogen and succinic acid. Their kinetic studies showed that the bimetallic Ru-Re/C catalyst decreased the apparent energy barrier of SA→GBL, whereby leading to superior activity of SA→GBL to monometallic Ru/C and Re/C catalysts.[62] Furthermore, the bimetallic Ru-Re phase was able to hinder the hydrogenolysis of SA to propionic acid, thereby enhancing the selectivity of GBL on the bimetallic Ru-Re/C catalyst in the hydrogenation process.[62]

1.3.3 Pt-based catalysts

Pt-based catalysts are also widely investigated in MA hydrogenation. For instance, Regenhardt and co-workers prepared a series of Pt-based catalysts supported on Al_2O_3, SiO_2 and SiO_2–Al_2O_3.[66] These Pt-based catalysts exhibited high activity in MA hydrogenation, while the main product was propionic acid (PA) (selectivity of PA > 80%) over these three catalysts.[66] In addition, they found that the selectivity of SA on the three Pt-based catalysts depended on the acidic strength of the supports: the increase of acidity reinforced the adsorption of MA on the catalysts, which led to the decomposition of MA into small molecules like methane, and decreased the selectivity of PA.[66]

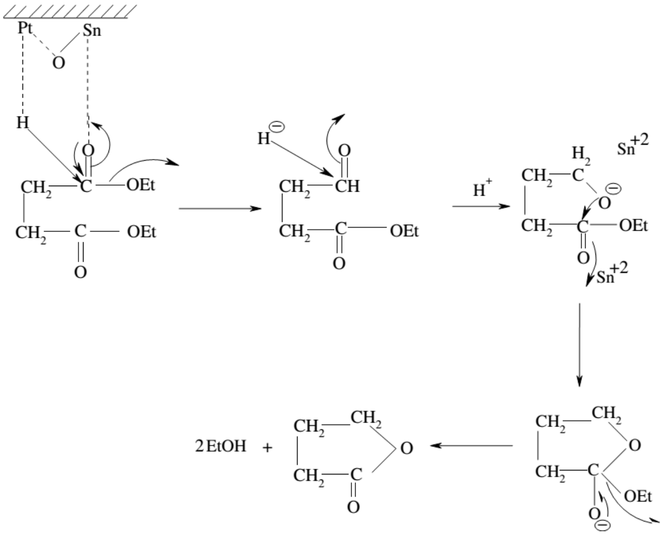

Figure 1.4 Plausible reaction pathway for selective GBL formation over Pt–Sn/Al_2O_3 catalyst[42]

Fabrication of bimetallic catalysts is a promising method to suppress the over-hydrogenation over Pt-based catalysts. Vaidya and co-workers added Sn into Pt/Al_2O_3 to fabricate the bimetallic Pt-Sn/Al_2O_3 catalyst and found that the Pt-Sn/Al_2O_3 catalyst was very selective to GBL (98%) in the liquid phase hydrogenation of diethyl succinate at 240°C and under 13.8 MPa of H_2 pressure.[42] Combined with the XPS results, the ionic Sn (Sn^{2+} and/or Sn^{4+}) was defined as a Lewis acid site in activating the C=O bond, as shown in Figure 1.4. However, the coverage of Sn on the Pt surface decreased the diethyl succinate hydrogenation conversion (~ 17.4%).[42]

It was reported that the Pt-Au/TiO_2 catalyst displayed high selectivity of GBL, arriving at 95% within 5 h in SA hydrogenation at 240°C and 5 MPa of H_2 pressure.[67]

The authors claimed that the metallic Pt species enhanced hydrogen dissociation on the gold surface and thus improved the activity of Au in the hydrogenation.[67] Although Pt-Au/TiO_2 catalysts were not effective for GBL production due to the long MA conversion time (5 h), the work evidencing the synergistic effects of the bimetallic Pt-Au species may play profound roles in enhancing selectivity; unfortunately, the authors did not define the nature of the synergistic effects.

In summary, noble metals such as Pd, Ru and Pt have been widely applied in MA hydrogenation due to their high activity in hydrogen activation. However, the intrinsic drawbacks of noble metals, either the weak adsorption of C=O on Pd, cracking the ring structure of MA into small molecules on Pt, or C-C cleavage over the Ru surface, are not beneficial for MA hydrogenation to high value-added products. Therefore, some additives, like Re, Sn and Zr, are added to tune surface properties of noble metals in order to block the side reactions and reduce the generation of less-value products. However, little research has been carried out to elucidate the effect of additives on the structure of catalysts, their interaction with the main active metal and to understand the catalytic mechanism at the molecular level, which play crucial roles in the design and development of effective catalysts for MA hydrogenation.

1.3.4 Cu-based catalysts

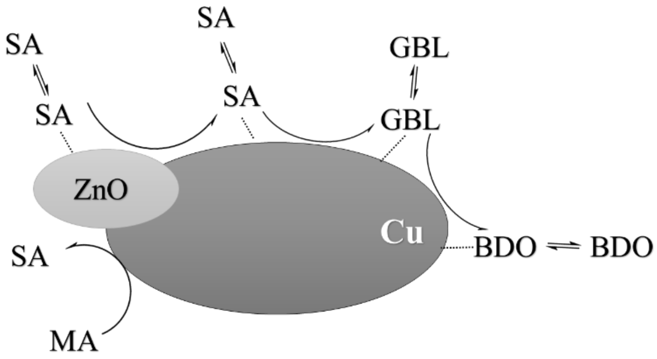

Figure 1.5 Pathway of MA hydrogenation to GBL and BDO over Cu-ZnO catalyst (adapted from Ref.[68])

Cu-based catalysts have been extensively investigated for the gas phase hydrogenation of MA. For example, Meyer group reported that the Cu/SiO_2 catalyst displayed high selectivity to SA (> 97% yield) in gas phase MA hydrogenation under ambient pressure and in the temperature range of 170-220°C, and the increase of temperature improved MA conversion on the Cu/SiO_2 catalyst.[40] In contrast, Cu-ZnO catalysts exhibited excellent activity in C=O hydrogenolysis, which facilitated MA hydrogenation to GBL and THF in the temperature range of 180-300°C at atmospheric pressure.[68, 69] Furthermore, Herrmann and co-workers conducted kinetic analysis of MA hydrogenation over Cu-ZnO catalysts and verified that, as shown in Figure 1.5, the presence of ZnO enhanced SA adsorption on the catalyst surface and facilitated SA diffusion to adjacent Cu species which acted as active sites for SA hydrogenolysis to GBL and BDO.[68] The Zn^{2+} species not only gave rise to an increasing yield of GBL but also led to the subsequent transformation of GBL into other by-products at high temperature.[69]

Except for the Zn^{2+} ions, other ionic species, such as Cr^{2+} and Cd^{2+}, were introduced to Cu-based catalysts to investigate their effects on the selectivity of GBL in MA hydrogenation.[69] Castiglioni and co-workers found that the Cr^{2+} species remarkably enhanced GBL production due to the strong inhibition of over-hydrogenation of GBL to other by-products, while Cd^{2+} diminished GBL production and resulted in a considerable deactivation of the Cu-based catalyst.[69] Since toxic Cr is unfavourable in the view of environmental protection, environmentally friendly alternatives to Cr were explored. For example, Cu-Zn-M-O (M=Cr, Al, Ga) catalysts were prepared to identify a suitable alternative to toxic Cr.[70] It was found that the catalysts containing Al and Ga were more active in MA hydrogenation to GBL than the Cr-containing catalyst.[70] Considering the high cost of Ga, Al is an economic and promising alternative to Cr for the hydrogenation catalyst. They further optimised the ratio of Cu/Zn/Al in the Cu-Zn-Al-O catalysts and found that the catalyst with an atomic ratio of Cu:Zn:Al=41.5:41.5:17 displayed the best catalytic performance of MA hydrogenation to GBL.[70]

Jiang group prepared a series of Cu-Zn-M-O (M=Ti, Zr and Ce) catalysts and compared their catalytic performance in the gas phase hydrogenation of MA within 220–280°C.[71, 72] They found the introduction of M_xO_y (M=Ti, Zr and Ce) into the Cu-Zn-O catalyst promoted the reduction of CuO and enhanced the dispersion of Cu^0. The presence of M_xO_y (M=Ti, Zr and Ce) also reinforced the adsorption of MA molecules on the surfaces of the catalysts, leading to the high activity of MA hydrogenation over Cu-Zn-M-O (M=Ti, Zr and Ce) catalysts.[71, 72] It is noteworthy that Cu-Zn-Ti-O and Cu-Zn-Zr-O catalysts favoured the hydrogenation of MA to THF, while the presence of CeO_2 preferred hydrogenation of MA to GBL.[71, 72]

It was reported that the Cu-based catalysts possessed excellent initial activity in MA hydrogenation but suffered from fast deactivation.[40, 73] For example, the Cu/Al_2O_3 catalyst exhibited relatively high selectivity to GBL (25%) with 50% conversion of MA in the initial 1 h course of the gas phase MA hydrogenation at 140 °C, while the GBL yield rapidly dropped down to ~ 5% as the reaction was prolonged to 7 h.[73] Yu and co-workers reported that $Cu\text{–}CeO_2\text{–}Al_2O_3$ (molar ratio of Cu:Ce:Al

=1:1:2) showed excellent catalytic performance in the gas phase hydrogenation of MA to GBL at 220–280°C, where both the conversion of MA and the selectivity of GBL remained 100% within 2h hydrogenation, but the catalysts also deactivated rapidly.[74] The severe deactivation was due to serious coverage of active Cu sites by wax-like polymers as observed by scanning electron microscopy (SEM).[74]

There are three main causes of the catalyst deactivation: (a) the carbon deposition on the surface of the catalyst during the reaction; (b) very strong adsorption of the reactant (MA) and/or main product (SA) on the surface of catalyst; (c) sintering of the accessible metallic fraction. To obtain more details on the deactivation of Cu-based catalyst, Meyer and co-workers conducted kinetic modelling using a deactivation model with residual activity (DMRA) to investigate the deactivation mechanism of the Cu/SiO_2 catalyst in the gas phase MA hydrogenation. They claimed that the severe deposition of carbonaceous compounds on the copper surface was responsible for catalyst deactivation.[40] According to DMRA modelling, the authors revealed that the type of MA adsorption on the Cu surface dominated SA production or coke formation. In detail, if MA interacted simultaneously with two neighbouring Cu^0 sites in di-σ mode (see Figure 1.7), SA production was preferential because the C=C bond was preferentially activated. However, if MA strongly adsorbed on a single Cu^0 site as π adsorption, the MA molecule preferred to polymerise to the coke precursor that masked the active sites and led to the deactivation of the catalyst.

In summary, a Cu-based catalyst, particularly Cu-Zn composites, can effectively convert MA molecules to GBL, THF and BDO. To tune the activity of selectivity, various additives, including Ti, Zr, Ce, Al and even toxic Cr, have been introduced to the Cu-Zn catalyst. The problem related to the complicated components of Cu-based catalysts is that the certain active sites and synergistic roles of the additional promoters in catalytic hydrogenation cannot be clearly identified, which restricts an in-depth understanding of the catalytic mechanism of MA hydrogenation over Cu-based catalysts. The other drawback of the Cu-based catalyst is the rapid deactivation due to coverage of polymers on the Cu^0 sites, observed on both monometallic Cu/SiO_2 catalyst and the $Cu–CeO_2–Al_2O_3$ catalyst with multiple components. The severe deactivation limits the industrial application of Cu-based catalysts. Therefore, it is highly desirable to synthesise a novel structure of the Cu-based catalyst with fewer components and higher stability for MA hydrogenation.

1.3.5 Ni-based catalysts

For MA hydrogenation, the Ni-based catalyst is deemed an eco-friendly and low-cost alternative to expensive noble metal catalysts. Because Ni is the fourth most abundant transition metal on the earth just after Fe, Ti and Zr, its price is much lower than that of noble metals (11.83 USD/kg, 1/2569 of the price of Pd).[11] More importantly, Ni-based catalysts are very active in the hydrogenation reaction due to the powerful ability of Ni in hydrogen activation.[44] Great efforts have been made to investigate the catalytic reactivity of Ni in MA hydrogenation and develop new Ni-based catalysts.

Raney Ni was the simplest nanoparticle Ni catalyst that can catalyse MA hydrogenation to SA in acetic anhydride at 100°C and 2.5 MPa of H_2 pressure, achieving 99.6% conversion of MA and 100% selectivity of SA in 360 min.[37] The activity of Ni nanoparticles is highly relevant to the synthesis methodology. Ni nanoparticles prepared by the reduction of nickel acetate using hydrazine hydrate displayed superior catalytic performance to Raney Ni with 99.8% MA conversion and 100% selectivity of SA at 80°C and 2 MPa of H_2 pressure. The superior catalytic performance of the novel Ni nanoparticles was mainly due to the smaller particle size and larger surface area.[37]

Relative to the bare metallic Ni nanoparticles, various supported Ni catalysts were more preferential in MA hydrogenation, including Ni/Clay[75], Ni/SiO_2[76] and Ni/Al_2O_3[73], displaying high activity in MA hydrogenation to SA under mild reaction conditions. Compared with other supported transition metals, the Ni-supported catalysts possessed higher catalytic activity in MA hydrogenation, as shown in Figure 1.6. The supported TM/CeO_2 catalysts showed higher activity but very similar activity trend to that observed on the TM/Al_2O_3 (see Chapter *4*), suggesting that Ni species are more active in MA hydrogenation.

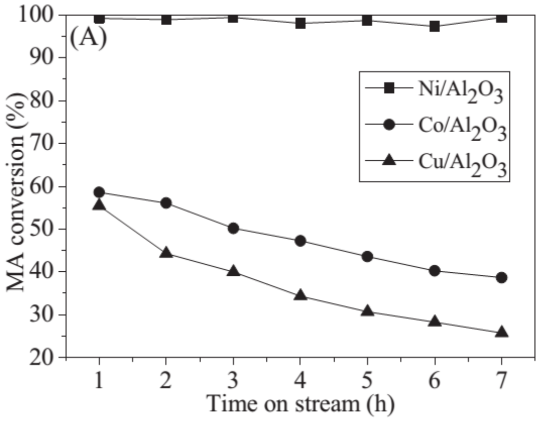

Figure 1.6 Comparative study of MA hydrogenation over Co/Al_2O_3, Ni/Al_2O_3 and Cu/Al_2O_3 catalysts at 140°C and 0.5 MPa[73]

One of the most important aspects in the design of the supported Ni-based catalysts is to determine the optimal Ni-loading amount. Li and co-workers prepared a series of xNi/HY-Al_2O_3 catalysts with different Ni loading. They found that the selectivity of MA hydrogenation over xNi/HY-Al_2O_3 catalysts was dependent on the amount of Ni loading: the 5Ni/HY-Al_2O_3 catalyst was inactive for GBL production, but the 30Ni/HY-Al_2O_3 catalyst exhibited the highest activity in GBL production.[43] The formation of large Ni particles with a dense surface in the large Ni loading catalysts was likely devoted to the high selectivity of GBL. Similar results were observed in the hydrogenation of crotonaldehyde on the Pt/SiO_2 catalyst, where the large Pt particles with a dense surface can provide a greater fraction of a closed-packed structure of the (111) surface to adsorb the C=O group.[77] Similarly, Gao and co-workers also found that the increasing Ni content can improve the GBL selectivity over the Ni/ZrO_2-SiO_2 catalyst, where 13Ni/ZrO_2-SiO_2 showed low selectivity to GBL (0.98%) at 100% MA conversion, while the GBL selectivity on the 30Ni/ZrO_2-SiO_2 catalyst was remarkably improved (14.98%) under the same reaction conditions.[78] Moreover, Meyer claimed that the loading-dependent selectivity of MA hydrogenation was related to the nickel particle size and Ni-support interaction: the small metallic Ni nanoclusters strongly interacted with the SiO_2-Al_2O_3 support and favoured improving SA selectivity, whereas the large Ni nanoparticles weakly bounded to the support which preferred to enhance GBL selectivity.[79] The Ni particle effects also related to the support and synthesis methodologies applied. For example, Bertone found that the Ni/SiO_2 catalyst of smaller Ni particles exhibited higher selectivity to GBL than the Ni/SiO_2 catalyst of larger Ni particles, where the former was prepared by the precipitation–deposition method and the latter by the impregnation method.[76] This result implied that many other properties besides the particle size of the Ni-based catalysts would affect their performance in MA hydrogenation.

Besides the size of nickel species, the catalyst support represents another crucial factor in determining the catalytic activity and selectivity of Ni-based catalysts for MA hydrogenation. Table 1.3 summarised several typical results extracted from recent publications. For example, Torres reported that the product selectivity of MA hydrogenation was not dependent on the Ni loading for Ni/TiO_2. They found that all of the Ni/TiO_2 catalysts with varying Ni loading (5 wt%, 10 wt% and 15 wt%) showed nearly 100% selectivity to SA even though higher MA hydrogenation rates were displayed on the samples with higher Ni loading.[82]

Table 1.3 Comparison of the liquid-phase maleic anhydride hydrogenation over Ni-based catalysts on different supports

Catalysts	Reaction condition	C(%)	S (%)		Ref
			SA	GBL	
15Ni/SiO_2	T=210°C, P=5 MPa, t= 8 h 0.1 g catalyst	100	88.0	12.0	Chapter 8
10Ni/Al_2O_3	T=210°C, P=5 MPa, t= 8 h 0.1 g catalyst	100	85.0	15.0	[26]
10Ni/TiO_2-SiO_2	T=240°C, P=5 MPa, t= 6 h 0.1 g catalyst	100	95.1	4.6	[80]
30Ni/ZrO_2-SiO_2	T=180°C, P=6 MPa, t= 4 h 0.1 g catalyst	100	31.6	69.4	[81]
10Ni/CeO_2	T=210°C, P=5 MPa, t= 8 h 0.1 g catalyst	100	65.0	35.0	[26]

Tailoring the support surface properties is an appropriate and effective strategy to tune the Ni-support interaction, which significantly affects their catalytic performance in MA hydrogenation. Regenhardt and co-workers comparatively studied the influences of different supports on Ni catalysts, where three classical supports-SiO_2, SiO_2-Al_2O_3 and zeolite H-BEA, were adopted for Ni catalysts in the gas phase MA hydrogenation.[83] Through estimating the H_2 consumption of three catalysts in the H_2 temperature-programmed reduction, they compared the reduction degree of Ni species in the three catalysts, and then ranked the strength of the Ni-support interaction as the following pattern: Ni/HBEA > Ni/SiO_2–Al_2O_3 > Ni/SiO_2, according to the reduction degree of Ni species. The Ni/H-BEA catalyst with the strongest metal-support interaction was more active in GBL production than the Ni/SiO_2-Al_2O_3 and Ni/SiO_2 catalysts which possessed medium and low degrees of Ni-support interaction.[83] However, the strongest Ni-support interaction contributed to the rapid deactivation of the Ni/H-BEA catalyst.[83] The quantitative analysis of the metal-support interaction and the nature of the interaction remain unsolved, leading to weak firmness in guiding catalyst development via tailoring metal-support interaction.

The researchers from the same group further investigated the surface properties of the supports for the Ni-based catalysts and correlated with their activity and selectivity of MA hydrogenation.[76] They found that the Ni/SiO_2-Al_2O_3

catalyst promoted GBL production in comparison with Ni/SiO_2. Based on NH_3 temperature-programmed desorption (TPD) results, the authors suggested that the strong Lewis acidity of the SiO_2-Al_2O_3 support was a key factor in enhancing GBL production.[83] In general, the Lewis acid sites can coordinate with O atoms in the carbonyl group and decrease the electron density of the C=O bond, thus improving the reactivity of the C=O bond.[6, 12]

Some researchers have suggested that the surface defects on the catalyst supports can interact with the C=O group and reinforce the adsorption of C=O, and consequently enhance the GBL selectivity. A typical example is that the ZrO_2 modified Ni/SiO_2 catalyst showed better GBL selectivity than the Ni/SiO_2 catalyst, which was assigned by the authors to the presence of Zr^{4+}-defects that selectively activated the C=O group.[81] Interestingly, the TiO_2 modified Ni/TiO_2-SiO_2 catalysts also exhibited superb performance of MA hydrogenation to GBL, in which the enhancement of TiO_2 was attributed to the strong Ni-TiO_2 interaction and the presence of Ni-TiO_x sites.[80] However, it is worth noting that the product selectivity of Ni/TiO_2-SiO_2 catalysts is different from Ni/TiO_2 catalysts.[82]

Ni-based bimetallic catalysts have also found widespread employment in MA hydrogenation. Compared to the monometallic Ni/Al_2O_3 and Pt/Al_2O_3 catalysts, the bimetallic Ni-Pt/Al_2O_3 catalysts exhibited higher catalytic activity and selectivity in the hydrogenation of MA to SA due to the formation of the Ni-Pt alloy.[84] In addition, Bertone and co-workers reported that adding a small amount of Cu into the Ni/SiO_2-Al_2O_3 catalyst facilitated the conversion of MA to GBL.[85] They found that the additional Cu^{2+} species improved the dispersion of Ni species with small particles and favoured the formation of the Ni^{2+} phase that strongly interacted with support. The strong Ni-support interaction favoured the formation of Ni^{2+} species that acted as the active sites for hydrogenolytic SA to GBL.[85] Due to the distinct physical and chemical properties of monometallic Ni catalysts, the bimetallic Ni-based systems have been extensively applied in the selective hydrogenation reactions,[6, 11] however, little knowledge on MA hydrogenation over bimetallic Ni catalysts has been correlated between the catalyst structure and surface properties.

In summary, Ni-based catalysts showed great promise for MA hydrogenation under relatively mild conditions. The individual Ni species display high activity in C=C hydrogenation, whereas the selective hydrogenolysis of C=O depends on the particle size of nickel, the metal-support interaction, dopants and support properties.

1.3.6 Catalytic challenges

The open literature and patents documented extensive efforts to develop effective catalysts in MA hydrogenation, particularly using various metals and oxides to tune the activity and selectivity of the catalysts for MA hydrogenation. However, the rational design of active and selective heterogeneous Ni-based catalysts is still a challenging task due to multiple interdependent factors determining the catalyst performance, including the metal and support selection, metal precursor, catalyst preparation and activation, as well as the reaction conditions and operational modes (e.g. gas or liquid phase hydrogenation).

Based on the above critical review of the present catalysts, three main challenges are concluded below:

(A) *to develop economic and effective alternatives to noble metal catalysts*. Current industrial catalytic systems involve precious metals, such as Pd, Ru, Pt and Re, but they are too expensive for large application. The Cu-based and Ni-based catalysts are regarded as potential alternatives to the costly noble metal catalysts; however, their activity, selectivity and stability need to be further improved. It has been realised that Cu-based catalysts possessed high activity and selectivity in the initial hydrogenation process, but they suffered from rapid deactivation, even in the 2h hydrogenation operation.[74] Ni-based catalysts are not very stable in hydrogenation either. For example, the Ni/HY-Al_2O_3 completely converted MA to SA with 95% selectivity at 190°C and 1 MPa H_2 flow in a fixed bed reactor for around 20h, whereas the SA yield and MA conversion dropped from 95% to 76% and 100% to 83%, respectively.[43]

(B) *to correlate the catalytic performance with the structure of the catalyst.* It is very important to rationalise the design of novel catalysts for MA hydrogenation. In the literature, many strategies, including adjusting the preparation of catalysts, the introduction of additives and promoters, and the modification of support properties, have tentatively proven effective methodologies to improve activity and selectivity of catalysts. For supported catalysts, the metals with various electronic configurations can exhibit different properties in hydrogenation. On the other hand, the nature of the support, such as porosity, acidity/basicity, and reducibility can play important roles in the catalytic performance. When catalysts contain diverse metals, it is difficult to define the active component for the hydrogenation reaction. Thanks to the complexity of catalysts, it is challenging work to establish a clear relationship between the catalytic performance and catalyst structures and properties.

(C) *to unfold the mechanism of hydrogenation and catalytic deactivation.* The rational design of active catalysts with specific selectivity relies on the solid knowledge of reaction mechanisms. A clear catalytic mechanism is conducive to define the active sites for C=C hydrogenation and C=O hydrogenolysis. Previous research has proven that catalytic hydrogenation is a multistep process, including adsorption, surface reactions and desorption of products.[6] Each step is rather complicated and involves many factors. For example, on adsorption, competitive/non-competitive adsorption or dissociative/non-dissociative adsorption should be taken into account. The adsorption geometries of reactants play a decisive role in the subsequent surface reactions. A surface reaction involves various intermediates and determines the selectivity of the reaction. Besides the evolution of intermediates, the energy change is also important which determines the energy barriers and rate-limiting step in the hydrogenation process. However, the single conventional experimental method usually fails to gain insights into the surface reaction, as the surface reaction is a transient process. Therefore, comprehensive methodologies, including experiments and computational ways are highly required to unfold the mechanism of hydrogenation.

1.4 The mechanism of MA hydrogenation

Based on the literature review of MA hydrogenation on various metal surfaces, MA hydrogenation involves multistep reactions, in particular two important reactions relate to C=C hydrogenation and C=O hydrogenolysis with their enthalpies as listed below.[86]

$$\mathrm{MA} + \mathrm{H_2} \rightleftharpoons \mathrm{SA} \qquad \Delta_f H^{\theta}_{MA\rightarrow SA} = -133.8\ \mathrm{kJ/mol} \tag{1.2}$$

$$\mathrm{SA} + 2\mathrm{H_2} \rightleftharpoons \mathrm{GBL} \qquad \Delta_f H^{\theta}_{SA\rightarrow GBL} = -108.7\ \mathrm{kJ/mol} \tag{1.3}$$

It is revealed that the hydrogenation of the C=C bond has high exothermicity of around 133.8 kJ/mol, while the C=O hydrogenolysis process releases slightly less heat (~ 108.7 kJ/mol). According to the van't Hoff equation:[87]

$$lnK = -\Delta H^{\theta}/(RT) + \Delta S^{\theta}/R \tag{1.4}$$

where K is the equilibrium constant, R is the universal gas constant, roughly 8.314 J/(mol·K), T is the absolute temperature and ΔH^{θ} and ΔS^{θ} are respective to the standard enthalpy and entropy of the reaction. Because the values of ΔH^{θ} for C=C hydrogenation and C=O hydrogenolysis are both negative, a decrease in the reaction temperature will increase the K, namely promoting the hydrogenation reactions. Moreover, the increase of H_2 pressure can also promote C=C hydrogenation and C=O hydrogenolysis according to Le Chatelier's principle.[87] The above discussions of MA hydrogenation thermodynamics reveal low reaction temperature and high H_2 pressure are beneficial to MA hydrogenation for higher MA conversion.

In practice, in order to control the selectivity of the reaction product, kinetic issues, including adsorption, transition states and desorption of products, which significantly affect the activity and selectivity of MA hydrogenation, should be carefully investigated. The recent advances in kinetics for MA hydrogenation are thus critically reviewed following.

1.4.1 MA adsorption on metal surface

After systematic investigations into the behaviour of MA adsorption on the metallic Pd surface through computational simulations, Pallassna and co-workers proposed three primary chemisorption modes: (1) atop (η^1) adsorption, (2) π adsorption and (3) di-σ adsorption, which are shown in Figure 1.7.[88, 89]

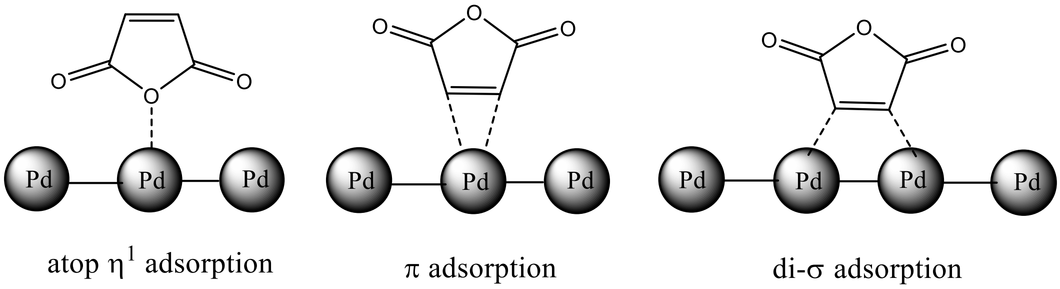

Figure 1.7 The proposed different adsorption modes of MA on metal surface[90]

In the atop (η^1) adsorption mode, the ring oxygen of MA is binding to the Pd surface. The π adsorption is binding of MA via a π bond through the ethylenic moiety where the cyclic plane of the MA is parallel to the Pd surface. For this mode, there likely exist additional interactions between the C=O groups and the catalyst surface. In the di-σ adsorption mode, maleic anhydride is binding to different Pd sites via two σ bonds from the ethylenic moiety, in which the cyclic molecular plane of MA is nearly parallel to the surface.[90] Owing to various geometric and electronic structures of metal surfaces, MA adsorption may display different configurations with varying binding energy (BE), as summarised in Table 1.4.

Based on the simulation results, Pallassana et al. proposed that the preferential adsorption mode of MA on the surface of Pd was di-σ adsorption with an adsorption energy of -83 kJ/mol, which is higher than the adsorption energies of η^1 and π modes. The results suggested that di-σ adsorption is the most stable mode and can lower the overall energy of the MA/Pd system.[88] However, for MA adsorption on Re(0001), π adsorption became the most favourable mode with the highest adsorption energy of -210 kJ/mol relative to η^1 and di-σ adsorption. The strongest π adsorption was due to additional interactions between carbonyl groups and the Re(0001) surface.[89]

Table 1.4 Binding energies of MA adsorption on different metal surfaces

Metal surface	BE of adsorption mode			Ref.
	atop (η^1) adsorption (kJ/mol)	π adsorption (kJ/mol)	di-σ adsorption (kJ/mol)	
Pd (111)	-28	-34	-83	[88]
Re(0001)	-38	-210	-200	[89]
Pd_{ML}/Re(0001)		-22	-72	[89]
Pd_{ML}/Mo(110)		-65	-66	[89]
Pt(111)		-29	-80	[91]

Note: the results were based on the monolayer (ML) adsorption

The same group also constructed bimetallic overlayers of Pd_{ML}/Mo(110) and Pd_{ML}/Re(0001) and found that the adsorption energies for MA on the bimetallic Pd_{ML}/Re(0001) and Pd_{ML}/Mo(110) surfaces were 10-20 kJ/mol weaker than that on monometallic Pd(111).[89] It is notable that the atop (η^1) adsorption mode on the bimetallic surface was even absent. The weaker interplay between C=C and the bimetallic surfaces was attributed to the strong Pd-Re and Pd-Mo interaction. The strong bimetallic interaction shifted the d band centre of the Pd layer away from the Fermi level.[86] These simulation results unravelled a crucial concept wherein the electronic structure can significantly influence the adsorption mode of MA on the metal surface and corresponding binding energy.

Sinha et al. gave an example of MA adsorption on the Pt(111) surface. They suggested that MA desorbed from the Pt(111) surface at 240 K and that the MA would decompose to produce C_2H_2, CO and CO_2 at 360 K.[91] The preferential adsorption of MA on the Pt(111) surface also followed the di-σ adsorption mode, bridging the two nearest neighbour Pt atoms. Unlike parallel adsorption of MA on the Pd surface, the MA adsorption on Pt(111) displayed a buckling effect, pushing the O atom in the C=O group far away from the Pt(111) surface.[91] This discrepancy was assigned to the different chemical properties of Pd and Pt surfaces.

1.4.2 MA adsorption on oxide surface

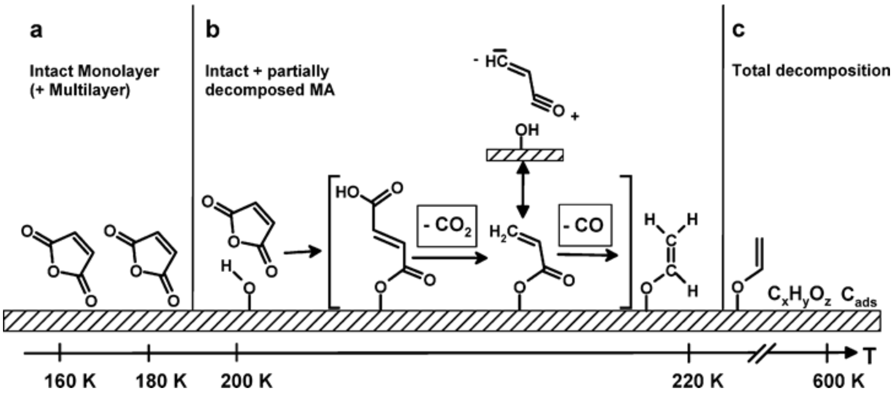

Figure 1.8 MA adsorption and decomposition on ZnO surface[92]

Besides the chemical adsorption of MA on the metal surface, the support surface can adsorb the MA more or less, which would influence the catalyst performance. Girol and co-workers explored the adsorption behaviour of MA on the (1010) surface of ZnO using in situ XPS and NEXAFS spectra.[92] The results revealed the MA adsorption mode was dependent on temperature, as schematically shown in Figure 1.8. As the temperature was below 180 K (region a), the MA adsorption on the crystal surface of ZnO was via oxygen of the carbonyl group and the ring structure of MA remained intact. Increasing the temperature to 220 K (region b), a fraction of the MA monolayer adsorbed on ZnO underwent decomposition: the first step was assumed to be a ring-opening reaction promoted by surface hydroxyl groups, and then proceeded via intermediary formed decarboxylation and decarbonylation products, respectively, giving rise to stable adsorbed surface species like ethenolate. Within the 180-220 K temperature regime, more complex surface reactions such as oligomerisation and polymerisation processes probably occurred too, leading to deactivation of the catalysts. The decomposition proceeded as the temperature increased above 220 K (regime c) until total decomposition at 600 K. They found the above adsorption modes highly depended on the sub-surface oxygen of ZnO. The near-stoichiometric surfaces exhibited only low reactivity, while the defect-rich surface showed the highest reactivity.[92]

Additionally, Johansson and co-workers deposited MA onto (101), (100), and (001) TiO_2 single crystal surfaces in an ultra-high vacuum and investigated the surface binding with electron spectroscopy.[93] They found that the MA ring opened when MA molecules adsorbed on both (101) and (100) surfaces to form bindings similar to two carboxylic groups on TiO_2. In contrast, a different adsorption geometry was evidenced by XPS, in which the oxygen atom directly bonded to a Ti atom without a ring-opening reaction on the TiO_2(001) surface.[93] The discrepancy in the MA adsorption on these surfaces was due to the different coordination of Ti atoms on the individual surfaces. On the (101) and (100) surfaces, fivefold coordinated Ti atoms can provide an extra O atom and react with the anhydride group (O=C-O-C=O) to form two carboxylic groups, while fourfold coordinated Ti atoms on the (001) surface can offer active sites to directly bind to the oxygen atom in the MA molecule.[93] These results suggest that the surface adsorption geometry of MA on the oxide surface is tuneable via selective exposure of the crystal faces of the supports.

The above research suggests that the MA molecule prefers to bind onto the oxide surface via the C=O group and anhydride group (O=C-O-C=O) rather than the C=C group, which is different from MA adsorption on metal surface via C=C bonding. Therefore, oxide supports play pivotal roles in C=O adsorption and activation, and thus affect the product selectivity. Furthermore, creating surface defects of reducible oxide supports (ZnO, ZrO_2, TiO_2, etc.) is expectable to exert profound effects on the MA adsorption behaviour of carbonyl and anhydride groups.

1.4.3 Mechanism of C=C hydrogenation

In terms of C=C hydrogenation, the Horiuti-Polanyi mechanism, which is used for C=C bond hydrogenation in ethylene, has been taken into consideration for MA hydrogenation to SA.[88, 89] In this path, SA forms through two sequential C-H bond formation elementary steps after MA adsorption and hydrogen dissociation, as presented below:

$MA + * \leftrightarrow MA^*$ maleic anhydride adsorption

$H_2 + 2* \leftrightarrow 2H^*$ dihydrogen chemisorption

$MA^* + H^* \leftrightarrow MAH^* + *$ C-H bond formation

$MAH^* + H^* \leftrightarrow SA + 2*$ C-H bond formation

where $*$ represents the active site for MA hydrogenation and MAH* means the maleic anhydryl intermediate.

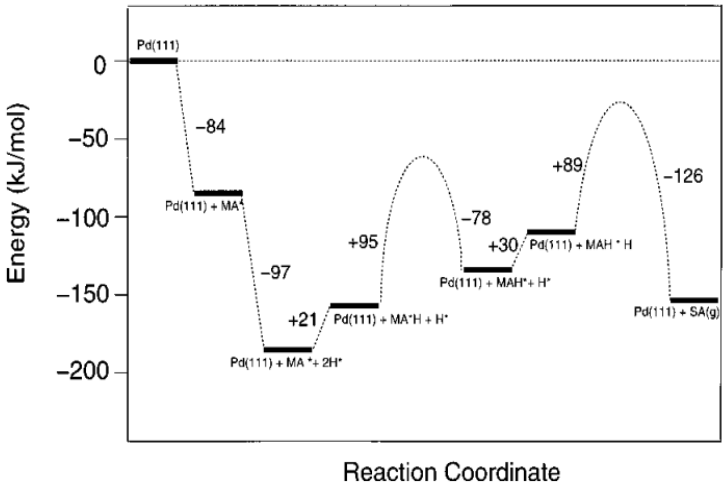

Figure 1.9 DFT-computed reaction energetics for the hydrogenation of maleic anhydride to succinic anhydride on a Pd(111) surface[88]

According to the Horiuti-Polanyi mechanism, Pallassana and co-workers simulated the pathway of MA hydrogenation to SA on the Pd (111) surface.[88] As shown in Figure 1.9, the calculated energies for individual elementary steps indicated that the hydrogen dissociation (-97 kJ/mol) and MA adsorption (-84 kJ/mol) on the surface of Pd were energetically more favourable (releasing energy). In contrast, the hydrogenation of maleic anhydride to maleic anhydryl possessed the highest intrinsic barrier (+95 kJ/mol) on Pd (111). The d band of Pd was found to be close to the antibonding σ_{CH*} orbital of maleic anhydryl, being able to strengthen the adsorption of C-H at Pd (111). As a result, extra energy was necessary for C-H desorption from the Pd (111) surface.

Furthermore, they compared the intrinsic barriers of hydrogenation of maleic anhydride to maleic anhydryl over Pd(111), Re(0001) and Pd_{ML}/Re(0001) surfaces and correlated the activation barrier with the d band position of three surfaces.[88] They found that the intrinsic barriers decreased as follows: Re(0001) (+118 kJ/mol) > Pd(111) (+95 kJ/mol) > Pd_{ML}/Re(0001) (+89 kJ/mol), contrary to their d band position relative to the Fermi level: Re(0001) (-1.16 eV) < Pd(111) (-1.98 eV) < Pd_{ML}/Re(0001) (-2.70 eV). The bimetallic Pd_{ML}/Re(0001) surface possessed the deepest d band position, which reduced the interaction between the C-H bond and the Pd-Re bimetallic surface, thus giving rise to the smallest C-H formation energy. Based on these results, the authors concluded that the average d band position of the surface metal layer far away from the Fermi level would benefit in decreasing the activation energy (Ea) of C-H bond formation.[88] They supposed that group IB metals, such as Cu, Ag and Au with full filled d orbitals (d^{10}), would exert profound influence on C-H formation.[88] However, the group IB metals were often not active enough for hydrogen activation[88], which restricted the overall reaction rate of MA hydrogenation. To date, there are no theoretical insights available into MA activation on other transition metals in publications.

1.4.4 Mechanism of C=O hydrogenolysis

There are few studies which have explicated the pathways for the C=O hydrogenolysis in MA hydrogenation over the heterogeneous catalysts. Hara and co-workers proposed a plausible pathway of SA hydrogenolysis to GBL over a homogeneous Ru-complex catalyst, as shown in Figure 1.10, wherein the C=O group coordinated with $RuHP_3$ and then anhydride ring opened to form a 3-formylpropionato Ru complex.[34] The 3-formylpropionato Ru complex was reduced by H_2 to form 3-formylpropionic acid which was subsequently subject to ring closure and forming GBL.[34] The authors noted that there was no solid experimental evidence proving the MA ring-opening process that they proposed; however, the presumed mechanism offered a clue with respect to unfolding the pathway of the C=O hydrogenolysis in MA hydrogenation. Interestingly, the MA ring-opening reaction mechanism for the homogeneous MA hydrogenation process was successfully applied to interpret the MA adsorption and decomposition on the ZnO[92] and TiO_2[93].

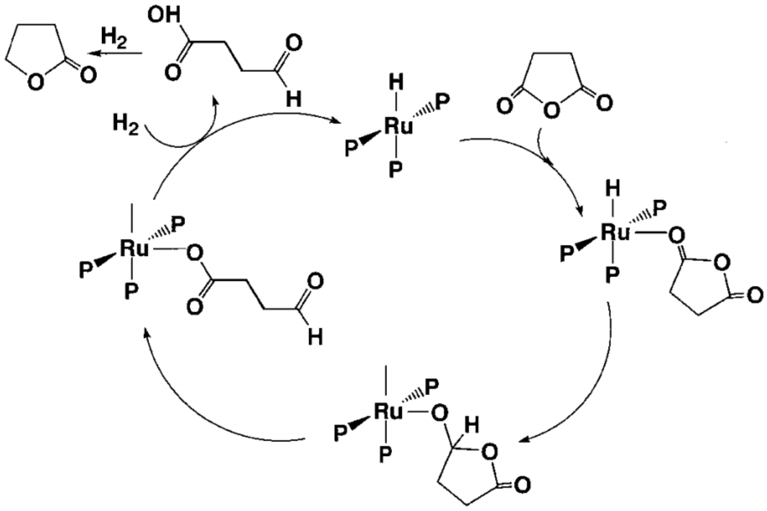

Figure 1.10 Presumed reaction mechanism over the Ru-based complex[34]

Although the mechanism of C=O hydrogenolysis in MA hydrogenation is not very clear, some crucial factors in C=O hydrogenolysis can be defined from studies on the selective removal of C=O groups of the multi-unsaturated aldehydes and ketones.[6, 12] The research efforts showed that the adsorption strength of the C=O group on the catalyst dominated the C=O reactivity in hydrogenation. As exemplified for the metallic Pd surface, the fully occupied orbitals ($4d^{10}$) of Pd are detrimental to the C=O adsorption, thus leading to the low activity of Pd in C=O hydrogenation.[2, 5] In contrast, the introduction of cationic promoters, such as Sn, Fe and Ge into Pd-based catalysts remarkably enhanced their catalytic activity in C=O hydrogenation[45]. The promotion effect of the cationic dopants was related to the activation of positively charged species $M^{\delta+}$ towards the C=O group, thus enhancing its reactivity in the hydrogenation reaction, as shown in Figure 1.11. A similar phenomenon is observed in the case of cupric chromite catalyst, wherein the C=O group strongly bonded with positive Cr^{3+} species and then showed high reactivity in C=O hydrogenation.[12] Based on these results, adding cationic species into supported catalysts was proven to be an effective strategy to enhance the reactivity towards C=O hydrogenolysis.[6]

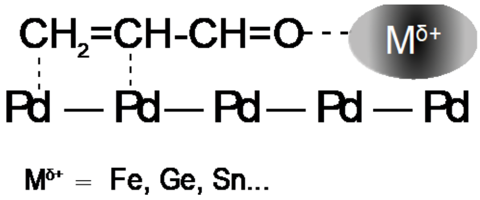

Figure 1.11 Schematic representation of the activation of the C=O bond in α , β - unsaturated carbonyls on Pd–$M^{\delta+}$[45]

As mentioned above, Re-, Sn- and Mo-modified Pd- and Pt-based catalysts have considerable activity in MA conversion to GBL, BDO and THF likely due to the enhancement of the cationic promoters in C=O activation.[46, 56] Besides the synergistic role of cationic promoters in C=O adsorption, the effect of promoters on the geometric and electronic structure of the main active metals and their subsequent impact on surface reaction, including hydrogen activation, insertion of atomic H into C=O bond and desorption, are highly desirable to unfold the structure-activity relationship in the selective hydrogenation.

1.5 Strategies for promoting MA hydrogenation catalyst

1.5.1 Active support-cerium oxide

As mentioned in the previous part, the catalyst support can exert a pivotal impact on the activity and selectivity of MA hydrogenation. In general, an important task for the support is to disperse the metallic active sites with a high proportion of surface atoms and protect them from sintering and aggregation during the reaction. A typical example is that mesoporous carbon with a high surface area promotes Ru dispersion and enlarges the metal surface area, and the resultant Ru/C catalysts showed excellent catalytic performance in converting SA to GBL.[61] Besides the surface area effects, the other properties of supports including pore volume, shape and morphology, acidity and basicity, and surface defects are crucial as well. From an atomistic and electronic mechanism point of view, the surface geometric configuration and the electronic properties of the support can modulate the properties of active metal, including the particle size, structure and component, shape, and chemical state, thus changing the catalytic reactivity. For example, the Ni/ZrO_2 catalyst promoted MA conversion to GBL due to the presence of ionic Zr^{4+}–O^{2-} bonds, which preferentially adsorbed the electron-rich C=O group.[81] Therefore, a suitable support choice is very important in tuning the activity and selectivity of MA hydrogenation.

Some reducible supports can offer active sites to activate the reactants and synergistically promote the conversion of reactants. These supports usually are reducible oxides, like TiO_2, ZnO and CeO_2, which easily form non-stoichiometric structures with surface defects. Such surface defects can coordinate with reactants and then enhance the catalytic performance[94-96], as evidenced by extensive characterisation using advanced electronic spectra, particularly for the uses of ZnO and TiO_2 oxides used as either additives or supports in MA hydrogenation catalysts. The XPS and near-edge x-ray absorption fine structure (NEXAFS) spectroscopy evidenced that a defect-rich ZnO surface can enhance MA adsorption and improve the reactivity of MA.[92] The FTIR characterisation indicated that TiO_{2-x} with defects enhanced MA adsorption via linking the C=O group to the oxygen vacancy (Ovac) on the surface.[48] Moreover, the improvement of ZnO and TiO_x in MA conversion to GBL was experimentally proven for the Cu-Zn[68] and Ni/SiO_2-TiO_2[80] catalysts. Another important reducible oxide CeO_2 was used as the additives to promote MA hydrogenation, enhancing the selectivity of GBL over the Cu-CeO_2-Al_2O_3 catalyst.[74] The survey of literature only found very few works which discussed the roles of the CeO_2 support in MA hydrogenation, although there have long been a plethora of studies in academia and in industry.[97]

CeO_2, as one of the most widely studied rare earth oxides, possesses a cubic fluorite structure with lattice constant a = 5.41134 Å and the space group Fm3m. As shown in Figure 1.12(A), fluorite CeO_2 consists of a face-centred cubic (fcc) unit cell, wherein Ce cation coordinates with eight oxygen anions but each O atom coordinates with four Ce cations and occupies the tetrahedral interstitial site. The unique electronic configuration ($4f^26s^2$) of cerium confers CeO_2 with a fast transformation of cerium cations ($Ce^{3+} \rightleftarrows Ce^{4+}$) and a remarkable capacity of oxygen storage. Owing to the special structure and electronic configuration, CeO_2-based materials have been widely used as catalysts or as non-inert supports for catalysts in various chemical reactions, such as CO oxidation[98-105], water-gas shift reaction[106-109], soot combustion[77] and various reforming reactions.[110-113]

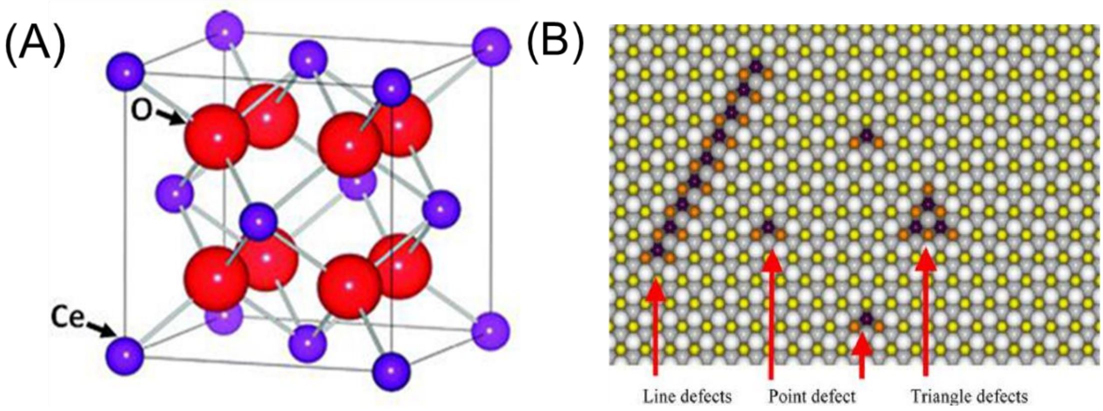

Figure 1.12 The perfect fluorite structures of CeO_2[114] and defects on the (111) surface of CeO_2 material (white large balls are on the top O^{2-} layer; grey large ones are on the third O^{2-} layer; yellow and orange ones are on the second Ce cation layers. Yellow indicates a Ce^{4+} cation and orange indicates a Ce^{3+} cation. Black ones are on the forth Ce^{4+} layer).[115]

One of the most important features of CeO_2 is its rich various oxygen vacancies (Ovac), as shown in Figure 1.12 (B), which can enhance the adsorption of oxygen-containing reactants on the surface of catalysts. The investigation by Albrecht and co-workers suggested that the chemical adsorption of methanol over the CeO_2 (100) and (111) surfaces resulted in the formation of methoxyl species[116], whereas the amount of stable methoxyl species on the former was almost two times that of on the latter. The authors attributed these to the more under-coordinated Ce cations and O anions on the CeO_2 (100) surface than those of the (111) surface. The surface states and the number of defect sites (Ovac population), probed by Wu et al. using mass spectra and *in situ* IR and Raman techniques, were evidenced to determine the adsorption modes (on top, bridging and three-coordinate modes) and the reactivity of methoxyl species on the CeO_2 surfaces.[117]

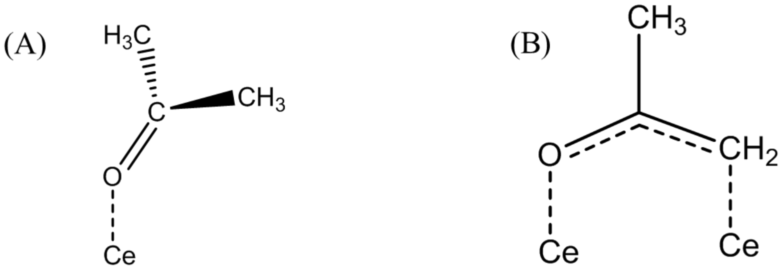

Figure 1.13 Acetone adsorption on the (A) fully oxidised and (B) reduced CeO_2(111) thin film [118]

Senanayake and co-workers comparatively investigated the acetone adsorption on the fully oxidised CeO_2 (111) and reduced CeO_x (111) thin films using XPS and NEXAFS.[118] They found that acetone weakly bonded with the stoichiometric CeO_2

(111) surface via the η^1 mode (Figure 1.13 (A)), while the adsorption of acetone on the O-defective CeO_x (111) surface was much stronger due to the formation of ketone carbanion via coordination of carbonyl group with Ce cations, as shown in Figure 1.13(B). The spectroscopic evidence confirmed that the Ovac-rich defective CeO_x (111) surface stabilised C=O adsorption through enhancing carbanion coordination with Ce cations, but the exact roles of Ovac and coordination states were unclear. Soon after, Overbury's group further investigated the adsorption and transformation of acetic acid on the CeO_2 (111) surface and found bridge bonded acetate species coexisted with the Ovac trapped acetate via acetic acid dehydrate.[119] Taking the strong interaction between Ovac and the anhydride group into account, Ovac in the reduced $CeO_{2-\delta}$ is expected to enhance the adsorption of the carbonyl group and thus facilitate GBL production in MA hydrogenation.

Due to the strong interaction with oxygen species, Ovac in the CeO_2 materials can serve as active sites for the catalytic reactions. For example, Liu and co-workers shed light on the reaction pathway for CO oxidation over CeO_2 nanorods, revealing that Ovac on the CeO_2 nanorods facilitated the activation and transportation of active oxygen species whilst providing effective adsorption sites for CO.[120] Moreover, Wang and co-workers unravelled the important roles of Ovac in the CO_2 methanation on the Ru/CeO_2 catalyst through *in situ* IR characterisation. They verified that CO_2 methanation over the Ru/CeO_2 catalyst underwent the formate route: $CO_2 \rightarrow CO_2^{\delta-} \rightarrow HCOO^-$(formate)$\rightarrow CH_2OH \rightarrow CH_4$ due to the presence of Ovac.[94] Compared with the CO dissociation route on the Ru metal surface, the formate route remarkably decreased the activation temperature of CO_2 methanation (190°C versus 250°C), accounting for the excellent catalytic performance of the Ru/CeO_2 catalyst in the reaction.[94]

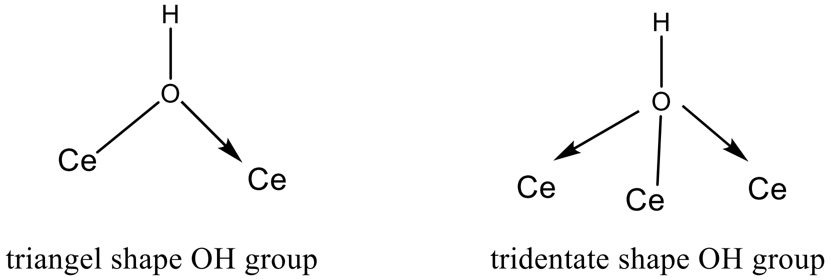

Figure 1.14 Diagram of H adsorption on the surface of CeO_2[121]

Besides the activation of oxygen-containing functional groups, recent research has shown the considerable potential of CeO_2 in activating H_2 in the hydrogenation reaction due to its strong interaction with hydrogen. DFT simulation indicated that the dissociation of H_2 on the stoichiometric CeO_2(111) surface was an exothermic process due to the formation of the OH group with strong interaction between H and the CeO_2 surface,[122] as shown in Figure 1.14. This result indicates CeO_2 is able to activate and dissociate the hydrogen molecule, and the lattice oxygen in the CeO_2 matrix can stabilise atomic hydrogen via the formation of the hydroxyl group.

Furthermore, Bernal and co-workers found that hydrogen species desorbed from the CeO_2 surface as H_2 (reversible adsorption) and H_2O (irreversible adsorption), where the reduced CeO_2 facilitated hydrogen desorption as molecular H_2.[123] Wu et al. employed spin-polarised DFT+ U calculations with the GGA-PW91 function to simulate the hydrogen diffusion and reaction over stoichiometric and reduced CeO_2(111) surfaces using the Vienna ab initio Simulation Package (VASP). Their results suggested that the reduced CeO_2(111) facilitated H diffusion and the reversible H_2 adsorption because the presence of Ovac weakened the strength of the O-H bond and diminished the energy barrier of H diffusion.[124, 125]

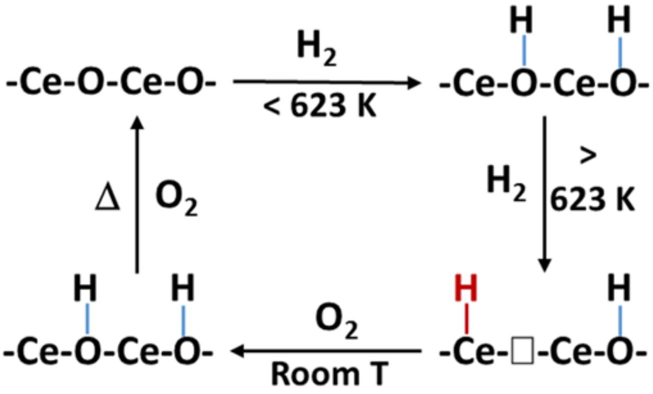

Figure 1.15 Illustration of H_2 interaction with CeO_2 with the formation of surface OH and Ce−H[126]

Through *in situ* inelastic neutron scattering characterisation, Wu and co-workers gained vibrational insight into hydrogen dissociation over the ceria surface and highlighted the significant roles of Ovac in the H-ceria interaction.[126] As shown in Figure 1.15, the homolytic cleavage of the hydrogen molecule occurred on the stoichiometric CeO_2 surface with the formation of two O-H bonds. Once the CeO_2 was reduced with formation of Ovac, one Ce-H intermediate was realised instead of the O-H group on the reduced $CeO_{2-\delta}$ surface after hydrogen dissociation. However, the vibration feature of Ce-H disappeared when the reduced CeO_2 was exposed to O_2 atmosphere, suggesting that the presence of Ovac played a crucial role in stabilising the Ce-H intermediate.[126] Furthermore, the authors claimed that the existence of Ce-H in the reduced $CeO_{2-\delta}$ sample facilitated the diffusion of atomic H on the surface or in the bulk, which can offer the active H species for the hydrogenation reaction.[125]

Owing to the capability of CeO_2 in hydrogen activation, the application of CeO_2 as catalysts towards hydrogenation reactions is attracting increasing attention. For example, Gianvito and co-workers reported that individual CeO_2 had high activity and selectivity in the partial hydrogenation of alkynes to olefins.[127] They further employed DFT to study the reaction mechanism at the molecular level. The results revealed that surface oxygen species played important roles in the hydrogenation: (a) in adsorbing and stabilising atomic H species; and (b) in facilitating the transformation of adsorbed acetylene to β-C_2H_4 radical species (the intermediate species in the acetylene hydrogenation) with a low activation barrier.[128]

Zhou and co-workers employed pure CeO_2 nanorods with well-defined (110) planes to hydrogenate various nitroaromatics, revealing that CeO_2 nanorods were economic, environmental and active catalysts for this reaction. They further suggested that CeO_2 materials showed facet-dependent activity in this hydrogenation, wherein the nanorods with (110) planes efficiently catalysed the reaction, while other shapes of CeO_2 with (100) or (111) planes showed lower activity.[129]

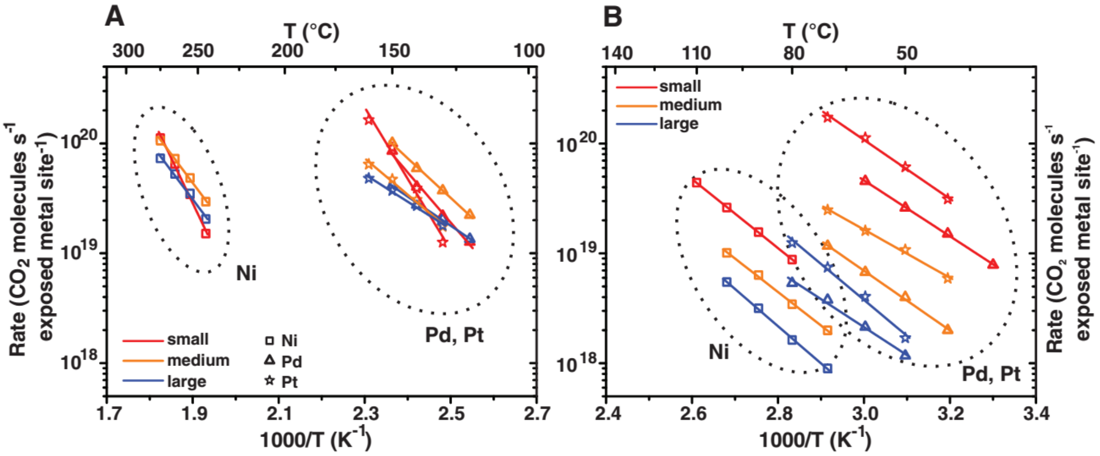

Figure 1.16 Kinetic data Arrhenius-type plots for CO oxidation over (A) Al_2O_3 and (B) CeO_2 supported catalysts[130]

Besides being used as catalysts, CeO_2 materials have been extensively employed as active supports in catalysis. In comparison with the catalysts supported on inert, non-reducible supports such as SiO_2 and Al_2O_3, CeO_2 supported catalysts displayed enhanced catalytic performance. As presented in Figure 1.16, CeO_2 supported catalysts had higher catalytic rates of CO oxidation than their alumina-supported counterparts, as evidenced by the much lower temperatures needed to completely oxidise CO.[130] The distinctive catalytic activity of CeO_2-supported catalysts was attributed to the promotion of metal dispersion,[131, 132] the strong metal-support interaction,[95, 106] metal-support synergistic effect,[94] and electronic structure modification.[133, 134]

CeO_2 support can maintain small metal particles and improve metal dispersion through strong metal-support bonding.[129] It was reported that Cu/CeO_2 catalysts displayed high catalytic performance in methanol production from the hydrogenation of dimethyl carbonate because Cu subnanoparticles (<1 nm) were readily formed in the Cu/CeO_2 catalysts due to their strong interaction with the CeO_2 surface.[132] Moreover, Farmer and Campbell compared the Ag nanoparticles supported on respective CeO_2 and MgO and reached the conclusion that Ag nanoparticles localised on reduced CeO_2(111) displayed higher stability than that on MgO(100) as a result of their strong binding to both defects and terraces of CeO_2.[131] Owing to the strong binding of metal on the surface, the supported metal species on CeO_2 exhibited high thermal stability and unusual resistance to sintering during high-temperature operation.[131, 135] Ta and co-workers provided visual evidence through environment transmission electron microscopy that CeO_2 layers intimately contacted with gold particles through buried interfacial atoms, leading to the reconstruction of a gold-ceria interface in the reduction atmosphere. As a result, Au strongly anchored on the surface, maintained the interface and, consequently, possessed high stability in the reaction.[136]

With respect to CeO_2 supported catalysts, the metal-ceria interface has attracted considerable interest of scientists due to its significant promotion on the catalytic properties.[137] For example, through tailoring the perimeter of Pd-ceria interface, Cargnello and co-workers defined the Pd-ceria interface as the active sites and clarified its pivotal role in the enhancement of CO oxidation over the Pd/CeO_2 catalysts.[130] Mudiyanselage and co-workers reported that a $CeO_x/Cu(111)$ system with the presence of a Cu-CeO_x interface increased more than one order of magnitude in the activity of the WGS reaction relative to the bare Cu(111) surface.[95] The *in situ* ambient-pressure XPS results pointed out that Cu-CeO_x interface acted as active sites in facilitating H_2O dissociation to the OH group.[95] Their DFT simulation results further confirmed that the Cu-CeO_x interface opened an efficient pathway for H_2O dissociation with a low activation barrier (+0.22 eV) in comparison with the same procedure on the Cu (111) surface with a high activation barrier (1.0-1.4 eV).[95]

To elucidate the electronic properties of metal at the M-ceria interface, Bruix and co-workers conducted valence photoemission experiments (UPS and XPS) on small Pt nanoparticles deposited on CeO_2(111) and CeO_2/TiO_2(110) surfaces. They found that the Pt-ceria contact produced large electronic perturbations for small Pt particles but this perturbation drastically decreased with the increasing size of Pt particles. Combined with DFT simulation, this strong Pt-ceria electronic interaction was devoted to significant enhancement of the Pt-ceria interface in dissociating the O-H bond in water.[133] In addition, a similar electronic perturbation was also observed in the Cu/CeO_2 system, leading to various Cu species with different valence states (Cu^{+}, Cu^{1-} and Cu^{2+}).[138] Such electronic interaction of Cu/CeO_2 catalysts improved the adsorption and dissociation of water molecules, contributing to its excellent catalytic performance in the WGS reaction.[138]

In summary, active CeO_2 supports can improve metal dispersion and prevent the supported metal species from sintering during the thermal operation. The strong metal-ceria interaction can change the geometry and tune the electronic structure of the supported metals at the interface. Thus, it is expected that the CeO_2 support would impart distinguished catalytic activity for MA hydrogenation.

1.5.2 Modification of surface metal active species

Based on the mechanism of MA hydrogenation on metal surfaces, tuning the activity and selectivity of MA hydrogenation is feasible by modifying the surface properties of metal species, which significantly determines the adsorption of MA and surface reactions. For example, the addition of Sn to Pd/SiO_2 modified the electronic structure of Pd species, which improved the selectivity of MA conversion to GBL.[46] The bimetallic Ni-Pt/Al_2O_3 catalyst displayed higher catalytic activity and selectivity of MA hydrogenation to SA than monometallic Ni/Al_2O_3 and Pt/Al_2O_3 due to the formation of the Pt-Ni alloy.[84] In addition, the supported Ni-Pt alloy on the Al_2O_3 support showed the similar activity to the homogeneous $RuCl_2(TPP)_3$ catalyst in MA hydrogenation. Other bimetallic catalysts like Pt-Au/TiO_2[67] and Ru-Re/C[62] displayed higher catalytic performance in comparison with monometallic catalysts in MA hydrogenation. These results indicate a profound role of bimetallic species in MA hydrogenation.

From an electronic point of view, the introduction of a second metal is an important approach to engineering the electronic and geometric structures of catalysts to enhance their catalytic activity and selectivity to products.[11] The introduced metal can exist as an adatom,[139] in an alloy[140] or ionic state[39], or isolated species on the surface of the main metals,[38] which dominates the geometric and electronic structure of bimetallic catalysts. The surface structure is dependent on the formation enthalpy of bimetallic species, which is summarised as follows[141]:

- The mixing enthalpy is very close to zero, which would lead to the formation of alloys that behave like ideal solutions;

- The small and negative mixing enthalpy can give rise to ideal or regular alloy formation. This case occurs when the radii of two metals are quite similar, e.g. the Pt-Cu alloy[5];
- The large and negative mixing enthalpy would result in the formation of intermetallic compounds or ordered solution, which could possess some covalent features instead of the metallic state[5];
- In the case of small and positive mixing enthalpy, such a system is mono or biphasic, according to the temperature of equilibration. A typical example is the Ni-Cu alloy in which the surface component of the Ni-Cu alloy relies on temperature[142];
- When the mixing enthalpy is large and positive, only surface alloying is possible, often under the formation of clusters of the additive, like with Ru–Cu[5].

Because of the varied formation enthalpies, the bimetallic catalysts could exhibit completely different physical and chemical properties and give rise to distinctive catalytic activity. For example, the Rh@Pt bimetallic catalyst with core-shell structure showed the highest activity in CO oxidation at 70 °C compared with the nano scale Rh-Pt alloy and monometallic Rh+Pt catalyst.[143] The Pt-Ni-Pt(111) structure was much more active and selective than the surface Ni-Pt-Pt(111) structure in the hydrogenolysis of the C=O group in the hydrogenation of acrolein, which was due to different electronic structures between Pt-Ni-Pt(111) and Ni-Pt-Pt(111).[144] To meet requirements in efficient conversion of MA to desirable products, it is important to establish a clear structure-activity relationship for bimetallic catalysts.

Metallic Ni species have been extensively applied to develop a composition-dependent bimetallic system for various catalytic applications, because of its alloying efficiency with all noble metals and many transition metals with wide mass ratios.[11] For MA hydrogenation, Ni-based catalysts are more active for hydrogen activation and C=C hydrogenation yet less selective to the products in comparison with other inexpensive metals.[41, 73, 84] Therefore, modulating the surface properties of Ni species by introducing other metals is crucial for the rational design of effective catalysts for MA hydrogenation. However, it still necessitates establishing the correlation between the catalytic structure and the performance of hydrogenation.

1.6 Aims and methodologies of this thesis

1.6.1 Objectives

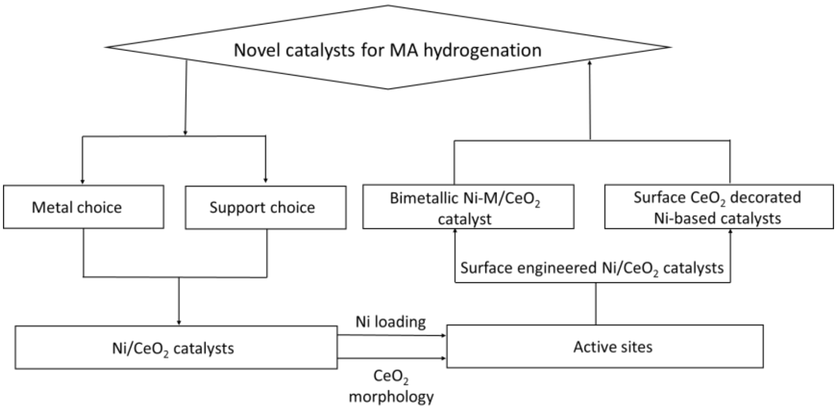
Novel catalysts for MA hydrogenation
Metal choice
Support choice
Bimetallic Ni-M/CeO2 catalyst
Surface CeO2 decorated Ni-based catalysts
Surface engineered Ni/CeO2 catalysts
Ni loading
Ni/CeO2 catalysts
Active sites
CeO2 morphology

Figure 1.17 The research flowchart for the PhD thesis

In my thesis, the core research objectives are as follows: (a) to design and develop novel and robust catalysts for liquid phase MA hydrogenation; (b) to define the active sites for H_2 activation, C=C hydrogenation and C=O hydrogenolysis; and (c) to establish a correlation between the catalyst reactivity and their synthesis and structure for a rational design of novel and desirable industrial catalysts.

To these ends, the main research tasks are proposed and illustrated in Figure 1.17. Firstly, through comparative studies on the CeO_2 and Al_2O_3 supported catalysts and various M/CeO_2 (M= Co, Ni and Cu) catalysts in MA hydrogenation, Ni/CeO_2 is chosen to be an effective material for MA hydrogenation. Then, via tuning the Ni loading and morphology of CeO_2 supports, the active sites for C=C hydrogenation and C=O hydrogenolysis will be defined. Based on knowledge of the active sites in C=C hydrogenation and C=O hydrogenolysis, the Ni-CeO_2 catalytic system will be further optimised by the surface engineering method so as to improve the activity and selectivity of MA hydrogenation.

1.6.2 Methodologies

A wet impregnation method is employed to prepare all catalysts in the thesis because impregnation methodology is widely used for industrial catalyst preparation and is flexible in adjusting the components of catalysts. The fundamental concepts of the impregnation method have been well documented in the review[145] and book[146] . In my thesis, the impregnation method is employed to minimise the influence of preparation methods on the catalytic performance of all the catalysts.

Liquid phase hydrogenation is used to evaluate the catalytic reactivity of catalysts in MA hydrogenation. Compared with the gas phase MA hydrogenation being operated at 210-280°C, the liquid phase hydrogenation is usually conducted at a lower temperature (190-210°C), in order to hinder the over-hydrogenation and decarbonylation of MA to by-products and the cracking of the MA molecule to small organic compounds, and even to CO_2 and CH_4.[41] In addition, liquid phase hydrogenation can resist coking in comparison with gas phase hydrogenation because solvent facilitates the removal of adsorbed hydrocarbons on the catalyst surface.

Diverse characterisation techniques are employed to study the physical and chemical properties of the catalysts. X-ray diffraction and Raman spectroscopy are used for structure determination, and x-ray photoelectron spectroscopy is applied to detect the electronic structure of catalysts. The redox properties of supported catalysts are determined by H_2 temperature-programmed reduction, while information on hydrogen activation over catalysts is obtained using H_2 temperature programmed desorption. These techniques have been well documented in the books[2, 5, 44, 147] and literature[6, 148, 149]. Details on the characterisation are presented in Chapter 2.

Chapter 2 Experimental methodologies

The following chapter summarises the materials used for catalyst preparation, methodologies for catalyst characterisation and catalyst evaluation procedure.

2.1 Materials

All the materials used for the catalysts preparation and catalytic evaluation are summarised in Table 2.1.

Table 2.1 Materials for catalyst preparation and evaluation

Chemicals	Molecule	Grade	Producer
Cerium(IV) nitrate	$Ce(NO_3)_3\cdot 6H_2O$	Analytical (> 99%)	Sigma-Aldrich Co. Ltd
Nickel(II) nitrate	$Ni(NO_3)_2\cdot 6H_2O$	Analytical (> 99%)	Sigma-Aldrich Co. Ltd
Aluminium (III) nitrate	$Al(NO_3)_3\cdot 9H_2O$	Analytical (> 99%)	Sigma-Aldrich Co. Ltd
Copper (II) nitrate	$Cu(NO_3)_2\cdot 3H_2O$	Analytical (> 99%)	Sigma-Aldrich Co. Ltd
Citric acid	$C_6H_8O_7$	Analytical (> 99%)	Sigma-Aldrich Co. Ltd
Sodium hydroxide	$NaOH$	Analytical (> 99%)	Sigma-Aldrich Co. Ltd
Maleic anhydride	$C_4H_2O_3$	Analytical (> 99%)	Sigma-Aldrich Co. Ltd
Succinic anhydride	$C_4H_4O_3$	Analytical (> 99%)	Sigma-Aldrich Co. Ltd
γ-butyrolactone	$C_4H_6O_2$	Analytical (> 99%)	Sigma-Aldrich Co. Ltd
Tetrahydrofuran	C_4H_8O	Analytical (> 99%)	Sigma-Aldrich Co. Ltd
Deionized water	H_2O	< 1μ s/cm	

2.2 Methodologies

2.2.1 Powder X-ray Diffraction

Powder X-ray diffraction is a powerful technique used to characterise the crystal structure and the crystallite size of poly-crystalline or powder solid samples. This method is also applied to identify unknown substances via comparing the obtained

XRD patterns with a database provided by the International Centre for Diffraction Data. XRD is also employed to characterise heterogeneous solid mixtures to determine their components in the crystal structure. The fundamental theory about XRD technology is presented in *Appendix A*.

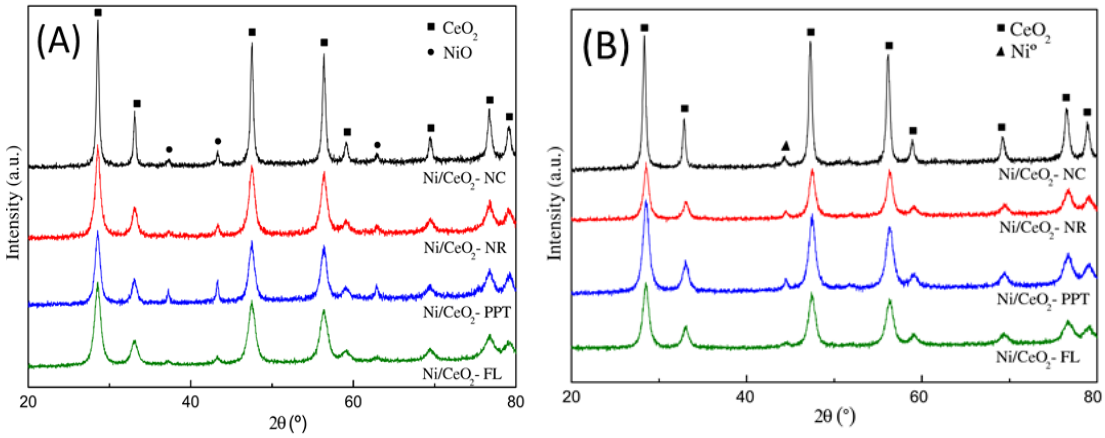

Figure 2.1 Typical XRD patterns of (A) NiO/CeO$_2$ precursors and (B) Ni/CeO$_{2-\delta}$ catalysts adapted from Ref.[150]

Figure 2.1 presents XRD patterns of NiO/CeO$_2$ precursors and Ni/CeO$_{2-\delta}$ catalysts. Besides the detection of crystal phase, XRD can provide additional information about the structure of catalysts. The lattice parameter (a_0) of CeO$_2$ can be estimated using interplane distances (d spacing) and Miller indices ($h\ k\ l$).[151] The interplane distance (d) can be calculated by the Bragg equation, and the formula to calculate lattice parameters of cubic crystal phase is presented as following

$$\mathrm{a} = d_{hkl} \times \sqrt{h^2 + k^2 + l^2} = \frac{n\lambda}{2sin\theta} \times \sqrt{h^2 + k^2 + l^2} \qquad (2.1)$$

In addition, the mean crystallite size of particles can be estimated using the Scherrer equation[152]:

$$\mathrm{D} = K\lambda/(\beta cos\theta) \qquad (2.2)$$

where K is the Scherrer constant, λ is the wavelength of x-radiation, θ and β are respective to the diffraction angle and the line broadening at half the maximum intensity (FWHM, in radian angle scale), D is the mean size of crystalline domains. The Scherrer equation is an approximation method, exclusively providing a finite boundary on the crystallite size (below 200 nm) due to a variety of factors, such as stacking, twin faults and sub-grain structures that influence the width of a diffraction peak.[152]

Besides the crystallite size, x-ray diffraction peak profiles can reflect dislocation structure of crystallite particles. The ideal powder diffraction consists of narrow and symmetrical peaks, positioned according to a well-defined unit cell.

The aberrations from the ideal powder pattern can be conceived as: (i) peak shift, (ii) peak broadening, (iii) peak asymmetries (iv) anisotropic peak broadening and (v) peak shape changing.[153] According to the theory of kinematical scattering, the broadened diffraction peak is related to either crystallite smallness or the presence of microstrain.[153] The microstrain can be arisen from lattice imperfection, including dislocation and various defects in the forms of step, kink, terrace and point.

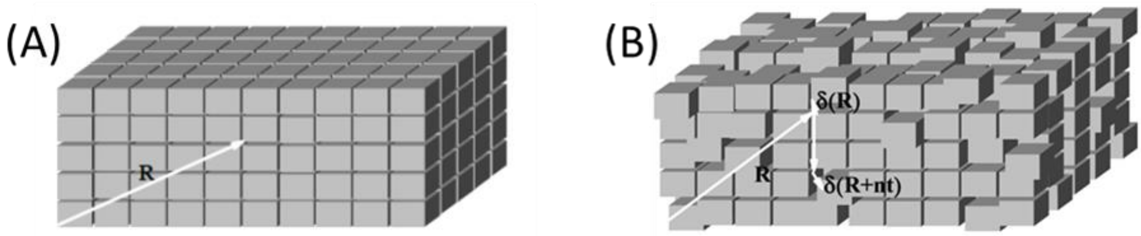

Figure 2.2 Simplified representation of a crystal (A) without and (B) with microstrain[154]

As shown in Figure 2.2(A) , the positon of each shell in a crystal free of any defects is described by the vector: $\vec{R}$ =u$\vec{a}$+ v$\vec{b}$+w$\vec{c}$. With respect to their original position, the defects in a crystal can cause the displacement of the three-dimensional repetition of identical cells, which is characterised by vector $\vec{\delta}$ .The microstrain corresponds to atom displacements with respect to their positions in perfect crystal that is free of any defects.[154] The contribution of the microstrain to the width of XRD peak can be described as:[155]

$$\varepsilon(\%) = \frac{[\delta(\mathrm{R+nt}) - \delta(\mathrm{R})]}{\delta(R)} = \frac{\Delta d}{d} = \frac{\beta}{4tan\theta} \tag{2.3}$$

where ε represents the microstrain, θ and β are the diffraction angle and the FWHM of the peaks. In general, the microstrain of CeO_2 are used to estimate the density of defects in the unit cell of CeO_2, which is caused by lattice imperfection with discrimination of dislocation, step, kink, terrace and different point defects.[151, 156]

Using the crystal lattice constants of the alloy into the Vegard's Law, one can estimate the approximate concentration of the two constituents in an alloy phase.[157] For example, one can calculate the ratio of Cu/Ni in the Cu-Ni alloy using the following equation in cubic crystal phase:

$$a_{CuNi} = \mathrm{x}a_{Ni} + (1-x)a_{Cu} \tag{2.4}$$

where a_{CuNi}, a_{Ni} and a_{Cu} are the lattice parameters of Cu-Ni alloy, Ni and Cu phase, respectively, and x represents the molar ratio of Ni in the Cu-Ni alloy. It is noteworthy that the Vegard's law is not limited to metallic alloys and cubic crystal phase but a general principle suiting various parameters along crystal vectors.

In my thesis, the XRD measurements for all the relevant samples were conducted on a Bruker D8 advance diffractometer using Cu Kα1 radiation (λ = 0.15418 nm) equipped with a Ni filter at University of Southampton. Analysis was carried out within the 2θ region of 10-80° by a continuous scan mode at 2°/min with a step size of 0.006°.

2.2.2 Raman spectroscopy

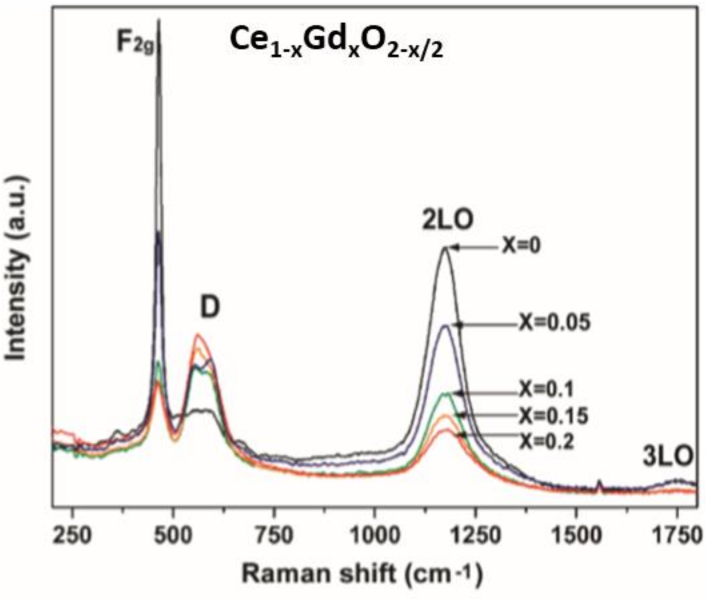

Figure 2.3 Raman spectra of Gd-doped CeO_2 samples adapted from Ref.[158]

Raman spectroscopy is a powerful tool to detect structural properties of nanomaterials, due to the strong sensitivity of the phonon characteristics to the crystalline nature of the material. Hence, Raman has been widely employed to characterise structures and defects of ceria-based nanomaterials.[96, 151, 158-160] For the NiO/CeO_2 system, the changes of the bands, including position, intensity and full width at half maximum can provide information pertaining the structure evolution of CeO_2 arisen from the introduction of NiO.[151, 161]The fundamental theory about Raman spectroscopy is briefly described in *Appendix A*.

For a typical Raman spectrum of CeO_2 as shown in Figure 2.3, a dominant vibration (F_{2g} mode) is observed at ~460 cm^{-1} due to the symmetrical stretching vibration of Ce-O bonds in the fluorite structure.[96] The serial LO bands, as 2LO band at ~1170 cm^{-1} and 3LO band at ~1750 cm^{-1}, are characteristics of multiphonon relaxation by the resonance Raman effect.[158] The weakest band (D band) at ~600 cm^{-1} is activated by the defects and oxygen vacancies in the matrix of the CeO_2

samples.[158] After Gd doped into CeO_2 as shown in Figure 2.3, the F_{2g} and 2LO bands got progressively broader, and the D band around 600 cm^{-1} became pronounced, indicating that Raman modes are sensitive to atomic scale disorder and defects in solids.[162] Additionally, Taniguchi and co-workers claimed that I_D/I_{F2g} was sensitive to the defect density, whereas I_{2LO}/I_{F2g} was comparable among the Gd-doped samples.[158] Based on their work, the relative intensity ratio of I_D/I_{F2g} is widely employed to estimate the Ovac concentration in the CeO_2-based samples.[151, 160, 161, 163, 164]

In my thesis, the Raman scattering is also employed to investigate the structure of CeO_2 and its evolution induced by H_2 reduction and loading metal or metal oxides. The estimation of the Ovac concentration relies on the relative intensity of corresponding Raman peaks. Raman spectra of all the catalysts in the thesis were recorded at University of Southampton, using a HORIBA Raman microscope with a laser wavelength of 532 nm (LabRAM HR Evolution) and the laser power of 20 mW.

2.2.3 X-ray photoelectron spectroscopy

X-ray photoelectron spectroscopy (XPS) is a surface-sensitive quantitative spectroscopic technique that measures the elemental composition, chemical state and electronic state of the elements at the surface of a material.[165] The fundamental theory of XPS is described in *Appendix A*. For the CeO_2-containing samples, XPS spectra are often used to detect the Ce^{3+} and Ce^{4+} components and quantitatively analyse their ratio at the surfaces.[94, 99] In addition, the oxygen species on the surface of samples can be distinguished by fitting the O1s core level spectrum.[99] Based on the concentrations of the Ce and lattice O species, the surface amount of structural Ovac can be estimated as well.[94, 99, 151, 166]

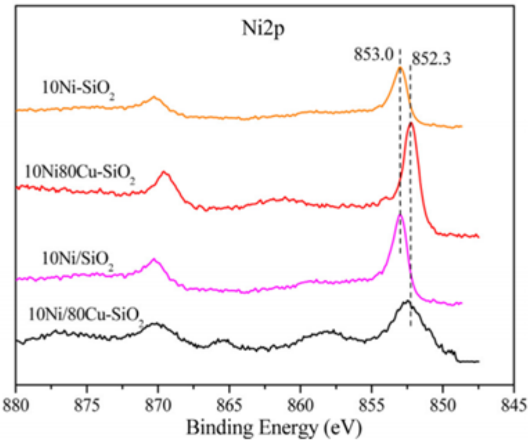

Figure 2.4 The core level XPS spectra of $Ni2p_{3/2}$ in the bimetallic Cu-Ni/SiO_2 catalysts adapted from Ref.[167]

The relative intensity or integrated XPS peak areas can provide the surface concentration of the element in question, while the chemical shift of core-level XPS peaks can deliver important information on its electronic state and chemical environment. Figure 2.4 presents typical XPS spectra of Ni species, where the binding energy (BE) of Ni in the bimetallic samples shifts to low energy compared with that in the monometallic sample.[167] The chemical shift indicates the changes of electronic structure of Ni species in the bimetallic samples. In principle, the blue shift of BE of the main peak for Ni is associated with the decrease of electron density of the nickel species. Versus vice, the red shift of BE of the main peak for Ni is due to increased electron density of nickel species.[168, 169]

In my thesis, all the XPS spectra were collected from a Thermo Scientific Escaplab 250 using monochromatized Al Kα as the X-ray source (1486.8 eV) at a constant dwell time of 100 ms and pass energy of 40 eV. The X-ray source was running at a reduced power of 150 W (15 kV and 10 mA). The working pressure in the analysis chamber maintained at 2×10^{-9} mbar.

Differing from the normal sample preparation, the atmosphere-sensitive catalysts containing reduced metallic nanoparticles or defective CeO_2 are stored in inert gas environment and transferred immediately into a vacuum desiccator to prevent the catalysts from re-oxidation. Thereafter, the reduced catalysts mounted on the standard sample stubs with double-sided adhesive tapes.

All the determined binding energies were referenced to the C 1s hydrocarbon peak at 284.70 eV, which was pre-calibrated. Spectral data were processed using XPEAKS 4.1 software using a combination of Gaussian and Lorentzian peak functions after subtracting Shirley background.

2.2.4 Hydrogen temperature programmed reduction/desorption

Temperature-programmed reduction (TPR) is an important technique to define the efficient reduction condition for the reduction of a given oxide, which was developed by John Ward Jenkins in order to develop heterogeneous catalysts at the Shell Oil company.[170] By analysis of the redox behaviour, one can extract crucial information on the examined catalysts, such as chemical states of metal species and their interaction with the support.

Temperature programmed desorption (TPD) is a useful method for monitoring the desorption behaviour of the pre-adsorbed molecules from the surface along increasing temperature. When molecules or atoms deposit onto the metal and/or oxide surface, they prefer to bind onto the specific position via a physical interaction or chemical bonds to minimize the system energy. The binding energy varies with the adsorbate and surface. As heated up to certain energy level, the adsorbed species will leave from the substrate surface due to heat energy transfer to overcome the adsorption energy. The desorption temperature corresponds to the adsorption energy.

The obtained TPD profiles are very useful to recognise the different adsorption conditions of the same molecule from the different adsorption sites, for instance, terraces and steps on the surface of catalysts.[171] The area of a desorption peak can reveal the amount of adsorbed species, which related to the population of active sites. Therefore, one can estimate the metal dispersion on the supported catalysts using desorption peak area only if the adsorption on the metal is unique or the support is inert in adsorption of the adsorbate.

In this thesis, H_2-TPR experiments were carried out using the Micromeritics AutoChem II 2950 automated catalyst characterization system equipped with a thermal conductivity detector (TCD). In a typical experiment, 30 mg of fresh sample was heated from ambient to 300°C at 10°C /min in argon and maintained at this temperature for 1 h to remove adsorbed moisture and air. After cooling down to ambient temperature in argon, the sample was heated to 800°C at a ramp of 10°C/min under a H_2/Ar (10 vol% H_2 in argon, 50 mL/min) flow, followed by naturally cooling down. The TPR profiles was recorded by TCD.

H_2-TPD measurements were conducted on the same apparatus. In the H_2-TPD test, 100 mg catalyst was first reduced at 350°C for 1 h in a pure H_2 flow, followed by purging with Ar for 1 h at 360°C to remove the excess hydrogen adsorbed on the surface and cooling down to 50°C in an argon flow. At the temperature of 50°C, the catalyst was exposed to the mixed H_2/Ar(10% H_2 in argon) gas with a flow of 50 mL/min for 60 minutes, followed by flushing in argon for another 60 minutes in order to remove physicosorbed hydrogen, and then heated in argon to 600°C at a heating rate of 10°C/min.

The correlation of TCD signal to hydrogen volume data follows the method, which is provided in the manual book of the AutoChem 2950 Automated Catalyst Characterization System. Prior to the H_2-TPR and H_2-TPD experiments, the instrument calibration is necessary to conduct using H_2/Ar mixture gas with known concentration.

The metal dispersion can be estimated according to the volume of chemisorbed H_2 using the following simplified equation[171]:

$$\text{Metal Dispersion }(\%) = \frac{2 \times V_{ad} \times M_{metal} \times SF}{m \times P \times V_M} \times 100\% \qquad (2.5)$$

where m is the weight of sample (g), P is the weight fraction of metal in the sample as determined by ICP-OES, V_m is the molar volume of H_2 (22414 mL/mol) at standard temperature and pressure (STP); V_{ad} (mL) is the volume of chemisorbed H_2 at STP measured in the TPD procedure. M_{metal} and SF are respective to the molecular weight of metal and the stoichiometric factor (M:H molar ratio in the chemisorption is taken as 1).

2.3 Auxiliary characterisation

The surface area and pore size for each catalyst was determined using a Micrometrics ASAP 2020 Surface Area Analyser. Approximately 0.1 g of the catalyst was degassed in a flow of N_2 at 250°C for 8 h in order to remove any adsorbed species from the surface. Measurements were used nitrogen as the adsorbate and conducted at -196°C.

The morphology of the materials was observed using a JEOL JEM-2010 transmission electron microscope (TEM) operated at 120.0 kV. The samples were dispersed in ethanol under 10 min ultrasonication. The TEM images were collected at Shanxi University.

The chemical analysis of the catalysts was conducted by inductively coupled plasma (ICP) spectroscopy with the iCAP 7400 ICP-OES (Thermo Fisher Scientific) equipment, which is settled in Shanxi University. The error of analysis for each element was Ni ± 0.70% and Ce ± 0.08%.

2.4 Catalyst evaluation

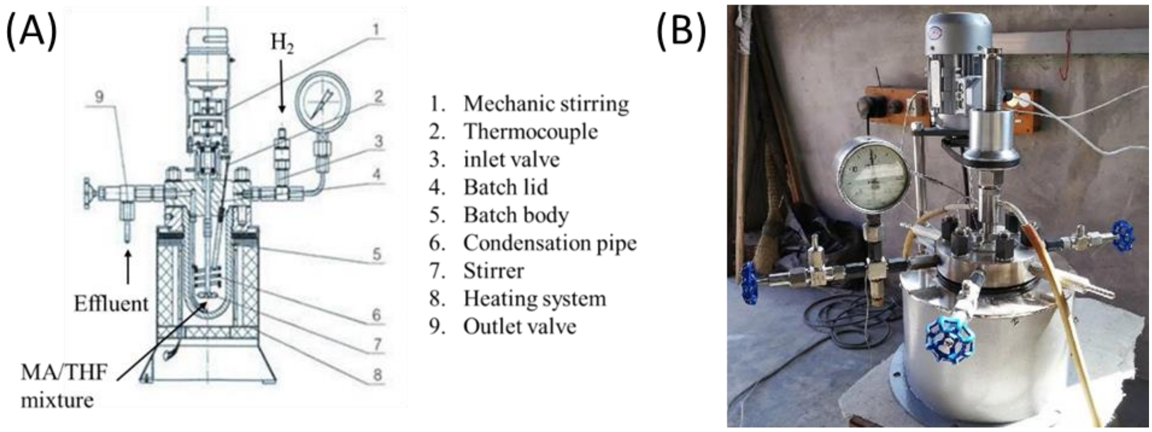

Figure 2.5 (A) Illustration and (B) photo of the batch reactor for MA hydrogenation

The performance of the liquid-phase hydrogenation of MA on the relevant individual catalyst was evaluated at Shanxi University, using a batch reactor (as shown in Figure 2.5). Before hydrogenation of MA, the catalyst was reduced in a quartz tubular reactor under a pure H_2 flow (20 ml/min). The reduced catalyst (0.1 g) was added into an autoclave (100 ml) containing mixed solution of THF (40 ml) and MA (4.9 g). This mixed process was carried out in a glove box to avoid oxidation of the reduced catalyst.

The autoclave containing the catalyst and reactants was purged five times with nitrogen to remove air before pressurising up to 4.0 MPa using hydrogen. Then, the reactor was heated to 210°C with the H_2 pressure up to 5.0 MPa. Diffusion restrictions due to internal and external diffusions were ruled out by sieving catalyst with confined particle sizes of 0.425-0.250 mm and stirring the mixed system at 500 rpm. Figure 2.6 presents the optimization of the reaction conditions to avoid the diffusion limits, where the optimal conditions were chosen in the catalyst evaluation experiments.

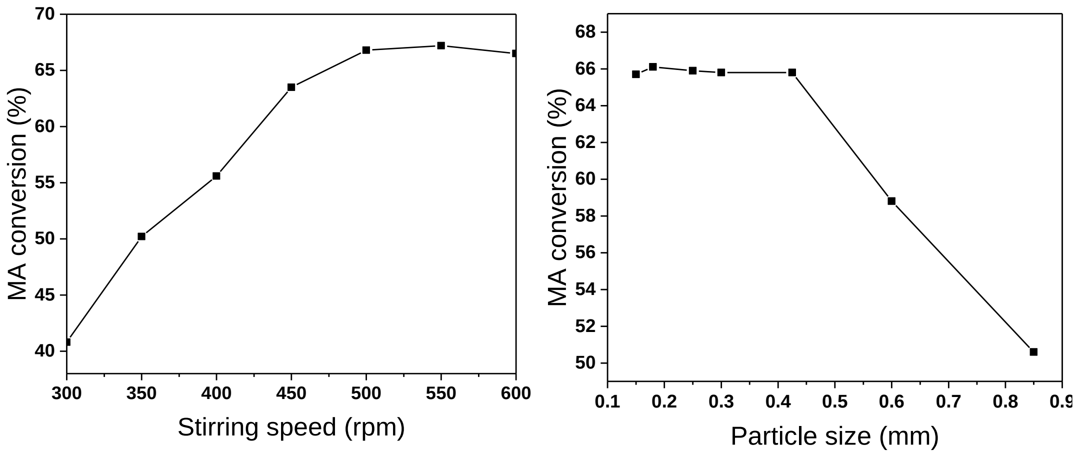

Figure 2.6 Conversion of MA against the stirring rate (A) and particle size of catalysts (B) over $15Ni/CeO_{2-\delta}$ catalyst. Reaction condition: 4.9 g MA, 0.1 g catalyst, 40 ml THF as solvent, 210°C and 5 MPa for 20 min

In the same evaluation system, the stability test of catalysts was conducted by cycling activity tests for 20 times of the MA hydrogenation reaction. After one circle of MA hydrogenation, the catalyst was separated by centrifugation and reused in the next hydrogenation cycle without further treatment. After the stability test, the used catalyst was calcined at 500°C in a N_2 flow to remove the surface adsorbed organic species.

The composition of the reaction effluent was analyzed using a gas chromatograph (7890A, Agilent, USA) equipped with a SE-52 (30m×0.32mm×1.0μm) capillary column and a flame ionization detector (FID). The temperature program of column chamber was set starting from 100°C to 120°C with a ramp of 5 °C/min in order to ensure the complete separation of individual component of the effluent. The temperatures of the injector and detector were set at 260°C and 190°C, respectively. The respective concentrations of MA, SA and GBL in the effluent were measured three times to obtain their average concentrations of individual components, in order to minimize errors from both GC instrumental errors and tests.

One can read the respective concentrations of MA, SA and GBL of the effluent from their standard curves (Figure 2.7) with very high accuracy. The standard curves were plotted using the GC peak areas versus corresponding concentrations of individual components, which were determined using MA/THF, SA/THF and GBL/THF solutions with certain concentrations. The typical GC diagram for MA, SA and GBL are presented in Figure B1 (*Appendix B*).

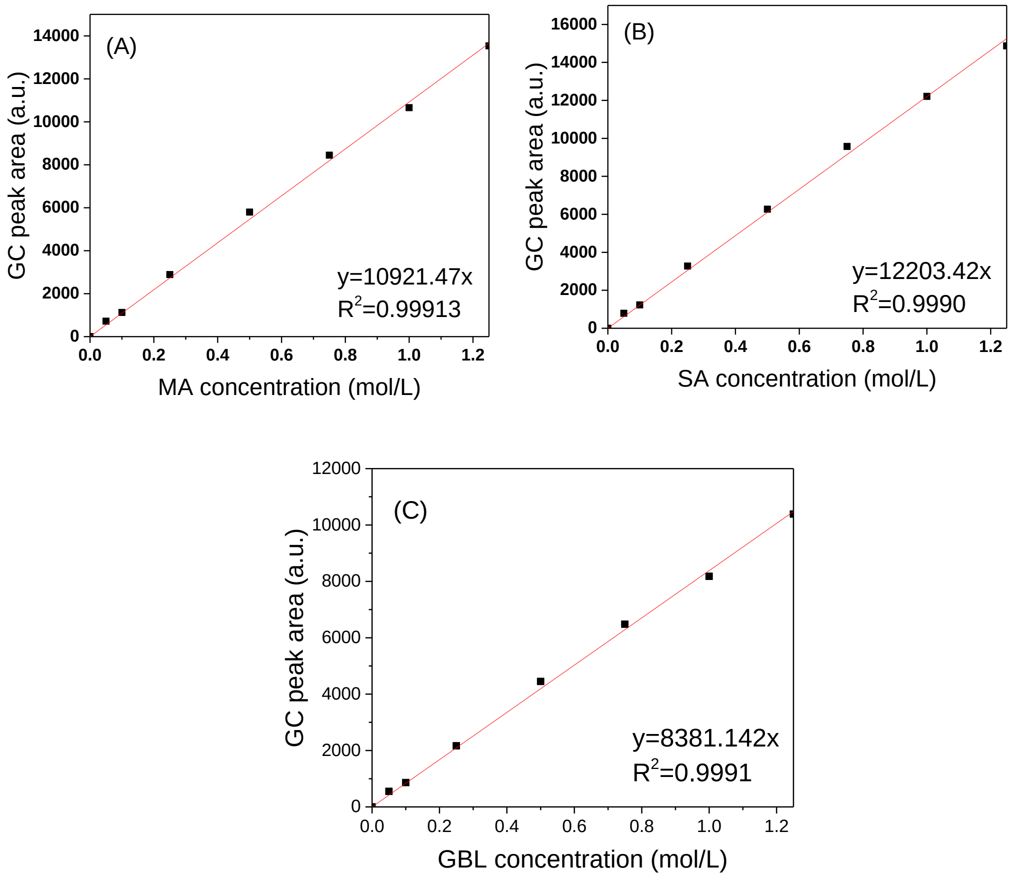

Figure 2.7 The calibration curves of MA, SA and GBL concentration

The MA conversion, yield and selectivity of the hydrogenation system were calculated by inserting the obtained concentrations of MA, SA and GBL into the following equations:

$$X_{MA}(\%) = \frac{C_{GBL}+C_{SA}}{C_{GBL}+C_{SA}+C_{MA}} \times 100\% \qquad (2.6)$$

$$S_{SA}(\%) = \frac{C_{SA}}{C_{SA}+C_{GBL}} \times 100\% \qquad (2.7)$$

$$Y_{SA}(\%) = \frac{C_{SA}}{C_{GBL}+C_{SA}} \times X_{MA} \times 100\% \tag{2.8}$$

$$Y_{GBL}(\%) = \frac{C_{GBL}}{C_{GBL}+C_{SA}} \times X_{MA} \times 100\% \tag{2.9}$$

where the C_{MA}, C_{SA} and C_{GBL} represent relevant concentrations of MA, SA and GBL, respectively. The X_{MA}, S_{SA}, Y_{SA} and Y_{GBL} are respective to the MA conversion, SA selectivity and yields of SA and GBL, respectively.

The turnover frequencies of MA hydrogenation to SA ($TOF_{MA\rightarrow SA}$) on Ni species were calculated using the following equation:

$$TOF_{MA\rightarrow SA} = n(MA)_{int.} \times X_{MA}/(t \times n(Ni)_{total}) \tag{2.10}$$

where the $n(MA)_{int.}$ is denoted the initial number of C=C (one C=C in per MA molecule), X_{MA} is the conversion of MA to SA at low MA conversion (<40%) and t is the reaction time (min). The $n(Ni)_{total}$ represents the total number of surface Ni atoms which were calculated using the hydrogen uptake data on nickel species and assuming $H_{ad}/Ni=1$. The data of hydrogen uptake on Ni atoms were estimated from the H_2-TPD profiles.

The turnover frequencies of SA hydrogenolysis to GBL ($TOF_{SA\rightarrow GBL}$) over the metallic Ni species are estimated using the following equation:

$$TOF_{SA\rightarrow GBL} = n(SA) \times Y_{GBL}/(t \times n(Ni)_b) \tag{2.11}$$

where n(SA), Y_{GBL} and t are denoted to the number of SA (mol) converted to GBL, the yield of GBL (%) and the reaction time (min) for conversion SA to GBL, respectively. The reaction time for conversion of SA to GBL is counting from the time of 100% MA conversion, which is varying on the dependence of catalyst. The $n(Ni)_b$ denotes the number of surface Ni^0 atoms of the catalyst, which is calculated from the hydrogen uptake on the surface of Ni^0 species based on the corresponding peak in the H_2-TPD profiles.

Chapter 3 The comparative studies of 10Ni/$CeO_{2-\delta}$ and 10Ni/Al_2O_3 catalysts on MA hydrogenation

3.1 Introduction

Catalytic hydrogenation of maleic anhydride (MA) is an important chemical process for mass-production of high-value intermediates and solvents, such as SA, GBL and THF, which are in high demand in the chemical, polymer, pharmaceutical and textile industries.[16] However, the pathway of MA hydrogenation can involve simultaneous C=C hydrogenation and C=O hydrogenolysis under similar condition, which can likely bring about mixed products.[76] Therefore, efficient and selective catalysts are highly desirable to reduce the energy penalty for product purification. The recent progress on MA hydrogenation reveals that supported Ni-based catalysts can be exceptional candidates for this process. For the industrial applications, the eco-friendly Ni-based catalysts are more appealing than both the expensive noble metal catalysts and toxic copper chromite catalysts. For supported Ni catalysts, the selected supports can significantly influence the catalytic performance. In general, supports have different properties, like surface area, pore volume, surface acidity and surface defects, which can modulate the geometric and electronic structure of active metal and tune the metal-support interaction.[6, 149] Therefore, suitable selection of support is of importance in rational design of selective catalyst for MA hydrogenation.

Compared with traditional supports like SiO_2, Al_2O_3 and zeolite, the ceria materials are generally featured with the swift redox cycles of cerium cations ($Ce^{3+}\leftrightarrow Ce^{4+}$), structural Ovac and remarkable capacity in oxygen storage, which confers CeO_2 with outstanding performance in catalytic CO oxidation[101, 172], water-gas shift reaction[173, 174] and reforming reactions.[110, 151] The CeO_2 support with Ovac can effectively promote metal dispersion and prevent sintering of the active metals during the thermal operations.[131] With increasing knowledge of CeO_2 material, CeO_2 has been regarded as an excellent candidate for hydrogenation due to its outstanding power in hydrogen adsorption and diffusion.[125,126] DFT simulation suggested that hydrogen dissociation on CeO_2(111) crystal plane is a strong exothermic process with a relatively low barrier energy (-2.82 eV).[127] Additionally, Ovac in CeO_2 also can enhance hydrogen diffusion and migration, which can offer abundant reactive H atoms for the hydrogenation. Moreover, Ovac is also demanded in MA hydrogenation in previous research that Ovac on catalytic support plays crucial roles in selectivity of MA hydrogenation.[92] It is reasonable to anticipate that Ni/CeO_2 will have an excellent performance in MA hydrogenation.

In this section, a novel Ni/CeO_2 catalyst was prepared through facile incipient wetness impregnation and was compared with the conventional Ni/Al_2O_3 for the liquid phase hydrogenation of MA at 210°C and 5 MPa of H_2 pressure. The catalysts were well characterised by XRD, N_2 adsorption-desorption, XPS, H_2-TPR, and H_2-TPD techniques to correlate MA hydrogenation performance with their physicochemical properties.

3.2 Experimental

3.2.1 Catalyst preparation

All chemical reagents, $Ce(NO_3)_3{\cdot}6H_2O$, $Ni(NO_3)_2{\cdot}6H_2O$, $Al(NO_3)_3{\cdot}9H_2O$, concentrated ammonia solution, were at analytic grade and used as-purchased without pre-purification.

The CeO_2 support was prepared via a simple decomposition of $Ce(NO_3)_3{\cdot}6H_2O$ in a quartz tube under the air flow (50 ml/min) at 500°C for 3 h.

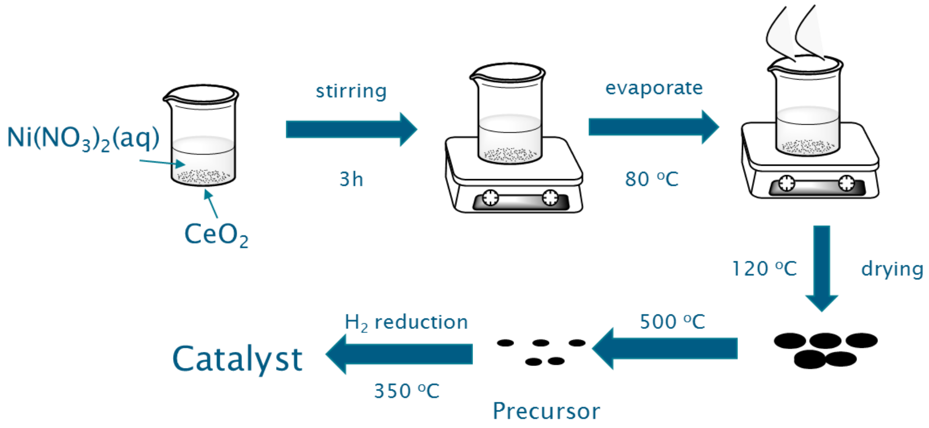

Figure 3.1 The schematic procedure for preparation of $10Ni/CeO_{2-\delta}$ catalyst

The obtained CeO_2 support was used to prepare the $10Ni/CeO_{2-\delta}$ catalyst via a wet impregnation with $Ni(NO_3)_2{\cdot}6H_2O$ solution. The pH of the $Ni(NO_3)_2{\cdot}6H_2O$ solution was not measured. The same $Ni(NO_3)_2$ solution was used to prepare the $10Ni/Al_2O_3$ catalyst too. The detailed procedure is illustrated in Figure 3.1. The CeO_2 support was wetted with certain amount of $Ni(NO_3)_2$ solution in order to achieve the theoretical Ni loading of 10 wt%. The hydrated precursor was dried at 120°C for 8h followed by calcination in air at 500°C for 3h to produce NiO/CeO_2. The Ni/CeO_2

was finally obtained through reduction of the NiO/CeO_2 in H_2 at 350°C for 3 h, denoted as 10Ni/$CeO_{2-\delta}$.

The 10Ni/Al_2O_3 reference was prepared via the wet impregnation of Al_2O_3 support synthesised by the sol-gel method. Briefly, dilute ammonia solution (5.0 wt%) was added slowly into the $Al(NO_3)_3 \cdot 9H_2O$ solution under continuous vigorous stirring at room temperature and controlled pH within 8-9. The obtained hydrogel was aged at 60°C for 8 h before washing with distilled water and absolute ethanol alternatively. The received hydrogel was dried at 80°C for 8 h before annealing in an airflow at 500°C for 3 h. The 10Ni/Al_2O_3 catalyst was obtained through similar impregnation procedures for 10Ni/$CeO_{2-\delta}$ except for reduction at 450°C for 3 h.

3.2.2 Catalyst characterisation and evaluation

The as-prepared 10Ni/$CeO_{2-\delta}$ and 10Ni/Al_2O_3 catalysts and their oxide precursors were characterised by XRD, H_2-TPR, N_2 adsorption-desorption, XPS and H_2-TPD techniques. The detailed procedures were described in *Chapter 2*. The catalytic performance of 10Ni/$CeO_{2-\delta}$ and 10Ni/Al_2O_3 catalyst were evaluated at 210°C and 5 MPa hydrogen pressure in a batch reactor within 0.1 g catalyst, 4.9 g MA and 40 mL THF as a solvent, which was also detailed in *Chapter 2*.

3.3 Results and discussion

3.3.1 Structure and texture of catalysts

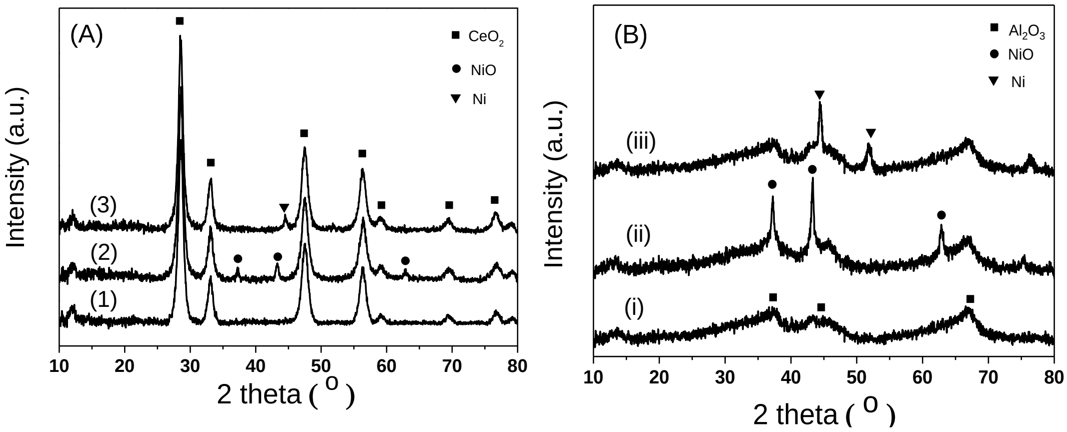

Figure 3.2 XRD patterns of (A) the CeO_2-based samples and (B) the Al_2O_3-based samples: (1) CeO_2, (2) 10NiO/CeO_2, (3) 10Ni/$CeO_{2-\delta}$ and (i) Al_2O_3, (ii) 10NiO/Al_2O_3, (iii) 10Ni/Al_2O_3

The XRD patterns of the as-prepared CeO_2 and Al_2O_3 supports are shown in Figure 3.2 A(1) and B(i). The Bragg diffraction peaks of the CeO_2 sample located at 28.5, 33.1, 47.5, 56.3, 59.1, 69.4 and 76° can be indexed to the well defined (111), (200), (220), (311), (222), (400) and (311) planes of the crystalline ceria of cubic fluorite-type phase (JCPDS file 34-0394, *Fm3m* space group).[175] No other diffraction peaks due to impurity can be observed. On the other hand, the XRD pattern of sol-gel Al_2O_3 only shows diffraction peaks at $2\theta = 37.2$, 45.9, and 60.6° belonging to the γ-Al_2O_3 phase.[176] The broadening and weak diffraction indicates poorly crystalline alumina existing in the Al_2O_3 support synthesised by the sol-gel method.[176]

The diffraction patterns of $10NiO/CeO_2$ and $10NiO/Al_2O_3$ are shown in Figure 3.2 A(2) and B(ii). Besides the characteristic diffraction of γ-Al_2O_3 and CeO_2 supports, the diffraction peaks at 37, 45 and 60° can be well attributed to the (111), (200), (220) faces of polycrystalline NiO species (JCPDS file 044-1159). Although the peaks of NiO diffraction appear at the identical 2θ for the $10NiO/CeO_2$ and $10NiO/Al_2O_3$, the intensity of NiO diffraction for the $10NiO/CeO_2$ is much weaker than that for the $10NiO/Al_2O_3$, suggesting that NiO species in the $10NiO/CeO_2$ has lower crystallinity than that in $10NiO/Al_2O_3$. The calculated mean crystallite size of NiO in $10NiO/CeO_2$ is approximately 10 nm, smaller than that of $10NiO/Al_2O_3$ (Table 3.1). Compared with the $10NiO/Al_2O_3$ sample, the $10NiO/CeO_2$ possesses smaller crystallite size of NiO, indicative of higher dispersion of NiO species. Considering the similar NiO loading amount, the different dispersion of NiO in the $10NiO/CeO_2$ and $10NiO/Al_2O_3$ catalysts may be arisen from the different interaction between NiO and the supports.

The XRD patterns of reduced the catalysts $10Ni/CeO_{2-\delta}$ and $10Ni/Al_2O_3$ are shown in Figure 3.2 A (3) and B (iii). In both cases, the peaks of CeO_2 and Al_2O_3 remain unchanged, revealing that CeO_2 and Al_2O_3 supports keep their own structures. However, the peaks of NiO vanish after H_2 reduction and Ni diffraction emerges, suggesting the supported NiO species are completely converted to Ni by hydrogen reduction. More importantly, in comparison to the $10Ni/Al_2O_3$ catalyst, rather weaker and broader Ni diffraction peaks are seen in the XRD pattern of $10Ni/CeO_{2-\delta}$, indicating the Ni species anchored on CeO_2 are smaller and highly dispersed.

Because ion diffusion can occur during thermal treatment, it is reasonable to expect the surface loading of NiO would change the structural parameters of ceria, for example, crystallite size (D) and lattice parameter (a).[177, 178] The structural parameters of the catalysts retrieved from XRD analyses are listed Table 3.1. It can be clearly seen that the loading of NiO reduced the d-spacing ($d_{(111)}$) and lattice parameter (a_{CeO2}) of ceria in $10NiO/CeO_2$. Because the radius of Ni^{2+} cation (0.072 nm) is smaller than that of Ce^{4+} (0.087 nm),[151] a small fraction of Ni^{2+} cations would diffuse into the CeO_2 lattice to form $Ni_xCe_{1-x}O_{2-y}$ solid solution on the NiO-CeO_2 interface, and thus $d_{(111)}$ and a_{CeO2} of 10NiO/CeO_2 become smaller than those of the bulk CeO_2. However, the increased crystallite size of ceria in the 10NiO/CeO_2 can be attributed to CeO_2 sintering during the thermal treatment with enhancement of ceria crystallinity. Adopting Kroeger notation, the doping may be interpreted by the dissolution of NiO into the CeO_2 matrices as shown in the following equations:[178]

$$NiO + 2Ce^{4+} \rightarrow Ni(Ce^{3+}) + 2Ce^{3+} + 1/2O_2 \qquad (3.1)$$

$$NiO + 2Ce^{4+} \rightarrow Ni_{\Delta} + 2Ce^{3+} + 1/2O_2 \qquad (3.2)$$

$$NiO + 2Ce^{4+} \rightarrow Ni(Ce^{3+}) + 2Ce^{4+} + Ovac \qquad (3.3)$$

where Ni_{Δ} is divalent nickel ions retained in the interstitial positions; $Ni(Ce^{4+})$ and $Ni(Ce^{3+})$ are divalent nickel ions located in the positions hosting tetravalent cerium ions in the CeO_2 lattice and Ovac represents oxygen vacancy. According to the above notation, NiO dissolved at the surface of CeO_2 support via Reactions (3.1) and (3.2) with some Ce^{4+} ions transforming to Ce^{3+} ions ($r(Ce^{3+})=0.102$ nm and $r(Ce^{4+})=0.087$ nm)[179]. These processes led to the decrease of the lattice constant and the formation of $Ni_xCe_{1-x}O_{2-y}$ solid solution penetrated to subsurface of CeO_2.

Table 3.1 The structure parameters of the CeO_2 and metallic Ni.

sample	$2\theta_{(111)}$ (°)	$d^a_{(111)}$ (nm)	a^b_{CeO2} (nm)	D^c_{CeO2} (nm)	D^c_{NiO} (nm)	D^c_{Ni} (nm)
CeO_2	28.56	0.3139	0.5437	9.1	-	-
10NiO/CeO_2	28.63	0.3131	0.5424	9.6	15.6	-
10Ni/$CeO_{2-\delta}$	28.54	0.3141	0.5441	10.1	-	12.2
Al_2O_3		-	-	-	-	-
10NiO/Al_2O_3		-	-	-	24.0	-
10Ni/Al_2O_3		-	-	-	-	16.5

Note: ^{a}The interplanar spacing (d) is calculated using the equation: $2d\sin\theta=n\lambda$. ^{b} The lattice parameter (a) of CeO_2 is estimated using the equation: $a = \sqrt{h^2+k^2+l^2} \times d$ based on the (111) crystal plane of cubic CeO_2. ^{c}The crystallite size is calculated using the Scherrer equation.

In addition, it is worth noting the crystallite size and lattice parameter of CeO_2 (Table 3.1) for the 10Ni/$CeO_{2-\delta}$ become bigger after H_2-reduction treatment. The increasing lattice parameter of ceria (a_{CeO2}) for the 10Ni/$CeO_{2-\delta}$ sample may arise from the removal of active lattice oxygen species by hydrogen and the transformation of the Ce^{4+} ions to larger Ce^{3+} with formation of negatively charged Ovac which distorts the CeO_2 lattice, as a consequence, the a_{CeO2} is raised.

Specific surface area (SSA) and porosity play crucial roles in determining the diffusion and transportation of the reactants in the heterogeneous catalytic MA hydrogenation reaction. Figure 3.3 displays the N_2 adsorption-desorption isotherms of $10Ni/CeO_{2-\delta}$ and $10Ni/Al_2O_3$ catalysts. The two materials display classical type IV isotherms with H1 hysteresis loops, which is typical isotherm shape for mesoporous materials[180].

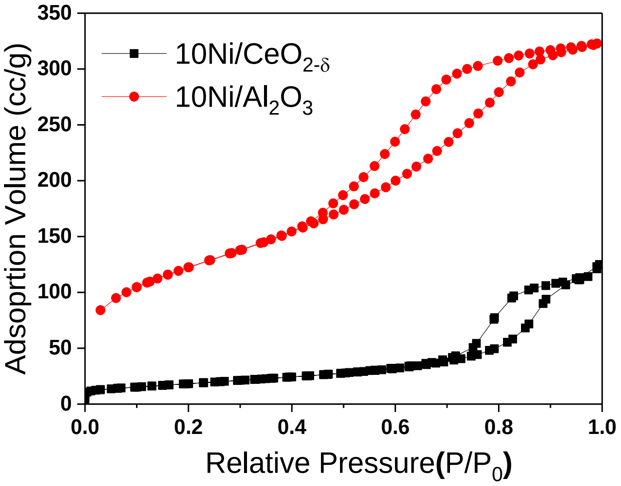

Figure 3.3 N_2 adsorption-desorption isotherms patterns of $10Ni/CeO_{2-\delta}$ and $10Ni/Al_2O_3$

Table 3.2 The textual properties of supports and catalysts

sample	Specific surface area (m^2/g)	Average pore diameter (nm)	Pore volume (cm^3/g)
CeO_2	80.4	12.3	0.24
Al_2O_3	200.5	10.7	0.62
$10Ni/CeO_{2-\delta}$	60.6	11.2	0.17
$10Ni/Al_2O_3$	150.7	9.0	0.46

The obtained textural properties of the supports and catalysts are summarized in Table 3.2. As expected the loading of Ni on the supports significantly reduces the SSA and pore volume of the support materials because the H_2-reduced Ni species cast on the external surfaces of catalysts and also the internal surface of the pores, leading to declining SSA and pore volumes. The reduced Ni particles might also block a fraction of the support pores and contribute to the decrease of SSA and pore volumes for the Ni-based catalysts with respect to supports. The SSA and pore volume of $10Ni/Al_2O_3$ and Al_2O_3 support remain nearly 2.5 times of those of $10Ni/CeO_{2-\delta}$ catalyst and CeO_2, though the $10Ni/CeO_{2-\delta}$ and CeO_2 support possess larger average pore sizes in comparison to 10Ni/Al_2O_3 and Al_2O_3 support, within a range of 9.0–12.3 nm that further prove they are mesoporous materials.

3.3.2 Redox properties of the catalysts

The H_2-TPR profiles of NiO, NiO/CeO_2 and NiO/Al_2O_3 samples are shown in Figure 3.4 where all the H_2-consumption peaks were fitted through the Gaussian multi-peaks fitting program embedded in Origin software. The broad TPR profile of the bulk NiO within 300 and 330°C can be attributed to the single step reduction of NiO to metallic Ni (Figure 3.4). This TPR profile can be fitted into two H_2 consumption peaks corresponding to the reduction of small NiO particle sizes low temperature (~300°C) and the reduction of bulk larger particles at ~330°C.[181] However, the reduction behaviour of the NiO species on the CeO_2 and Al_2O_3 supports exhibits significant difference from the bulk NiO reduction.

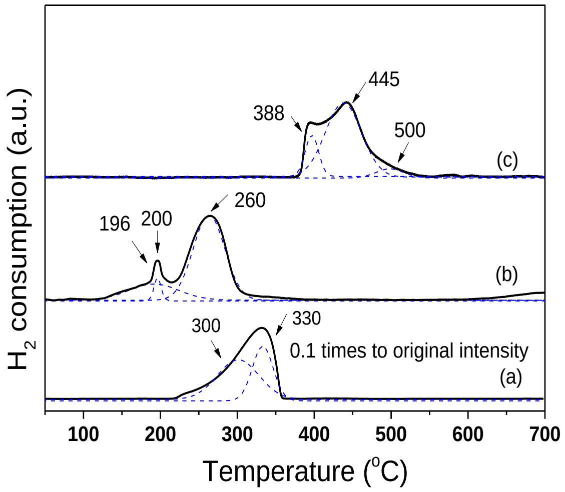

Figure 3.4 The H_2-TPR profiles of (a) NiO, (b) 10NiO/CeO_2 and (c) 10NiO/Al_2O_3

For the 10NiO/CeO_2 sample, there are three H_2 consumption peaks centring at 190, 200 and 260°C in the TPR profiles presented in Figure 3.4. The fitted major H_2 consumption peak centring at 260°C is due to the reduction of the isolated NiO on CeO_2. The temperature of maximum reduction of this peak is much lower than the reduction of bulk NiO yet closer to the small NiO particles (Figure 3.4), suggesting the CeO_2 supported free NiO possesses smaller particle sizes and/or takes special interaction with CeO_2 support. The H_2 consumption peaks centring at lower temperature of 190 and 200°C can be ascribed to the reduction of surface adsorbed oxygen species linked to the surface Ovac of the catalysts.[182] As discussed in the XRD section, Ovac would be generated once Ni incorporated CeO_2 lattice and partially substituted Ce^{4+} and/or Ce^{3+} cations to form solid solution. The Ovac would result in charge unbalance and lattice distortion of CeO_2 which can adsorb oxygen molecule on the oxide surface. The adsorbed oxygen molecules are very reactive and ready to be reduced by H_2 at the relatively low temperature, within 100 to 200°C as shown in our case of 10NiO/CeO_2.

After H_2 reduction treatment, the negatively charged oxygen vacancies in the 10Ni/$CeO_{2-\delta}$ catalyst would be exposed, neighbouring to metallic Ni and thus strongly interact with the metallic Ni species, accordingly, which enhances the ability of Ni as an electron donor in hydrogenation reaction. Theoretically, in the reduced CeO_2 materials, there would be excess H_2 adsorbed on the CeO_2 surface to form hydroxyl group,[183] leading to expansion of CeO_2 unit cell. Indeed, the increased crystal parameters of the 10Ni/$CeO_{2-\delta}$ materials are determined by XRD analysis. The reduction of bulk CeO_2 usually occurs at higher temperature,[163] starting at around 600°C in our case.

The H_2 reduction of 10NiO/Al_2O_3 occurs at higher temperature and displays a distinctively different TPR profile (Figure 3.4) in comparison to those of NiO and 10NiO/CeO_2. The three reduction peaks centring at 390, 445 and 500°C can be due to the highly dispersed NiO, isolated bulk NiO and NiO species with the strong interaction (chemical bonded) with support, respectively.[184] The major NiO reduction of the 10NiO/Al_2O_3 maximizes at 445°C. The reduction at 500°C may be induced by the reduction of spinel $NiAl_2O_4$ or other impurity.[184] In comparison to 10NiO/CeO_2, the TPR peaks of 10NiO/Al_2O_3 appear at rather higher temperatures, revealing there is stronger interaction between NiO and Al_2O_3.

3.3.3 Surface properties of 10Ni/$CeO_{2-\delta}$ catalyst

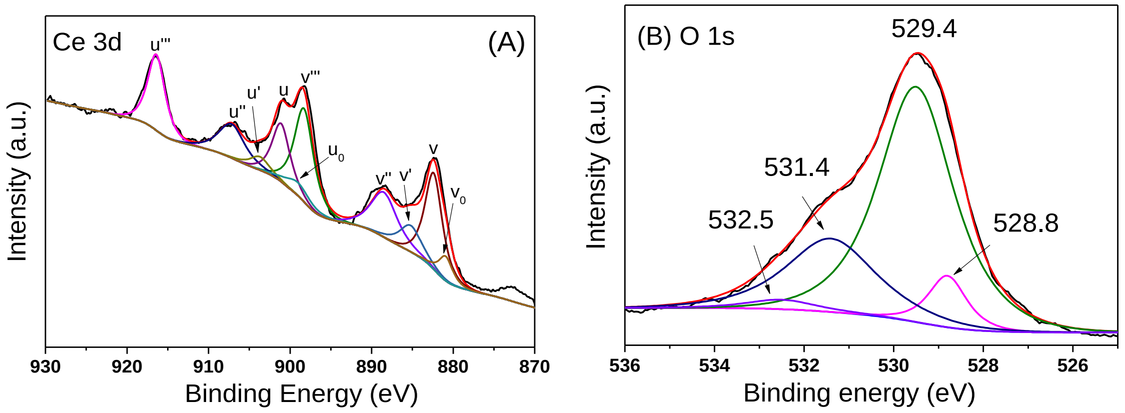

Figure 3.5 The core-level XPS spectra of the reduced 10Ni/$CeO_{2-\delta}$ catalyst (A) Ce 3d and (B) O1s.

The Ce 3d and O1s core level XPS spectra of the reduced 10Ni/$CeO_{2-\delta}$ catalyst are shown in Figure 3.5 (A) and (B), respectively. As shown in Figure 3.5 (A), the Ce 3d core-level XPS spectrum was deconvoluted into 10 Gaussian peaks and labelled in accordance to the deconvolution performed by Burroughs et al.[185] The observed peaks marked as u, u″, u‴, (v, v″, v‴) refer to $3d_{3/2}$ ($3d_{5/2}$) and are characteristic of Ce^{4+} 3d final states; while u′ and u_0 (v′ and v_0) refer to $3d_{3/2}$ ($3d_{5/2}$) for Ce^{3+} 3d final state.[186] The corresponding B.E. values are listed in Table 3.3. The peaks corresponding to Ce^{4+} are the u‴ (916.7 eV, $3d_{3/2}$) and v‴ (898.2 eV, $3d_{5/2}$) which result from Ce ($3d^94f^0$) O ($2p^6$) final states. The additional peaks of Ce^{4+} locating at 907.3 (u″, $3d_{3/2}$) and 888.8 eV (v″, $3d_{5/2}$) can be assigned to Ce ($3d^94f^1$) O ($2p^5$) final state, while the peaks of u and v at 901.2 ($3d_{3/2}$) and 882.4 eV ($3d_{5/2}$) are result of Ce ($3d^94f^2$) O ($2p^4$) final state. In the case of Ce 3d of Ce^{3+}, BE peaks of Ce 3d consist of two pair of doublets (u_0, v_0, u′ and v′). The highest BE peaks u′ ($3d_{3/2}$) and v′ ($3d_{5/2}$) appear at 903.4 and 885.02 eV, respectively, corresponding to Ce ($3d^94f^1$) O ($2p^6$) final state. The lowest BE peaks u_0 ($3d_{3/2}$) and v_0 ($3d_{3/2}$) appear at 880.2 and 898.2 eV, related to Ce ($3d^94f^2$) O ($2p^5$) final state.

Table 3.3 Quantitative analyses of the fitted Ce 3d core level XPS peaks

Valance	Ce^{4+} 3d						Ce^{3+} 3d			
Label	u‴	v‴	u″	v″	u	v	u′	v′	u_0	v_0
Peak BE (eV)	916.7	898.2	907.3	888.8	901.1	882.5	903.7	885.2	899.3	880.8
Attribution	$3d_{3/2}$	$3d_{5/2}$	$3d_{3/2}$	$3d_{5/2}$	$3d_{3/2}$	$3d_{5/2}$	$3d_{3/2}$	$3d_{5/2}$	$3d_{3/2}$	$3d_{5/2}$
Area	2739.4	3775.6	1860.9	2468.9	2183.9	3544.0	533.7	1200.4	672.2	707.9
FWHM	2.5	2.8	3.79	3.81	2.6	2.55	2.75	3.15	3.55	2

Employing the Ce 3d XPS peak areas (Table 3.3) into the following equation,

$$Ce^{3+}\,(\%) = \frac{S_{u'} + S_{v'} + S_{u_0} + S_{v_0}}{\sum(S_u + S_V)}$$

the relative concentration of Ce^{3+} cation ($[Ce^{3+}]$) was acquired to be 15.8 atm% of the overall Ce cations. In order to balance the charges of Ce cations, the required oxygen is determined according to the following equation:

$$\mathrm{X} = \frac{[O]}{[Ce^{3+}] + [Ce^{4+}]} = 1.5[Ce^{3+}] + 2[Ce^{4+}] = 1.88$$

However, the experimental [O]/[Ce] ratio is 1.77 (calculated from the areas of relevant XPS peaks) that is 4.9% lower than the theoretical value 1.88, revealing the existence of Ovac (estimated as ~5.9%) in the ceria support. The quantitation results of the Ce 3d core level XPS verify the existence of trivalent Ce^{3+} cations either in the sesquioxide Ce_2O_3 or around Ovac in CeO_2.

The oxygen species existing in the 10Ni/CeO_2 catalyst was determined via assessing its core level O1s XPS. As shown in Figure 3.5, the O1s XPS was fitted into four peaks and the obtained data are summarised in Table 3.4. The two lower energy peaks locating from 529 to 530.6 eV are attributed to lattice oxygen species

(O^{2-}) binding to Ce^{3+} and Ce^{4+},[187] whereas those peaks at higher BE side are assigned to surface oxygen species.[188] The peak centring at 532.5 eV is usually assigned to Ovac,[188] which is accounting for 4.7 atm% of the overall oxygen. The Ovac concentration here is slightly less than the above estimated Ovac value (5.9%), suggesting there might be more Ovac signal turning up at other BE position. The other locates at 531.4 eV may be associated with surface hydroxyl group (O_{SOH}), Ovac and surface adsorbed oxygen (O_{ad}) linked to Ce^{3+} cations.[188] Because the catalyst was well reduced, the O_{ad} can be excluded, hence, we can conclude that the peak at 531.4 eV is mainly related to the surface OH groups and oxygen vacancies.

Table 3.4 Quantitative analyses of the fitted O1s core level XPS peaks

O 1s XPS Peaks	Deconvoluted peaks			
Peak BE (eV)	528.8	529.6	531.4	532.5
Area	799	2245.6	936.0	199
FWHM	1.4	1.87	2.24	2.2
O species	O_{Latt}[187]	O_{Latt}[187]	O_{SOH}, O_{vac}, O_{ad}[187, 188]	O_{vac}[188]

3.3.4 Hydrogen activation on the catalysts

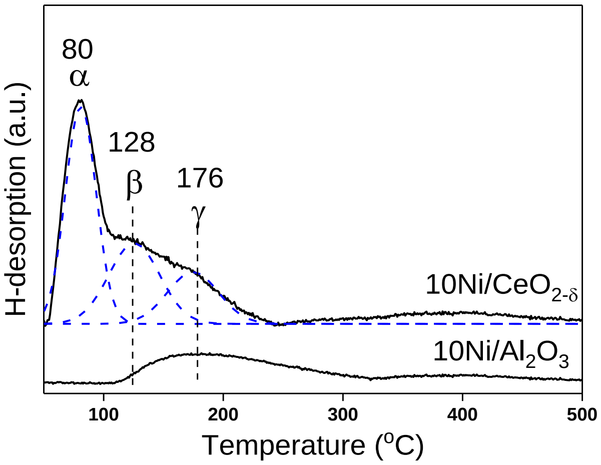

Figure 3.6 H_2-TPD profiles of (a) the 10Ni/$CeO_{2-\delta}$ and (b) the 10Ni/Al_2O_3 catalysts

Hydrogen temperature-programmed desorption (H_2-TPD) is an effective measure to analyse the ability of H_2 activation of the hydrogenation catalysts. Figure 3.6 comparatively shows the H_2-TPD profiles of the 10Ni/$CeO_{2-\delta}$ and 10Ni/Al_2O_3. The 10Ni/$CeO_{2-\delta}$ displays three-staged H_2 desorption, suggesting there are three sorts of active sites for H_2 dissociation. The peak centring at 80°C is assigned to the desorption of hydrogen filled in the Ovac.[177] Moreover, the other two peaks locate at higher temperature can be related to the desorption of strongly chemisorbed hydrogen on the surface of nickel species. The peak at 120°C is associated with dissociative H-species uptake at highly dispersed Ni species with a large density of surface defects which can enhance the hydrogen diffusion and reduce energy barrier for hydrogen dissociation.[189] The peak at 178°C is associated with hydrogen chemisorption on isolated metallic Ni nanoparticles.[190] The 10Ni/Al_2O_3 catalyst displays a distinct H_2-TPD profile from 10Ni/$CeO_{2-\delta}$ catalyst. There is no H_2-TPD signal observed at 80°C for the 10Ni/Al_2O_3 (Figure 3.6), probably because of the absence of Ovac in the Al_2O_3 support. In addition, a broad and overlapped peak starting at 100°C and tailing to 300°C can be attributed to hydrogen desorption from the Ni species[190].

In order to understand the difference in the ability of hydrogen activation between the two catalysts, quantitative analysis of H desorption was carried out and the results are listed in Table 3.5. The H_2 desorption amount of the two samples was calculated and it is 65.55 μmol/g (including 28.35 μmol/g vacancy-adsorbed H_2, 22.6 μmol/g interface-adsorbed H_2 and 14.6 μmol/g chemically adsorbed H_2 on free Ni) for 10Ni/$CeO_{2-\delta}$ catalyst, 2 times of that on 10Ni/Al_2O_3 (32.3 μmol/g). The high H_2 uptake amount for the metallic Ni on the 10Ni/$CeO_{2-\delta}$ suggests it has higher dispersion and smaller particle size, which is in accordance with the XRD results. As discussed in the XRD and TPR sections, the H_2-TPD results here further reveal the stronger interaction existing between free Ni and CeO_2 as compared to metallic Ni and Al_2O_3.

Table 3.5 H_2 chemisorption capability of the reduced samples

Sample	Ni loading (%)	H_α (μmol/g)	H_β (μmol/g)	H_γ (μmol/g)	n(Ni_{surf}) (μmol/g)	Ni dispersion (D)^b (%)
10Ni/$CeO_{2-\delta}$	9.8	28.35	22.6	14.6	74.4	4.4
10Ni/Al_2O_3	10.2	-	-	32.3	64.6	3.8

Note: Ni loading was measured by ICP-OES technique. H_α, H_β and H_γ represent the estimated amount of adsorbed hydrogen, which were calculated based on the areas of α, β and γ peaks, respectively. The percentage of Ni dispersion was calculated using the equation: Ni dispersion was calculated using the Equation 2.5 in Chapter 2 with the amount of H_2 uptake at metal surface.

The quantitative analysis of H_2-TPD data in Table 3.5 also suggests the 10Ni/$CeO_{2-\delta}$ catalyst would have either greater capability to adsorb and activate hydrogen in comparison to 10Ni/Al_2O_3 in the low temperature region (due to Ovac) or high temperature (associated with smaller Ni particles). The synergism of the Ovac, the high dispersion of Ni species and the Ni-CeO_2 interaction would promote

H_2 dissociation on 10Ni/CeO$_{2-\delta}$. In addition, through the comparative analyses of H_2-TPR and H_2-TPD for the two catalysts, one can conclude that the 10Ni/CeO$_{2-\delta}$ catalyst possesses more active sites for reversible adsorption-desorption of H species, leading to a fast conversion between H_2 and the dissociated H species on the catalyst in the MA hydrogenation process, thus facilitating the MA conversion rate. Hence, the 10Ni/CeO$_{2-\delta}$ catalyst is more active in hydrogenation reaction.

3.3.5 Catalytic performance

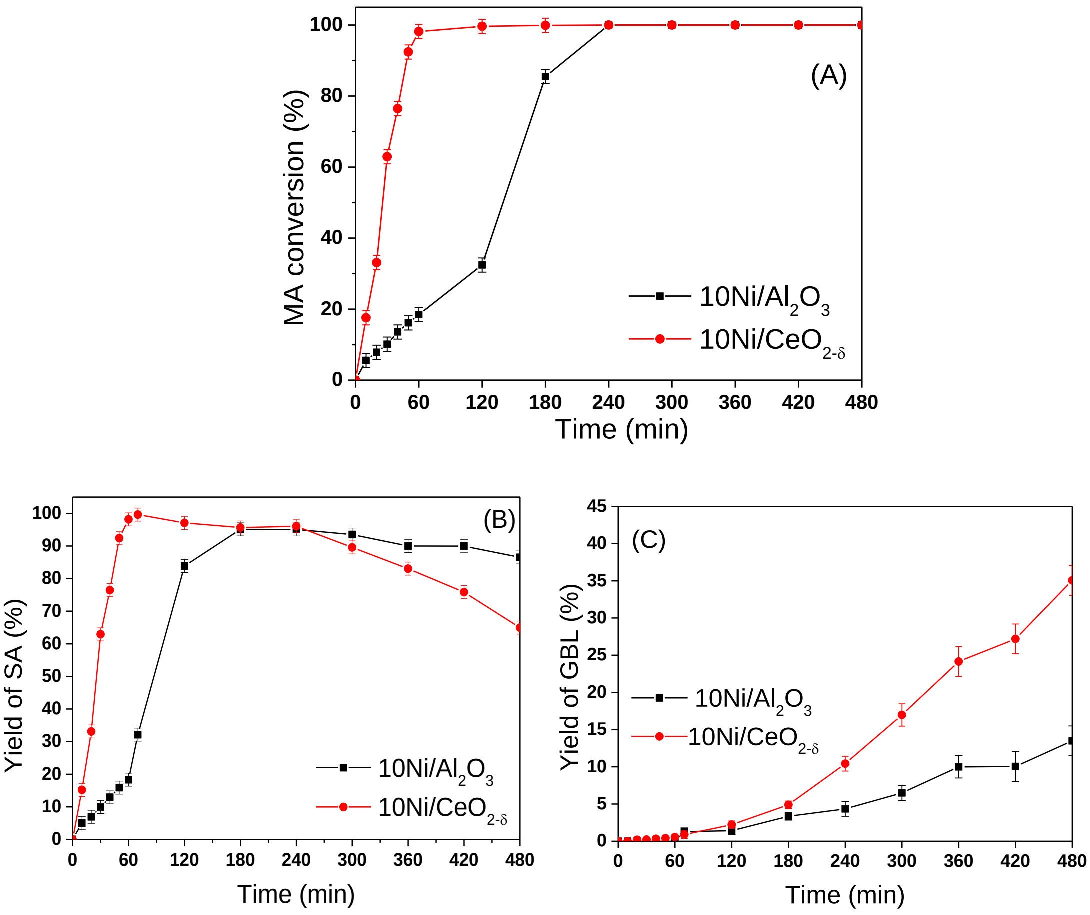

Figure 3.7 Conversion of MA (A) and yields of SA (B) and GBL over 10Ni/CeO$_{2-\delta}$ and 10Ni/Al$_2$O$_3$ catalysts at 210°C under 5 MPa for 8h duration.

The hydrogenation of MA on the 10Ni/CeO$_{2-\delta}$ and 10Ni/Al$_2$O$_3$ catalysts was performed in a batch reactor at 210°C and the pressure reached 5.0 MPa during hydrogenation reaction due to elevated temperature. The results of MA conversion and yields of SA and GBL are plotted in Figure 3.7. It can be clearly seen that MA was completely converted into SA on the 10Ni/CeO$_{2-\delta}$ catalyst within 1.0 h MA hydrogenation reaction. In contrast, less than 20% of MA converted on the 10Ni/Al$_2$O$_3$ under similar conditions and MA hydrogenation duration. Additionally, in terms of the initial conversion per unit surface area, the specific activity of MA hydrogenation on 10Ni/CeO$_{2-\delta}$ is 12.5 times that on the 10Ni/Al$_2$O$_3$ catalyst. The

$TOF_{MA\rightarrow SA}$ for $10Ni/CeO_{2-\delta}$ is 118.1 min^{-1}, while the $TOF_{MA\rightarrow SA}$ for $10Ni/Al_2O_3$ is 35.29 min^{-1}. It is worth noting that the $TOF_{MA\rightarrow SA}$ on $10Ni/CeO_{2-\delta}$ catalyst is 3.3 times that over $10Ni/Al_2O_3$, which is higher than the Ni dispersion ratio between $10Ni/CeO_{2-\delta}$, and $10Ni/Al_2O_3$ ($D_{10Ni/CeO2}/D_{10Ni/Al2O3}$=1.57, Table 3.5). In terms of the specific property ratios between $10Ni/CeO_2$ and $10Ni/Al_2O_3$, it is apparent that the $TOF_{MA\rightarrow SA}$ ratio (3.3 times) and specific apparent activity ratio (12.5 times) are remarkably higher than the Ni dispersion ratio (1.57 times), suggesting there should be other factors besides the high Ni dispersion that enhance MA conversion rate on $10Ni/CeO_{2-\delta}$ catalyst. We suppose that it is the Ovac on $10Ni/CeO_{2-\delta}$ that significantly contributes to the enhanced activity of MA hydrogenation to SA since its surface area is fairly lower than that of $10Ni/Al_2O_3$.

It is worth noting there were no other side products only SA produced in the initial 1.0 h MA hydrogenation, thereafter GBL generation started (Figure 3.7 B and C). The results reveal that MA hydrogenation is a multiple step reaction and SA generation is a fast reaction. GBL can be thought as a derivative from SA in the subsequent hydrogenation. The selectivity of the two catalysts differs in the prolonged hydrogenation process of 8.0 hours. As shown in Figure 3.7 B and C, the initial yield of GBL over the two catalysts remains similar in the initial 3.0 hour on stream, though the generation of GBL on the $10Ni/CeO_{2-\delta}$ increases faster after the 3h hydrogenation course. 37% selectivity of GBL was achieved over the $10Ni/CeO_{2-\delta}$ catalyst but only 12.5% on the $10Ni/Al_2O_3$ in the continuous hydrogenation for 8.0 hours. The gradually enhanced selectivity may be associated to the increased concentration of oxygen vacancies of CeO_2 in $10Ni/CeO_{2-\delta}$ along with prolonged MA hydrogenation time. Meanwhile, the calculated $TOF_{SA\rightarrow GBL}$ for $10Ni/CeO_{2-\delta}$ is 3.89 min^{-1}, which is 1.69 times that for $10Ni/Al_2O_3$ ($TOF_{SA\rightarrow GBL}$ = 2.29 min^{-1}), much closer to the Ni dispersion ratio (1.57 times) between the two catalysts. Obviously, Ni dispersion is a key factor in determining the conversion of SA to GBL and thus the apparent GBL selectivity yet the oxygen vacancies on $10Ni/CeO_{2-\delta}$ would also favour GBL production.

Based on the different ratios between $TOF_{MA\rightarrow SA}$ and $TOF_{SA\rightarrow GBL}$ over the two Ni-based catalysts, we proposed that the hydrogenation of MA to SA and GBL take different mechanistic paths that involve different active sites or require different properties of support surface. The TOF data also suggest that Ovac would be paramount in SA generation and help subsequently produce GBL. However, we cannot exclude the contribution of different energy requirements for C=C hydrogenation and C=O hydrogenolysis to the selectivity since the C=C bond (1.33 Å, 611 kJ/mol) is weaker than the C=O bond (1.20 Å, 728 kJ/mol).[191]

The different activity and selectivity results along with time on the stream suggest the support also plays vital roles in determining the initial activity and selectivity of MA hydrogenation to SA yet the metallic Ni dispersion dominates the performance of SA to GBL. The support plays pivotal roles in promoting the MA hydrogenation rate in terms of the TOFs (MA→SA) and specific activity for the two catalysts. Combining the comparative characterisation results in our cases, we can conclude that CeO_2 may improve the dispersion of metallic Ni species, offer Ovac and stronger interaction between Ni and the support. As a consequence, the $10Ni/CeO_{2-\delta}$ catalyst shows much better reactivity in MA hydrogenation than the $10Ni/Al_2O_3$ catalyst.

The generation of GBL can be viewed as a subsequent process of MA hydrogenation to SA that is featured with selective hydrogenolysis of one C=O bond but remaining another in SA.[83] The previous reports in the literature proved that Ovac in nonstoichiometric oxides, such as ZnO[92] and TiO_x[80] can selectively adsorb, polarise the C=O bond and consequently reduce the activation energy of its hydrogenolysis. In comparison to ZnO and TiO_2 supports, CeO_2 is much easier to generate and tune Ovac due to its swift shift between the Ce^{3+} and Ce^{4+} oxidation states. Owing to the excess hydrogen existing in MA hydrogenation process, the CeO_2 support would be further reduced and generate more Ovac and lead to more active hydrogen species, in particular the active hydrogen corresponding to the first-stage H_2-TPD peak around 80°C. The increasing concentration of oxygen vacancies in $10Ni/CeO_{2-\delta}$ would accelerate SA production and display higher yield of SA in the prolonged hydrogen duration. However, Al_2O_3 cannot generate more oxygen vacancies in MA hydrogenation process, so that the enhanced SA yield during hydrogenation can only be attributed to the increased active hydrogen species on $10Ni/Al_2O_3$.

3.4 Conclusion

A novel $10Ni/CeO_{2-\delta}$ catalyst was prepared via a simple impregnation of mesoporous CeO_2 followed by the H_2 reduction process. In comparison with the $10Ni/Al_2O_3$ catalyst with larger surface area, the $10Ni/CeO_{2-\delta}$ catalysts exhibited faster rates in hydrogenation of MA to SA at the initial hydrogenation stage, and higher selectivity to GBL in the prolonged hydrogenation process. Through analyses of the reactivity and the crystal structure, porosity and redox properties of the catalysts collected from effective characterization by XRD, N_2 isotherm, H_2-TPR/D and XPS techniques, we conclude that the superior performance of 10Ni/$CeO_{2-\delta}$ to 10Ni/Al_2O_3 was closely related to the high dispersion of metallic Ni species, the existence of oxygen vacancies and large pore sizes of the $CeO_{2-\delta}$ support, and strong interaction between Ni and $CeO_{2-\delta}$.

The highly dispersed Ni species and their strong interaction with the $CeO_{2-\delta}$ support facilitated higher conversion rate of MA to SA, meanwhile, Ovac also favoured the production of GBL during hydrogenation of SA to GBL process. Ovac in the $CeO_{2-\delta}$ support may be generated by H_2 reduction in the pre-treatment of the catalysts, the MA hydrogenation process as well as partial incorporation of Ni into its matrix across the Ni-$CeO_{2-\delta}$ interface. The time-on-stream tests of MA hydrogenation over our Ni-based catalysts process enabled us to conclude MA hydrogenation is a multiple-step process in which the Ni species determines the initial reactivity and support promotes reaction rate, which offers great potential to control the product selectivity through tuning the catalyst composition.

Chapter 4 MA hydrogenation over $CeO_{2-\delta}$ supported transition metal catalysts

4.1 Introduction

For MA hydrogenation, current catalysts widely applied in the MA hydrogenation process are noble metal catalysts, such as Pd,[33, 192] Ru[60] and Pt,[66, 193] though they are either costly or limited resources. For developing low-cost alternative MA hydrogenation catalysts, great efforts have been made on exploring active transition metal catalysts, such as Ni[37, 41, 83], Co[41] and Cu[72, 194] based catalysts. For example, Meyer and co-workers compared the catalytic performance of Ni/SiO_2 and Co/SiO_2 catalysts in MA hydrogenation and found the Ni/SiO_2 catalyst displayed higher activity and more selective to GBL than the Co/SiO_2 catalyst.[41] Furthermore, the Co/SiO_2 catalyst suffered from the rapid deactivation in comparison with Ni/SiO_2 due to the deposition of carbonaceous species on the surface.[41] Li and co-workers prepared supported Ni/Al_2O_3, Cu/Al_2O_3 and Co/Al_2O_3 catalysts for MA hydrogenation and found that the Ni/Al_2O_3 catalyst exhibited higher catalytic activity and stability in MA hydrogenation compared with Co/Al_2O_3 and Cu/Al_2O_3 catalysts.[73] It is tentatively shown that metallic Ni seems to exhibit higher catalytic performance in MA hydrogenation, however, previous research advances in MA hydrogenation catalysts revealed that their activity and selectivity depend greatly on the proper selection of metal, the selected support and the corresponding metal-support interaction. For understanding the roles of transition metals in MA hydrogenation, it is necessary to extend the support selection and investigate their catalytic performance in the hydrogenation.

In the previous chapter, $10Ni/CeO_{2-\delta}$ catalyst displays the superior activity and selectivity in MA hydrogenation to $10Ni/Al_2O_3$ catalyst due to the high Ni dispersion, the strong $Ni\text{-}CeO_{2-\delta}$ interaction and the presence of Ovac. This result indicates that structure-defective CeO_2 support plays a profound role in the hydrogenation reaction. In theory, Ovac in $CeO_{2-\delta}$ may modify the geometric and electronic structure of the active metal[133, 134], as well as enforce the metal-support interaction.[131] On the other hand, the property of Ovac in the CeO_2 supported catalysts is significantly related to the metal species because the supported metal species can diffuse into the CeO_2 lattice and modulate the population of Ovac in mixed oxides with dependence of the ionic radius and the valence state of the metal species.[195] Although $M/CeO_{2-\delta}$ catalysts have been examined in various catalytic reactions, there is very limited knowledge of the metal influence on the $CeO_{2-δ}$ supports, particularly for the activity and selectivity in MA hydrogenation.

In this chapter, various transition metals (Co, Ni and Cu) supported on ceria were prepared by a simple wet impregnation method and employed in the liquid phase hydrogenation of MA at 210˚C and 5 MPa of H_2 pressure. Through careful characterization, the catalytic activity and selectivity in MA hydrogenation on the $M/CeO_{2-δ}$ catalysts were investigated and correlated with the properties of the materials.

4.2 Experimental

All chemical reagents, citric acid (CA), $Ce(NO_3)_3·6H_2O$, $Ni(NO_3)_2·6H_2O$, $Cu(NO_3)_2·3H_2O$ and $Co(NO_3)_2·6H_2O$ were at analytic grade and used as-purchased without pre-purification.

4.2.1 Preparation of ceria support

Ceria supports were prepared by a sol-gel process. First, 5.00 g $Ce(NO_3)_3·6H_2O$ was dissolved into 20 ml deionized water containing 6.56 g CA under rigorous stirring. The solution was heated in a water bath at 80 ˚C until porous dry gel was obtained. During this process, the colourless solution became light yellow and finally brown. The obtained gel was then dried at 120°C for 8 h to form a spongy material, which is subject to calcination for 3 h at 500°C with a heating ramp of 3°C/min. The resulting cerium oxide was used as the support to prepare corresponding catalysts.

4.2.2 Preparation of $M/CeO_{2-δ}$ (M=Co, Ni and Cu) catalysts

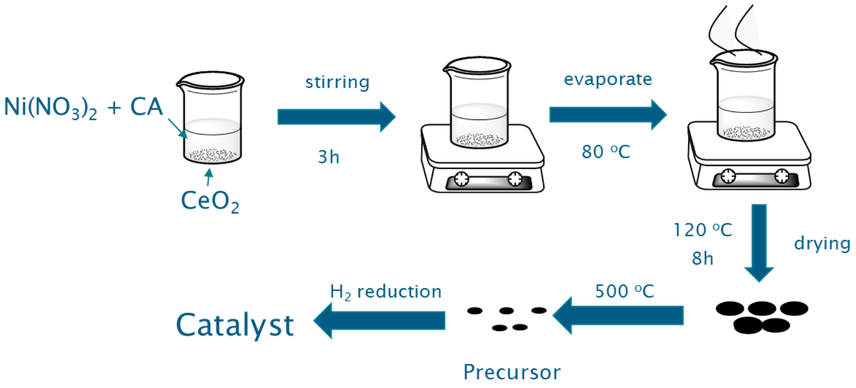

Figure 4.1 The scheme of catalyst preparation for the $Ni/CeO_{2-δ}$ catalyst

The $M/CeO_{2-δ}$ (M=Co, Ni and Cu) catalysts (metal loading=10 wt%) were prepared by a CA-assisted wet impregnation method developed in the University of Southampton. The process for preparation of the $Ni/CeO_{2-δ}$ catalyst is shown in

Figure 4.1. In detail, 1.01 g $Ni(NO_3)_2{\cdot}6H_2O$ and 0.667 g CA (mole ratio of CA/Ni=1) were dissolved in 10 ml the ethanol/DI water (1:1 volumetric ratio) solution, and then 2.00 g of CeO_2 support was added into the mixed solution. The pH of impregnation solution for the $M/CeO_{2-\delta}$ catalysts was not measured because the amount of CA depended on the metal amount to keep the mole ratio of CA/M constant (CA/M=1). The mixed solution was heated on a hotplate at 80°C under rigorous stirring to evaporate the solvent before drying at 120°C for 8 h in a convection oven. The obtained sample was calcined at 500°C for 3 h in a muffle furnace with the heating ramp of 3°C/min. The received oxide sample was reduced at 350°C (heating ramp of 2°C/min) in a H_2 flow for 3 h to obtain the $Ni/CeO_{2-\delta}$ catalyst for MA hydrogenation. The $Cu/CeO_{2-\delta}$ and $Co/CeO_{2-\delta}$ catalysts were prepared using the similar procedure, but $Cu/CeO_{2-\delta}$ and $Co/CeO_{2-\delta}$ were reduced at 250°C and 450°C, respectively, which ensured all the transition metal species were fully reduced at optimum temperature as determined by H_2-TPR. The catalysts are denoted as $10Co/CeO_{2-\delta}$, $10Ni/CeO_{2-\delta}$ and $10Cu/CeO_{2-\delta}$ with their metal loading amount.

4.2.3 Catalyst characterisation and evaluation

The as-prepared $M/CeO_{2-\delta}$ catalysts and their oxide precursors were characterised by XRD, H_2-TPR, N_2 adsorption-desorption, XPS and H_2-TPD techniques. The detailed procedures were described in Chapter 2. The catalytic performance of $M/CeO_{2-\delta}$ catalysts were evaluated at 210°C and 5 MPa hydrogen pressure in a batch reactor within 0.1 g catalyst, 4.9 g MA and 40 mL THF as a solvent, which was also detailed in Chapter 2.

4.3 Results and discussion

4.3.1 Structure and morphology

Figure 4.2 shows the XRD patterns of CeO_2 and MO_x/CeO_2 (M=Co, Ni, Cu, respectively) precursors. For the CeO_2 and MO_x/CeO_2 samples, the major Bragg diffraction peaks at 28.5, 33.1 and 47.5° are clearly resolved and attributed to the diffraction from (111), (200) and (220) planes of the cubic fluorite-type ceria (JCPDS file 34-0394), respectively. The weak diffraction peaks are associated with isolated metal oxides and indexed to CuO (JCPDS file 48-1548), NiO (JCPDS file 78-0643) and Co_3O_4 (JCPDS file 43-1003) (Figure 4.2(A)). The diffraction peaks of CeO_2 in the MO_x/CeO_2 catalysts slightly shift to greater 2θ angles than those of bare CeO_2, revealing that small portions of the $M^{\delta+}$ ions have diffused into the ceria matrix and partially substituted cerium cations ($r(Ce^{4+})$=0.084 nm). Indeed, the metal doping induces lattice distortion and shrinkage of CeO_2 lattice to the different level (Table 4.1), due to the smaller radii of the doping cations (r(Co^{2+})=0.074 nm and r(Co^{3+})=0.063 nm, r(Ni^{2+})=0.072 nm and r(Cu^{2+})=0.073 nm). The changes of the lattice parameters for CeO_2 in the samples are insignificant because of the low metal doping levels.

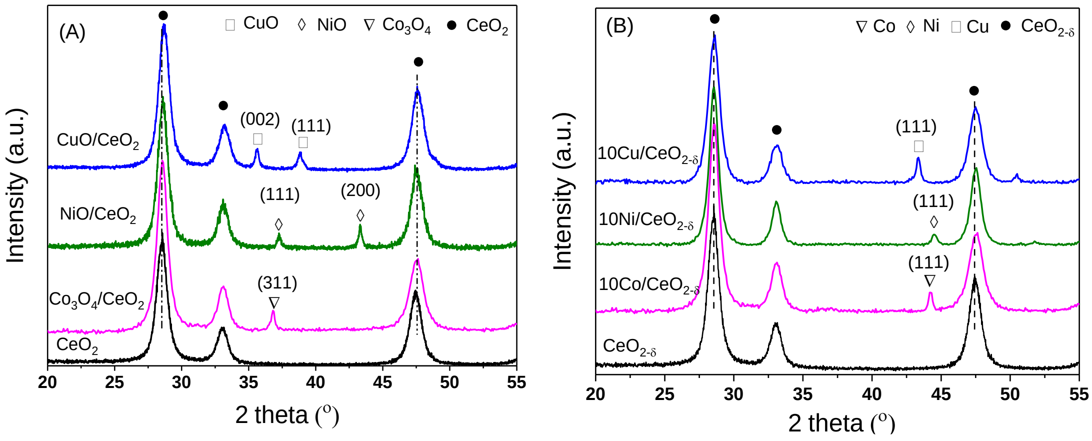

Figure 4.2 XRD pattern of (A) the MO_x/CeO_2 precursors and (B) the M/$CeO_{2-\delta}$ catalysts (M= Co, Ni and Cu, respectively).

The calculated mean crystalline sizes of Co_3O_4, NiO, CuO and CeO_2 are listed in Table 4.1. It is found NiO possesses the smallest crystallite size, while CuO has the largest crystallite size. The CeO_2 supports exhibit different crystallite sizes even though the MO_x are loaded at the similar amount. The varying crystallite sizes of MO_x and CeO_2 are due to their different MO_x-CeO_2 interaction and the corresponding lattice distortion.

Table 4.1 Properties of the MO_x/CeO_2 precursors and corresponding M/$CeO_{2-\delta}$ catalysts

Sample	a(CeO_2) (nm)	a'($CeO_{2-\delta}$) (nm)	Loading (wt%)	Crystallite size (nm)			
				D(CeO_2)	D($CeO_{2-\delta}$)	D(MO_x)	D(M)
CeO_2	0.5438	0.5438	-	12.5	12.9	-	-
10Co/$CeO_{2-\delta}$	0.5430	0.5442	10.3	14.3	15.2	15.7	12.8
10Ni/$CeO_{2-\delta}$	0.5424	0.5441	9.8	12.5	16.5	13.2	9.8
10Cu/$CeO_{2-\delta}$	0.5413	0.5442	9.7	13.2	15.7	16.7	13.4

Note: The lattice parameter (a(CeO_2) and a'($CeO_{2-\delta}$)) of CeO_2 was estimated using the equation: $a = \sqrt{h^2 + k^2 + l^2} \times d$, based on the (111) crystal plane of cubic CeO_2. The amount of metal loading was measured using ICP-OES. The crystallite sizes of CeO_2, MO_x and metal species were estimated using the Scherrer equation.

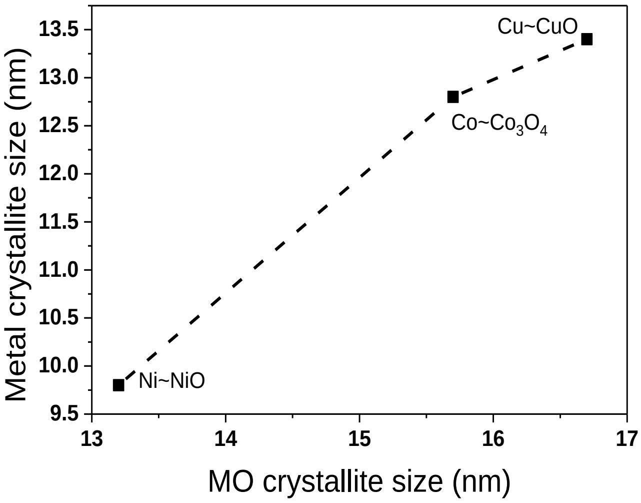

Figure 4.3 The dependence of metal crystallite sizes on those of metal oxides

After H_2 reduction treatments, metal phases of Ni, Co and Cu emerge in the XRD patterns of the reduced M/$CeO_{2-\delta}$ catalysts (Figure 4.2(B)), while the MO_x diffraction peaks vanish since the crystalline MO_x species are converted to corresponding metals. Compared with Co and Cu, Ni species display relatively weaker diffraction, suggesting that Ni might be highly dispersed on the surface of $CeO_{2-\delta}$ with smaller crystallite size. Furthermore, a reliance of metal crystallite sizes on their corresponding metal oxides is proportional, as presented in Figure 4.3, suggesting the interaction between M and $CeO_{2-\delta}$ largely inherit that in the MO_x/CeO_2 samples.

As shown in Table 4.1, the lattice parameters of ceria in the M/$CeO_{2-\delta}$ catalysts appear quite similar but become larger than those of MO_x/CeO_2 samples. The increasing crystallite sizes of ceria in M/$CeO_{2-\delta}$ catalysts may be induced by comprehensive factors, including a fraction of Ce^{4+} cations being reduced to Ce^{3+} with larger ionic radius (r(Ce^{3+})=0.102 nm[183]) that expands the ceria lattice parameter, the thermal sintering of ceria and the metal exiting from ceria matrices during the reduction process.

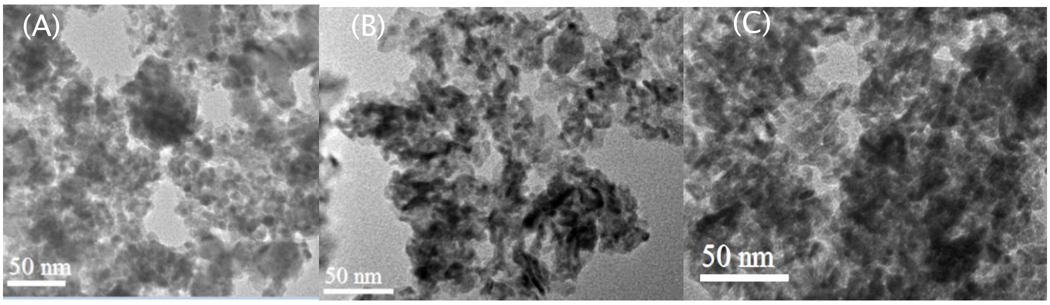

Figure 4.4 TEM images of M/$CeO_{2-\delta}$ samples. (A) 10Co/$CeO_{2-\delta}$, (B) 10Ni/$CeO_{2-\delta}$ and (C) 10Cu/$CeO_{2-\delta}$.

Figure 4.4 shows TEM images of reduced M/$CeO_{2-\delta}$ catalysts. It is found that most CeO_2 observed in the M/$CeO_{2-\delta}$ samples are of spherical or random polyhedral morphologies, independent of the deposited metals. From the TEM images, it is difficult to distinguish the metal particles because the sizes of metals are quite similar to the CeO_2 support (shown in Table 4.1).[196] In addition, larger $CeO_{2-\delta}$ particle is seen in the 10Co/$CeO_{2-\delta}$ catalyst compared with 10Ni/$CeO_{2-\delta}$ and 10Cu/$CeO_{2-\delta}$, which is likely associated with the slight sintering of the ceria support during the reduction at higher temperature.

4.3.2 Reduction behaviour of the MO_x/CeO_2 precursors

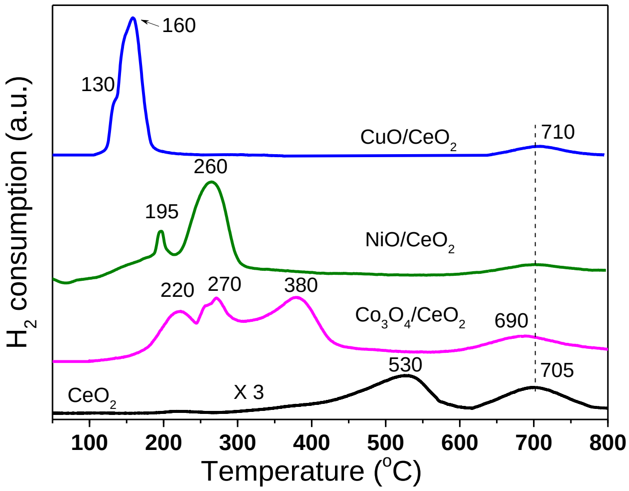

Figure 4.5 H_2-TPR profiles of MO_x/CeO_2 samples

Figure 4.5 shows the H_2-TPR profiles of MO_x/CeO_2 samples. The TPR profiles at the temperature below 400°C are due to the reduction of supported MO_x in the three MO_x/CeO_2 samples. For the CuO/CeO_2 sample, the strong peak centred at 160°C is attributed to the reduction of isolated CuO species with weak CuO-CeO_2 interaction, while the shoulder peak located at 130°C is due to the reduction of adsorbed O species on Ovac sites and the highly dispersed CuO with strong CuO-CeO_2 interaction.[197] For the NiO/CeO_2 sample, the reduction of surface adsorbed O species starts from an even lower temperature (~ 100°C) with a sharp reduction peak at 195°C, which can be related to the reduction of highly dispersed NiO on CeO_2.[182] The main TPR peak at 260°C is assigned to reduction of NiO clusters aggregated on the CeO_2 surface.[182] For the Co_3O_4/CeO_2 sample, three distinct TPR peaks are observed, ascribed to the reduction of $Co_3O_4 \rightarrow CoO$ (220°C), $CoO \rightarrow Co$ (270°C) and isolated CoO species (380°C), respectively.[196] It is worth noting that the CeO_2 reduction occurs at lower temperature for Co_3O_4/CeO_2 relative to other samples, because CoO_x can enhance H_2 spillover from the reduced Co species towards CeO_2 which decreases the CeO_2 reduction temperature.[198] The different interaction between MO_x and CeO_2 of MO_x/CeO_2 samples, as indicated by their distinct TPR profiles, would determine the dispersion of the metals with $CeO_{2-\delta}$ in the $M/CeO_{2-\delta}$ catalysts and thus affect their ability to activate hydrogen.

The two broad reduction peaks located at 530 and 705°C for CeO_2 are attributed to the respective reductions of surface oxygen species and the bulk lattice oxygen within ceria.[102] However, for the three MO_x/CeO_2 samples, their reduction peaks due to the removal of lattice oxygen from CeO_2 support display in very similar temperature region (600~800°C), suggesting the different MO_x species impact slightly on the reducibility of lattice oxygen within CeO_2. In contrast, the reduction of surface oxygen (~530°C) is absent for the MO_x/CeO_2 since the metal species can improve the surface oxygen removal from CeO_2 support due to their strong M-ceria interaction[199] and the H_2 spillover from metal onto the vicinity oxygen species on the ceria surface.

4.3.3 Surface structural analysis

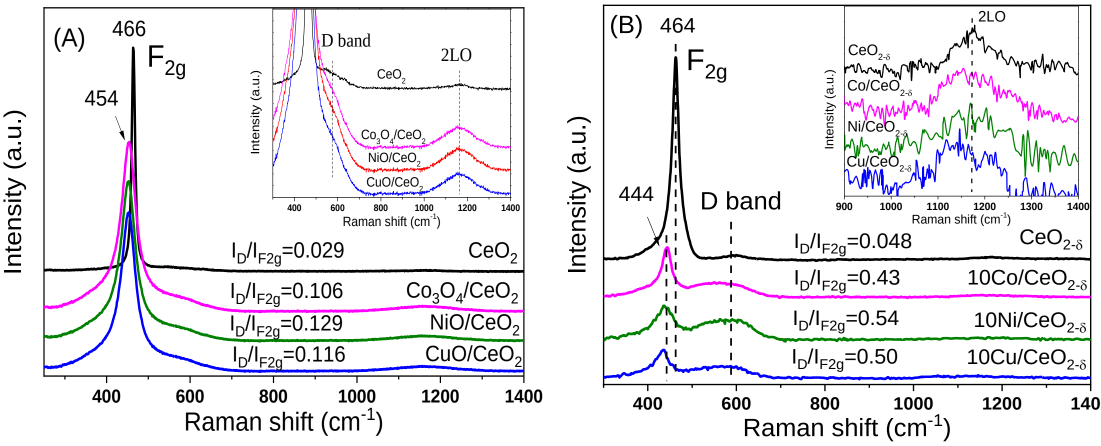

Figure 4.6 Raman spectra of (A) MO_x/CeO_2 precursors and (B) reduced $M/CeO_{2-\delta}$ catalysts

Raman spectroscopy was employed to investigate the surface structure of the MO_x/CeO_2 precursors and the $M/CeO_{2-\delta}$ catalysts. As shown in Figure 4.5 (A), the strong vibration mode (F_{2g}, ~466 cm^{-1}), due to the symmetrical stretching vibration of Ce-O bonds, dominates the Raman spectrum of CeO_2.[200] Upon metal loading, the F_{2g} modes red shift to 454 cm^{-1} with peak broadening due to the strong interaction between MO_x and CeO_2 that gives rise to distortion of the $CeO_{2-\delta}$ lattice and creates electron-rich Ovac for maintaining the system charge neutrality.[200] Besides the F_{2g} band, two broadening bands within the 600~700 cm^{-1} and 1100~1250 cm^{-1} regions are observed on the MO_x/CeO_2 samples, which can be attributed to the Frenkel defect-induced modes (D band) and second-order longitudinal optical mode (2LO band), respectively.[96]

The D and 2LO bands are related to Ovac that originated from reducing Ce^{4+} to Ce^{3+}. Compared to CeO_2, MO_x/CeO_2 samples show broader and stronger vibrations of D bands and 2LO modes, suggesting that loading of MO_x species facilitates creation of Ovac thanks to metal substitution of lattice Ce, which is in good agreement with the discussion of XRD results. The density of Ovac in the ceria supports due to metal incorporation are quantified tentatively through the relative ratios of I_D/I_{F2g}, which are inserted in Figure 4.6 (A). The I_D/I_{F2g} in the MO_x/CeO_2 samples are more than 3 fold that in bare CeO_2, namely, Ovac density descends in the order of NiO/CeO_2 > CuO/CeO_2 > Co_3O_4/CeO_2>>CeO_2. The results clearly reflect that the Ovac concentration created by MO_x loading highly depends on the metal species, likely due to their different ionic radius and valence state of the dopants.[195]

The modes of F_{2g}, D band and 2LO can be clearly identified in the reduced $M/CeO_{2-\delta}$ catalysts and $CeO_{2-\delta}$ sample, as plotted in Figure 4.6 (B), but much weaker than those of the MO_x/CeO_2 precursors, in particular the F_{2g} modes. Moreover, the F_{2g} modes of $M/CeO_{2-\delta}$ catalysts red shift further from 454 to 444 cm^{-1}. The relative changes of Raman signals for the $M/CeO_{2-\delta}$ catalysts to their precursors are the consequence of the decreased structure symmetry of the $M/CeO_{2-\delta}$ catalysts. However, the I_D/I_{F2g} ratios of the $M/CeO_{2-\delta}$ catalysts and $CeO_{2-\delta}$ are much greater than those in the corresponding oxides (as compared in Figure 4.6 (B)), suggesting that reduction process significantly promotes the Ovac density. It is worth noting that the Ovac concentration of the metal loaded catalysts is enhanced approximately nine- to ten-fold that of $CeO_{2-\delta}$, further confirming that metal introduction can dramatically improve the Ovac formation. The results are in good accordance to the TPR characterization. It is also noted that the Ovac density variation for the $M/CeO_{2-\delta}$ catalysts follows the descending order of $10Ni/CeO_{2-\delta}$ > $10Cu/CeO_{2-\delta}$ > $10Co/CeO_{2-\delta}$ >> $CeO_{2-\delta}$, which inherits the Ovac concentration order of their precursor oxides.

4.3.4 Hydrogen activation on the M/$CeO_{2-\delta}$ catalysts

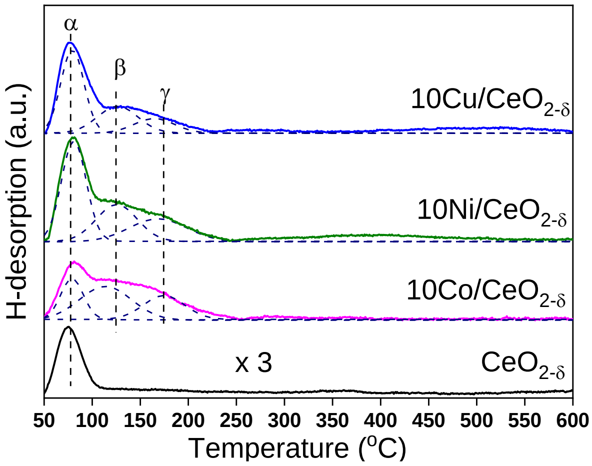

Figure 4.7 H_2-TPD profiles of $CeO_{2-\delta}$ and M/$CeO_{2-\delta}$ catalysts

Figure 4.7 shows the H_2-TPD profiles of the M/$CeO_{2-\delta}$, which are deconvolved into three peaks. The α peaks for the M/$CeO_{2-\delta}$ catalysts appear at very similar temperature to that of the single H_2-TPD peak of unsupported $CeO_{2-\delta}$. Such α peaks are therefore assigned to desorption of H_2, which takes up the surface Ovac sites of $CeO_{2-\delta}$.[183] The areas of α peaks (Table 4.2) are related to the Ovac density of the M/$CeO_{2-\delta}$ catalysts which depends on the supported metal species. The Ovac density on the 10Ni/$CeO_{2-\delta}$ and 10Cu/$CeO_{2-\delta}$ is almost the same, which is much larger than that of the 10Co/$CeO_{2-\delta}$ and $CeO_{2-\delta}$ support. The variations of Ovac density and its dependence on metal species well agree with those observed by Raman and TPR characterisation.

Table 4.2 H_2 uptake, metal dispersion and hydrogenation rate constants on M/$CeO_{2-\delta}$ catalysts

Sample	Hα (μmol/g)	H_β (μmol/g)	H_γ (μmol/g)	$\Sigma(H_\beta+H_\gamma)$ (μmol/g)	ΣH (μmol/g)	D_M(%)	$k_{MA\rightarrow SA}$ (min^{-1})
10Co/$CeO_{2-\delta}$	17.2	24.1	11.8	35.9	53.1	3.9	0.0216
10Ni/$CeO_{2-\delta}$	28.4	22.6	14.6	37.2	65.6	4.4	0.0588
10Cu/$CeO_{2-\delta}$	28.7	14.2	8.2	22.4	52.1	2.9	-
$CeO_{2-\delta}$	7.8	/	/	/	7.8	/	0.0037

Note: H_α, H_β and H_γ represent the estimated amount of adsorbed hydrogen, which were calculated based on the areas of α, β and γ peaks, respectively. D_M represents the metal dispersion of the examined M/$CeO_{2-\delta}$ catalysts, which was calculated using Equation 2.5 in *Chapter 2*. $k_{MA\rightarrow SA}$ is the rate constant of MA hydrogenation to SA over the M/$CeO_{2-\delta}$ catalysts.

The β and γ peaks located within 100-250°C region are due to the H_2 desorption from the different corresponding metal species. The β peaks are due to the dissociative H_2 adsorbed on the highly dispersed metal species that resides close to surface defects with large density. The previous research showed that surface defect can reduce the energy barrier for hydrogen dissociation and enhance hydrogen diffusion on the metal surface.[189] The γ peaks are associated to the chemisorbed hydrogen on the isolated metal clusters of large particle size.[190] The areas of β and γ peaks of the $10Co/CeO_{2-\delta}$ and $10Ni/CeO_{2-\delta}$ catalysts are comparable, but much greater than that of $10Cu/CeO_{2-\delta}$, as presented in Table 4.2. The low uptakes of H_β and H_γ on $10Cu/CeO_{2-\delta}$ suggest the capability of Cu to activate hydrogen is relatively weak because its valence electron shells mainly comprise of fully filled 3d orbitals ($3d^{10}$).[201]

According to the assignments of the H_2-TPD peaks, the metal dispersion (D_M) can be quantified using only the metal-related hydrogen activation (H_β and H_γ) rather than the overall H_2 uptakes on the catalysts. As listed in Table 4.2, the metal dispersion of the $M/CeO_{2-\delta}$ catalysts is found to be decreasing in the order of $10Ni/CeO_{2-\delta}$ > $10Co/CeO_{2-\delta}$ > $10Cu/CeO_{2-\delta}$.

4.3.5 Catalytic hydrogenation of maleic anhydride

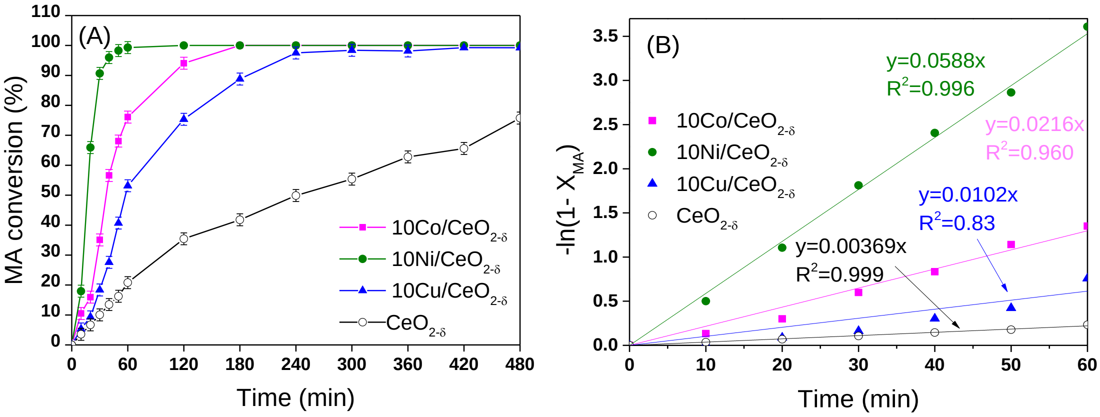

Figure 4.8 (A) Conversion of MA over the $M/CeO_{2-\delta}$ catalysts at 210°C and 5 MPa for 8 h and (B) kinetic curves of the $M/CeO_{2-\delta}$ catalysts for MA conversion

Figure 4.8 (A) presents MA conversion (X_{MA}) on the $M/CeO_{2-\delta}$ catalysts in a batch reactor at 210°C and hydrogen pressure of 5.0 MPa. Among the examined catalysts, $10Ni/CeO_{2-\delta}$ showed the highest activity of MA conversion, reaching ~ 100% MA conversion in one hour. However, the MA conversion on $10Cu/CeO_{2-\delta}$ and $10Co/CeO_{2-\delta}$ in one hour only achieved 50.3% and 70%, respectively. The MA transformation completed in 3 hours on $10Co/CeO_{2-\delta}$ and 4 hours on $10Cu/CeO_{2-\delta}$.

Moreover, the estimated $TOF_{MA \rightarrow SA}$ values of MA transformed to SA over $M/CeO_{2-\delta}$ catalysts further distinguished the activity of the catalysts. The $TOF_{MA \rightarrow SA}$ of $10Ni/CeO_{2-\delta}$ catalyst is 61.7 min^{-1}, nearly twice that of $10Co/CeO_{2-\delta}$ catalyst ($TOF_{MA \rightarrow SA}$ =31.2 min^{-1}) and five-fold that of $10Cu/CeO_{2-\delta}$ ($TOF_{MA \rightarrow SA}$=13.2 min^{-1}). The considerable difference of MA conversion on the $M/CeO_{2-\delta}$ catalysts cannot only be attributed to the particle size or metal dispersion effects. We speculate there exist other factors, such as intrinsic properties (e.g. electronic configuration) of individual metals, M-support interaction and the amount of Ovac, to influence the catalytic performance synergistically.

Figure 4.8 (B) presents the curves of $-ln(1-X_{MA})$ versus time within the initial one hour which are fitted according to the first order kinetic law in terms of MA conversion on the $M/CeO_{2-\delta}$ catalysts.[82] The linear kinetic plots over $10Ni/CeO_{2-\delta}$ and $10Co/CeO_{2-\delta}$ catalysts suggest the C=C hydrogenation follows the quasi first-order reaction in terms of MA conversion, while the non-linear kinetic plot on $10Cu/CeO_{2-\delta}$ suggests its initial hydrogenation follows a complicated kinetic mechanism. The MA hydrogenation rate coefficients ($k_{MA \rightarrow SA}$) on the $10Ni/CeO_{2-\delta}$ and $10Co/CeO_{2-\delta}$ catalysts are determined according to the gradients of their linear plots. As listed in Table 4.2, the $k_{MA \rightarrow SA}$ for $10Ni/CeO_{2-\delta}$ is much greater than that for $10Co/CeO_{2-\delta}$, indicating that $10Ni/CeO_{2-\delta}$ is more active than $10Co/CeO_{2-\delta}$ in the hydrogenation of MA to SA.

In principle, the electronic configurations of the active metals are profound in the activation of MA for hydrogenation reaction. Previous DFT simulation demonstrated the adsorption and activation of MA on the metal surface is primarily controlled by the back-donation of electron from the metal onto the anti-bonding π* orbital of maleic anhydride.[89] Therefore, the metallic Cu possesses filled $3d^{10}$ electronic configuration without unpaired electron, thus having weak capability of electron-donation to the MA molecule. In contrast, the unpaired electrons of Co ($3d^7$) and Ni (Ni $3d^8$) favour the coordination and activation of MA, so as to exhibit much higher activity.

Besides the intrinsic properties, the Ovac density is regarded as another factor to enhance C=C hydrogenation because Ovac can enrich the electron density of active metals that promotes electron-donating ability and facilitates H_2 dissociation.[125] In this study, the $10Ni/CeO_{2-\delta}$ catalyst possesses more Ovac, thus donating more electrons to metallic Ni in comparison to $10Co/CeO_{2-\delta}$. Further, the smaller particle size of Ni also strengthens the short-range electron transfer from Ovac onto the adjacent metal clusters. Hence, both the abundant Ovac and stronger

Ovac→M electronic donation are responsible for the higher activity of $10Ni/CeO_{2-\delta}$ than $10Co/CeO_{2-\delta}$ in MA hydrogenation. However, $10Ni/CeO_{2-\delta}$ and $10Cu/CeO_{2-\delta}$ catalyst have similar Ovac density but display different activity, suggesting that intrinsic electron structure of active metal dominates MA hydrogenation.

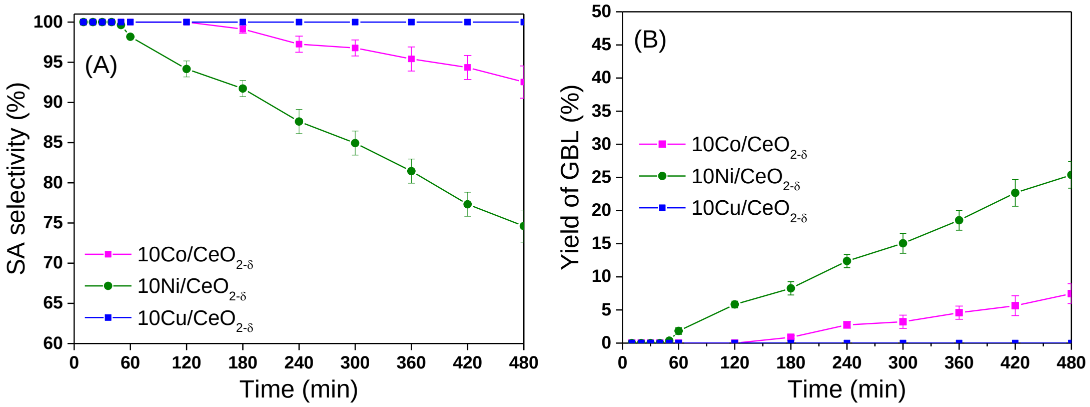

Figure 4.9 (A) Selectivity of SA and (B) yield of GBL over $M/CeO_{2-\delta}$ catalysts at 210°C and 5 Mpa for 8 h

Figure 4.9 shows SA selectivity of the $M/CeO_{2-\delta}$ catalysts in the prolonged MA hydrogenation for 8 hours. One can see that the $10Cu/CeO_{2-\delta}$ and reduced $CeO_{2-\delta}$ sample exhibit 100% selectivity to SA in the 8 h continuous MA hydrogenation without GBL in the products, indicating they are inert for SA hydrogenolysis to GBL. The estimated $TOF_{SA\rightarrow GBL}$ values over $10Ni/CeO_{2-\delta}$, $10Co/CeO_{2-\delta}$ and $10Cu/CeO_{2-\delta}$ are 3.08 min^{-1}, 0.87 min^{-1} and 0, respectively, where $10Ni/CeO_{2-\delta}$ shows the highest hydrogenation rate for the SA→GBL transformation. It is worth noting that the generation of GBL occurs on the $10Ni/CeO_{2-\delta}$ unless it fully converts MA to SA, as evidenced by the fact that 100% SA selectivity remains on the $10Ni/CeO_{2-\delta}$ catalyst in the initial 40 min time-on-stream of MA hydrogenation before declining due to the following GBL generation. The generation of GBL on $10Co/CeO_{2-\delta}$ also commences when the conversion of MA to SA is complete. The yield of GBL (Figure 4.9) reaches ~25% on the $Ni/CeO_{2-\delta}$ and ~5% on $10Co/CeO_{2-\delta}$ in 6 hours with much slower rates than those of MA→ SA transformation. The results suggest that MA hydrogenation on $M/CeO_{2-\delta}$ is a multiple-step process: MA conversion to SA is a rapid process that occurs then GBL starts to generate from hydrogenolysis of SA without the existence of MA exists in the system.

There were a few accessible investigations of MA adsorption and hydrogenation on noble metals,[88, 89] though the mechanism of the MA hydrogenation on the $M/CeO_{2-\delta}$ systems remains inexplicit owing to the complexity. However, the theoretical and experimental understanding of the H_2 adsorption, activation and cycling on CeO_2 and supported metal catalysts in various redox reactions can provide useful clues.[125, 201] Based on our experimental characterization data and the reported fundamental data regarding thermodynamics and kinetics of MA hydrogenation reaction, we attempted to rationale the stepwise MA hydrogenation with distinct reaction rate and selectivity on the $M/CeO_{2-\delta}$ catalyst systems.

From the thermodynamic point of view, MA hydrogenation to SA and GBL is possible to involve the following reactions:

$$MA + H_2 = SA \qquad \Delta_f H^{\theta}_{MA \rightarrow SA} = -133.8 \text{ kJ/mol} \qquad (4.1)$$

$$SA + 2H_2 = GBL + H_2O \qquad \Delta_f H^{\theta}_{SA \rightarrow GBL} = -108.7 \text{ kJ/mol} \qquad (4.2)$$

$$MA + 3H_2 = GBL + H_2O \qquad \Delta_f H^{\theta}_{MA \rightarrow GBL} = -241.7 \text{ kJ/mol} \qquad (4.3)$$

Here, $\Delta_f H^{\theta}_{MA \rightarrow SA}$ and $\Delta_f H^{\theta}_{SA \rightarrow GBL}$ are adopted from literature[90], while the $\Delta_f H^{\theta}_{MA \rightarrow GBL}$ of the global reaction (3) is calculated applying Hess's law to reaction (4.1) and (4.2). Applying Gibbs-Helmholtz equation, one can easily realise that their standard Gibbs's formation free energy ($\Delta_f G^{\theta} = \Delta_f H^{\theta} - T\Delta_f S^{\theta}$) would be less negative than the corresponding $\Delta_f H^{\theta}$, namely, the spontaneous tendency of the individual reactions can be roughly judged from their $\Delta_f H^{\theta}$.

The present research adopted the reaction conditions of constant pressure and elevated temperature higher than standard conditions, thus reaction 4.1 is thermodynamically more favourable than reaction 4.2 because of the greater enthalpy (more negative) of reaction 4.1. In the present research, there was no GBL produced in the initial stage of MA hydrogenation, which verifies the above inference and suggests reaction 4.3 less favourable in spite of the highest $\Delta_f H^{\theta}$ of reaction 4.3.

From the molecule reaction kinetics perspective, it is the number of active molecules involved in the reaction determining the rate and selectivity. The proceeding of Reaction 4.1 apparently requires the least number of reactants so that MA→SA transformation is more favourable and faster than the SA→GBL and MA→GBL transformations that request more molecules. Indeed, previous research the C=C group is kinetically more active than the C=O group.[202] This interpretation from kinetics aspect is reliable, as evidenced by the fact that GBL generation commenced unless MA→SA transformation completed on the $M/CeO_{2-\delta}$ catalysts.

As for the distinct selectivity of the chosen $M/CeO_{2-\delta}$ systems, we supposed that the surface electron configurations of the metal catalysts play pivotal roles, in particular the electrons on the outermost *d* shells of the transition metals. The H_2

activation on the supported transition metal usually depends on the configuration of the outermost electronic shell, which generally determined the overall hydrogenation reaction.[88, 127] In this work, the H_2-TPD data (Figure 4.6 and Table 4.2) show that the smallest amount of H_β and H_γ species on the 10Cu/$CeO_{2-\delta}$ displays its weakest ability to activate hydrogen due to its $3d^{10}$ outermost electronic configuration. The amount of metal-activated H species on 10Ni/$CeO_{2-\delta}$ is identical to that of 10Co/$CeO_{2-\delta}$, so that the higher activity and selectivity of 10Ni/$CeO_{2-\delta}$ is also relevant to the greater amount of active H_a species due to Ovac on the $CeO_{2-\delta}$ support (Table 4.2).

The surface adsorption of the C=O group is another crucial factor to determine SA→GBL transformation.[12] Previous research showed that the Cu^0 surface is not active in the C=O group activation[6], because the fully filled $3d^{10}$ shell of Cu leads to weak binding of C=O on Cu^0 surface. Therefore, it is reasonable that the 10Cu/$CeO_{2-\delta}$ is not active for SA→GBL transformation from the adsorption energy point of view. In contrast, metallic Ni and Co with partially filled 3*d*-orbitals facilitate the coordination between metal and C=O group, which benefits C=O hydrogenolysis.[6] Therefore, the d band electronic configurations of Ni and Co also contributed to the higher activity of 10Ni/$CeO_{2-\delta}$ and 10Co/$CeO_{2-\delta}$ catalysts.

The beneficial contributions of Ovac in C=O hydrogenolysis have been widely accepted.[48, 68] Ovac in the non-stoichiometric oxides, such as ZnO[92]and TiO_x[80] can polarise and activate the C=O group and thus reduce the energy barrier of C=O conversion to display reasonable hydrogenolysis selectivity. In this work, the amount of Ovac in the 10Ni/$CeO_{2-\delta}$ catalyst is around 1.5 times that in the 10Co/$CeO_{2-\delta}$ catalyst, suggesting $CeO_{2-\delta}$ support of 10Ni/$CeO_{2-\delta}$ can offer more active sites for C=O activation. However, the calculated $TOF_{SA\rightarrow GBL}$ of 10Ni/$CeO_{2-\delta}$ is nearly triple that of 10Co/$CeO_{2-\delta}$, which is larger than relative Ovac ratio between the two catalysts. Therefore, the electronic configuration of the transition metal outermost d shells is the dominant factor to determine the catalytic hydrogenolysis of SA to GBL, meanwhile, the Ovac on $CeO_{2-\delta}$ can facilitate C=O conversion on 10Ni/$CeO_{2-\delta}$ due to the electron donating and selective adsorption effects of Ovac.

4.4 Conclusion

In this chapter, three M/$CeO_{2-\delta}$ catalysts, 10Ni/$CeO_{2-\delta}$, 10Co/$CeO_{2-\delta}$ and 10Cu/$CeO_{2-\delta}$, were prepared via a CA-assisted wet impregnation method. The catalysts were well characterised applying XRD, TEM, Raman, TPR and TPD techniques, in order to unravel the dependence of MA hydrogenation performance on the redox properties and the M-$CeO_{2-\delta}$ interactions.

It was found that metal dispersion of M/$CeO_{2-\delta}$ catalysts declined in the order: 10Ni/$CeO_{2-\delta}$ > 10Co/$CeO_{2-\delta}$ > 10Cu/$CeO_{2-\delta}$, in the opposition to the order of metal crystallite sizes. The small metal crystallite sizes of the M/$CeO_{2-\delta}$ catalysts were proportional to those of the oxide precursors, revealing the strong MO_x-CeO_2 interaction played crucial roles to govern metal dispersion and particle sizes of the M/$CeO_{2-\delta}$ catalysts. In addition, the concentration of Ovac in the M/$CeO_{2-\delta}$ catalysts was enhanced more than one magnitude relative to that of $CeO_{2-\delta}$, in the increasing sequence of 10Cu/$CeO_{2-\delta}$ > 10Ni/$CeO_{2-\delta}$ > 10Co/$CeO_{2-\delta}$ > >$CeO_{2-\delta}$. The increased Ovac concentration in M/$CeO_{2-\delta}$ catalysts is mainly due to H_2 spillover from the metals to ceria that favours creation of Ovac in the ceria matrices.

The $CeO_{2-\delta}$ support showed notable activity in MA hydrogenation to SA but inert for hydrogenolysis of SA towards GBL, evidencing it is an active support for SA generation. The metal loading greatly enhanced the activity of MA hydrogenation and SA selectivity on the M/$CeO_{2-\delta}$ catalysts. The apparent activities and turnover frequencies of MA hydrogenation to SA ($TOF_{MA\rightarrow SA}$) increased following the trend of 10Ni/$CeO_{2-\delta}$> 10Co/$CeO_{2-\delta}$> 10Cu/$CeO_{2-\delta}$ >> $CeO_{2-\delta}$. Among the examined catalysts, 10Ni/$CeO_{2-\delta}$ displayed the highest activity and selectivity to SA in the initial 40 min. The $TOF_{MA\rightarrow SA}$ (61.7 min^{-1}) for 10Ni/$CeO_{2-\delta}$ was twice and five times that for 10Co/$CeO_{2-\delta}$ ($TOF_{MA\rightarrow SA}$=31.2 min^{-1}) and 10Cu/$CeO_{2-\delta}$ ($TOF_{MA\rightarrow SA}$=13.2 min^{-1}), respectively. 10Ni/$CeO_{2-\delta}$ also showed higher activity and selectivity than 10Co/$CeO_{2-\delta}$ in SA→ GBL transformation, while no GBL produced on 10Cu/$CeO_{2-\delta}$ and $CeO_{2-\delta}$ catalysts.

MA hydrogenation to SA on the 10Ni/$CeO_{2-\delta}$ and 10Co/$CeO_{2-\delta}$ catalysts followed the first order kinetic law, but 10Cu/$CeO_{2-\delta}$ took a more complex kinetics mechanism. The defective $CeO_{2-\delta}$ support was active for catalytic conversion of MA to SA due to Ovac in $CeO_{2-\delta}$. Ovac of the $CeO_{2-\delta}$ support favoured the MA hydrogenation on the 10Ni/$CeO_{2-\delta}$ catalyst, though Ovac was not the dominant factor to the enhanced SA hydrogenolysis to GBL, which was evidenced by the fact that both $CeO_{2-\delta}$ and the Ovac-richest 10Cu/$CeO_{2-\delta}$ catalyst were inert in SA hydrogenolysis. The electronic configurations of the transition metals were supposed to be crucial for the activation and adsorption of H_2 and hydrogenation of MA and SA. In all, the distinct catalytic hydrogenation behaviour on the catalysts arose from the synergistic contributions of the metal dispersion, Ovac concentration and the electronic configurations of metal outermost d electron shells, which determined the activation of hydrogen and surface adsorption of MA and SA.

Chapter 5 **Loading effect of Ni on MA hydrogenation over xNi/$CeO_{2-\delta}$ catalysts**

5.1 Introduction

It is well known that the MA molecule is a multifunctional compound and its hydrogenation process involves C=C hydrogenation and C=O hydrogenolysis. Distinguishing the roles of catalytic active sites in catalytic hydrogenation of MA is critical for developing robust and highly selective hydrogenation catalysts. For the Ni-based catalysts, it is highly desirable to specify and understand the intrinsic active sites, including Ni nanoparticles, Ni-support interaction and support defects and their contribution to MA hydrogenation.

Li and co-workers found the selectivity of MA hydrogenation over xNi/HY-Al_2O_3 catalysts was dependent on the particle size of Ni species, where small Ni particles facilitated SA production while large ones enhanced GBL generation.[43] Meyer and co-workers suggested the size-dependant selectivity related to the varying Ni-support interactions. They found that small metallic Ni nanoclusters, which strongly interacted with SiO_2-Al_2O_3 support favoured SA selectivity, whereas GBL selectivity was enhanced on the large Ni nanoparticles weakly bound to the support.[79] However, Bertone and co-workers reported that the Ni/SiO_2-Al_2O_3 catalyst with smaller Ni^0 particles was more active to GBL generation than the Ni/SiO_2 catalysts of bigger Ni particles. They assigned the difference to the presence of Lewis acid sites on the SiO_2-Al_2O_3 support that enhanced C=O adsorption.[76] Their results manifest that besides the nature of Ni, the support properties can tune the selectivity in MA hydrogenation.

For the modified catalysts without significant change to surface acidity, the surface electronic effects were thought to be responsible for the modulated catalysts performance. Superior activity and selectivity were achieved on the ZrO_2 modified Ni/SiO_2 catalyst to that of Ni/SiO_2 catalyst, which was attributed to the presence of Zr^{4+}-defects that selectively activated the C=O group.[78] In generally, metal catalysts supported on the partially reduced oxides with abundant surface defects, like Ni/TiO_2 enabled to promote GBL production in the prolonged MA hydrogenation duration.[80] The IR spectral data evidenced that the nonstoichiometric Ni-TiO_X interface stabilised the C=O group, thus promoting C=O hydrogenolysis in crotonaldehyde hydrogenation.[77]

The previous chapters showed that $CeO_{2-\delta}$ support with rich Ovac can promote the catalytic activity of Ni species in MA hydrogenation in comparison with Al_2O_3 support. For the ceria-supported catalysts, the $Ni/CeO_{2-\delta}$ catalyst exhibited higher activity than the $Cu/CeO_{2-\delta}$ and $Co/CeO_{2-\delta}$ catalysts in the MA hydrogenation to SA and enhanced SA→GBL transformation by hydrogenolysis. These results indicate that Ni-CeO_2 catalytic system is suitable for MA hydrogenation. However, the specific contribution of the intrinsic active sites (Ni nanoparticles, Ni-support interface and support defects) in the Ni/CeO_2 catalyst are still obscure.

In this chapter, a fine control of Ni loading on $xNi/CeO_{2-\delta}$ catalysts (x denotes Ni loading, varying from 0 to 30 wt%) were synthesized via our modified wet impregnation method and evaluated by the liquid phase hydrogenation of MA at 210°C and 5 MPa of H_2 pressure. The catalysts were well characterised to gain insights to the synergistic effects between Ni and CeO_2 on MA hydrogenation.

5.2 Experimental

5.2.1 Catalyst preparation

The CeO_2 support was prepared by the same sol-gel method as that detailed in Chapter 4. The $xNi/CeO_{2-\delta}$ catalysts with varying amount of Ni loading were prepared by the CA-assisted impregnation method, which is illustrated in Figure 4.1. The recipe for the $xNi/CeO_{2-\delta}$ catalysts are summarised in Table 5.1.

Table 5.1 Recipe for preparation of $xNi/CeO_{2-\delta}$ catalysts

Sample	$m(CeO_2)$/g	$m(Ni(NO_3)_2\ 6H_2O)$/g	m(citric acid)/g	Ethanol-DI water (1:1)/mL
$2Ni/CeO_{2-\delta}$	2.00	0.202	0.146	10
$5Ni/CeO_{2-\delta}$	2.00	0.521	0.377	10
$10Ni/CeO_{2-\delta}$	2.00	1.101	0.796	10
$15Ni/CeO_{2-\delta}$	2.00	1.748	1.263	10
$17.5Ni/CeO_{2-\delta}$	2.00	2.102	1.518	10
$20Ni/CeO_{2-\delta}$	2.00	2.477	1.789	10
$30Ni/CeO_{2-\delta}$	2.00	4.246	3.068	10

To briefly the preparation procedure, the $5Ni/CeO_{2-\delta}$ catalyst was chosen as an example. 0.521 g $Ni(NO_3)_2\ 6H_2O$ was dissolved in a 10 ml ethanol/DI water (1:1 volumetric ratio) solution, and then 2.00 g CeO_2 support and 0.377 g CA (mole ratio of CA/Ni=1) were added into the mixed solution to form a slurry. The slurry was stirred using a magnetic stirrer and heated at 80°C to evaporate the solvent, then subject to drying at 120°C for 8 h in a convection oven. It should be noted that the pH of the precursor solutions to prepare the xNi/$CeO_{2-\delta}$ varied slightly because different mount of CA added in line with the Ni loading to keep a constant molar ratio of CA to Ni (CA/Ni=1). The obtained dry gel was calcined at 500°C (heating ramp of 3°C/min) for 3 h in a muffle oven to receive the xNiO/CeO_2 samples.

The xNiO/CeO_2 samples were reduced at 350°C (heating ramp of 2°C/min) with a flow of 10 vol% H_2 in argon for 3 h before MA hydrogenation. Other catalysts were prepared using the similar procedure. All the catalysts were denoted 2Ni/$CeO_{2-\delta}$, 5Ni/$CeO_{2-\delta}$, 10Ni/$CeO_{2-\delta}$, 15Ni/$CeO_{2-\delta}$, 17.5Ni/$CeO_{2-\delta}$, 20Ni/$CeO_{2-\delta}$ and 30Ni/$CeO_{2-\delta}$ in accordance with Ni loading. The reduced $CeO_{2-\delta}$ support was considered as a catalyst with zero Ni loading.

5.2.2 Catalyst characterisation and evaluation

The as-prepared xNi/$CeO_{2-\delta}$ catalysts and their oxide precursors were characterised by XRD, H_2-TPR, TEM, XPS, Raman and H_2-TPD techniques. The detailed procedures for the characterisation were described in Chapter 2. The catalytic performance of xNi/$CeO_{2-\delta}$ catalysts were evaluated at 210°C and 5 MPa hydrogen pressure in a batch reactor within 0.1 g catalyst, 4.9 g MA and 40 mL THF as a solvent, which was also detailed in Chapter 2.

5.3 Results and discussion

5.3.1 Structure evolution of the xNi/$CeO_{2-\delta}$ catalysts

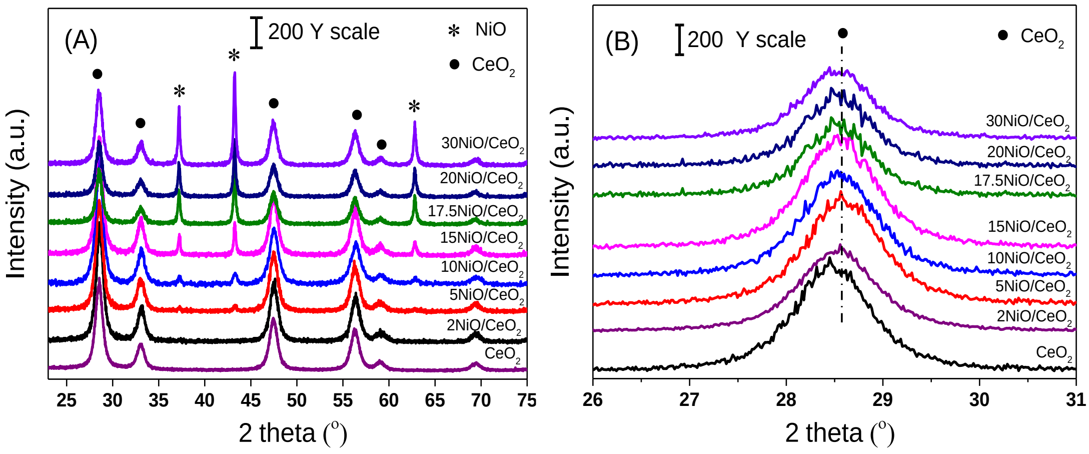

Figure 5.1 (A) XRD patterns of calcined xNiO/CeO_2 samples and (B) the enlarged pattern at the range of 26-31°

The XRD patterns of the xNiO/CeO_2 samples are presented in Figure 5.1. One can see the ceria phase in the xNiO/CeO_2 remains the face-centred cubic phase same as the fluorite structured CeO_2 (JCPDS file 34-0394, *Fm3m* space group). However, the characteristic (111) Bragg diffraction peak shifts slightly to a higher angle after Ni loading (Figure 5.1(A)), suggesting a lattice contraction that is caused by the incorporation of the smaller Ni cation (r_{Ni}^{2+}=0.72 nm) into CeO_2 (r_{Ce}^{4+}=0.81 nm) to form a NiO-CeO_2 solid solution.[178] The calculated crystallite sizes of ceria in the xNiO/CeO_2 samples are larger than that of the pure CeO_2 due to the NiO-induced lattice distortion of CeO_2 or thermal sintering.[151]

Besides the peaks related to the cubic CeO_2 phase, NiO diffraction peaks in the xNi/CeO_2 samples are observed at 37.0, 43.0 and 62.9°. For the 2NiO/CeO_2 sample, the absence of NiO peaks suggests that NiO species either highly disperse on the CeO_2 surface or incorporate into the CeO_2 lattice.[164] As the Ni loading rises from 5 to 30 wt%, the NiO diffraction peaks are gradually enhanced. The calculated NiO sizes increase from 10.1 to 35.1 nm (Table 5.2), which could lead to different NiO-CeO_2 interaction as well as affect their reducibility and surface structure of the xNi/$CeO_{2-\delta}$ catalysts.

Table 5.2 The surface areas (S_{BET}), Ni loading and the average crystallite sizes of CeO_2, NiO and metallic Ni in the reduced catalysts

Sample	D(CeO_2)^a (nm)	Surface area^b (m^2/g)	Ni loading^c (wt%)	D(NiO)^a (nm)	D(Ni)^a (nm)	Dispersion (Ni)^d [%]
CeO_2	11.6	35.6	-		-	-
2Ni/$CeO_{2-\delta}$	13.4	35.2	1.9	-	-	16.9
5Ni/$CeO_{2-\delta}$	13.4	35.8	4.8	10.1	-	9.3
10Ni/$CeO_{2-\delta}$	13.8	37.5	10.2	21.6	10.7	5.2
15Ni/$CeO_{2-\delta}$	13.3	34.2	15.3	24.7	15.2	4.7
17.5Ni/$CeO_{2-\delta}$	13.8	32.1	17.2	28.2	17.5	4.1
20Ni/$CeO_{2-\delta}$	13.7	28.4	20.5	30.5	18.9	3.2
30Ni/$CeO_{2-\delta}$	13.1	22.2	29.1	35.1	36.6	1.4

Note: ^{a} The crystallite size of CeO_2, NiO and Ni particles were calculated using the Scherrer equation. ^{b} The surface area was measured by N_2 adsorption-desorption. ^{c} The Ni loading is determined by the ICP-OES technique. The percentage of Ni dispersion was calculated using the equation: Ni dispersion was calculated using the Equation 2.5 in Chapter 2 with the amount of H_2 uptake at metal surface.

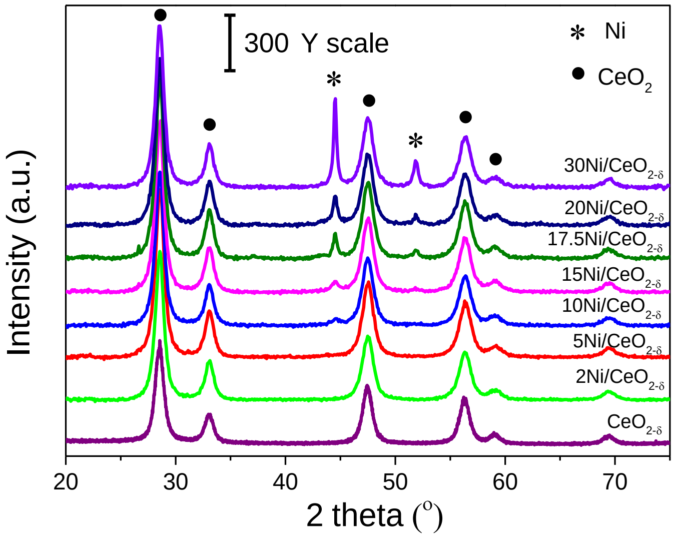

Figure 5.2 XRD patterns of reduced xNi/CeO$_{2-\delta}$ catalysts

Figure 5.2 shows the XRD patterns of the H$_2$-reduced xNi/CeO$_{2-\delta}$ catalysts, where the metallic Ni^0 (JCPDS 01-1258) and CeO$_2$ phases can be identified. There is no NiO phases in the XRD patterns, suggesting all the reduction of the crystallite NiO species was complete at 350°C. The diffraction peaks of Ni^0 are absent for 2Ni/CeO$_{2-\delta}$ and 5Ni/CeO$_{2-\delta}$ catalysts because their crystalline domains are too small (< 4 nm) to be resolved by XRD.[79] The intensity of Ni^0 diffraction increases as increasing Ni loading amount and the calculated Ni^0 crystallite sizes become larger (shown in Table 5.2).

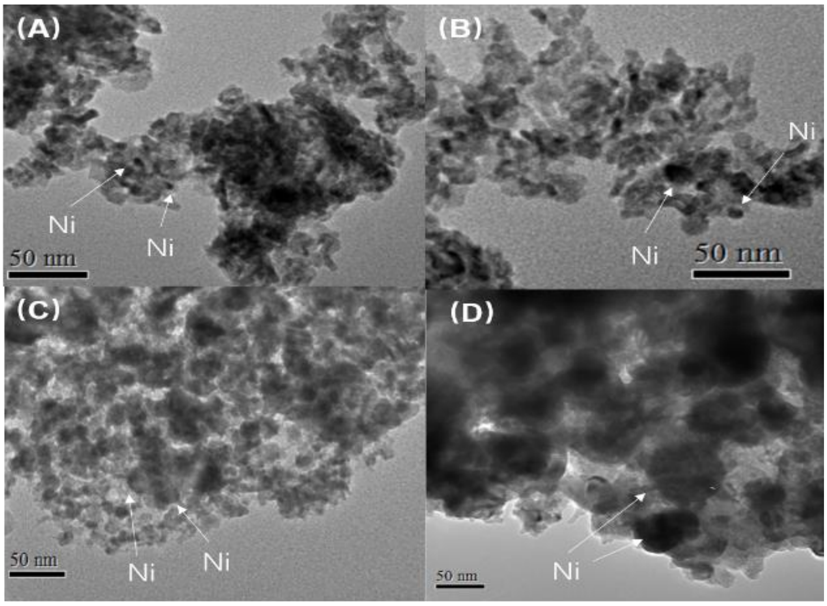

Figure 5.3 TEM images of typical catalysts (A) 5Ni/CeO$_{2-\delta}$; (B) 10Ni/CeO$_{2-\delta}$; (C) 17.5Ni/CeO$_{2-\delta}$ and (D) 30Ni/CeO$_{2-\delta}$ catalysts

TEM observations further confirm that the particle size of Ni nanoparticles increases with rising Ni content. As shown in Figure 5.3 (A), small black dots in the

$5Ni/CeO_{2-\delta}$ catalyst, with the diameter about ~3.5 nm, are due to Ni nanoparticles, which are highly dispersed on the surface of ceria. The TEM images shown in Figure 5.3 (A-D) reveal, as the Ni loading on $CeO_{2-\delta}$ up to 10 wt%, 17.5 wt% and 30 wt%, the average sizes of the Ni^0 particles grow up to 10.8 nm, 28.4 nm and 44.1 nm as measured, respectively. The dependence of Ni particle size on the Ni loading amount as observed by TEM is consistent with the XRD results.

5.3.2 The reducibility of $xNiO/CeO_2$ sample

Figure 5.4 (A) presents the H_2-TPR profiles of the $xNiO/CeO_2$ samples. The weak peaks (denoted as peak α) at ca. 150°C observed for all the oxide precursors can be attributed to the removal of oxygen species on the CeO_2 support surface, in particular those adsorbed on the intrinsic surface Ovac sites.[96, 182] In principle, a small amount of NiO can penetrate into the CeO_2 matrices that leads to the lattice distortion and creates Ovac for readily absorbing oxygen species. Therefore, the intensity of peak α can reflect the population of Ovac on the oxides.

As shown in Figure 5.4(B), the $2NiO/CeO_2$ and $5NiO/CeO_2$ samples show stronger α peaks, while α peaks of $15{\sim}30NiO/CeO_2$ samples appear much weaker. The Ovac is due to the highly dispersed NiO species that can strongly interact with the CeO_2 support. The strong interaction would lower the symmetry of CeO_2 unit cell and thus promote Ovac formation. However, increase of Ni loading leads to larger NiO clusters residing on the CeO_2 and the reduction of the Ovac density of CeO_2 supports, so that smaller α peaks are shown in their TPR profiles.

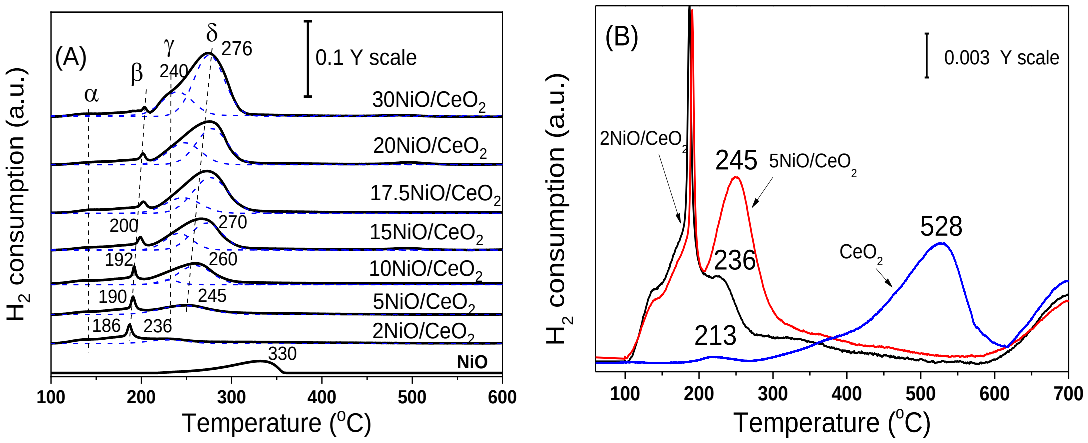

Figure 5.4 (A H_2-TPR profiles of $xNiO/CeO_2$ precursors and (B) closer observation to the TPR profiles of the $2NiO/CeO_2$, $5NiO/CeO_2$ and CeO_2

The sharp peaks (denoted as peak β) observed at ca 200°C are due to rapid hydrogen consumption. Similar result was observed in the TPR of the $Ce_{1-x}Ni_xO_{2-y}$ solid solution oxides,[164] where the abrupt hydrogen consumption was assigned to

H_2 dissociating and forming the OH group at the surface of CeO_2. The sharp H_2-TPR peaks reflected the rapid H_2 reduction kinetics that promoted by the Ovac and/or the interface sites between the local Ni and Ce moieties on the Ni/CeO_2 catalysts. In the present research, the peak β gradually shifts to a high temperature and becomes weaker as increasing Ni loading, suggesting that excess Ni species hinder hydrogen activation and dissociation, which is due to Ovac being masked by large NiO particles.

The reduction of the isolated NiO supported on CeO_2 occurs in the 200-300°C temperature region. Their temperature of maximum reduction gradually increases from 235 to 270°C with increasing NiO loading up to 15 wt%, then remains unchanged (~275°C). The asymmetric NiO reduction peaks can be fitted into two peaks at ca. 240°C (peak γ) and 270°C (peak δ), respectively. The γ peaks are ascribed to the reduction of NiO species closely affinity at NiO/CeO_2 interface, where strong NiO-CeO_2 interaction facilitates the reduction of NiO.[199] The δ peaks are due to the reduction of aggregated NiO particles. One can see the reduction of the aggregated NiO particles on the surface of CeO_2 support occurs at a lower temperature compared to that of bare NiO (330°C).

The lower reduction temperature of γ peaks reflects the enhanced reducibility, due to the preferentially reduction of Ni species at Ni-CeO_2 interface and Ovac. The preferential reduction at interface and near Ovac can facilitate hydrogen dissociation to atomic H and enhance the hydrogen spilling over to the large isolated NiO particles (through adjacent O atoms). The H spillover eventually catalyses the reduction of larger NiO particles isolated on CeO_2 (δ peaks), which is responsible for the lower reduction temperature of NiO on CeO_2 than that of unsupported bulk NiO. However, the δ peaks shift gradually to the high temperature as increasing Ni loading, which is due to the lower Ovac amount and larger NiO size that would block the H-spilling path and hinder NiO reduction.

5.3.3 The surface properties of xNi/CeO$_{2-\delta}$ catalysts

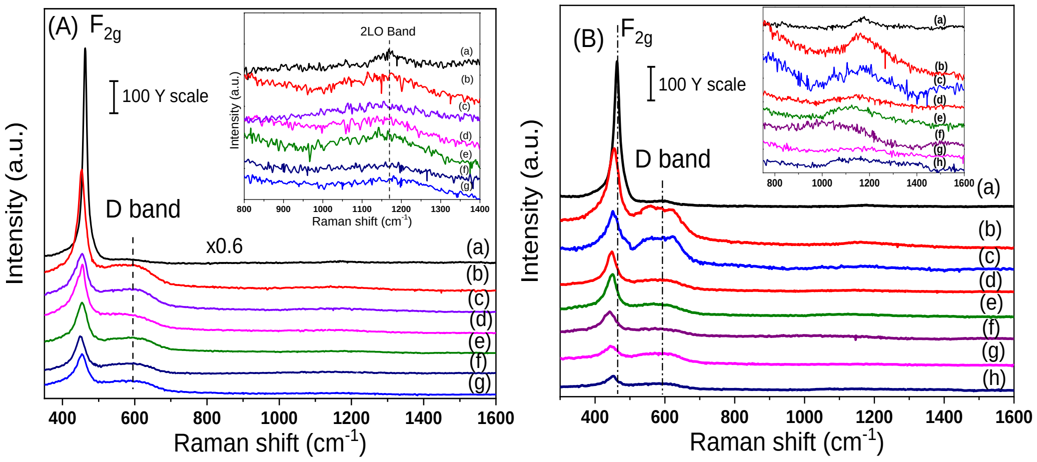

Figure 5.5 Raman spectra of (A) the xNiO/CeO$_2$ precursors and (B) reduced xNi/CeO$_{2-\delta}$ catalysts: (a) CeO$_{2-\delta}$; (b) 2Ni/CeO$_{2-\delta}$; (c) 5Ni/CeO$_{2-\delta}$; (d) 10Ni/CeO$_{2-\delta}$; (e) 15Ni/CeO$_{2-\delta}$; (f) 17.5Ni/CeO$_{2-\delta}$; (g) 20Ni/CeO$_{2-\delta}$; (h) 30Ni/CeO$_{2-\delta}$

Figure 5.5 (A) and (B) show the Raman spectra for the xNiO/CeO$_2$ precursors and xNi/CeO$_{2-\delta}$ catalysts, respectively. The Raman shifts at 462 cm^{-1} (F$_{2g}$ mode) are due to a symmetrical stretching vibration of eight Ce-O bonds in the fluorite structure, which dominates the Raman spectrum of CeO$_2$.[200] Upon NiO loaded, the Raman vibration due to F$_{2g}$ modes becomes weaker, broader and red-shifted, because the strong interaction between Ni and CeO$_2$ gives rise to distortion of CeO$_2$ lattice and creation of Ovac.[96]

Besides the F$_{2g}$ vibration, the broadening bands at 550~600 cm^{-1} and at 1000~1300 cm^{-1} regions are attributed to the defect-induced mode (D band) and second-order longitudinal optical modes (2LO band at ~1170 cm^{-1}), respectively.[96] Generally, the D band is induced by the presence of the Ovac.[158] In our samples, the D bands in the 2Ni/CeO$_{2-\delta}$ and 5Ni/CeO$_{2-\delta}$ catalysts are much stronger than those in other catalysts, which is due to higher Ovac density. However, the intensity of D bands in other xNi/CeO$_{2-\delta}$ catalysts decreases with increasing Ni loading, suggesting that the existence of larger Ni particles reduces the surface Ovac density.

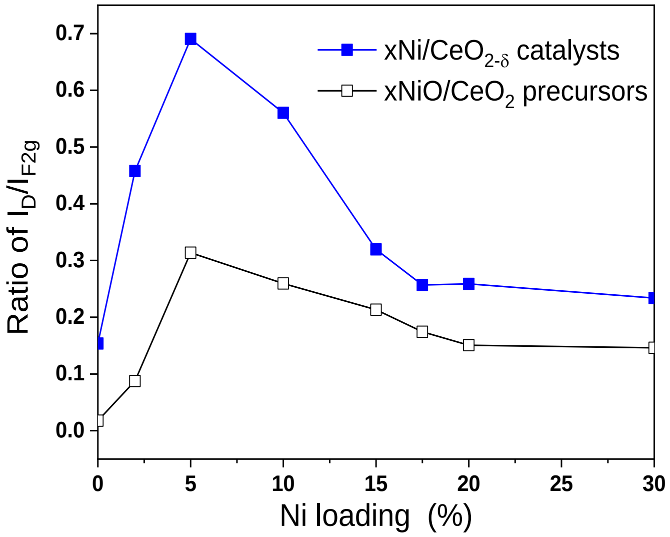

Figure 5.6 Ratios of I_D/I_{F2g} for the xNiO/CeO$_2$ precursors and xNi/CeO$_{2-\delta}$ catalysts

The relative intensity ratio of I_D/I_{F2g} can empirically reflect the Ovac density.[158] The obtained ratios for the xNiO/CeO$_2$ samples and xNi/CeO$_{2-\delta}$ catalysts are plotted in Figure 5.6. All the NiO/CeO$_2$ samples show greater I_D/I_{F2g} ratios than the CeO$_2$, suggesting Ni loading enhances Ovac formation. The Ovac density reaches the maximum at relatively low doping level of 5NiO/CeO$_2$, indicating that only a small fraction of NiO penetrates into CeO$_2$ lattice but creates significant amount of Ovac. The increasing NiO content from 5 wt% to 20 wt% is thought to reduce Ovac, because the gradual formation of large isolated NiO particles that mask the surface Ovac sites.

Compared with the xNiO/CeO$_2$ samples, the xNi/CeO$_{2-\delta}$ catalysts display larger I_D/I_{F2g} ratios with respective to their Raman peaks, indicating that H_2 reduction facilitates the formation of Ovac. It is notable in Figure 5.6 that H_2 reduction creates greater Ovac on the catalysts with low Ni loading below 10 wt%, whereas the majority of Ovac is inherited from oxide precursors as further increasing Ni loading over 17.5 wt%. The evolution of Ovac density with Ni loading indicates that a small fraction of Ni can significantly promote the reduction of CeO$_2$ and favour the formation of Ovac due to the strong Ni-CeO$_2$ interaction. However, excess Ni loading can weaken the Ni-CeO$_2$ interaction and thus hinder the reducibility of CeO$_2$.

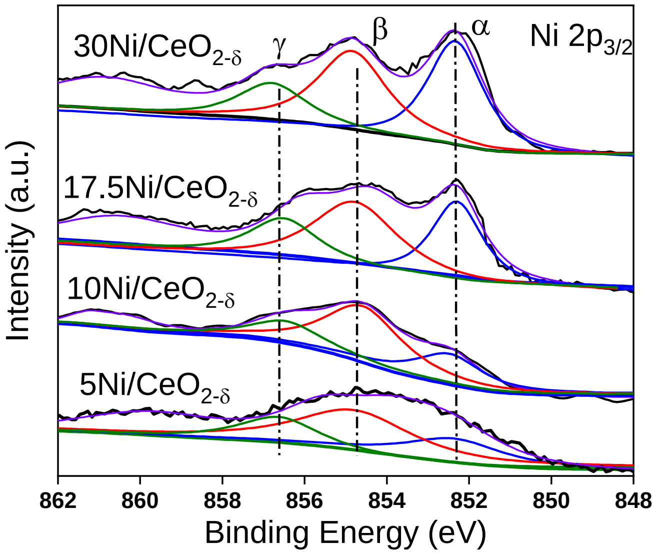

Figure 5.7 XPS spectra of $Ni2p_{3/2}$ for reduced $xNi/CeO_{2-\delta}$ catalysts

The chemical oxidation states of the Ni species in the four typical catalysts ($5Ni/CeO_{2-\delta}$, $10Ni/CeO_{2-\delta}$, $17.5Ni/CeO_{2-\delta}$ and $30Ni/CeO_{2-\delta}$) were detected by XPS. Except for the shake-up peaks of $Ni2p_{3/2}$ state at binding energy of 861 eV, the major XPS spectra of $Ni2p_{3/2}$ for the $xNi/CeO_{2-\delta}$ catalysts were fitted into three groups, which were denoted as peak α, peak β and peak γ as shown in Figure 5.7. The α peaks at ~852.8 eV are assigned to metallic Ni^0 species, while β peaks at ~854.1 eV and γ peaks at ~856.5 eV are thought to pertain to ionic Ni^{2+}[151] and Ni^{3+}[203], respectively. The $Ni2p_{3/2}$ XPS results confirm that besides the presence of metallic Ni species, ionic Ni species ($Ni^{\delta+}$) could also exist on the surface of $CeO_{2-\delta}$ support due to strong electronic interaction between Ni and ceria, which is justified below.

Although the Ni^{2+} species due to the re-oxidation of metallic Ni^0 species during the catalyst characterisation cannot be ruled out, the Ni^0 re-oxidation should not be the major reason because the samples were well protected before XPS measurements. Previous reports showed that metallic Ni species on CeO_2 can be oxidised to Ni^{2+} species by the adjacent Ce^{4+} due to the strong electronic perturbation from Ce^{4+} towards Ni species.[106, 134] Therefore, the Ni^{2+} species in the reduced samples are due to Ni species that intimately contact with $CeO_{2-\delta}$ at the $Ni/CeO_{2-\delta}$ interface and such interface Ni species take Ni^{2+} state stabilised by strong metal-support interaction. The Ni^{3+} species (γ peaks) in these catalysts are thought to originate from the Ni atom penetrating into the subsurface of the $CeO_{2-\delta}$ to form a thin layer of $Ni_xCe_{1-x}O_{2-y}$ solid solution.[161]

The calculated relative ratios of the three Ni species using the peak areas of the Ni components are listed in Table 5.3. The rising concentration of Ni^0 species is considered reasonable as more metallic Ni are exposed and aggregated on the $CeO_{2-\delta}$ surface with increasing Ni loading. However, the Ni^{2+} concentrations for 5Ni/$CeO_{2-\delta}$ and 10Ni/$CeO_{2-\delta}$ catalysts with high Ni dispersion are higher relative to those for 17.5Ni/$CeO_{2-\delta}$ and 30Ni/$CeO_{2-\delta}$ catalysts. This result agrees with the previous findings that small Ni particles in close contact with ceria support exist in oxidation state owing to electronic interaction between Ni-$CeO_{2-\delta}$, whereas large Ni particles can weaken the electronic Ni-$CeO_{2-\delta}$ interaction[106, 134], leading to less Ni^{2+} species but more Ni^0.

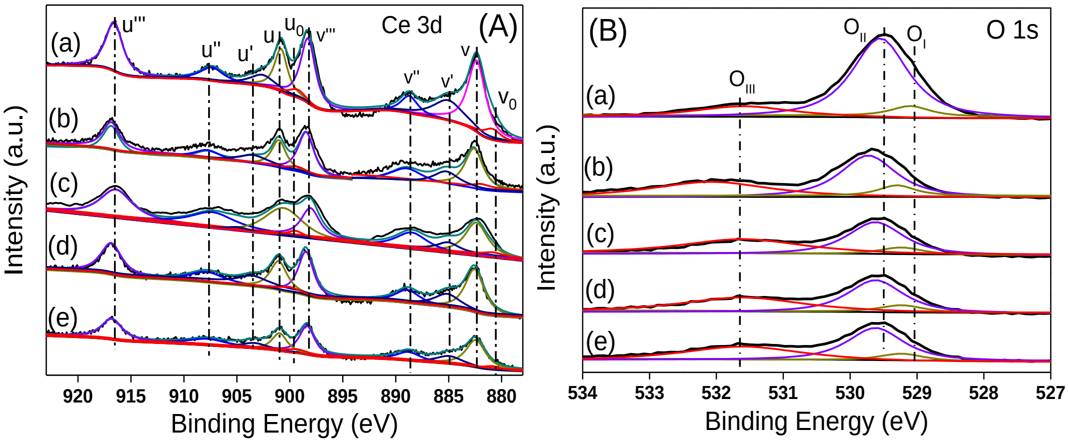

Figure 5.8 (A) Ce3d and (B) O1s core-level XPS spectra of the xNi/CeO_2 catalysts (a) $CeO_{2-\delta}$, (b) 5Ni/$CeO_{2-\delta}$, (c) 10Ni/$CeO_{2-\delta}$, (d) 17.5Ni/$CeO_{2-\delta}$ and (e) 30Ni/$CeO_{2-\delta}$

Figure 5.8(A) displays the Ce3d core-level spectra of reduced $CeO_{2-\delta}$ and the 5Ni/$CeO_{2-\delta}$, 10Ni/$CeO_{2-\delta}$, 17.5Ni/$CeO_{2-\delta}$ and 30Ni/$CeO_{2-\delta}$ catalysts. The complex spectra of Ce 3d, plotted in Figure 5.8 (A), were fitted into five pairs: three pairs of $3d_{5/2}$→$3d_{3/2}$ spin-orbit-split doublets (denoted as u and v, u″ and v″, u‴ and v‴) attributed to Ce^{4+} ions and two doublets (u′ and v′, u_0 and v_0) attributed to the presence of Ce^{3+} ions.[186] Compared to the reduced $CeO_{2-\delta}$ sample, it is worth noting that all the three doublets related to Ce^{4+} in the examined catalysts are blue-shifted, indicating the strong electronic interaction between Ni and Ce^{4+}. It is due to the short-range Ni→Ce electron transfer on the Ni-CeO_x interface. Similar M→Ce electron-transfer phenomena have been observed on the Pt/CeO_2[134] and Cu/CeO_2[204] catalysts.

The molar ratios of Ce^{3+}/(Ce^{3+}+Ce^{4+}) for the xNi/$CeO_{2-\delta}$ catalysts differ from that of $CeO_{2-\delta}$ sample (Table 5.3), suggesting that a fraction of Ce^{3+} existing in the xNi/$CeO_{2-\delta}$ catalysts are created due to Ni loading. The existence of Ce^{3+} induces the formation of Ovac, so that the concentration of Ce^{3+} and Ovac in the xNi/$CeO_{2-\delta}$ catalysts are dependent on the Ni loading, which is consistent with the Raman analysis. The concentration of Ce^{3+} increases up to 5 wt% Ni loading then declines as increasing Ni loading, suggesting that excess surface Ni species can mask the surface Ce^{3+} or large Ni particles weaken the Ni-$CeO_{2-\delta}$ interaction that hinders the formation of Ce^{3+} species.

Table 5.3 XPS analysis of the xNi/$CeO_{2-\delta}$ catalysts

Sample	$Ce^{3+}/(Ce^{3+}+Ce^{4+})$	$O_{III}/(O_I+O_{II}+O_{III})$	$O_I/(O_I+O_{II}+O_{III})$	Ni^0: Ni^{2+}:Ni^{3+}
$CeO_{2-\delta}$	0.162	0.207	0.047	
5Ni/$CeO_{2-\delta}$	0.178	0.414	0.056	0.12 : 0.64 : 0.24
10Ni/$CeO_{2-\delta}$	0.164	0.374	0.046	0.25 : 0.56 : 0.19
17.5Ni/$CeO_{2-\delta}$	0.146	0.364	0.042	0.34 : 0.45 : 0.20
30Ni/$CeO_{2-\delta}$	0.139	0.334	0.034	0.43 : 0.39 : 0.18

The O1s XPS spectra of the representative catalysts were fitted into three groups due to different oxygen species. As shown in Figure 5.6(B), the O_I and O_{II} peaks are ascribed to lattice oxygen in different coordination environments. The O_{II} band (~529.5 eV) is due to O-Ce^{4+}-O , while the O_I band (~529.0 eV) is assigned to oxygen species bound to Ce^{3+} (O-Ce^{3+}-O) that emits photoelectrons at lower energy.[166] The O_I and O_{II} peaks for the xNi/$CeO_{2-\delta}$ catalysts blue shift relative to that of the $CeO_{2-\delta}$ sample. Combined with blue shift as observed in Ce3d XPS of xNi/$CeO_{2-\delta}$ catalysts, one can conclude the loading Ni on $CeO_{2-\delta}$ surface can tune the surface electronic structure of $CeO_{2-\delta}$ due to strong electronic interplay between Ni and $CeO_{2-\delta}$. As shown in Table 5.3, the ratios of $O_I/(O_I+O_{II}+O_{III})$ decrease with the increase of Ni loading, which is consistent with variation of $Ce^{3+}/(Ce^{3+}+Ce^{4+})$ for the xNi/$CeO_{2-\delta}$ catalysts, confirming that excess Ni species reduce the amount of Ce^{3+} species.

The O_{III} peak at 531.4 eV is assigned to surface hydroxyl groups and adsorbed O_2 species anchoring at Ovac sites with low coordination.[151] The estimated molar ratios of $O_{III}/(O_I+O_{II}+O_{III})$ related to adsorbed O species suggest that the population of surface oxygen species is dependent on Ni loading too. The concentration of surface oxygen species of the xNi/$CeO_{2-\delta}$ catalysts, as listed in Table 5.3, is greater than those of $CeO_{2-\delta}$, because Ni species can facilitate the formation of Ovac, which promotes the adsorption of oxygen species.

In summary, the Ni-dependent variation of Ce^{3+} amount and Ovac density obtained by quantitative analysis of Ce3d and O1s XPS peak is consistent with the

Raman results. This result confirms that Ni species can enhance the formation of Ce^{3+} and Ovac at low Ni loading level due to the strong Ni-$CeO_{2-\delta}$ interaction, while increased Ni loading reduces the Ni-$CeO_{2-\delta}$ interaction and masks Ce^{3+} sites, thus decreasing the surface amount of Ce^{3+} and Ovac density.

5.3.4 Hydrogen activation on the xNi/$CeO_{2-\delta}$ catalysts

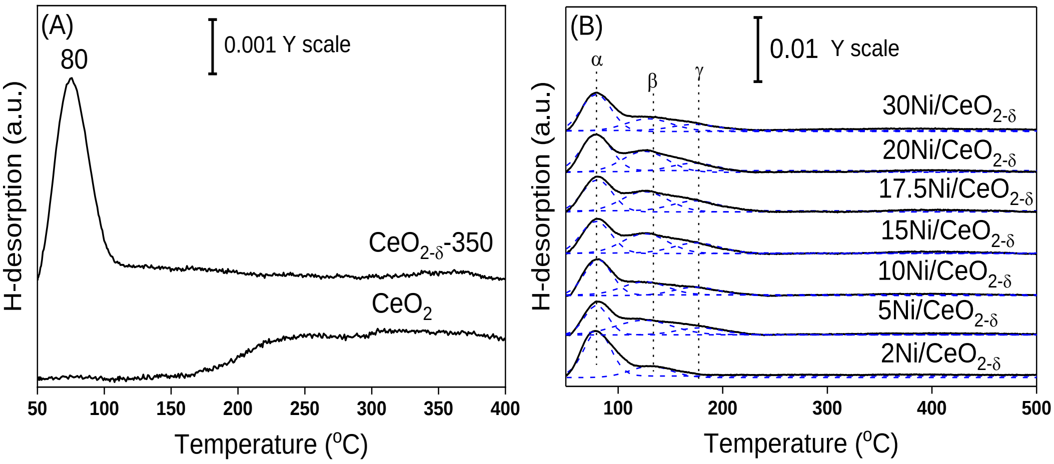

Figure 5.9 H_2-TPD profiles of (A) the unreduced and reduced CeO_2 and (B) xNi/$CeO_{2-\delta}$ catalysts

As shown in Figure 5.9 (A), the hydrogen desorption behaviour observed on the stoichiometric CeO_2 differs from that on the $CeO_{2-\delta}$ sample. A sharp H_2 desorption peak displays at 80°C on the $CeO_{2-\delta}$ sample while a broad peak is observed on CeO_2 in the 150-400°C region. The results agree with the previous report that CeO_2 can dissociate H_2 to atomic H and form surface hydroxyl group but the Ovac significantly affects the adsorbed hydrogen species on the $CeO_{2-\delta}$ surface.[124] In order to characterise different behaviour of hydrogen desorption from the two surfaces, we applied GC-Mass to monitor the effluents from the H_2-TPD experiments on the CeO_2 and $CeO_{2-\delta}$ samples.

In the H-TPD profiles recorded by GC-MS, as illustrated in Figure 5.10, a broad peak within 150-400°C for the CeO_2 is attributed to H_2O desorption, suggesting irreversible hydrogen desorption occurs due to strong O-H bond (in form of OH group) formation at the CeO_2 surface.[123] In contrast, the sharp desorption peak at 80°C for the $CeO_{2-\delta}$ sample is due to H_2 releasing. These results suggest that the presence of Ovac facilitates the recombination of atomic H to H_2, because the negative electrons trapped by Ovac can reduce energy barrier of H_2 generation from the hydroxyl species and block the O-H bond formation.[125]

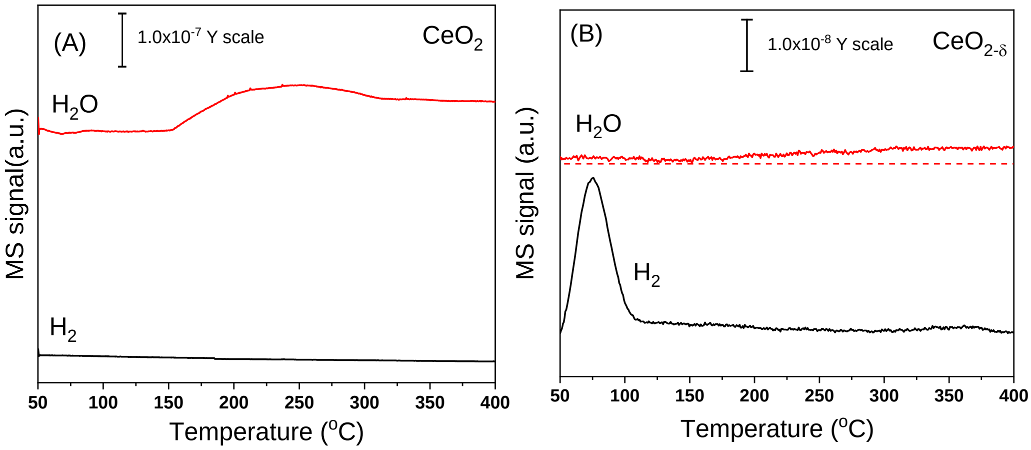

Figure 5.10 H_2-TPD-MS profiles of (A) unreduced CeO_2 and (B) reduced $CeO_{2-\delta}$ samples

The H_2-TPD profiles of xNi/$CeO_{2-\delta}$ catalysts (Figure 5.9 (B)) were fitted to three groups of peaks at ~80, 128 and 178°C, denoted as α, β and γ, respectively, due to three different sites taken up hydrogen. The H-TPD peak α, at the same temperature as that of $CeO_{2-\delta}$ sample, can be assigned to the Ovac-induced hydrogen desorption from the surface of $CeO_{2-\delta}$.[183] The peak γ is associated with hydrogen chemisorption on isolated Ni^0 nanoparticles, which shows similar features in the H_2-TPD profiles of Ni/Al_2O_3 and Ni/SiO_2 catalysts regardless of support types.[190] The peaks β located between peaks α and γ can be ascribed to dissociative H_2 residing at the Ni-CeO_2 interface which nickel species strongly interact with $CeO_{2-\delta}$. These interface Ni species possesses strong Ni-ceria interaction that perturbs the electronic interaction between Ni species and dissociative H atom, so that their H_2 desorption occurs at low temperature, corresponding to low H_2 activation barrier.[205] It is worth noting that the H_2-TPD, H_2-TPR and XPS results verify consistently that there exist distinct Ni species in the xNi/$CeO_{2-\delta}$ catalysts, whereas the H_2-TPD results can reflect the H-activation and surface chemistry of the catalysts, very crucial for hydrogenation reactions.

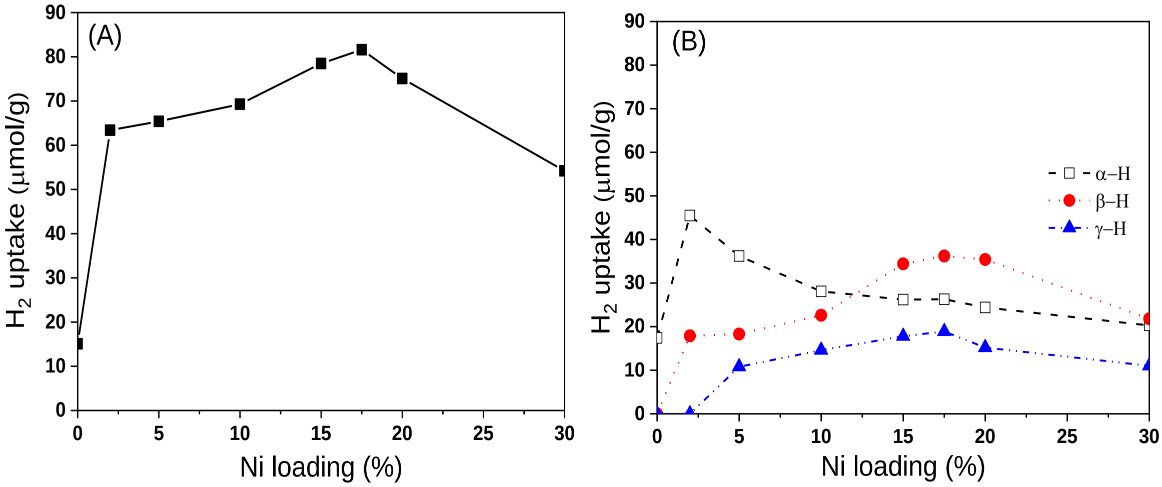

Figure 5.11 Total (A) and site-defined (B) hydrogen uptake on the xNi/CeO$_{2-\delta}$ catalysts

Figure 5.11 (A) depicts a volcano-like curve of the global H_2 uptake on the xNi/CeO$_{2-\delta}$ catalysts. Compared with CeO$_{2-\delta}$, 2Ni/CeO$_{2-\delta}$ shows a dramatic increase of H_2 uptake (300% increase) with 2 wt% Ni loading on the defective CeO$_{2-\delta}$. As gradually increasing Ni loading amount to 17.5 wt%, the H_2 uptake on xNi/CeO$_{2-\delta}$ rises linearly up to the maximum on the 17.5Ni/CeO$_{2-\delta}$ catalyst then declines as further increasing Ni loading. Low H_2 uptake, namely low H_2 activation ability, is observed on the xNi/CeO$_{2-\delta}$ with aggregated Ni^0 species (see XRD and Table 5.1).

Such a volcano-like H_2-uptake dependence on Ni loading should not be arisen from the Ni^0 dispersion only, but also should consider the Ni species and their synergistic interaction with Ovac, because varying Ni amount in a wide region only causes relatively smaller changes of H_2 desorption amount. Based on the attributions of different H-TPD peaks, we suppose the large Ni^0 particles would hinder Ovac formation and reduce the Ni-CeO$_{2-\delta}$ interaction, thus reducing H_2 adsorption and activation on the xNi/CeO$_{2-\delta}$ catalysts.[206, 207]

The H_2 uptakes on different active sites (Ovac, highly dispersed Ni^0 with strong Ni-CeO$_2$ interaction and the aggregated Ni^0) for xNi/CeO$_{2-\delta}$ catalysts were further quantified and presented in Figure 5.11 (B). 2Ni/CeO$_{2-\delta}$ has the largest α-H amount that declines systematically as increasing the Ni loading. The variation of α-H suggests that a small amount of Ni loading can greatly enhance H_2 activation, while H_2 activation will be suppressed by greater Ni^0 particles which either reduces Ovac-Ni interaction or Ovac concentration. The concentrations of β-species and γ-H species showed the similar evolution trends, with the maximum H-uptake on the sample with 17.5 wt% loading.

The quantitative analyses unravel that H_2 can be activated at different sites on the xNi/$CeO_{2-\delta}$ catalysts: aggregated Ni^0 particles, highly dispersed Ni^0 clusters with strong Ni-$CeO_{2-\delta}$ interaction, and the Ovac that greatly promote hydrogen adsorption through Ni-Ovac interaction.

5.3.5 Catalyst performance

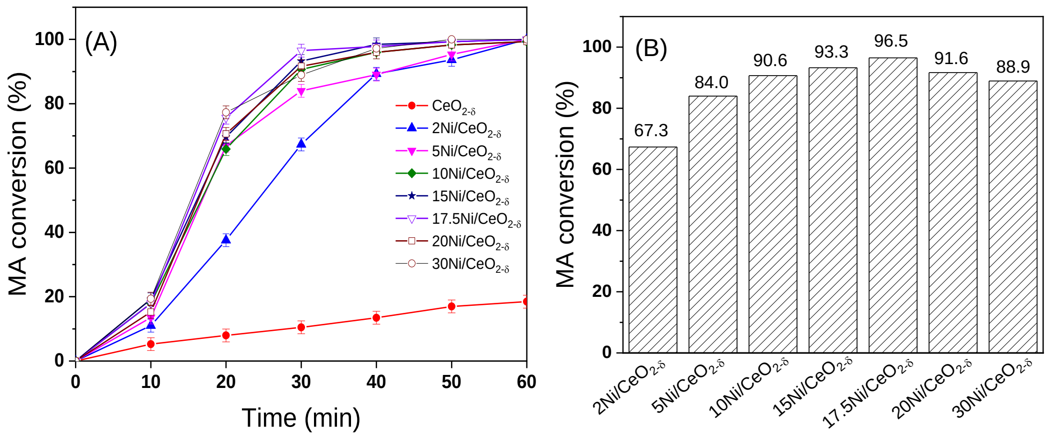

Figure 5.12 (A) MA conversion over the reduced xNi/$CeO_{2-\delta}$ catalysts in 1h and (B) the specific MA conversion over the xNi/$CeO_{2-\delta}$ catalysts at 30 min

Figure 5.12 presents the hydrogenation of MA on the xNi/$CeO_{2-\delta}$ catalysts in a batch reactor at 210°C and under 5.0 MPa hydrogen pressure. One can see that MA completely converted into SA within 1 h on the xNi/$CeO_{2-\delta}$ catalysts, without other side products being detected apart from SA. The $CeO_{2-\delta}$ without Ni loading can catalyse MA conversion to SA, suggesting that $CeO_{2-\delta}$ is an active support for MA hydrogenation. The 2Ni/$CeO_{2-\delta}$ catalyst with only 2 wt% Ni loading shows a remarkable enhancement of MA conversion of 85% in 40 minutes, which is 6-fold that on the $CeO_{2-\delta}$. The increase of Ni loading from 5 wt% to 17.5 wt% only slightly enhances MA conversion in the initial hydrogenation stage (Figure 5.12(A)), whereas MA hydrogenation is depressed as the Ni loading over 17.5 wt% (Figure 5.12(B)). The results presented in Figure 5.12 indicate that the Ni species is the major active species relative to the $CeO_{2-\delta}$ support, while the different Ni species and the surface properties of catalysts may be crucial for MA hydrogenation.

Figure 5.13 (A) shows the selectivity of SA in the 8 h continuous MA hydrogenation on the catalysts. The reduced $CeO_{2-\delta}$ displays 100% selectivity to SA in the 8 h time-on-stream of hydrogenation. The xNi/$CeO_{2-\delta}$ catalysts exhibit 100% selectivity to SA in the initial 40-60 min on the dependence of the Ni-loading. Once the MA conversion completed, SA selectivity dropped due to GBL generation. Figure 5.13(B) shows the yield of GBL (< 40%) grew slowly in the rest 7 h hydrogenation process. The results suggest that MA hydrogenation on the xNi/$CeO_{2-\delta}$ catalysts is a multiple-step process: the hydrogenation of MA to SA occurs firstly and quickly while the sequential SA hydrogenolysis to GBL is a very slow process.

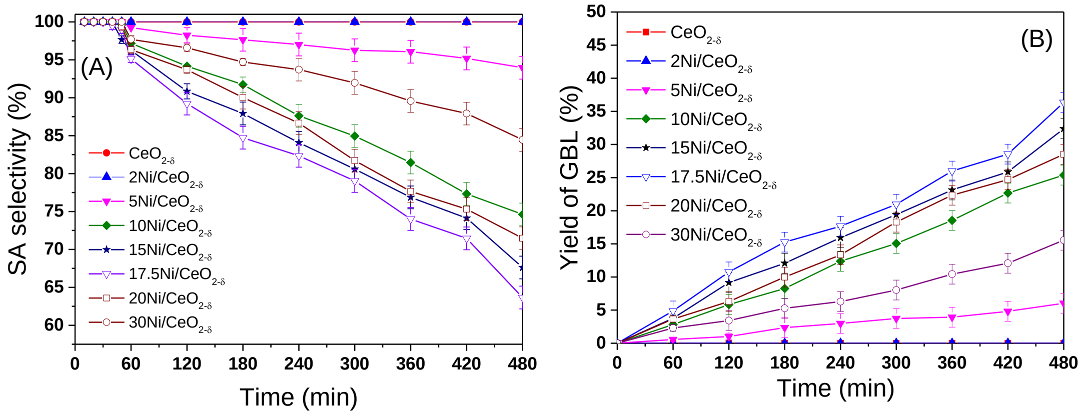

Figure 5.13 (A) Selectivity of SA and (B) yield of GBL over the reduced xNi/CeO$_{2-\delta}$ catalysts at 210℃ and 5 MPa for 8 h

As shown in Figure 5.13(B), no GBL was detected on 2Ni/CeO$_{2-\delta}$ and CeO$_{2-\delta}$ in the 8 h hydrogenation process. However, GBL yield on the xNi/CeO$_{2-\delta}$ was enhanced as Ni content increasing from 5 wt% and reached the highest GBL yield (36.5%) on 17.5Ni/CeO$_{2-\delta}$. The yield of GBL dropped down to 28.5% and 15.5% on 20Ni/CeO$_{2-\delta}$ and 30Ni/CeO$_{2-\delta}$, respectively. The results imply that SA hydrogenolysis are governed by the Ni species, the active sites distinct from those for MA hydrogenation to SA. It was reported that the large Ni^0 particles[43] and strong surface acidity[76] promoted GBL selectivity. However, the 17.5Ni/CeO$_{2-\delta}$ catalyst does not have the largest Ni^0 particle and the CeO$_{2-\delta}$ support is an electron donor (more Lewis basic than acidic). Furthermore, the 2Ni/CeO$_{2-\delta}$ catalyst with rich Ovac concentration cannot catalyse SA→GBL transformation, implying that Ovac is not key active sites for C=O hydrogenolysis. Therefore, besides the suitable Ni particle size, the strong Ni-CeO$_{2-\delta}$ interaction rather than Ovac determines the GBL selectivity in the long-time hydrogenation process.

5.4 Discussion

5.4.1 C=C hydrogenation over xNi/CeO$_{2-\delta}$ catalysts

In the present research, it was found that SA was produced by hydrogenating MA on the reduced CeO$_{2-\delta}$ sample, suggesting that CeO$_{2-\delta}$ can catalyse C=C hydrogenation. A similar catalytic phenomenon was reported by Vile and co-workers[127] that CeO$_2$ can effectively hydrogenate alkynes to olefins due to the excellent ability of CeO$_2$ in hydrogen activation. The previous DFT simulation showed that the adsorption of dissociative H on the pristine CeO$_2$ is an exothermic process (-2.82 eV) due to the formation of O-H bond on the surface.[183] In contrast, $CeO_{2-\delta}$ with H_2-induced Ovac can weaken the surface O-H bond and facilitate H diffusion due to the electron donation ability of Ovac.[126] The H_2-TPR and H_2-TPD results in this study suggested that Ovac in the $xNi/CeO_{2-\delta}$ catalysts can enhance hydrogen activation and diffusion. Combined the H_2-TPD results and MA hydrogenation on the $CeO_{2-\delta}$, we can conclude that Ovac in $CeO_{2-\delta}$ can offer active H species to the MA→SA transformation, which is crucial for C=C hydrogenation on the $CeO_{2-\delta}$ and $xNi/CeO_{2-\delta}$ catalysts.

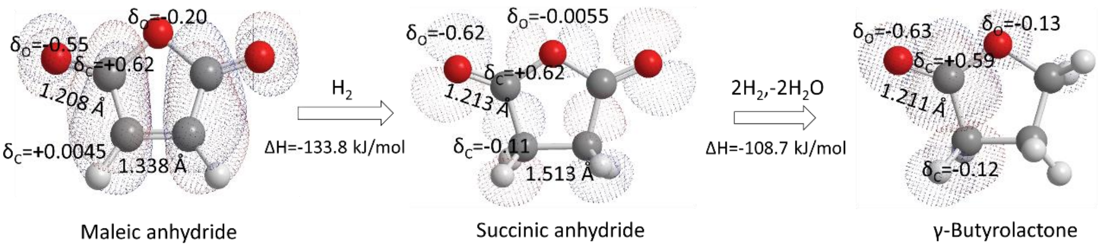
δ_O=-0.20
δ_O=-0.55
δ_C=+0.62
1.208 Å
δ_C=+0.0045
1.338 Å
Maleic anhydride
H_2
ΔH=-133.8 kJ/mol
δ_O=-0.0055
δ_O=-0.62
δ_C=+0.62
1.213 Å
δ_C=-0.11
1.513 Å
Succinic anhydride
$2H_2$,$-2H_2O$
ΔH=-108.7 kJ/mol
δ_O=-0.63
δ_O=-0.13
δ_C=+0.59
1.211 Å
δ_C=-0.12
γ-Butyrolactone

Figure 5.14 Pathway of MA hydrogenation with low unoccupied molecular orbital, charge and bond length

Besides the crucial role of Ovac in hydrogen activation, the anionic Ovac can play a pivotal role in the C=C adsorption and activation due to the strong electron donating character of Ovac.[208] In order to understand the interaction of Ovac with the reactants and products, the electronic structure of MA, SA and GBL molecules, including low occupied molecular orbitals, element charge and bond length were simulated using the MM2 module embedded in the Chem3D software. The simulated electronic structures of the three molecules are illustrated in Figure. 5.14. The C moieties of the C=C bond in the MA molecule are positively charged, which would strengthen MA adsorption on the $CeO_{2-\delta}$ surface through their strong interaction with anionic Ovac. Such strong interaction is possibly attributed to the partial transfer of electron from the anionic Ovac into the antibonding π* orbital of C=C in the MA molecule.[202] In contrast, the C-C bond in both SA and GBL possesses negatively charged carbon moieties, so that such C-C bonds of SA or GBL would leave or weakly adsorb on Ovac. Combined the enhanced H_2 activation and preferential adsorption of C=C groups on the Ovac site, we suppose that Ovac served as active sites for MA hydrogenation to SA over the $CeO_{2-\delta}$ surface. However, $CeO_{2-\delta}$ possessed relatively low activity in MA hydrogenation because of the limited density of Ovac, as seen in Figure 5.11(A).

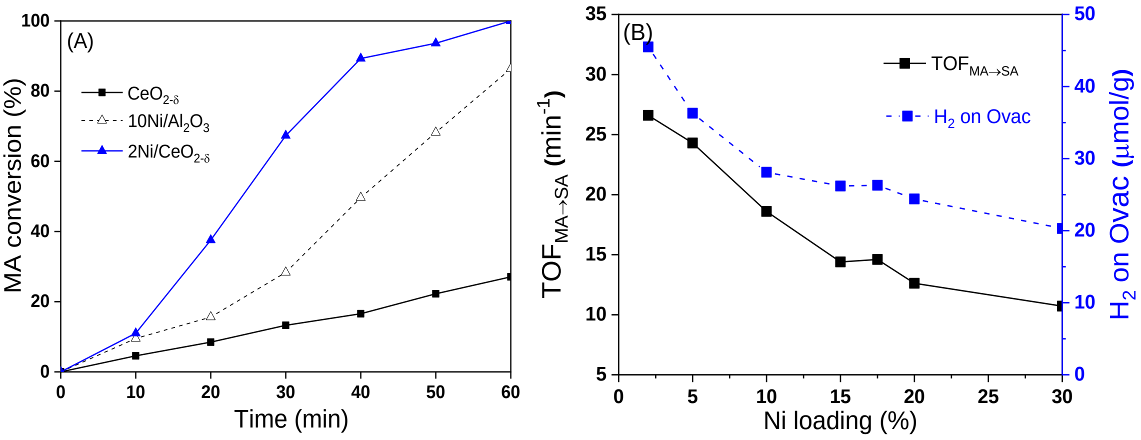

Figure 5.15 (A) Comparison of MA conversion over representative catalysts and (B) nickel loading dependence of $TOF_{MA\rightarrow SA}$ and Ovac-induced hydrogen desorption

Despite the fact that Ovac is the major active sites on $CeO_{2-\delta}$, as shown in Figure 5.15(A), adding only 2 wt% of Ni on $CeO_{2-\delta}$ can considerably enhance MA conversion, much more active than $10Ni/Al_2O_3$ catalyst, indicating a significant role of Ovac in enhancing C=C hydrogenation on Ni species. For in-depth understanding of the C=C hydrogenation on the xNi/$CeO_{2-\delta}$ catalysts, the turnover frequencies of MA hydrogenation to SA ($TOF_{MA\rightarrow SA}$) over Ni species were calculated using the Equation (2.10) in Chapter 2. The conversion of MA in the initial 10 min with only SA generation was used for calculation of $TOF_{MA\rightarrow SA}$ (see Figure B1, *Appendix B*). As comparatively presented in Figure 5.15 (B), the Ni-loading dependence of $TOF_{MA\rightarrow SA}$ well matches Ovac-induced hydrogen activation rather than the overall H_2 activation on the xNi/$CeO_{2-\delta}$ (see Figure 5.11(A)) in the whole Ni loading region, verifying the crucial enhancement of Ovac in the C=C hydrogenation on the xNi/$CeO_{2-\delta}$ catalysts.

In the open literature, the electron-donating character of Ovac to its adjacent metal species has been regarded as a crucial factor in enhancing the C=C hydrogenation. For example, the Pd/$CeO_{2-\delta}$ catalyst with abundant Ovac displayed high activity in the styrene hydrogenation because the surface Ovac enriched the electron density of Pd, thereby improving the H_2 dissociation and the affinity of styrene on Pd.[209] The electron-rich gold particles supported on ZrO_2 and TiO_2 gave considerable activity of C=C hydrogenation in the hydrogenation of acrolein on the Au/ZrO_2 and Au/TiO_2 catalyst due to the electron-donating feature of Ovac to Au.[202] Therefore, the Ovac-enhanced C=C hydrogenation over the xNi/$CeO_{2-\delta}$ catalysts can be interpreted by the Ovac-Ni interaction, in which Ovac would donate electrons to the supported Ni species[206] and facilitate the adsorption of MA and H_2 (see H_2-TPD section).

Based on the analyses of the Ovac→Ni charge transfer and the charge population of MA, in particular the C=C bond (Figure 5.14), a mechanism for MA hydrogenation over the xNi/$CeO_{2-\delta}$ catalysts is proposed, as illustrated in Scheme 5.1. The mechanism supposes the C=C bond prefers to adsorb on the Ni species in the di-σ mode by which the positively charged C atoms of C=C bond accept electrons from the electron-enriched Ni species arisen from Ovac→Ni^0 charge transfer. Such adsorption mode favours the insertion of adjacent H species activated by either Ni^0 or Ovac on the catalyst.

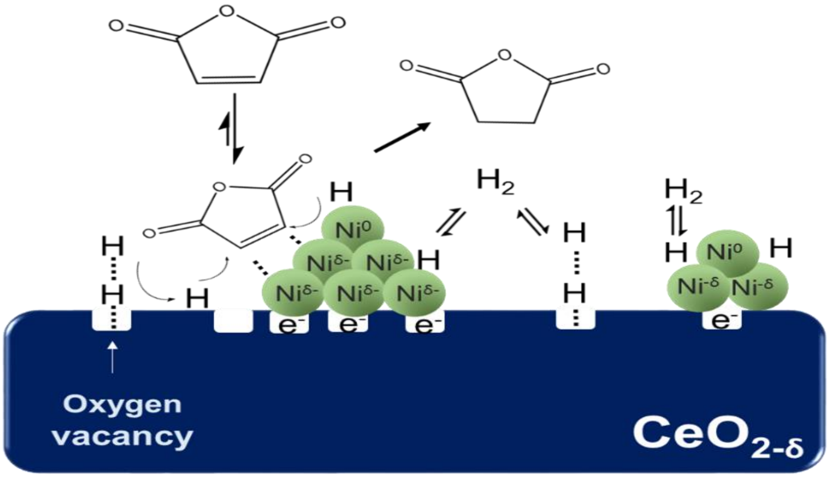

Scheme 5.1 The enhancement of Ovac in C=C hydrogenation

Besides the significant roles of Ovac and Ni-Ovac in C=C hydrogenation, the crystallite size of Ni species plays important roles in the MA hydrogenation, though the reported impacts of Ni particles size on MA hydrogenation activity and product selectivity were controversial in the literature.[79, 82] Figure 5.16 (B) compares the Ni-loading dependence of $TOF_{MA\rightarrow SA}$ with crystallite sizes of Ni particles. The Ni loading was chosen from 10 wt% to 30 wt% because the x-ray diffraction of the Ni species was absent in their XRD patterns for the xNi/$CeO_{2-\delta}$ catalysts of low Ni loading (2~5 wt%). It is clearly seen that the $TOF_{MA\rightarrow SA}$ values decline drastically with increased mean crystallite sizes of Ni species, suggesting that small crystallite size of Ni benefits the C=C hydrogenation activity. This phenomenon is reasonable because large Ni particles would mask Ovac and weaken the Ni-Ovac interaction, as evidenced by Raman, H_2-TPR and H_2-TPD results, then suppress the electron donation from Ovac to Ni species.[206] Since the electronic perturbation between Ovac and Ni may exist in relatively short distance, the samples with smaller Ni crystallite sizes and more Ovac (low Ni loading) exhibit stronger Ovac→Ni electron donating effect and thus higher activity (greater $TOF_{MA\rightarrow SA}$). In contrast, the C=C hydrogenation activity on xNi/$CeO_{2-\delta}$ with larger Ni loading (x >17.5 wt%) decreases because their larger Ni particles mask Ovac and weaken the interaction between Ni and Ovac.

5.4.2 C=O hydrogenolysis over xNi/$CeO_{2-\delta}$ catalysts

In terms of C=O hydrogenolysis, previous research showed that increased metal particle size can enhance the C=O hydrogenolysis. For example, a considerable increase of selectivity towards the unsaturated alcohol with increasing Pt particle size has been observed in the hydrogenation of crotonaldehyde over the Pt/SiO_2 and Pt/TiO_2 catalyst.[77] Similarly, the larger gold nanoparticles gave higher formation rates of the allylic alcohol than smaller gold particles in the hydrogenation of acrolein.[202] The large metal particles can provide more fraction of closed-packed structure of the (111) surface, on which the C=O group can adsorb in a di-σ_{CO} mode and be preferentially activated.[77] For MA hydrogenation, large Ni particles can improve the selectivity of GBL, as observed in the study of MA hydrogenation on Ni/HY-Al_2O_3[43], Ni/SiO_2-Al_2O_3[79] and Ni/ZrO_2-SiO_2[81], likely due to the fact that large metallic Ni particles can offer high fraction of dense (111) surface for C=O activation. In our case, the effect of increased Ni particle size can be effective to explain the enhanced GBL selectivity with Ni loading up from 5 wt% to 17.5 wt%, as shown in Figure 5.13(B); however, it is insufficient to interpret the reduced GBL selectivity of 20Ni/$CeO_{2-\delta}$ and 30Ni/$CeO_{2-\delta}$ with larger Ni particles. This result indicates that other crucial factors dominate GBL selectivity besides the particle size of Ni on the xNi/$CeO_{2-\delta}$ catalysts.

To understand C=O hydrogenolysis on the xNi/$CeO_{2-\delta}$ catalysts, the $TOF_{SA\rightarrow GBL}$ on metallic Ni species was estimated using the Equation (2.11) in Chapter 2. As shown in Figure 5.16 (A), the Ni-loading dependence of $TOF_{SA\rightarrow GBL}$ is a volcano-like curve, distinct from the curve of the $TOF_{MA\rightarrow SA}$ (Figure 5.16(B)), revealing that active sites for C=O hydrogenolysis differ from those for C=C hydrogenation in the same xNi/$CeO_{2-\delta}$ catalysts and the C=O hydrogenolysis is sensitive to Ni loading amount. However, the plot of $TOF_{SA\rightarrow GBL}$ versus Ni loading agrees neither with the H_2 activation on Ni^0 nor with Ni^0 dispersion, which is different from the results reported in some literature[76, 79, 83], suggesting other factors determine the C=O hydrogenolysis on the xNi/$CeO_{2-\delta}$ catalysts.

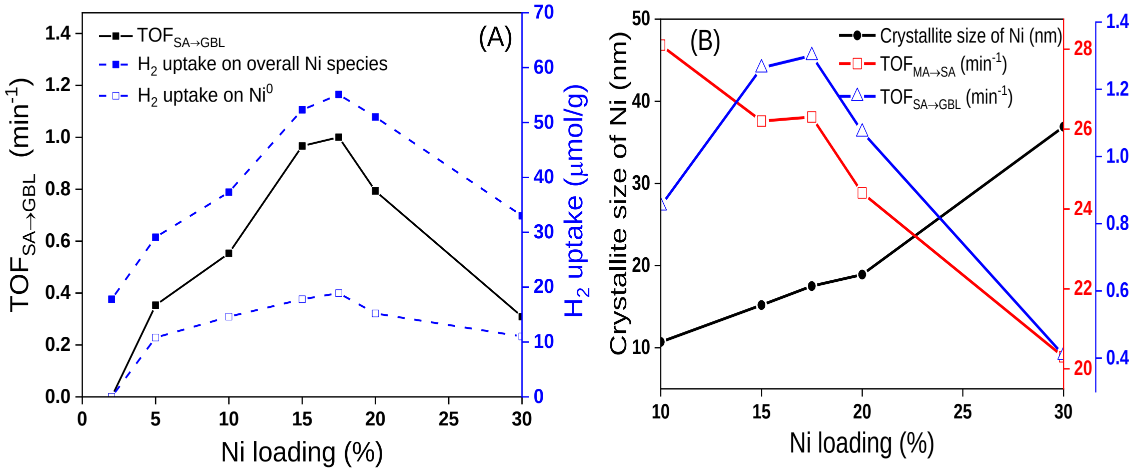

Figure 5.16 (A) Ni loading dependence of TOF$_{SA\rightarrow GBL}$ against H_2 uptake on nickel species for the xNi/$CeO_{2-\delta}$ catalysts and (B) effect of nickel crystallite size on the TOF$_{MA\rightarrow SA}$ and TOF$_{SA\rightarrow GBL}$

As seen in Figure. 5.16 (A), the variation of TOF$_{SA\rightarrow GBL}$ well agrees with the total H_2 activation on the metallic Ni^0 and highly dispersed Ni species on the xNi/CeO_2 catalysts, indicative of their synergistic role in C=O hydrogenolysis. As increasing nickel loading in xNi/$CeO_{2-\delta}$, the total amount of H_2 activated by isolated Ni^0 and highly dispersed Ni species increases and reaches the maximum at 17.5 wt% Ni loading, so that 17.5Ni/$CeO_{2-\delta}$ displays the highest TOF$_{SA\rightarrow GBL}$. The result suggests that adjacent binary Ni active sites, metallic Ni^0 and highly dispersed Ni species, may play a synergistic role in the hydrogenolysis of SA to GBL.

In the case of xNi/$CeO_{2-\delta}$ catalysts, the highly dispersed Ni species can strongly interact with CeO_2 support, thus facilitating the formation of coordinative CeO_X species with unsaturated Ce cations (Ce^{3+}), as evidenced by the Raman and XPS results. Moreover, the H_2-TPD results show that highly dispersed Ni species possess weaker interaction with dissociative H atom in comparison with bulk Ni^0 species due to the strong metal-support interaction that perturbs electronic structure of these Ni species.[210] The electronic interaction between Ni and CeO_2 support has been investigated by DFT simulation, showing that nickel atoms in close contact with CeO_2 support can donate their electrons to the localized f-states of neighbouring Ce cation, leading to the formation of cationic $Ni^{\delta+}$ species[106, 161]. Based on experiment and simulation results, it is reasonable to indicate that the highly dispersed Ni species could be surrounded by coordinative CeO_X species with unsaturated Ce cations and be cationised ($Ni^{\delta+}$) to some extent due to the strong Ni-CeO_2 interaction.

With respect to the C=O hydrogenolysis, the carbonyl group can strongly interact with the cationic metal species and/or coordinative metal oxide by donating a lone pair of electrons of oxygen to the electron deficient sites. As a result, the coordination decreases the electron density of the C=O bond, hence, increases its reactivity. For example, the presence of coordinative TiO_x with unsaturated Ti cations on Pt/TiO_2[48, 77] and Ni/TiO_2[48] strengthened the adsorption of the carbonyl group, leading to the enhancement of C=O hydrogenolysis in crotonaldehyde hydrogenation. Additionally, the Ni/TiO_2 catalyst displayed high selectivity of cinnamyl alcohol in cinnamaldehyde hydrogenation because a small amount of cationic $Ni^{\delta+}$ at the surface can adsorb and activate the C=O group, thus enhancing the selectivity.[211] Therefore, it is reasonable to define the highly dispersed Ni species surrounded by the coordinative CeO_x species as active sites to strongly interact with negative O atom in the C=O group, thus facilitating C=O adsorption on the catalysts. However, it is worth noting that these active sites are not active for C=O hydrogenation, as evidenced by the negligible SA→ GBL transformation activity on the 2Ni/$CeO_{2-\delta}$ catalyst with the greatest Ni dispersion. The highly dispersed Ni species can polarize and activate C=O bond, however, the strong Ni-CeO_2 interaction increases the strength of C-O bond, as evidenced by simulating CO adsorption and dissociation on $Ni_1/CeO_2(111)$ surface[207], making significantly difficult to cleave the C-O bond. In contrast, the bulk Ni species can strongly interact with C moieties in the CO molecule that enhances the CO dissociation.[207] Hence, metallic Ni species is required to cleave the C-O bond. Therefore, the synergy between highly dispersed Ni species and metallic Ni active sites can be envisaged in Scheme 5.2: highly dispersed Ni species ($Ni^{\delta+}$) with coordinative CeO_x species can adsorb and activate C=O group and thus facilitate hydrogenolysis on adjacent Ni^0.

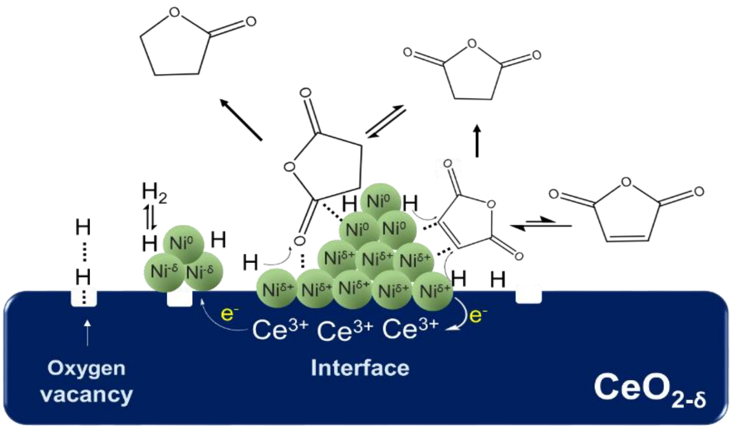

Scheme 5.2 Synergy between ionic and metallic Ni active site in C=O hydrogenolysis over xNi/$CeO_{2-\delta}$ catalyst

It is worth noting that the $TOF_{SA\rightarrow GBL}$ reaches the maximum as Ni loading up to 17.5 wt%, then drastically declines at higher Ni loading (20 wt% and 30 wt%) with larger Ni^0 particle size. This result suggests that the oversized Ni particles hinder the synergism in enhancing C=O hydrogenolysis. The synergistic interaction between bulk Ni^0 and highly dispersed nickel species only presents in short distance, and it is inevitably reduced by long distance from the surface metallic species of the large Ni particles to the highly dispersed Ni species that are in close contact with CeO_2 support. Therefore, it is reasonable to note that the 30Ni/$CeO_{2-\delta}$ catalyst of the largest Ni crystallite size and least amount of highly dispersed Ni species, showed the lowest GBL yield.

The dominant role of Ovac in C=O hydrogenolysis can be ruled out because no GBL generated on $CeO_{2-\delta}$ and 2Ni/$CeO_{2-\delta}$ with abundant density of Ovac, as shown in Figure 5.13(B), and the Ni loading dependence of $TOF_{SA \rightarrow GBL}$ is distinct from Ovac variation along Ni loading as discussed in Raman, XPS and TPD sections. The weak activity of $CeO_{2-\delta}$ and 2Ni/$CeO_{2-\delta}$ catalyst in SA →GBL can be due to the repulsive interaction between anionic Ovac and the negative oxygen moieties of the carbonyl group, which retards the C=O adsorption and activation. Moreover, it was reported that Ovac prefers to interact with the oxygen atom in the maleic anhydride ring rather than the carbonyl oxygen, as observed MA adsorption on the Mo(110)[212], Re(0001)[88] and TiO_2[93] surfaces. However, as evidenced by H_2-TPD characterisation, Ovac can enhance H_2 dissociation and provide active H species for C=O hydrogenolysis, so that Ovac could be beneficial to GBL production to some marginal content.

5.5 Conclusion

The xNi/$CeO_{2-\delta}$ catalysts with varying Ni loading were prepared via the impregnation method and were assessed in MA hydrogenation. The catalysts were well characterised by XRD, H_2-TPR, TEM, XPS, Raman and H_2-TPD. Ovac, Ni^0 and Ni-CeO_2 interface were defined as active sites in MA hydrogenation and their different roles in C=C hydrogenation and C=O hydrogenolysis were specified.

For C=C hydrogenation, reduced $CeO_{2-\delta}$ with Ovac can catalyse MA conversion to SA due to the electron donating character of Ovac to activate hydrogen and MA molecule, but low activity was limited by the concentration of Ovac on the $CeO_{2-\delta}$ surface. On the other hand, introducing Ni on $CeO_{2-\delta}$ surface greatly improved the activity of MA hydrogenation and the activity depended on Ni loading amount over the xNi/$CeO_{2-\delta}$ catalysts, indicating a pivotal role of Ni species in MA hydrogenation to SA. Among the xNi/$CeO_{2-\delta}$ catalysts, 2Ni/$CeO_{2-\delta}$ displayed the largest $TOF_{MA \rightarrow SA}$ due to the strongest Ni-Ovac interaction with electron donation (Ovac→Ni), while the increase of Ni loading reduced $TOF_{MA\rightarrow SA}$ because the isolated Ni^0 would mask the short-range electronic Ovac→Ni interaction.

In terms of C=O hydrogenolysis, the yield of GBL depended primarily on Ni loading in the xNi/$CeO_{2-\delta}$ catalysts and the specific activity of SA hydrogenolysis to GBL per Ni atom ($TOF_{SA\rightarrow GBL}$) showed a volcano-like relationship with Ni loading. Despite the fact that Ni^0 was indispensable for GBL production, the coexistence of Ni^0 and highly dispersed Ni species synergistically governed the GBL yield: the highly dispersed Ni species can adsorb and activate C=O group and thus facilitate hydrogenolysis on adjacent Ni^0. Such synergism was dependent on the nickel loading and only presented in a short range on the xNi/$CeO_{2-\delta}$. This finding well interprets that the maximum GBL yield turned on 17.5Ni/$CeO_{2-\delta}$ but it declined with further increasing Ni loading and larger Ni^0 particle size.

Chapter 6 The effects of CeO_2 morphology on MA hydrogenation over the $Ni/CeO_{2-\delta}$ catalysts

6.1 Introduction

In ceria involved heterogeneous catalysis, whatever as a catalyst or a support, the morphology of ceria has been considered as a crucial parameter to remarkably influence the performance of the catalysts.[213, 214] For example, CeO_2 nanorods that mainly expose (110) and (100) crystal planes exhibited higher catalytic activity in CO oxidation than CeO_2 nanoparticles that expose (111) crystal planes due to much better reducibility and higher Ovac density of CeO_2 nanorods.[215] Another morphology-dependent catalytic performance of CeO_2 was reported by Tana et al. that CeO_2 nanowires displayed higher oxygen storage capacity and catalytic CO oxidation activity in comparison with CeO_2 nanorods and nanoparticles due to larger portion of (110) and (100) planes exposed on CeO_2 nanowires.[216] Such morphology related phenomena come from selective exposure of crystal planes on a uniform shaped ceria that determine the surface composition and structure.[217-220] Based on the previous DTF simulation, the structure of three low index surfaces (111), (110) and (100), which are predominantly exposed on CeO_2 nanocrystals, are summarised in Table 6.1. The different structures of three crystal planes with varying Ovac formation energy contribute to the morphology-dependent reducibility, Ovac density and catalytic activity of nanocrystal ceria.

Besides the morphology effect on Ovac density and reducibility, the morphology of ceria significantly affects the metal-support interaction and thus catalytic performance of the CeO_2 supported catalysts. Si and co-workers investigated the shape and crystal-plane effects of ceria on the Au/CeO_2 catalyst. Their results showed that Au^{3+} and Au^{+} species were the main species on the CeO_2 nanorod or polyhedron samples, while metallic Au^0 was prevailing on the CeO_2 nanocube.[156] Such results indicated that the morphology of CeO_2 dominated the chemical state of supported Au species, which consequently led to their different activity in water-gas shift reaction with a decreasing order: Au/CeO_2-nanorods > Au/CeO_2-polyhedra ≫ Au/CeO_2-cubes.[156] Tan and co-workers found that Pd/CeO_2 nanocube is a promising catalyst for ambient oxidation of formaldehyde with high activity and stability because CeO_2 nanocube can stabilise metallic Pd species and prevent Pd^0 species from being oxidised in the oxygen atmosphere.[221] Zhang and co-workers observed high activity of alkene hydrogenation on the Pd/CeO_2 nanorod catalyst, which was attributed to high dispersion of Pd and the rich Ovac on the nanorod surface.[209] Their DFT studies deduced that Ovac can enrich the electron density of Pd, thus enhancing its capability of H_2 dissociation. These results inspire us to investigate the effects of CeO_2 morphology on the metal-ceria interaction and their catalytic hydrogenation activity.

Table 6.1 The structure of three low index surfaces of ceria and their Ovac formation energy

Crystal plane	Structure illustration[222]	Coordination number[217]		Ovac formation energy[218] (eV)
		Ce	O	
(111) plane	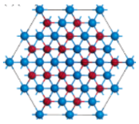	7	3	+3.30
(110) plane	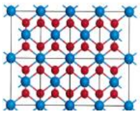	6	2	+2.69
(100) plane	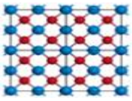	6	3	+2.97

In this chapter, a hydrothermal method was employed to fabricate CeO_2 supports with rod, cube and irregular morphologies, following with the wet impregnation of Ni salts to prepare the Ni/$CeO_{2-\delta}$ catalysts for MA hydrogenation. The detailed characterisation revealed that the morphology-dependent MA hydrogenation on the Ni/CeO_2 catalysts are due to their different surface Ovac density and the Ni-ceria interaction.

6.2 Experimental

6.2.1 Preparation of CeO_2 supports with different morphology

CeO_2 nanorods (CeO_2-NR), nanocubes (CeO_2-NC), and nanoparticles (CeO_2-NP) were prepared by a hydrothermal method as reported previously.[219] Typically, 1.96 g of $Ce(NO_3)_3·6H_2O$ was dissolved in 40 ml of deionised water, and 16.88 g of NaOH was dissolved in 30 mL of deionised water. Then, the NaOH solution was dropped into the $Ce(NO_3)_3$ solution under vigorous stirring at room temperature. The solution was stirred for 30 min at room temperature and then transferred the milky solution into a 100 mL Teflon bottle. The Teflon bottle was tightly sealed in a stainless-steel autoclave and heated at 180℃ for 24 h. After cooling down to ambient temperature, the obtained white precipitate was collected, washed with water and then dried at 80°C for 12 h. Then the acquired yellow powder was calcined in a muffle oven at 500°C for 3 h to fabricate CeO_2 cubes. The procedure for CeO_2 rods was the same as that for CeO_2 cubes except that the hydrothermal treatment temperature was 100°C. The CeO_2 nanoparticles was synthesised by the hydrothermal temperature at 100°C with the NaOH concentration of 0.1 M.

6.2.2 Preparation of $Ni/CeO_{2-\delta}$ catalysts

All three Ni/CeO_2 catalysts were prepared using a wet impregnation method. The Ni loading amount was 5 wt%. Typically, 0.505 g of $Ni(NO_3)_2 \cdot 6H_2O$ were dissolved in 10 ml deionized water, and then 2.00 g of CeO_2 and 0.348 g of CA (mole ratio of CA/Ni=1) were added into the mixed solution. The sample was continuously mixed using a magnetic stirrer whilst being heated on a hotplate at 80°C aiming to evaporate the solvent, then transferred to a convection oven and heated at 120°C for 8 h. The obtained dry gel was calcined at 500°C (heating ramp of 3 °C/min) for 3 h in a muffle oven. The sample was reduced at 350°C (heating ramp of 2 °C/min) with a flow of 10 vol% H_2/Ar for 3 h before MA hydrogenation. The catalysts related to their morphologies were denoted as $5Ni/CeO_{2-\delta}$-NP, $5Ni/CeO_{2-\delta}$-NR and $5Ni/CeO_{2-\delta}$-NC.

6.2.3 Catalyst characterisation and evaluation

The as-prepared $5Ni/CeO_{2-\delta}$ catalysts with different morphologies and their oxide precursors were characterised by XRD, TEM, H_2-TPR, XPS, Raman and H_2-TPD techniques. The detailed procedures for the characterisation were described in Chapter 2. The catalytic performance of $5Ni/CeO_{2-\delta}$ catalysts were evaluated at 180°C and 5 MPa hydrogen pressure in a batch reactor within 0.1 g catalyst, 4.9 g MA and 40 mL THF as a solvent, which was also detailed in Chapter 2.

6.3 Results and discussion

6.3.1 Morphology and structure of various CeO_2 supports

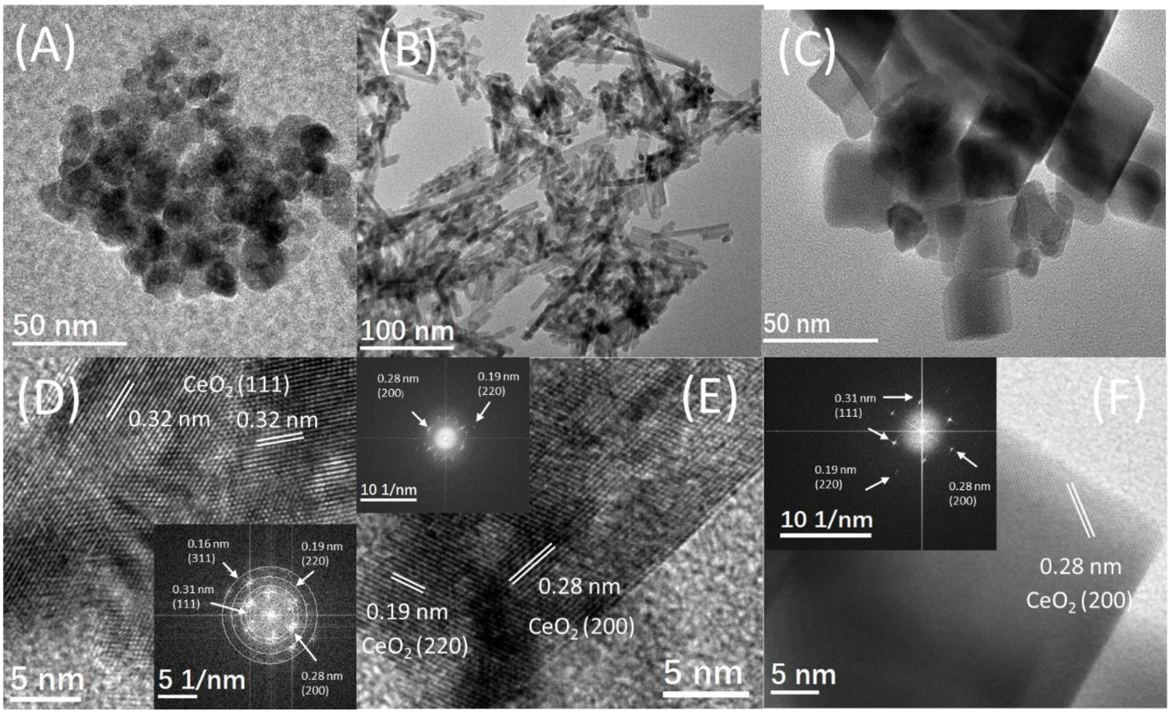
(A)
50 nm
(B)
100 nm
(C)
50 nm
(D)
CeO2 (111)
0.32 nm
0.32 nm
0.16 nm (311)
0.19 nm (220)
0.31 nm (111)
0.28 nm (200)
5 nm
5 1/nm
0.28 nm (200)
0.19 nm (220)
10 1/nm
(E)
0.19 nm
CeO2 (220)
0.28 nm
CeO2 (200)
5 nm
0.31 nm (111)
0.19 nm (220)
0.28 nm (200)
10 1/nm
(F)
0.28 nm
CeO2 (200)
5 nm

Figure 6.1 TEM, HRTEM and FT images of CeO_2-NP (A, D), CeO_2-NR (B, E) and CeO_2-NC (C, F) supports

Figure 6.1 presents TEM images of the CeO_2 supports synthesised using the hydrothermal method. The TEM image shown in Figure 6.1 (A) indicates the CeO_2-NP samples possess irregular shapes, with particle sizes of about 10-20 nm. Figure 6.1 (B) shows the CeO_2-NR particles are nanorods with uniform diameter of ~ 10 nm but varied length from 20 to 150 nm. As observed in the TEM image of the CeO_2-NC samples (Figure 6.1(C)), they possessed cubic morphologies with sharp edges and the particle sizes in the range from 10 to 50 nm. The respective BET surface areas of the CeO_2-NP, CeO_2-NR and CeO_2-NC are 60.3 m^2/g, 80.2 m^2/g and 15.4 m^2/g, as listed in Table 6.2. The results indicate that the specific surface areas of the CeO_2 samples are relevant to their morphologies.

These ceria samples with different morphologies were closely observed using HRTEM. Figure 6.1 (D) corresponds to the CeO_2-NP sample, which shows the (111) lattice fringe with an interplanar spacing of 0.32 nm, suggesting the nanoparticles of the CeO_2-NP sample are mainly enclosed by the (111) crystal planes. The rings presented in the Fast Fourier Transform (FFT) image (inset of Figure 6.1 (D)) of selected region are due to the multiple orientations of selected ceria crystallites. The rings corresponding to 0.32, 0.28, 0.20 and 0.16 nm are related to the (111), (200), (220) and (311) crystal planes of the face-centred CeO_2 structure. Although the CeO_2-NP shows various crystal planes in its FFT and HRTEM images, the (111) terminations are dominant as observed in the Figure 6.1 (D).

Figure 6.1 (E) shows the HRTEM image of CeO_2-NR sample, where the interplanar spacing of 0.19 and 0.28 nm on the typical ceria nanorod are due to (220) and (200) crystal planes. These results are well consistent with the previous results for the CeO_2-NR support with predominant exposures of the (220) and (200) crystallographic planes.[151] The FFT image inserted in Figure 6.1 (E) further reveals the (220) and (200) crystallographic planes are the predominant surfaces of the CeO_2-NR sample.

The CeO_2-NC sample displays smooth surfaces as shown in Figure 6.1 (F), due to very high crystallinity of the nanocube. The lattice fringes of 0.28 nm shown in the HRTEM image reveals the exposed surfaces of the CeO_2-NC are due to (200) crystallographic planes. The sharp and discrete spots corresponding to lattice spacing of 0.31 nm of the (111) plane, as shown in the FFT image, suggest that the (111) and (200) planes are preferentially exposed in the CeO_2-NC samples.

Table 6.2 Structure and physical parameters of various CeO_2 supports and $5Ni/CeO_{2-\delta}$ catalysts

Sample	Ni loading [a] (wt%)	S_{BET} [b] (m^2/g)	D (CeO_2) [c] (nm)	Microstrain (ε) [d] (%)		
				(111)	(200)	(220)
CeO_2-NP	-	60.3	12.8	0.98	0.67	0.58
CeO_2-NR	-	80.2	10.6	1.04	0.79	0.62
CeO_2-NC	-	20.4	24.5	0.43	0.29	0.26
$5Ni/CeO_{2-\delta}$-NP	5.2	56.6	11.8	1.19	0.77	0.68
$5Ni/CeO_{2-\delta}$-NR	4.7	78.7	11.2	1.24	0.89	0.72
$5Ni/CeO_{2-\delta}$-NC	4.8	18.6	26.8	0.53	0.39	0.28

Note: [a] The Ni loading was determined by ICP-OES. [b] The surface areas (S_{BET}) were measured by N_2 adsorption-desorption. [c] The crystallite size of CeO_2 was estimated by XRD using the Scherrer equation. [d] The microstrain of the CeO_2 supports was estimated using the equation: equation: $\varepsilon\ (\%) = \Delta d/d = \beta/4\tan\theta$.

.

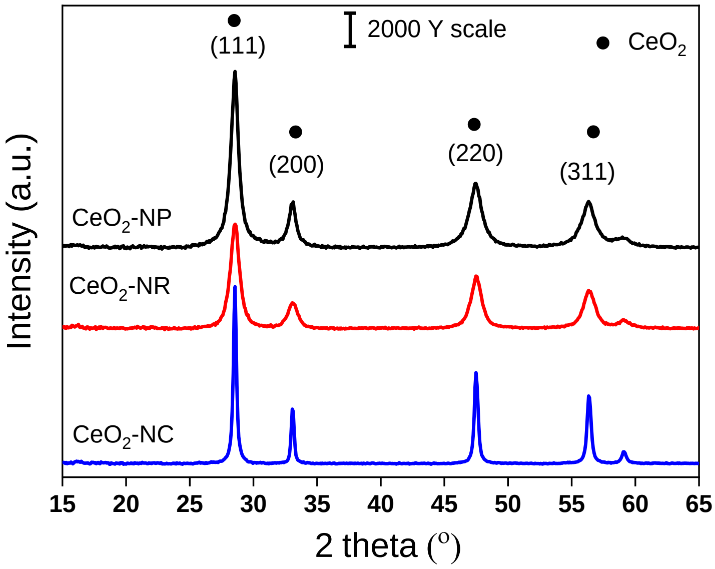

Figure 6.2 XRD patterns of various CeO_2 supports

Figure 6.2 presents the XRD patterns of the various ceria supports, where all the peaks are indexed to the face-cantered cubic fluorite structure of Fm-3m space group (JCPDS 34-0394). Among the three samples, CeO_2-NC shows the strongest and narrowest diffraction peaks, indicating that CeO_2-NC has highest crystallinity.[221] The mean crystallite size of CeO_2 supports calculated using the Scherrer equation to the (111) crystal surface is 24.6 nm for CeO_2-NC, much larger than those of 10.5 nm and 12.8 nm respective to the CeO_2-NR for CeO_2-NP samples.

Besides the crystallite size, the microstrain also contributes to broadening the diffraction peaks.[155] The microstrain can reflect the percentage of lattice atom displacement that arises from the lattice defects, including kinks, steps, dislocations and vacancies.[153] We calculated the microstrain of the CeO_2 samples from their broadening diffraction peaks using the pseudo-Voigt profile function.[155] As shown in Table 6.1, the CeO_2-NR possesses the greatest lattice strains in three major directions, while the CeO_2-NP and the CeO_2-NC have the medium and the least lattice strains, respectively. The data of the microstrain suggest that the defect density decreases in the sequence of CeO_2-NR > CeO_2-NP > CeO_2-NC.

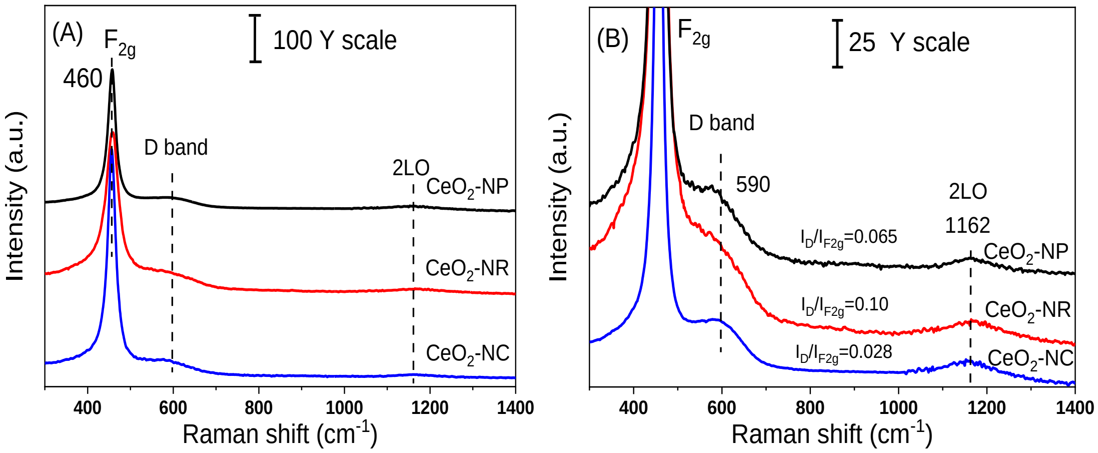

Figure 6.3 Raman spectra of (A) various CeO_2 support and (B) enlarged the corresponding Raman spectra

Figure 6.3 (A) presents the visible (λ_{ex}=532 nm) Raman spectra of the CeO_2 samples. The strongest Raman vibrations (F_{2g} mode) at 460 cm^{-1} of the three samples are due to the symmetrical stretching vibration of oxygen atoms around cerium ions.[223] The nanorods and nanoparticles give broader F_{2g}, which can be explained by the inhomogeneous strain broadening associated with particle size and by phonon confinement.[200] The conclusion is consistent with the XRD and TEM analyses where ceria nanorods and nanoparticles possessed smaller particle sizes than that of nanocubes.

The weak Raman band at 590 cm^{-1}, denoted as D band, is attributed to the Frenkel-type Ovac. As evidenced by neutron scattering studies, some oxygen anions located at tetrahedral sites can transfer to the octahedral sites, leaving vacancies in the tetrahedral sites and resulting in the formation of the Frenkel-type anion defects.[96] The Raman band at 1170 cm^{-1} is due to second-order longitudinal optical mode (2LO).

The ratio of I_D/I_{F2g} can be an indicator for the concentration of defect sites in ceria samples. As shown in Figure 6.3(A), the CeO_2-NR support has the largest ratio of I_D/I_{F2g}, 1.5 and 3.57 times those of CeO_2-NP and CeO_2-NC support, respectively. The result suggests that nanorods have the most abundant intrinsic Ovac, followed by nanoparticles and nanocubes, in good accordance with the XRD results.

6.3.2 Redox properties of the 5Ni/CeO$_{2-\delta}$ catalyst precursors

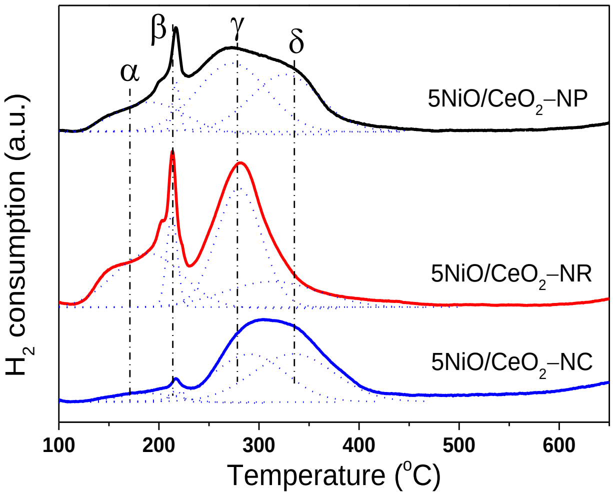

Figure 6.4 H$_2$-TPR profiles of 5NiO/CeO$_2$ precursors

H$_2$-TPR is a powerful tool to investigate the reducibility of catalysts, also sensitive to detect the nickel species and their interaction with support. As shown in Figure 6.4, a hydrogen consumption peak (denoted as peak α) at 160°C is related to the reduction of the reactive oxygen species adsorbed on the surface Ovac, such as peroxide and superoxide.[96] One can see that 5NiO/CeO$_{2-\delta}$-NR has the largest area of peak α, indicating that 5NiO/CeO$_{2-\delta}$-NR can offer the largest surface Ovac sites for oxygen species adsorption. In contrast, the smallest area of peak α suggests the lowest Ovac density in 5NiO/CeO$_{2-\delta}$-NC. The Ovac density in the 5NiO/CeO$_{2-\delta}$ catalysts decreases in the sequence of 5NiO/CeO$_{2-\delta}$-NR > 5NiO/CeO$_{2-\delta}$-NP > 5NiO/CeO$_{2-\delta}$-NC, which is consistent with the Raman results.

In Figure 6.4, there are notably steep and sharp peaks (denoted as peak β) at 210°C in the TPR profiles, reflecting rapid hydrogen consumptions around the temperature. The abrupt hydrogen consumption is related to H$_2$ dissociating and forming the OH group, which is driven by Ovac and/or interface sites between the local Ni and Ce moieties presented at the NiO/CeO$_2$ sample.[164] In addition, the intensity decreases of the β peaks on the NiO/CeO$_2$ samples are consistent with the decline order of their Ovac density, suggesting that the paramount role of Ovac in hydrogen activation.

The reduction peaks at the high temperature region (> 250°C) are assigned to the reduction of surface NiO species. In principle, NiO can be directly reduced to metallic Ni^0 species without intermediate oxide.[151] The peaks at 270°C (γ peaks) are due to the reduction of highly dispersed NiO species on the surface with strong Ni-CeO$_2$ interaction, while the peaks at 350°C (δ peaks) is assigned to the reduction of bulk NiO species.[160] Additionally, the CeO_2 support can improve NiO reduction at low temperature due to the electronic factor of the strong metal-support interaction.[199] In the TPR profile of the $5NiO/CeO_{2-\delta}$-NR catalyst, there are a major hydrogen consumption at 270°C with a small hump at 350°C, indicating that most of the NiO species is highly dispersed on the CeO_2-NR surface with small portion of isolated NiO particle. In contrast, the γ and δ peaks in the $5NiO/CeO_{2-\delta}$-NP and $5NiO/CeO_{2-\delta}$-NC are comparable, suggesting that the amount of aggregated NiO species is comparable to those highly dispersed NiO species on the CeO_2-NP and CeO_2-NC surface. Combined with the results of BET, Raman and XRD measurements, one can deduce that the CeO_2 nanorod support possesses abundant Ovac and large surface area which facilitates to enhance NiO dispersion, consequently reducing the size of Ni nanoparticles.[131]

6.3.3 Structure and morphology of $5Ni/CeO_{2-\delta}$ catalysts

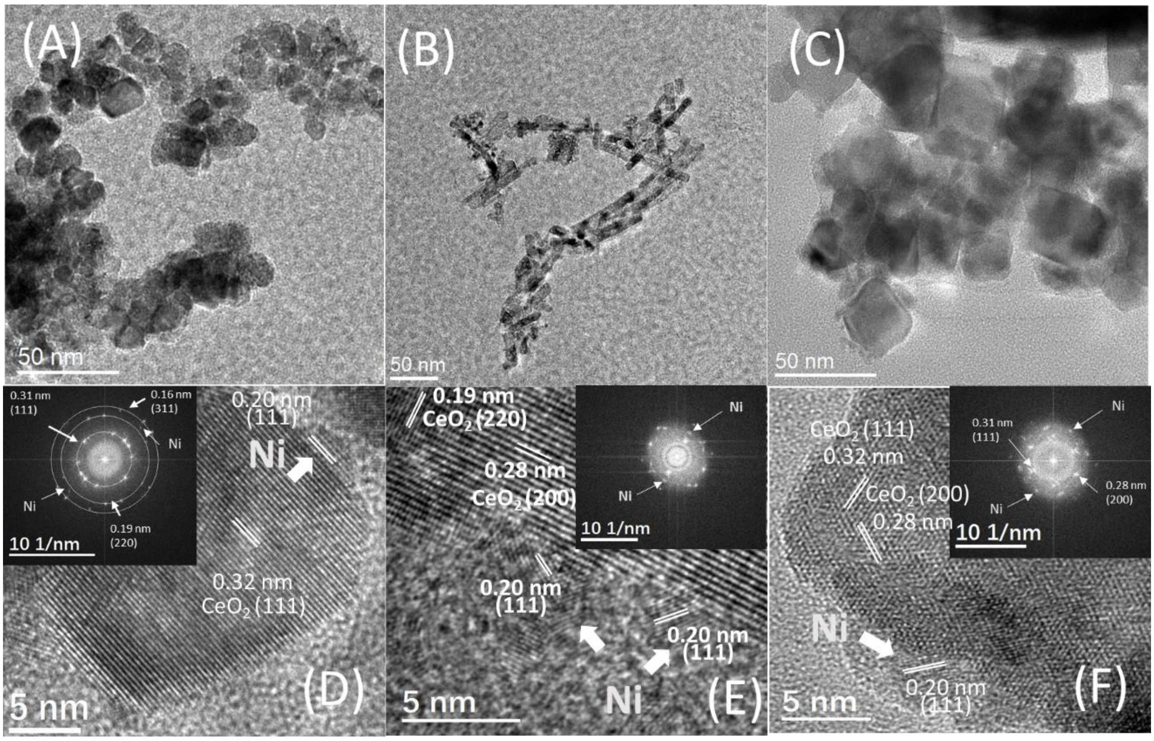
(A)
50 nm
(B)
50 nm
(C)
50 nm
0.31 nm (111)
0.16 nm (311)
Ni
Ni
0.19 nm (220)
10 1/nm
0.20 nm (111)
Ni
0.32 nm CeO₂ (111)
5 nm
(D)
0.19 nm CeO₂ (220)
0.28 nm CeO₂ (200)
Ni
Ni
10 1/nm
0.20 nm (111)
0.20 nm (111)
Ni
5 nm
(E)
CeO₂ (111) 0.32 nm
CeO₂ (200) 0.28 nm
Ni
0.31 nm (111)
0.28 nm (200)
Ni
10 1/nm
Ni
0.20 nm (111)
5 nm
(F)

Figure 6.5 TEM, HRTEM and FT images of (A, D) $5Ni/CeO_{2-\delta}$-NP, (B, E) $5Ni/CeO_{2-\delta}$-NR and (C, F) $5Ni/CeO_{2-\delta}$-NC supports

The morphologies of $5Ni/CeO_{2-\delta}$ catalysts were characterised by TEM. As shown in Figure 6.5 (A), (B) and (C), the $5Ni/CeO_{2-\delta}$-NP, $5Ni/CeO_{2-\delta}$-NR and $5Ni/CeO_{2-\delta}$-NC remain the original shapes of their corresponding supports, indicating Ni deposition and catalyst preparation, including impregnation, calcination and reduction did not change the morphologies of supports. Figure 6.5 (D) shows a representative HRTEM image of $5Ni/CeO_{2-\delta}$-NP catalyst, in which the lattice fringes of 0.32 nm spacing are due to the (111) planes of ceria. The interplanar spacing of 0.20 nm for a hemispheric nanoparticle (diameter of ca. 3 nm), which anchored at the (111) plane of the $CeO_{2-\delta}$–NP support, is related to the (111) crystal plane of metallic Ni nanoparticle. Furthermore, in the inserted FFT image, the spots at 0.20 nm correspond to (111) planes of the Ni nanoparticle, confirming the analysis of HRTEM.

Figure 6.5 (E) shows a representative image of the 5Ni/$CeO_{2-\delta}$-NR catalysts, where the lattice fringes at 0.19 nm and 0.28 nm are ascribed to the (220) and (200) plane of CeO_2. The lattice fringe with 0.20 nm spacing is due to the (111) plane of metallic Ni nanoparticles, which corresponds to the spots at 0.20 nm in the FFT image. The Ni particle is of round shape with the diameter of ~3 nm.

In Figure 6.5 (F), the lattice fringes with spacing of 0.31 nm and 0.28 nm are attributed to the (111) and (200) planes of $CeO_{2-\delta}$, respectively. The nickel particles anchored on the support show the lattice fringe spacing of 0.2 nm, due to the (111) plane of metallic Ni species. The diameter of the Ni particle on the $CeO_{2-\delta}$-NC is ~5 nm, larger than the sizes of Ni particles on the $CeO_{2-\delta}$-NR and $CeO_{2-\delta}$-NP supports. The dependence of Ni particle sizes on the $CeO_{2-\delta}$ morphology is likely due to their different surface area and metal-support interaction. It is reasonable the smallest surface area of $CeO_{2-\delta}$-NC leads to low dispersion of Ni particle and largest particle sizes. However, there is large difference in specific surface areas for the $CeO_{2-\delta}$-NR and $CeO_{2-\delta}$-NP samples, while their Ni particle sizes are similar. The discrepancy in particle size should be related to the different metal-support interaction because their exposed surfaces are terminated with distinct atom configurations.

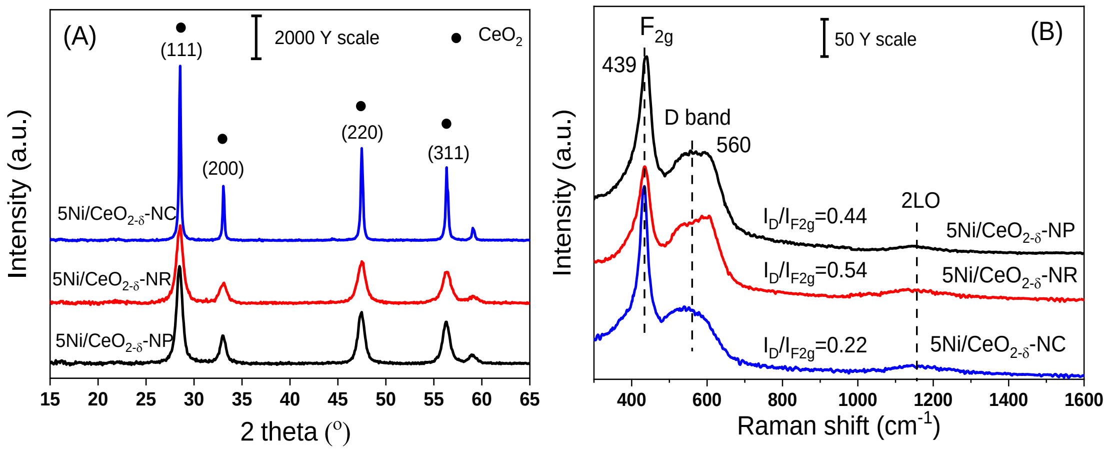

Figure 6.6 (A) XRD patterns and (B) Raman spectra of various 5Ni/$CeO_{2-\delta}$ catalysts

Figure 6.6 (A) shows the XRD patterns of 5Ni/$CeO_{2-\delta}$ catalysts. After Ni loading, the characteristic peaks of CeO_2 are clearly observed in Figure 6.6 (A), indicating that CeO_2 supports remain the face-centred cubic structure. However, the diffraction peak due to metallic Ni phase is absent in Figure 6.6 (A), due to high dispersion of Ni with a small particle size.[79] The crystallite sizes of CeO_2 supports in the 5Ni/$CeO_{2-\delta}$ catalysts are slightly larger than those of the pure ceria supports (Table 6.2) due to the sintering of ceria support caused by calcination and subsequent reduction during the preparation procedures. Furthermore, the microstrain of 5Ni/$CeO_{2-\delta}$ catalysts is estimated and presented in Table 6.2. 5Ni/$CeO_{2-\delta}$ catalysts have larger microstrain than their corresponding supports, suggesting that Ni incorporation or the reduction process enhances the defect formation. For the 5Ni/$CeO_{2-\delta}$ catalysts, the data of the microstrain suggest that the defect density decreases in the sequence of 5Ni/$CeO_{2-\delta}$-NR > 5Ni/$CeO_{2-\delta}$-NP > 5Ni/$CeO_{2-\delta}$-NC.

To investigate the surface structure of the 5Ni/$CeO_{2-\delta}$ catalysts, Raman scattering was conducted for three catalysts and the obtained results are shown in Figure 6.6 (B). Compared with the Raman spectra of 5NiO/CeO_2 in Figure 6.3, the F_{2g} modes of the 5Ni/$CeO_{2-\delta}$ catalysts shift from 460 to 439 cm^{-1} and become weaker and broader, indicating that the loading of Ni leads to the decrease of symmetry of the Ce-O bonds in CeO_2. In addition, the D bands appear broader, higher and red shifted from 590 to 560 cm^{-1}, which are caused by the formation of reduction-induced Ovac and the transformation of Ce^{4+} to Ce^{3+}.[96] The comparison of the relative Ovac density, estimated from the Raman ratios of I_D/I_{F2g} for the 5Ni/$CeO_{2-\delta}$ catalysts, reveals that 5Ni/$CeO_{2-\delta}$-NR catalyst possesses the largest Ovac density while the 5Ni/$CeO_{2-\delta}$-NC catalyst has the least, which is consistent with XRD results.

6.3.4 Surface element analysis

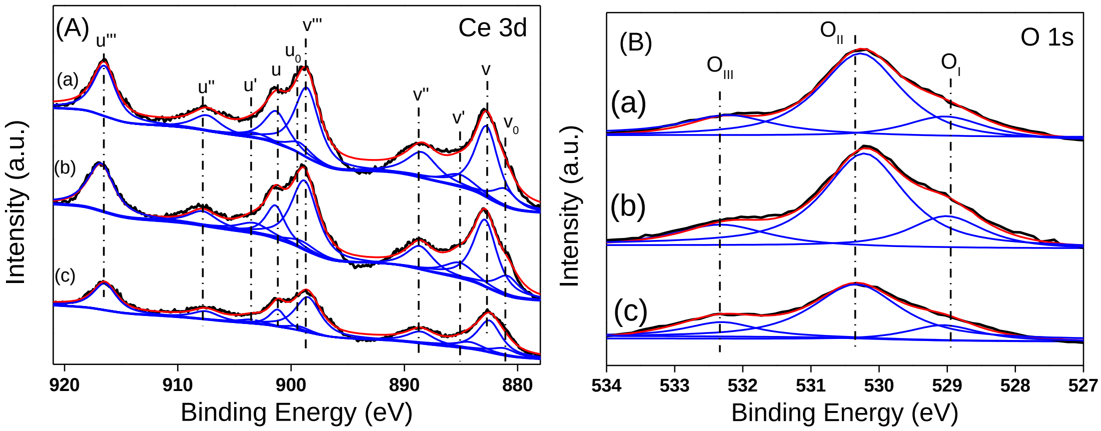

Figure 6.7 XPS spectra of (A) Ce3d and (B) O1s for reduced 5Ni/$CeO_{2-\delta}$ catalysts (a) 5Ni/$CeO_{2-\delta}$-NP, (b) 5Ni/$CeO_{2-\delta}$-NR and (c) 5Ni/$CeO_{2-\delta}$-NC

XPS is a powerful tool to investigate the chemical state and surface species in the 5Ni/$CeO_{2-\delta}$ catalysts. Figure 6.7 (A) shows the Ce3d core-level XPS spectra of 5Ni/$CeO_{2-\delta}$ catalysts. The complex Ce3d XPS spectra were fitted to ten components and denoted following the deconvolution performed by Burroughs et al.[185] In detail, three pairs of u‴ (v‴), u″(v″) and u(v) peaks are characteristic of Ce^{4+}, while the rest two pairs of u′(v′) and $u_0(v_0)$ are assigned to Ce^{3+} ions. The results confirm the coexistence of Ce^{3+} and Ce^{4+} cations on the surface of 5Ni/$CeO_{2-\delta}$ catalysts. The relative amount of Ce^{3+} is estimated according to the peak areas of Ce^{4+} and Ce^{3+}, and the results are listed in Table 6.3. One can see that the concentration of surface Ce^{3+} of the 5Ni/$CeO_{2-\delta}$ catalysts decreases in the sequence of 5Ni/$CeO_{2-\delta}$-NR > 5Ni/$CeO_{2-\delta}$-NP > 5Ni/$CeO_{2-\delta}$-NC.

In principle, the Ce^{3+} ions are induced by the formation of Ovac via the transformation: $4Ce^{4+} + O^{2-} \rightarrow 2Ce^{4+} + 2Ce^{3+} + Ovac + 0.5O_2$.[224] Therefore, one can calculate the Ovac density of Ni/$CeO_{2-\delta}$ catalysts, decreasing in the order: 5Ni/$CeO_{2-\delta}$-NR > 5Ni/$CeO_{2-\delta}$-NP > 5Ni/$CeO_{2-\delta}$-NC, which is in good consistence with the Raman results. It is notable that the two doublets, u‴ (v‴) and u(v) related to Ce^{4+} ions of 5Ni/$CeO_{2-\delta}$-NR and 5Ni/$CeO_{2-\delta}$-NP are slightly blue-shifted in comparison with that of 5Ni/$CeO_{2-\delta}$-NC catalyst, which is likely due to the electronic perturbation of anionic Ovac on Ce^{4+}.

The changes in the oxidation of Ce correlate well with the relative intensity of different lattice oxygen species at the surface and/or subsurface. As shown in Figure 6.7 (B), there are three states of surface oxygen species for the 5Ni/$CeO_{2-\delta}$ catalysts. The bands at 528.9 eV and 530.4 eV, labelled as O_I and O_{II}, are attributed to the lattice oxygen species bonded with Ce^{3+} and Ce^{4+} ions, respectively.[99] The BE band at 532.4 eV, denoted as O_{III}, is related to the surface chemisorbed oxygen species (hydroxyl group, adsorbed water, etc.). As presented in Table 6.3, the ratio of $O_I/(O_I+O_{II}+ O_{III})$ decreases in the sequence 5Ni/$CeO_{2-\delta}$-NR > 5Ni/$CeO_{2-\delta}$-NP > 5Ni/$CeO_{2-\delta}$-NC, in agreement with the XPS ratio of $Ce^{3+}/(Ce^{4+}+Ce^{3+})$. This result confirms that the 5Ni/$CeO_{2-\delta}$-NR possesses the largest concentration of Ce^{3+} and Ovac among the three catalysts. Moreover, the 5Ni/$CeO_{2-\delta}$-NR catalyst displays the highest ratio of $O_{III}/(O_I+O_{II}+ O_{III})$, indicative of the largest amount of adsorbed oxygen species on the surface. It was reported that Ovac can act as the active sites to trap the oxygen species.[99] Therefore, from the obtained ratio of $O_{III}/(O_I+O_{II}+ O_{III})$, one can conclude that 5Ni/$CeO_{2-\delta}$-NR catalyst possesses the highest amount of Ovac while 5Ni/$CeO_{2-\delta}$-NC catalyst has the smallest Ovac density. The O_{II} peaks of 5Ni/$CeO_{2-\delta}$-NR and 5Ni/$CeO_{2-\delta}$-NP catalysts slightly shift to lower BE, indicating Ovac with excess electrons can enrich the electron density of oxygen species as bond to Ce^{4+}. Combined with the shift of XPS peaks related to Ce^{4+}, it is reasonable to deduce that anionic Ovac can modify the electronic structure of the catalysts.

Table 6.3 Quantitative XPS analysis of the $5Ni/CeO_{2-\delta}$ catalysts

Sample	$Ce^{3+}/(Ce^{4+}+Ce^{3+})$ [%]	$O_I/(O_I+O_{II}+ O_{III})$ [%]	$O_{III}/(O_I+O_{II}+ O_{III})$ [%]
$5Ni/CeO_{2-\delta}$-NP	15.5	18.6	13.5
$5Ni/CeO_{2-\delta}$-NR	18.7	30.5	25.4
$5Ni/CeO_{2-\delta}$-NC	14.6	12.3	9.4

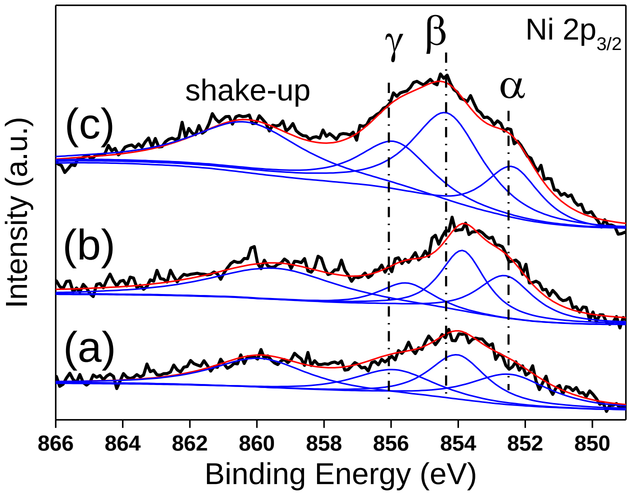

Figure 6.8 $Ni2p_{3/2}$ XPS spectra of reduced $5Ni/CeO_{2-\delta}$ catalysts (a) $5Ni/CeO_{2-\delta}$-NP, (b) $5Ni/CeO_{2-\delta}$-NR and (c) $5Ni/CeO_{2-\delta}$-NC

Figure 6.8 shows the $Ni2p_{3/2}$ XPS spectra of reduced $5Ni/CeO_{2-\delta}$ catalysts. Besides the shake-up peaks of $Ni2p_{3/2}$ state at 861.0 eV, the major $Ni2p_{3/2}$ XPS spectra of the $5Ni/CeO_{2-\delta}$ catalysts were fitted into three peaks (denoted as peak α, β and γ , respectively). The α peak at ~852.8 eV is assigned to metallic Ni^0 species, while the β peak at ~ 854.1 eV and the peak γ at ~856.5 eV are attributed to ionic Ni^{2+} and Ni^{3+}.[203] The Ni^{3+} species are considered to originate from Ni atoms penetrating into the subsurface of the $CeO_{2-\delta}$ support to form a thin layer of $Ni_xCe_{1-x}O_{2-y}$ solid solution.[161] With regard to the ionic Ni^{2+} species, it cannot be excluded that the Ni^{2+} species would come from the re-oxidation of metallic nickel phase during the catalyst characterisation. However, the metallic Ni^0 species can be oxidised to Ni^{2+} species by the adjacent Ce^{4+} due to the strong electronic attraction of Ce^{4+} towards Ni species.[106, 134] Moreover, as shown in Figure 6.8, the red shift of β and γ peaks of the $5Ni/CeO_{2-\delta}$-NP and $5Ni/CeO_{2-\delta}$-NR is notable in comparison to those of $5Ni/CeO_{2-\delta}$-NC. The red-shifts suggest the increased electronic density of ionic Ni resided on the $CeO_{2-\delta}$-NR and $CeO_{2-\delta}$-NP supports, which is caused by the strong interaction between Ni species and anionic Ovac.[206]

6.3.5 Hydrogen activation over 5Ni/$CeO_{2-\delta}$ catalysts

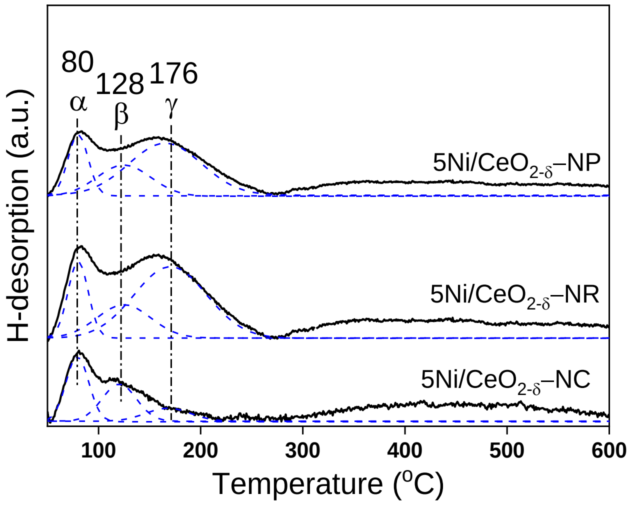

Figure 6.9 H_2-TPD profiles of 5Ni/$CeO_{2-\delta}$ catalysts

Figure 6.10 shows the H_2-TPD profiles of 5Ni/$CeO_{2-\delta}$ catalysts. As justified in the previous chapters, the α peak at 80°C can be assigned to the weak adsorption of hydrogen at surface Ovac of the $CeO_{2-\delta}$. The β and γ peaks at 128°C and 176°C are due to hydrogen uptake at different nickel species. The β peak is related to dissociative hydrogen species desorbed from the nickel species of strong interaction with $CeO_{2-\delta}$ support[189], while the γ peak is due to hydrogen desorption from the bulk nickel species. The broad peak observed at the temperature beyond 300°C is assigned to the H_2 adsorbed in the subsurface layers of Ni atoms and/or to the spillover H species anchoring at the $CeO_{2-\delta}$ surface.[225] The H_2-TPD profiles reveal the different Ni species resident on the surface of 5Ni/$CeO_{2-\delta}$ catalysts and the H_2 uptakes closely relate to the morphology of $CeO_{2-\delta}$ supports.

The H_2 desorption peaks correspond to different species that can adsorb and activate hydrogen, so their integration areas may reflect the concentration and distribution of various active species. Table 6.4 lists the amount of H_2 uptake at individual active sites of the 5Ni/$CeO_{2-\delta}$ catalysts. One can see that the 5Ni/$CeO_{2-\delta}$-NR catalyst possesses the largest uptake of H_α, likely due to its largest surface area that can provide the most active sites for weak adsorption of hydrogen molecule. The 5Ni/$CeO_{2-\delta}$-NR catalyst also possesses the greatest H_β and H_γ uptakes in the three catalysts, suggesting the largest amount of active nickel species exposes on the 5Ni/$CeO_{2-\delta}$-NR catalyst. The nickel dispersion, calculated from the total uptake of H_β and H_γ and shown in Table 6.4, declines in the order of $5Ni/CeO_{2-\delta}$-NR > $5Ni/CeO_{2-\delta}$-NP > $5Ni/CeO_{2-\delta}$-NC. This result agrees with the previous studies that rod-like $CeO_{2-\delta}$ support can enhance Ni dispersion due to the large surface area and abundant surface defects.[151, 224]

Table 6.4 H_2 uptake and metal dispersion of the $5Ni/CeO_{2-\delta}$ catalysts

Sample	H_α (μmol/g)	H_β (μmol/g)	H_γ (μmol/g)	Ni dispersion (%)
$5Ni/CeO_{2-\delta}$-NP	29.8	29.7	84.5	25.7
$5Ni/CeO_{2-\delta}$-NR	48.8	56.3	208.0	66.1
$5Ni/CeO_{2-\delta}$-NC	21.7	30.6	13.5	10.9

Note: H_α, H_β and H_γ represent the amount of adsorbed hydrogen on different active sites, which were estimated based on the areas of α, β and γ peaks, respectively. Ni dispersion was calculated based on the hydrogen uptake at Ni species using the Equation 2.5 in Chapter *2*.

6.3.6 Catalytic performance

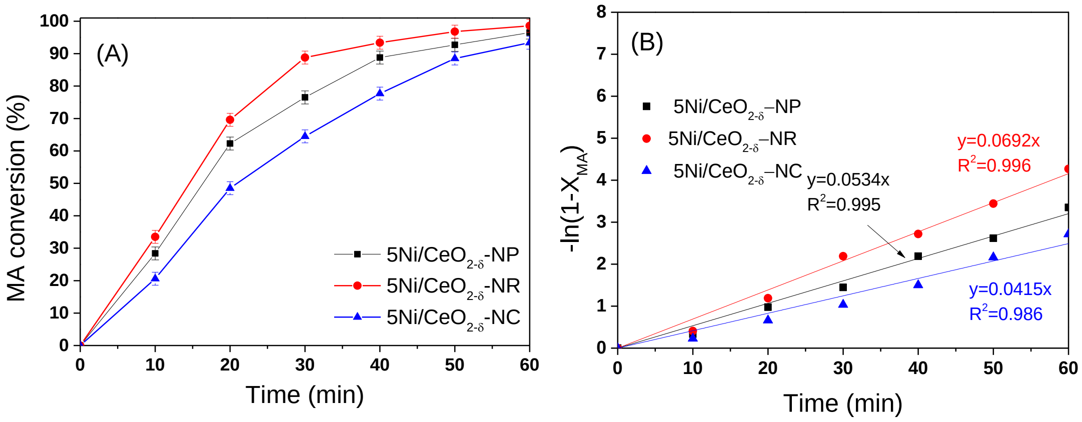

Figure 6.10 MA conversion over $5Ni/CeO_{2-\delta}$ catalysts at 180°C and under 5 MPa of hydrogen pressure

Figure 6.10 (A) presents MA conversion (X_{MA}) along the hydrogenation courses on $5Ni/CeO_{2-\delta}$ catalysts in a batch reactor at 180°C and under 5.0 MPa of hydrogen pressure. All the three catalysts displayed different activity of MA conversion (X_{MA}) in the 1 h continuous MA hydrogenation, although they showed 100% selectivity of SA. $5Ni/CeO_{2-\delta}$-NR showed the highest activity of MA conversion, followed by $5Ni/CeO_{2-\delta}$-NP and $5Ni/CeO_{2-\delta}$-NC showed the lowest activity. The MA hydrogenation activity on the catalysts was fitted according to the first order law in terms of MA conversion, as presented in Figure 6.11(B). The linear curves of the $-\ln(1-X_{MA})$ versus time indicate that the MA hydrogenation on the 5Ni/$CeO_{2-\delta}$ catalysts follows the pseudo-first order reaction with respect to the MA conversion, which is in line with the finding in Chapter 4. According to the slope of the linear plots, the rate constants (k) of MA hydrogenation over the three catalysts were estimated and followed the trend of 5Ni/$CeO_{2-\delta}$-NR > 5Ni/$CeO_{2-\delta}$-NP > 5Ni/$CeO_{2-\delta}$-NC. The results confirm that the 5Ni/$CeO_{2-\delta}$-NR catalyst possesses superior activity to other two catalysts in MA hydrogenation.

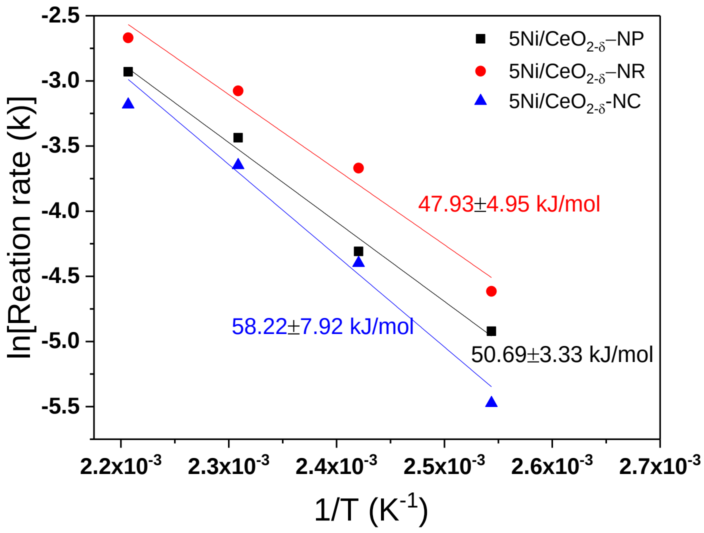

Figure 6.11 Arrhenius plots of ln (k) versus 1/T for MA conversion over different shaped 5Ni/$CeO_{2-\delta}$ catalysts.

For in-depth understanding of MA hydrogenation over different shaped 5Ni/$CeO_{2-\delta}$ catalysts, we examined the MA hydrogenation over the three catalysts at different temperatures in order to acquire their apparent activation energies (E_a). The E_a can be calculated using the Arrhenius equation, $\ln k=(-E_a/RT)+\ln A$, where k, E_a, R, T and A stand for the rate constant, the activation energy, the reaction temperature in Kelvin scale, the universal gas constant (~8.314 J/mol·K) and the pre-exponential factor, respectively. As shown in Figure 6.11, the calculated E_a values for the C=C hydrogenation on the 5Ni/$CeO_{2-\delta}$-NR, 5Ni/$CeO_{2-\delta}$-NP and 5Ni/$CeO_{2-\delta}$-NC are 47.93±4.95, 50.69±3.33 and 58.22±7.92 kJ/mol, respectively. The support-dependent E_a further suggests the $CeO_{2-\delta}$ morphology is a crucial factor in affecting the Ni catalyst performance for C=C hydrogenation. The smallest E_a of the 5Ni/$CeO_{2-\delta}$-NR catalyst suggests the rod-like $CeO_{2-\delta}$ supported Ni catalyst can reduce the energy barrier of C=C hydrogenation, thus giving rise to high activity in MA hydrogenation to SA.

Compared with the E_a of MA hydrogenation over 5Ni/TiO_2 catalyst (E_a = 61.7 kJ/mol)[82], the smaller value of E_a for 5Ni/$CeO_{2-\delta}$ catalysts suggests CeO_2 support can enhance MA hydrogenation on the Ni species regardless of morphology effect. Furthermore, the Ea value of $5Ni/CeO_{2-\delta}$-NR are much smaller than that previously observed for the heterogeneous hydrogenation of the C=C bonds of the α,β-unsaturated compounds.[226, 227] For example, Yang and co-workers reported that the activation barrier for C=C hydrogenation on the bimetallic Pd-Au/SiO_2 catalyst was 57 kJ/mol.[227] Zaramello et al. reported that the E_a of C=C hydrogenation on the Ni nanoparticles deposited on SiO_2 and stabilised by octanoic acid was 76.5 kJ/mol.[226] Compared with the reported results, it is expected that $Ni/CeO_{2-\delta}$ nanorod catalyst has huge potential for C=C hydrogenation in various unsaturated molecules.

For MA hydrogenation on the metallic catalysts, H_2 dissociation and MA adsorption occur at the same active sties (usually at metal surface),[88-90] so that the large amount of active sites is desired for MA hydrogenation, which facilitates to eliminate the competitive adsorption between MA and H_2. Besides the amount of active sites in the MA hydrogenation, the hydrogen dissociation and diffusion play crucial roles because they determine the kinetic accessibility of atomic H to the adsorbed C=C bond.[209] In the present study, $5Ni/CeO_{2-\delta}$-NR possesses higher Ni dispersion that can provide more active sites for H_2 and MA activation in comparison with $5Ni/CeO_{2-\delta}$-NP and $5Ni/CeO_{2-\delta}$-NC. Moreover, the $5Ni/CeO_{2-\delta}$-NR catalyst possesses the highest capability in hydrogen activation as shown in the H_2-TPR and H_2-TPD results, which contributes to the remarkable performance in C=C hydrogenation.

Besides the geometric effect of $5Ni/CeO_{2-\delta}$ catalysts on MA hydrogenation, the electronic structure of the active sites determine not only the adsorption and activation of MA and H_2 but also the rates for formation of the maleic anhydryl intermediate[88, 89], which is regarded as the rate-limiting step in MA hydrogenation. The previous theoretical investigation (DFT simulation) suggested that the increased electron density of metal species favours to reduce the formation energy and the binding energy of maleic anhydryl intermediates on the metal surfaces, which promote their desorption from the metal surface. In this study, the Raman and XPS characterisation evidenced that the $5Ni/CeO_{2-\delta}$-NR catalyst possesses the highest surface Ovac and Ce^{3+} amount that would enrich the electron density of the supported Ni^0 species. The enhanced electronic density on Ni^0 can promote the formation of maleic anhydryl intermediate and reduce the energy barrier of MA hydrogenation[88, 89, 209], so that higher activity of MA hydrogenation was observed on the $5Ni/CeO_{2-\delta}$-NR catalyst.

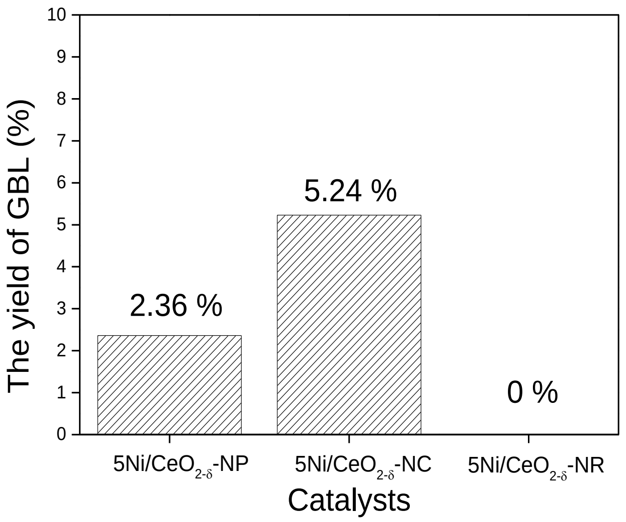

Figure 6.12 Yields of GBL over the 5Ni/$CeO_{2-\delta}$ catalysts in the 8 h MA hydrogenation at 210°C and 5 MPa hydrogen pressure

The selectivity of 5Ni/$CeO_{2-\delta}$ catalysts towards C=C and C=O hydrogenation was evaluated by monitoring GBL yields in the prolonged MA hydrogenation process for 8 h. The obtained results are presented in Figure 6.12, where the GBL yields of 5.24%, 2.36% and 0% are observed for the 5Ni/$CeO_{2-\delta}$-NC, 5Ni/$CeO_{2-\delta}$-NP and 5Ni/$CeO_{2-\delta}$-NR catalysts, respectively. The results of GBL yields and the MA→SA transformation reveal that the 5Ni/$CeO_{2-\delta}$-NR catalyst is a robust catalyst for MA hydrogenation to SA with 100% selectivity. Irrespective of morphology of $CeO_{2-\delta}$ supports, the notably low GBL yields over the 5Ni/$CeO_{2-\delta}$ catalysts are consistent with the result reported in previous research where the Ni/$CeO_{2-\delta}$ catalyst containing 5 wt% Ni is not a robust catalyst for GBL production. Moreover, the 5Ni/$CeO_{2-\delta}$-NR catalyst with the highest Ovac density is inert for GBL production, though the 5Ni/$CeO_{2-\delta}$-NP and 5Ni/$CeO_{2-\delta}$-NC catalyst with lower Ovac density are less active for GBL generation. The results suggest that Ovac is not an active centre for C=O hydrogenolysis and even block C=O hydrogenolysis at suitable amount. The inertia of Ovac in C=O hydrogenolysis can be attributed to the repulsive interaction between the anionic Ovac and the electron-rich C=O group, which inhibits C=O adsorption and activation on the surface of catalysts.

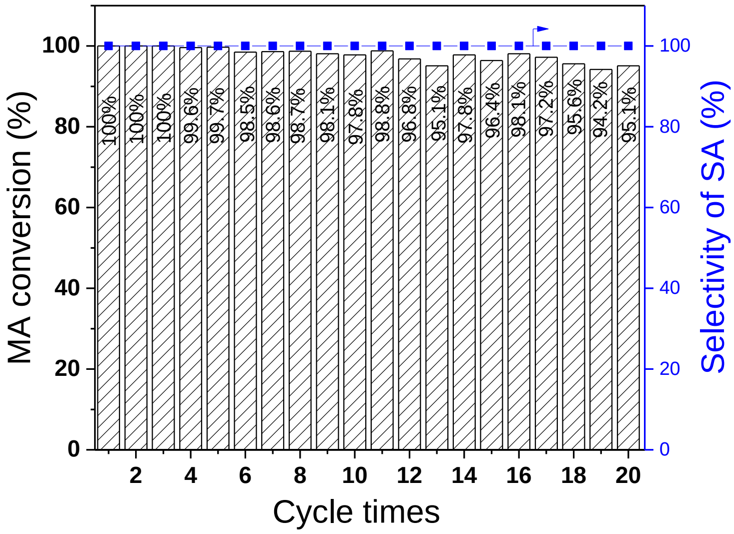

Figure 6.13 Stability of $5Ni/CeO_{2-\delta}$-NR catalyst in MA hydrogenation at 180°C and 5 MPa of H_2 for 1 h. Reaction condition: 4.9 g MA, 40 ml THF and 0.5 g catalyst.

The stability of $5Ni/CeO_{2-\delta}$-NR catalyst in MA hydrogenation was investigated by cycling MA hydrogenation for 20 times on the 0.5 g $5Ni/CeO_{2-\delta}$-NR catalyst. The mass of the post-catalyst was of 0.42 g after 20 cycling tests, with total catalyst loss of 0.08 g that was caused by the multiple centrifugations for recycling the catalyst. Although up to 16 wt% mass loss of the catalyst after 20 cycles, the MA conversion on $5Ni/CeO_{2-\delta}$-NR catalyst only slightly decreases from 100% to 95% and the SA selectivity remained 100% in the 20 cycles (Figure 6.13). We suppose it was the catalyst loss caused the decline of MA conversion because the catalyst mass composition remained, however, we cannot rule out the catalyst deactivation by coking. The result suggests that $5Ni/CeO_{2-\delta}$-NR catalyst is highly selective (100% SA selectivity) and stable, showing great potential for long-term highly selective MA hydrogenation.

The structure and morphology of the used $5Ni/CeO_{2-\delta}$-NR catalyst were characterised by the TEM, XRD and Raman techniques. Before the characterisations, the used catalyst was subject to calcination at 500°C in a N_2 flow to remove the adsorbed organic species on the surface of catalyst. As shown in Figure 6.14 (A), though the nanorod morphology of the $5Ni/CeO_{2-\delta}$-NR catalyst was not damaged, the edges of nanorod became uneven and rougher. Additionally, the HRTEM image of the used catalyst shows clear lattice fringes with spacing of 0.31 nm, which are due to the (111) planes of $CeO_{2-\delta}$, suggesting the (111) surface is the predominantly exposed crystal surface of ceria in the used $5Ni/CeO_{2-\delta}$-NR catalyst. It is worth noting that no (220) planes of $CeO_{2-\delta}$ can be observed in the HRTEM images. Additionally, the diffraction spots corresponding to the (111) and (200) planes are seen at 0.31 and 0.28 nm, while the diffraction spots related to (220) planes are not detected. We suppose that the (220) plane might have transformed into the (111) plane during the hydrogenation reaction because the (111) plane is energetically more stable than the (220) plane.[228] The crystal surface transformation is a result of structure reconstruction, consequently leading to rougher edges of the $CeO_{2-\delta}$ nanorods.

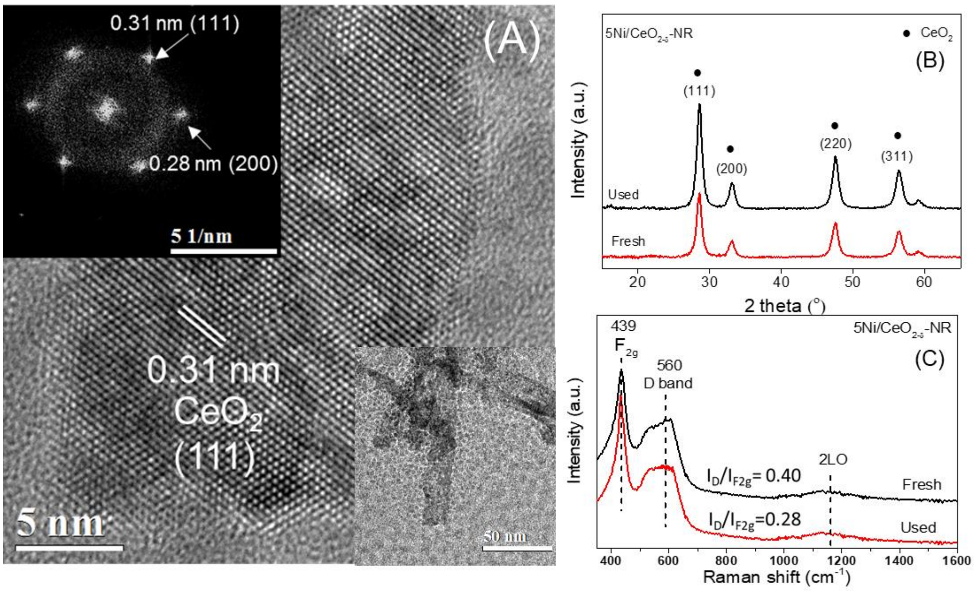

Figure 6.14 (A) TEM and HRTEM images, (B) XRD patterns and (C) Raman spectra of $5Ni/CeO_{2-\delta}$-NR catalyst

As shown in Figure.6.14 (B), the used $5Ni/CeO_{2-\delta}$-NR catalyst displays sharper and stronger XRD diffraction peaks than the fresh catalyst due to the growth of the crystallite size or the increased crystallinity of the $CeO_{2-\delta}$-NR in the used catalyst. Figure 6.14 (C) compares the Raman spectra and the relative Raman ratios of I_D/I_{F2g} for the fresh and used $5Ni/CeO_{2-\delta}$-NR catalysts, the results, in particular the relative ratios, reveal the Ovac density of the used catalyst slightly decreased in comparison with that of the fresh catalyst. The discrepancies between the used and fresh $5Ni/CeO_{2-\delta}$-NR catalysts suggest that the morphology of the $CeO_{2-\delta}$-NR support was changed, which is likely resulting from the thermal treatment of the catalyst during the hydrogenation process. As determined by ICP-OES, the Ni loading of the post-catalyst remained 4.6 wt%, comparable to that of fresh catalyst, indicating that no Ni loss in the stability tests and the catalyst is very stable in the hydrogenation process.

6.4 Conclusion

The hydrothermal syntheses in aqueous solutions with different NaOH concentrations were adopted successfully to prepare CeO_2 materials in different morphologies of irregular nanoparticles (NP), nanorods (NR) and nanocubes (NC). Their derived 5Ni/$CeO_{2-\delta}$ catalysts with 5 wt% Ni loading exhibited morphology-dependent catalytic activities in the liquid phase MA hydrogenation. Among the three 5Ni/$CeO_{2-\delta}$ catalysts, the 5Ni/CeO_2-NR sample displayed the highest MA→SA activity and 100% SA selectivity in the long-term MA hydrogenation cycling tests, showing the great potential of the catalysts for practical application. In contrast, the 5Ni/$CeO_{2-\delta}$-NP showed weaker activity in MA→SA transformation and the 5Ni/$CeO_{2-\delta}$-NC the least active, meanwhile they both yielded GBL in the 8 h MA hydrogenation course.

The detailed characterisation revealed that the CeO_2-NR and 5Ni/$CeO_{2-\delta}$-NR possessed the higher specific surface areas and Ovac density, as compared to their counterparts, leading to the enhanced Ni dispersion and the interaction between Ni and the $CeO_{2-\delta}$-NR support. There is correlation between the support morphology and the MA→SA conversion as well as the GBL yield on the three 5Ni/$CeO_{2-\delta}$ catalysts, which suggests the Ovac can benefit the MA→SA conversion but is inert for the SA→GBL transformation, so that the 5Ni/$CeO_{2-\delta}$-NR displayed the highest activity and selectivity in the MA→SA conversion.

Chapter 7 MA hydrogenation over bimetallic Ni-Cu/$CeO_{2-δ}$ catalysts

7.1 Introduction

In the previous chapters, we evidenced the pivotal roles of Ovac in the $CeO_{2-δ}$ supports for the MA hydrogenation and realised that the Ovac density in the catalysts were dependent on support morphologies (Chapter 6) and the Ni-loading (Chapter 5) once the same $CeO_{2-δ}$ support applied. The critical roles of Ovac in the MA hydrogenation mainly exhibited on the aspects of tuning the dispersion of Ni nanoparticles and providing additional active sites for both H_2 activation and MA→SA conversion. In nature, the roles of Ovac of $CeO_{2-δ}$ are due to the metal-support interaction between Ni and $CeO_{2-δ}$.[164, 206]

In principle, the anionic Ovac can activate hydrogen at low temperature and enrich the electron density of the adjacent Ni species to facilitate hydrogen dissociation on Ni at moderate temperature, which both can enable reducing the activation energy of C=C hydrogenation.[209] The Ovac density may be tuned by the control of the duration and temperature of H_2 reduction or by adopting morphology of CeO_2. However, from the large-scale industrial practice point of view, the control of the morphology of $CeO_{2-δ}$ via a hydrothermal method and the increased H_2 reduction treatments are extremely challenging due to the high cost and environment concerns. Hence, it is highly desirable to develop a more convenient and efficient strategy to tune the geometric and electronic properties of active Ni species.

In theory, adding a second metal to form a bimetallic catalyst may offer an opportunity to change the geometric structure and engineer the electronic structure of an active metal. The previous reports showed that the second metal can coexist with the major metallic catalytic species in various states, likely as an adatom[139], in an alloy state[140] and/or ionic state[39] or isolated species on the surface of the main metals.[38] The bimetallic catalysts often display considerably different performance in energy and environmental applications because the close contacted metals usually display different geometric and electronic features from their parent metals due to electron transfer and redistribution between the two metals.[11]

For MA hydrogenation, there were some pioneering reports regarding the enhanced catalytic activity and selectivity of bimetallic catalysts. For example, Jung and co-workers reported that the introduction of Sn into the Pd/SiO_2 catalyst led to enhanced GBL production and catalytic stability in MA hydrogenation, as a result of the electron donation from Sn to Pd within the binary Pd-Sn species.[46] In another case, the bimetallic $Ni\text{-}Pt/Al_2O_3$ catalyst was more active and selective for the hydrogenation of MA to SA than monometallic Ni/Al_2O_3 and Pt/Al_2O_3.[84] Based on the DFT simulation results, Pallassana and co-workers claimed that the bimetallic Pd-Re surface can modulate the adsorption energy of MA on the Pd atoms due to a strong electronic interaction between Pd and Re[89], which tuned the activity of MA hydrogenation. However, the different combination of the two metals would give rise to varied surface composition and electronic structure, thus, the bimetallic catalysts with the same components may display different catalytic performance on the dependence of synthesis methodology. For example, the Pt-Ni-Pt(111) surface showed higher activity and selectivity than the Ni-Pt-Pt(111) surface in the hydrogenation of the C=O group of acrolein.[144] Therefore, it is important to understand the structure of their bimetallic catalysts and correlate the catalytic activity and selectivity with the physical and electronic structures.

In this chapter, a series of $Ni\text{-}Cu/CeO_{2-\delta}$ catalysts with varying Ni/Cu ratios were prepared using an impregnation method and evaluated for the liquid-phase hydrogenation of MA. Through the careful characterisation by XRD, H_2-TPR, XPS, H_2-TPD, the alloy effect of the bimetallic Ni-Cu phase on the catalytic activity and selectivity in MA hydrogenation was investigated. The choice of Ni-Cu as the bimetallic catalyst to be optimised was based on the catalyst screening to various bimetallic $Ni\text{-}M/CeO_{2-\delta}$ (M=Fe, Co, Cu and Zn) catalysts prepared using the same methods, as compared in *Appendix C*.

7.2 Experimental

7.2.1 Catalyst preparation

Ceria supports were prepared by a sol-gel process, which has been described in *Chapter 4*.

In the catalyst preparation, 2 g of CeO_2 support was added into an ethanol/DI water (10 ml, 1:1 volumetric ratio) solution, in which the copper (II) nitrate and nickel (II) nitrate were dissolved, which corresponded to 10 wt% of the ceria support. The 10 wt% loading of metal nitrate was made up from the molar ratio of nickel to copper. The citric acid was added into the solution with a mole ratio of CA/metal =

1. The mixed solution was stirred at 80°C until the water was fully vaporised and kept overnight at 120°C in a convection oven. Then, the samples were calcined in air at 500°C for 3 h to obtain the xNiOyCuO/CeO_2 mixed oxides as precursors of the targeted catalysts. The bimetallic catalysts were obtained by reduction of the obtained mixed oxide precursors in a hydrogen flow at 300°C for 3 h, which were denoted as xNiyCu/$CeO_{2-\delta}$ (e.g. 10Ni/$CeO_{2-\delta}$, 8Ni2Cu/$CeO_{2-\delta}$, 6Ni4Cu/$CeO_{2-\delta}$, 4Ni6Cu/$CeO_{2-\delta}$, 2Ni8Cu/$CeO_{2-\delta}$ and 10Cu/$CeO_{2-\delta}$, respectively).

7.2.2 Catalyst characterisation and evaluation

The as-prepared bimetallic xNiyCu/$CeO_{2-\delta}$ catalysts with different Ni/Cu ratios and their oxide precursors were characterised by XRD, H_2-TPR, XPS and H_2-TPD techniques. The detailed procedures for the characterisation were described in *Chapter 2*. The catalytic performance of xNiyCu/$CeO_{2-\delta}$ catalysts were evaluated at 210°C and 5 MPa hydrogen pressure in a batch reactor within 0.1 g catalyst, 4.9 g MA and 40 mL THF as a solvent, which was also detailed in *Chapter 2*.

7.3 Results and discussion

7.3.1 Structure evolution of bimetallic xNiyCu/$CeO_{2-\delta}$ catalysts

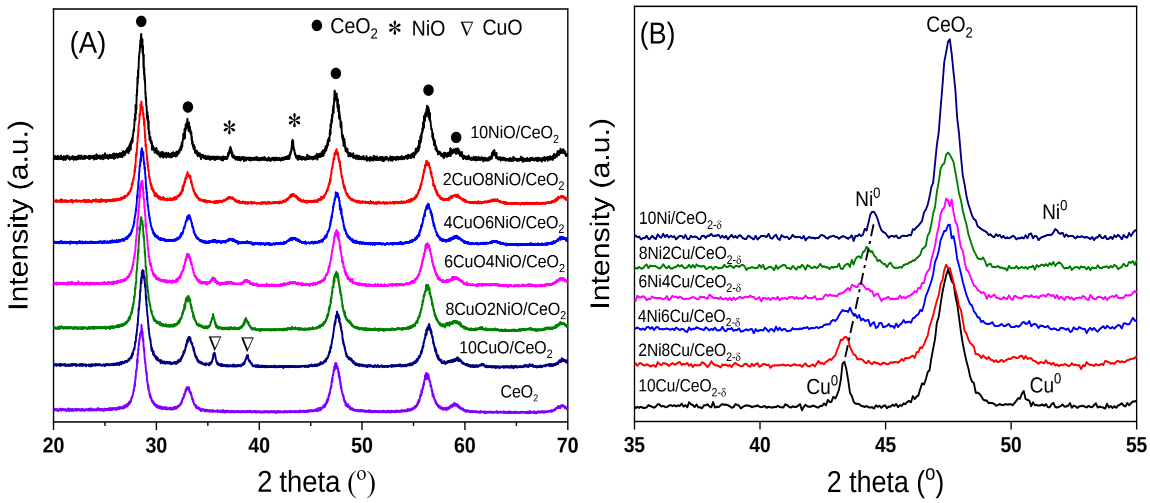

Figure 7.1 (A) XRD pattern for unreduced bimetallic xNiyCu/CeO_2 precursors and CeO_2 support and (B) Enlarged XRD pattern for reduced xNiyCu/$CeO_{2-\delta}$ catalysts

Figure 7.1 (A) presents the XRD patterns of mixed xNiOyCuO/CeO_2 precursors and CeO_2 support under ambient conditions. The XRD peaks corresponding to cubic fluorite-type ceria (JCPDS 34-0394) are observed for all the CeO_2-supported catalysts. There are two diffraction peaks at 2θ of 35.6 and 38.7° in 10CuO/CeO_2, 8CuO2NiO/CeO_2 and 6CuO4NiO/CeO_2 samples, ascribed to crystalline CuO (JCPDS file 48-1548). Similarly, the two diffraction peaks located at 2θ= 37.3 and 44.3° are observed in 10NiO/CeO$_2$, 8NiO2CuO/CeO$_2$ and 6NiO4CuO/CeO$_2$ samples, which relate to the (101) and (012) planes of NiO (JCPDS file 78-0643). However, the diffraction peaks due to NiO and CuO crystal phases are absent in the respective Cu-rich and Ni-rich samples, indicating that the NiO species and CuO species either are highly dispersed or form solid solution in ceria.[229] More importantly, CuO and NiO diffraction peaks emerge at their intrinsic positions in the bimetallic precursors, suggesting that nickel oxide and copper oxide are mostly isolated on the ceria support without formation of metal oxide alloy or solid solution.

Figure 7.1 (B) shows XRD patterns of the reduced xNiyCu/CeO$_{2-\delta}$, 10Ni/CeO$_{2-\delta}$ and 10Cu/CeO$_{2-\delta}$catalysts from 35 to 55°. Besides the diffraction peaks of CeO$_2$, the diffraction angles at 44.6 and 51.9° in the 10Ni/CeO$_{2-\delta}$ catalyst are attributed to (111) and (200) planes of metallic nickel (JCPDS 04-0850), while diffraction peaks at 43.4 and 50.6° are assigned to (111) and (200) planes of metallic copper in the 10Cu/CeO$_2$ (JCPDS 04-0836). The absence of NiO or CuO diffraction in the XRD patterns suggests that both NiO and CuO species were reduced to metallic species by the hydrogen reduction treatment at 300°C.

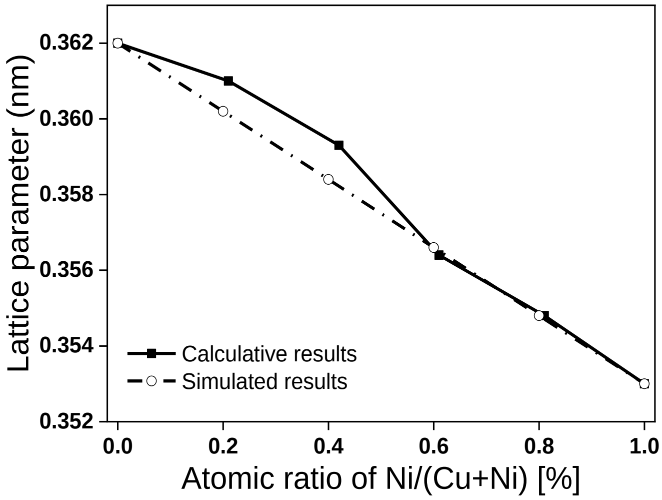

Figure 7.2 The lattice parameters of metallic species from both experimental tests and simulated by the Vegard law for the xNiyCu/CeO$_{2-\delta}$ catalysts

For the reduced bimetallic xNiyCu/CeO$_{2-\delta}$ catalysts, their diffraction peaks due to the metallic phases are observed between the peaks of monometallic Ni and Cu, confirming that the Ni-Cu alloy was formed during the H$_2$ reduction processes.[230, 231] Using the diffraction of the (111) crystal plane of the Ni-Cu alloy, the lattice parameters of the Ni-Cu alloy in the bimetallic xNiyCu/CeO$_{2-\delta}$ catalysts were calculated, which are plotted versus the Ni content in Figure 7.2. The calculated lattice parameters of the Ni-Cu alloy were compared to the theoretical results by using the Vegard's Law (refer to Chapter 2).[232] The experimental lattice parameters of the Ni-Cu alloys in the Ni-rich catalysts well fit the theoretical results, suggesting that a substitutional type solid solution between Ni^0 and Cu^0 formed in the Ni-rich catalysts.[230, 233] However, the lattice parameters of the Cu-richer Ni-Cu alloys are larger than the simulated values, in spite that smaller than that of 10Cu/$CeO_{2-\delta}$ catalyst. The lattice parameter deviations of Cu-rich samples suggest that some Ni species probably separated with Cu^0 and aggregated on the surface of $CeO_{2-\delta}$ rather than alloyed with Cu^0 species. The Ni^0 segregation was reported on the Cu-Ni/TiO_2 bimetallic catalysts where the preferential reduction of CuO and a higher Tamman temperature of Ni than Cu were attributed to the Ni isolation.[142] Tamman temperature is corresponding to the temperature at which the atoms of the solid acquired sufficient energy for their bulk mobility and reactivity. In our case, Cu and CuO have lower Tamman temperature than Ni and NiO. Thus, on the CeO_2 surface, Cu species diffuse faster than Ni species, giving rise to the rapid formation of Cu crystals. Another probability for Ni segregation is due to the strong John-Teller effects of Cu^0 that repels the incorporation of Ni at Cu-rich conditions.[234]

Table 7.1 The structure parameters of metallic Ni-Cu alloy, Ni and Cu in the xNiyCu/CeO_2 catalysts

Sample	2θ angle (°)	d-spacing [a] (nm)	Lattice parameter [b] (nm)	D [c] (nm)
10Ni/$CeO_{2-\delta}$	44.49	0.2037	0.3530	20.7
8Ni2Cu/$CeO_{2-\delta}$	44.24	0.2048	0.3548	17.2
6Ni4Cu/$CeO_{2-\delta}$	43.99	0.2058	0.3564	10.1
4Ni6Cu/$CeO_{2-\delta}$	43.57	0.2078	0.3599	9.7
2Ni8Cu/$CeO_{2-\delta}$	43.39	0.2086	0.3610	16.0
10Cu/$CeO_{2-\delta}$	43.34	0.2090	0.3620	23.0

Note: [a] The d-spacing of the Ni-Cu alloy was calculated using the equation: $2d\sin\theta=n\lambda$. [b] The lattice parameter of Ni-Cu alloy was estimated using the equation: $a=\sqrt{h^2+k^2+l^2}\times d$ based on the (111) crystal plane of cubic Ni-Cu alloy. [c] The crystallite size was calculated using the Scherrer equation. The percentage of metal dispersion was calculated the Equation 2.5 in Chapter 2 with the amount of H_2 uptake at metal surface.

Compared with the monometallic Ni and Cu supported on ceria, all the Ni-Cu bimetallic catalysts display weaker and broader diffraction peaks, indicating that the Ni-Cu alloy species possess smaller mean crystallite size or lower crystallinity. As shown in Table 7.1, the monometallic 10Cu/$CeO_{2-\delta}$ and 10Ni/$CeO_{2-\delta}$ catalysts show the largest crystallite sizes of Cu^0 (23.01 nm) and Ni^0 (20.70 nm) species. In contrast, the bimetallic catalysts possess smaller crystallite sizes, which are varying on the dependence of the Ni/Cu ratios, suggesting there exists the strong interaction between Ni and Cu for the bimetallic catalysts. In addition, the crystallite size of bimetallic catalysts is not linearly dependent on the Ni/Cu ratio. The crystallite sizes of the metal cluster in 6Ni4Cu/$CeO_{2-\delta}$ and 4Ni6Cu/$CeO_{2-\delta}$ catalysts are 10.1 and 9.7 nm, respectively, which is smaller than that of 2Ni8Cu/$CeO_{2-\delta}$ (16.01 nm) and 8Ni2Cu/$CeO_{2-\delta}$ (17.16 nm).

7.3.2 Redox properties of xNiyCu/$CeO_{2-\delta}$ catalysts

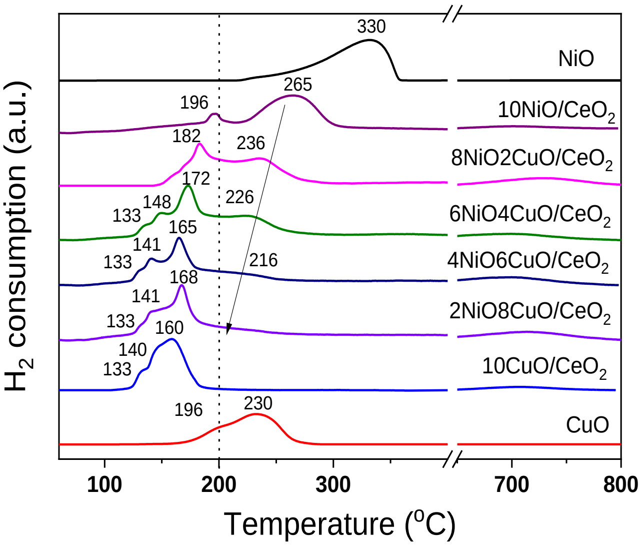

Figure 7.3 H_2-TPR profiles of bimetallic xNiOyCuO/CeO_2 precursors and pure NiO and CuO

Figure 7.3 presents the reduction profiles of the xNiOyCuO/CeO_2 precursors and those of pure NiO and CuO for comparison. In general, the main TPR peaks corresponding to NiO and CuO in the xNiOyCuO/CeO_2 precursors terminate below 300°C, suggesting that the optimal temperature for the catalyst reduction is 300°C that enables complete conversion of NiO and CuO into their metallic states. It is notable that there is a small amount of H_2 consumption at ca. 700°C, which is attributed to the partial reduction of the bulk CeO_2.[111]

For the 10CuO/CeO_2 catalyst, its three major reduction peaks at 130, 140 and 160°C are due to the reduction of adsorbed oxygen species on Ovac and/or highly dispersed CuO cluster, the CuO cluster interacting with ceria, and the surface-isolated bulk copper species, respectively.[229, 231] For the pure 10NiO/CeO_2 sample, two major reduced peaks located at 196 and 265°C are attributed to reduction of surface oxygen in CeO$_2$[26] and reduction of NiO to metallic Ni.[231] One can clearly see that the CuO and NiO species supported on CeO$_2$ are able to reduce at lower temperature regions than the unsupported bare CuO and NiO, suggesting that CeO$_2$ facilitates the reduction of the supported metal oxide particles.

For the bimetallic system, the TPR profiles can be approximately divided into two regions of (i) 100–200°C (region I) and (ii) above 200°C (region II). Peaks at the low temperature region are due to the reduction of CuO, while the peaks in the high temperature region are attributed to NiO reduction.[231] As shown in Figure 7.3, the supported CuO species is preferentially reduced at a relatively lower temperature than the NiO species on CeO$_2$, which is arisen from the lower free energy of reduction for CuO (-100.65 kJ/mol) than that of NiO (-12.31 kJ/mol).[235] It is important to underline that the reduction temperature of NiO in the binary Ni-Cu mixed oxide system decreases from 260°C (pure 10NiO/CeO$_2$) to 200°C (4NiO6CuO/CeO$_2$ sample) when the Cu content increases. This observation is line with the previous reports that the addition of Cu to NiO can dramatically lower the reduction temperature of Ni oxides.[142, 236]

7.3.3 Surface element analysis

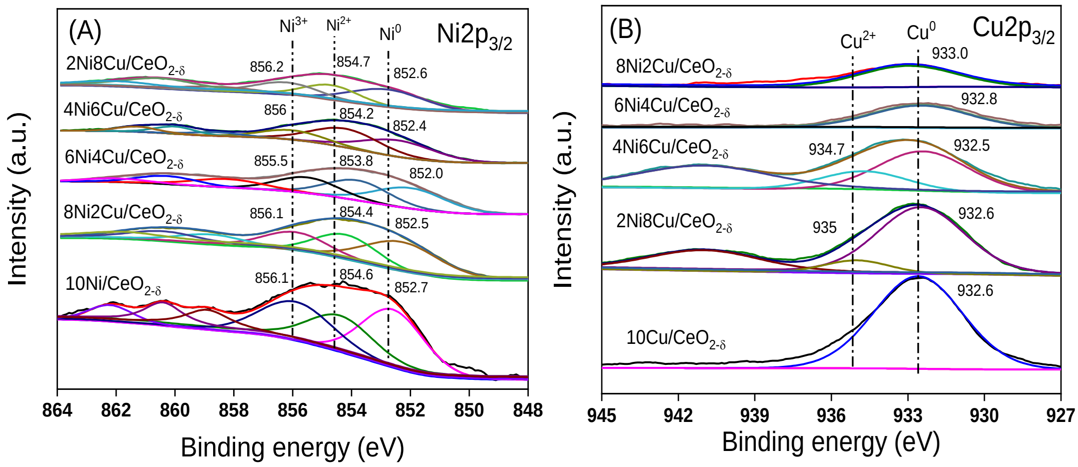

Figure 7.4 (A) Ni2p$_{3/2}$ and (B) Cu2p$_{3/2}$ XPS spectra of xNiyCu/CeO$_{2-\delta}$ catalyst reduced at 300°C for 3 h.

Figure 7.4 (A) shows the core level of Ni2p$_{3/2}$ spectra of the reduced xNiyCu/CeO$_{2-\delta}$ catalysts, in which the Ni2p$_{3/2}$ spectra at 852.7 and 854.6 eV indicate the co-existence of metallic Ni^0 and Ni^{2+} species.[203] With regard to the ionic Ni^{2+} species, although it is not able to rule out the re-oxidation of the metallic phase during the catalyst characterisation, the metallic Ni^{2+} species can be mainly arisen from the electron transfer from Ni^0 to the adjacent Ce^{4+} of the support. Such electron transfer is mainly due to the strong electronic attraction from ionic Ce^{4+}

towards Ni species.[106, 134] Moreover, the binding energy of Ni2$p_{3/2}$ emerges at 856.1eV, 1.5eV higher than that of Ni^{2+}, which is due to Ni^{3+} species within the $Ni_xCe_{1-x}O_{2-y}$ solid solution.[161]

In the bimetallic xNiyCu/$CeO_{2-\delta}$ catalysts, the B.E. values related to Ni^0 in the 8Ni2Cu/$CeO_{2-\delta}$, 6Ni4Cu/$CeO_{2-\delta}$, 4Ni6Cu/$CeO_{2-\delta}$ and 2Ni8Cu/$CeO_{2-\delta}$ catalysts are at 852.5, 852.0,852.4 and 852.6 eV, respectively, systematically lower than that of the monometallic 10Ni/$CeO_{2-\delta}$ at 852.7 eV (Figure 7.4 (A)). The gradual red shift of binding energy for Ni species indicates the electronic density of Ni^0 is enhanced.[168, 169] The similar phenomena were observed on Ni-Cu/Al_2O_3 catalyst[237] and Ni-Th alloy[168], where the d hole density of Ni was filled by adjacent electropositive components (Cu and Th). In our case of bimetallic xNiyCu/$CeO_{2-\delta}$ catalyst, the red shift of binding energy for the Ni species infers an increase of electron density of the Ni species from Cu to Ni due to the formation of Ni-Cu alloy. Additionally, it is noteworthy that B.E values of Ni species in the bimetallic catalysts initially decrease (Ni/Cu>6/4), then increase as an increase of the Cu content in the bimetallic xNiyCu/$CeO_{2-\delta}$ catalyst, suggesting that the Ni/Cu ratio also play important roles to determine the electron density distribution of Ni species.

Figure 7.4 (B) shows the Cu2$p_{3/2}$ core level spectra of the xNiyCu/$CeO_{2-\delta}$ catalysts. In general, the XPS signals of Cu^+ and Cu^0 species appear around 932.4 eV, while the main XPS signal of Cu^{2+} species displays at the BE of 934.7 eV, followed by the satellite lines of 941.0 eV.[238, 239] In the XPS of all the Cu-containing samples (Figure 7.4 B), the major broad peaks at ca.932.6 eV are assigned to Cu^+/Cu species and the humps at ca. 934.7 eV are related to Cu^{2+} species. The XPS results suggest that Cu^+/Cu and Cu^{2+} species coexist in these catalysts.

It is not avoidable the Cu^0 species was re-oxidised when transferring reduced samples for XPS analysis. However, the re-oxidation should not be main reason because the gradual blue shifts of the Cu2$p_{3/2}$ XPS spectra in the Ni-rich samples confirms that the electron transfer from Cu to the adjacent Ni.[240] For the Cu-rich samples, 4Ni6Cu/$CeO_{2-\delta}$ and 2Ni8Cu/$CeO_{2-\delta}$, the shifts of Cu2$p_{3/2}$ XPS spectra are negligible, suggesting that the electronic structure of Cu species was slightly modified by Ni. Such Ni-induced negligible XPS shifts of Cu species are closely related to the John-Teller effects of Cu, in that Cu matrix can only host very few Ni atoms to form alloy, which is well consistent with the XRD and Ni2$p_{3/2}$ XPS results.

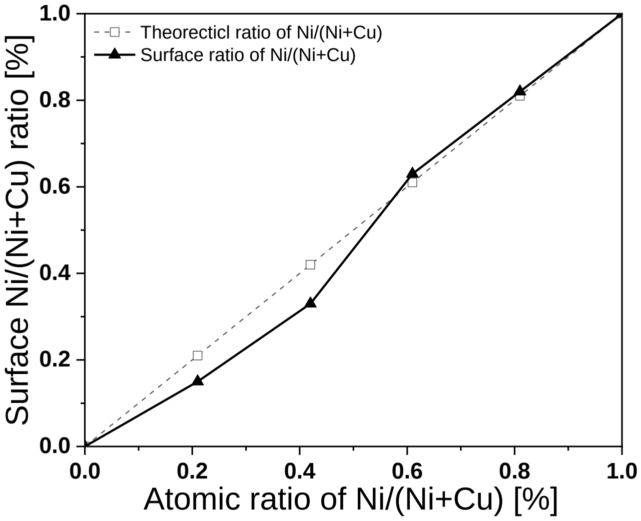

Figure 7.5 Surface and bulk ratios of Ni/(Ni+Cu) estimated by XPS the bimetallic xNiyCu/CeO$_{2-\delta}$ catalysts

Based on the quantitative analysis of Ni2p$_{3/2}$ and Cu2p$_{3/2}$ XPS peaks, the surface ratio of Ni/(Ni+Cu) was estimated and presented in Figure 7.5. Compared to the theoretical ratios of Ni/(Ni+Cu) obtained according the mass of copper (II) nitrate and nickel (II) nitrate used in the preparation of the catalysts, one can see that the surface ratios of Ni/(Ni+Cu) well fit the theoretical results in the Ni-rich catalysts, indicative of the formation of uniform Ni-Cu alloy. In contrast, the surface ratios of Ni/(Ni+Cu) appear smaller than the theoretical ratios in the 4Ni6Cu/CeO$_{2-\delta}$ and 2Ni8Cu/CeO$_{2-\delta}$ catalysts, suggesting the surface segregation of Cu occurs at the Cu-rich catalysts. The similar results were reported in Ni-Cu/TiO$_2$[142]and Ni-Cu/SiO$_2$[236] catalyst, where the surface of alloy is enriched by Cu species to minimize the surface free energy.

7.3.4 Hydrogen activation on the xNiyCu/$CeO_{2-\delta}$ catalysts

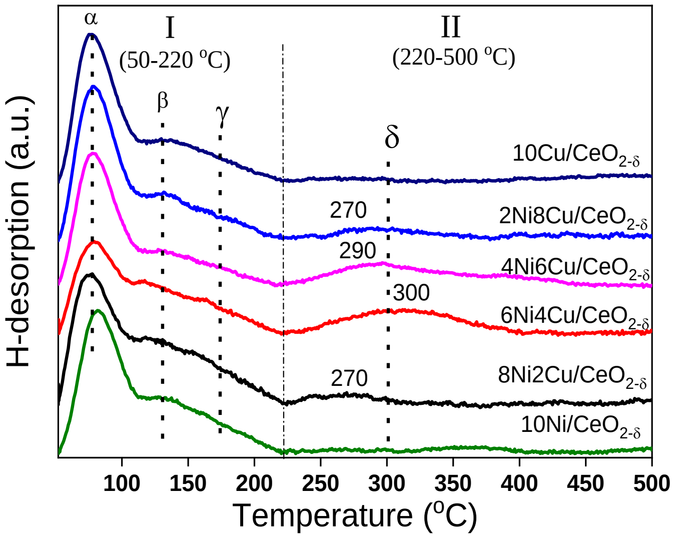

Figure 7.6 H_2-TPD profiles of the 10Ni/$CeO_{2-\delta}$, 10Cu/$CeO_{2-\delta}$ and xNiyCu/$CeO_{2-\delta}$ catalysts

Figure 7.6 presents the H_2-TPD profiles of various catalysts with different Ni/Cu ratios. According to the temperatures and shapes of the H_2-desorption peaks, the H_2-TPD profiles of the monometallic and bimetallic catalysts can be divided into two regions: a low-temperature region (50-220°C, including α, β and γ peaks) and a high-temperature region (greater than 220°C). The details of fitting peaks are presented in *Appendix C* (see Figure C4). As discussed in the previous chapters, the α peaks are related to hydrogen desorption from Ovac sites of $CeO_{2-\delta}$, while the β peaks at 130°C and γ peaks at 170°C correspond to the dissociative hydrogen atom uptake at highly dispersed and bulk metal species, respectively.

It is worth noting that the broad δ peaks at the high temperature region are more significant in the bimetallic catalysts, but absent in the monometallic catalysts, indicating a new active site was generated on the bimetallic catalysts. Combined with the XRD and XPS results, we suppose the new sites for the δ hydrogen uptake would be the Ni-Cu alloy. According to the XPS analysis, the electron distribution is uneven on the surface of Ni-Cu alloy, which would enable the polarization of the H-H bond and facilitate the hydrogen dissociation, eventually stabilise the surface-adsorbed hydrogen moieties.

The H_2 desorption peaks correspond to different species that can adsorb and activate hydrogen, so their integration areas may reflect the concentration and distribution of various active species. Table 7.2 lists the amount of H_2 uptake at individual active sites of the xNiyCu/$CeO_{2-\delta}$ catalysts. One can see that all the xNiyCu/$CeO_{2-\delta}$ catalysts have comparable amount of H_α, indicating that they have similar amount of Ovac regardless of Ni/Cu ratio. In contrast, the ratio of Ni/Cu significantly affects H_2 adsorption on the metal surface. As listed in Table 7.2, the amounts of H_β and H_γ gradually decreases with increased Cu contents due to the weak capacity of Cu in activating hydrogen molecule.[201] It is worth noting that the 6Ni4Cu/$CeO_{2-\delta}$ and 4Ni6Cu/$CeO_{2-\delta}$ have comparable amount of H_δ, around 4-fold that of the 8Ni2Cu/$CeO_{2-\delta}$ and 2Ni8Cu/$CeO_{2-\delta}$ catalysts. This result indicates that 6Ni4Cu/$CeO_{2-\delta}$ and 4Ni6Cu/$CeO_{2-\delta}$ can have more active sites to stabilise the H species due to their smaller crystallite size in comparison with 8Ni2Cu/$CeO_{2-\delta}$ and 2Ni8Cu/$CeO_{2-\delta}$, as evidenced by XRD results.

Table 7.2 H_2 uptake of the xNiyCu/$CeO_{2-\delta}$ catalysts

Sample	H_α (μmol/g)	H_β (μmol/g)	H_γ (μmol/g)	H_δ (μmol/g)	$\Sigma(H_\beta+H_\gamma+H_\delta)$ (μmol/g)
10Ni/$CeO_{2-\delta}$	28.4	22.6	14.6	0	37.2
8Ni2Cu/$CeO_{2-\delta}$	29.3	30.2	19.6	6.5	56.3
6Ni4Cu/$CeO_{2-\delta}$	25.5	23.8	18.8	23.9	66.0
4Ni6Cu/$CeO_{2-\delta}$	30.9	18.6	18.5	27.0	64.1
2Ni8Cu/$CeO_{2-\delta}$	30.8	17.3	17.5	6.4	41.2
10Cu/$CeO_{2-\delta}$	28.7	14.2	8.2	0	22.4

Note: H_α, H_β, H_γ and H_δ represent the amount of adsorbed hydrogen on different active sites, which were estimated based on the areas of α, β, γ and δ peaks, respectively.

In comparison with monometallic 10Ni/$CeO_{2-\delta}$ and 10Cu/$CeO_{2-\delta}$ catalysts, the bimetallic catalysts remarkably enhance H_2 adsorption on the surface, suggesting that the formation of Ni-Cu alloy can offer more active sites for the H_2 activation due to the reduction of crystallite size of metal species, as evidenced by XRD. Additionally, the Ni-Cu alloy also can tune the electronic structure of active sites, as evidenced by XPS, which favours the activation of H_2 and the reactants.

7.3.5 Catalytic performance

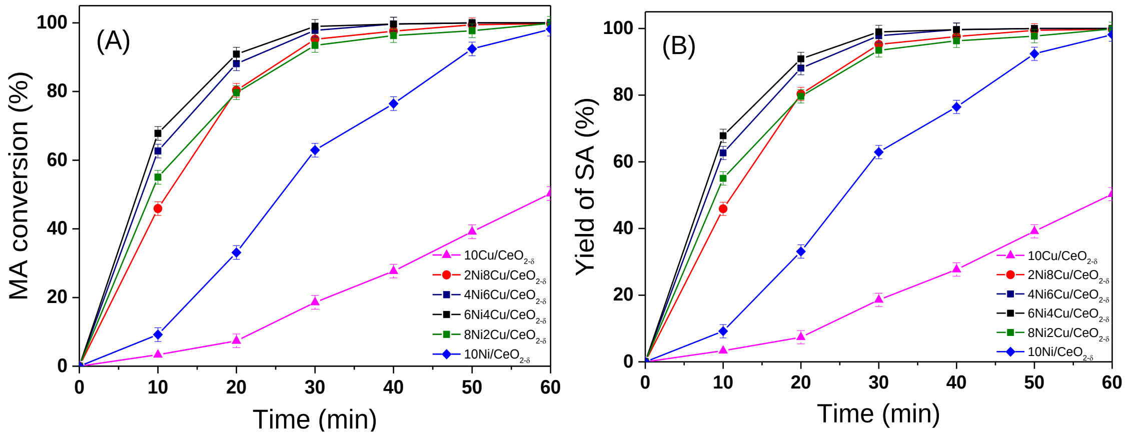

Figure 7.7 (A) Conversion of MA and (B) yields of SA on xNiyCu/$CeO_{2-\delta}$ catalysts at 210°C and under 5 MPa for 1 h duration

The catalytic activity of MA hydrogenation on the 10Ni/$CeO_{2-\delta}$, 10Cu/$CeO_{2-\delta}$ and xNiyCu/$CeO_{2-\delta}$ catalysts was assessed using a batch reactor at 210°C and 5.0 MPa hydrogen pressure. Figure 7.7 presents the results of MA conversion and SA yields on the catalysts. No other byproducts were detected in the 1 h MA hydrogenation reaction, suggesting that all the catalysts are highly selective to SA in MA hydrogenation. Moreover, the Ni-containing catalysts completely converted MA into SA within 1.0 h, whereas, only 50.3% of MA converted to SA over the 10Cu/$CeO_{2-\delta}$ catalyst. The results reveal that Cu is not an effective hydrogenation catalyst due to the limitation of dissociative hydrogen chemisorption.[88] It is worth noting that all the bimetallic catalysts are more active for MA→SA transformation than the monometallic 10Ni/$CeO_{2-\delta}$ and 10Cu/$CeO_{2-\delta}$ catalysts, verifying that the Ni-Cu alloy can serve as active sites to facilitate MA conversion to SA.

In order to unveil the dependence of the hydrogenation activity on metallic components, the $TOF_{MA\rightarrow SA}$ values of MA hydrogenation to SA on the bimetallic catalysts are compared in Figure 7.8 (A). It is found that $TOF_{MA\rightarrow SA}$ values for bimetallic catalysts are remarkably enhanced in comparison with monometallic catalysts, confirming that bimetallic Ni-Cu phases are very active in MA hydrogenation. Additionally, the $TOF_{MA\rightarrow SA}$ values of MA hydrogenation to SA are comparable among the bimetallic xNiyCu/$CeO_{2-\delta}$ catalysts, indicating that reaction rate of MA hydrogenation on the bimetallic catalysts is similar. As shown in Figure 7.8 (B), it is worth noting that the activity of MA hydrogenation in the initial 10 min well matches the sum of H_2 uptake at metal surface (H_β+H_γ+H_δ), suggesting that the ratio of Ni/(Ni+Cu) plays crucial roles in tuning the number of active sites for MA conversion.

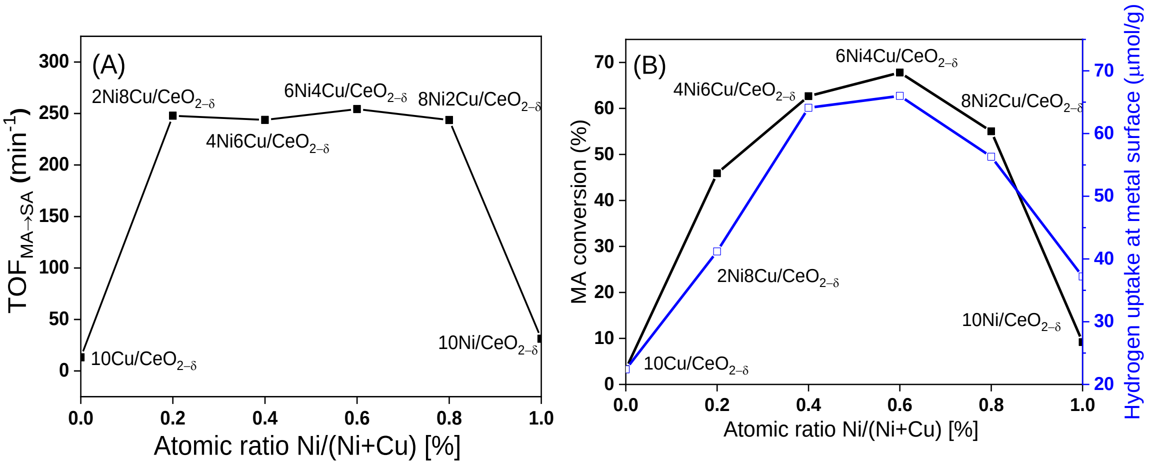

Figure 7.8 (A) Conversion of MA and (B) TOF$_{MA\rightarrow SA}$ versus the atomic ratio of Ni/(Ni+Cu) in initial 10 min course of the hydrogenation process

Based on DFT simulations, Pallassana and Neurock proposed that the hydrogenation of the C=C bond follows the Horiuti-Polanyi mechanism[88], in which the rate of MA conversion is dependent on the adsorption of MA and hydrogen as well as the formation of C-H bonds of the intermediates.

For the hydrogen adsorption, the electron-rich Ni species in the Ni-Cu alloy can stabilise the dissociative hydrogen moieties on the catalyst surface, as evidenced by the H_2-TPD results. The negative Ni species can also enhance the MA adsorption because the excess electron at the Ni species can transfer to the antibonding π^* orbital of maleic anhydride.[89] Due to the enhanced adsorption and activation of the H_2 and MA molecule on the bimetallic catalysts, the activation energy barriers for the MA→SA transformation would be considerably decreased.

As for the C-H formation, the previous DFT simulation revealed that the d-band position of metal far away from the Fermi level can facilitate the insertion of atomic H into the C=C bond to form saturated C-H moieties and advance the desorption of the as-formed saturated C-H moieties due to weaker interaction between C-H bonds and metal surface.[88] That is why the group IB metals, such as Cu, Au and Ag with closed *d* orbitals (d^{10}) as outermost valence electron shells, possess lower intrinsic activation energy barriers for the formation of C-H bond. In the present research, the Cu species in the Ni-Cu alloys facilitate the desorption of the as-hydrogenated C-H bonds from the alloy surface, thus enhancing their reactivity in the MA→SA transformation. However, as the Cu loading excesses the optimal Ni/Cu ratio, the isolated Cu^0 would restrict the MA→SA transformation because of the higher activation energy for the H_2 dissociative adsorption on Cu, which accounts for the lower hydrogenation activity of 2Ni8Cu/CeO$_{2-\delta}$ and 10Cu/CeO$_{2-\delta}$.

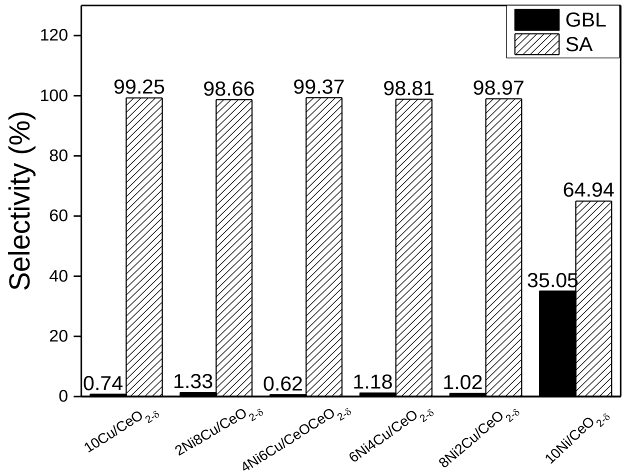

Figure 7.9 Selectivity of bimetallic xNiyCu/$CeO_{2-\delta}$, 10Cu/$CeO_{2-\delta}$ and 10Ni/$CeO_{2-\delta}$ catalysts after 8 h

To evaluate the selectivity of the corresponding catalysts, the duration of the hydrogenation process was extended to 8 h and the obtained product selectivity is plotted in Figure 7.9. One can see that the selectivity of GBL is only 1% over the 10Cu/$CeO_{2-\delta}$, but 35% on the 10Ni/$CeO_{2-\delta}$ catalyst. The results suggest that Cu is chemically inert for C=O hydrogenolysis under the hydrogenation conditions applied in this research, which is highly consistent with the results obtained in Chapter 4. As for the 10Ni/$CeO_{2-\delta}$ catalyst, its electron-mild Ni surface can adsorb the C=O group, eventually catalyses the hydrogenolysis of C=O in SA to form GBL.

It is notable that all the bimetallic catalysts, regardless of Ni/Cu ratios, show remarkably low selectivity to GBL, suggesting that the hydrogenolysis of C=O is distinctly hindered on the bimetallic catalysts, in spite of the formation of Ni-Cu alloy or metallic mixture. The Ni-Cu alloy catalysts are more appealing than the Cu-isolated Ni-Cu catalysts supported on the $CeO_{2-\delta}$ supports for selective hydrogenation of MA to SA.

In conclusion, the synergistic electronic effects of Ni and Cu in the bimetallic catalysts significantly contributes to MA→SA transformation. When the Ni/Cu ratio is close to 1.0, such as 6Ni4Cu/$CeO_{2-\delta}$ and 4Ni6Cu/$CeO_{2-\delta}$ catalysts, the catalysts achieve the optimal catalytic activity for the MA→SA transformation and depressed GBL production, which is due to the highest metal dispersion and appropriate electronic effects of the metallic species.

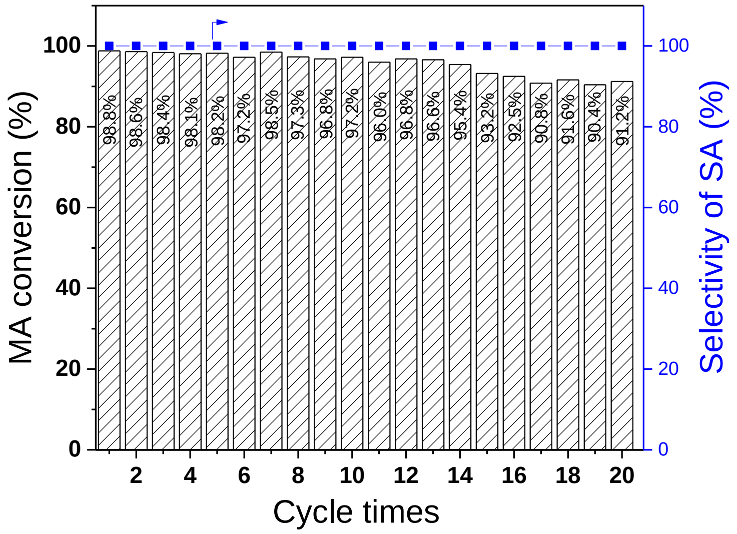

Figure 7.10 Stability of the 6Ni4Cu/$CeO_{2-\delta}$ catalyst in cycling MA hydrogenation

The stability test was conducted in a batch reactor at 210°C and 5 MPa hydrogen pressure with repeated use of 0.5 g the 6Ni4Cu/$CeO_{2-\delta}$ catalyst. The catalyst was separated by centrifugation after each hydrogenation cycle, and then reused for the next run without further treatment. Figure 7.10 shows that the SA selectivity remains as high as fresh catalyst in the 20 cycles of MA hydrogenation tests, although the conversion of MA starts a slight declining from ~99% down to 92% after 20 cycles.

For the one sight, the declined MA conversion is easily assigned to the catalyst loss in catalyst recycles after individual repeating tests. This seems reasonable because the net weight of the used catalyst after 20 runs is 0.43 g, ~14% mass loss, which is much more significant as compared to the decline of MA conversion. However, it is necessary to consider the catalyst sintering in the thermal catalytic reaction cycles, hence the used 6Ni4Cu/$CeO_{2-\delta}$ catalyst was characterised by XRD to investigate the structure of the catalyst after stability tests. Before the XRD characterisation, the used catalyst was collected after 20 cycling tests and calcined at 500°C in a N_2 flow to remove the adsorbed organic species.

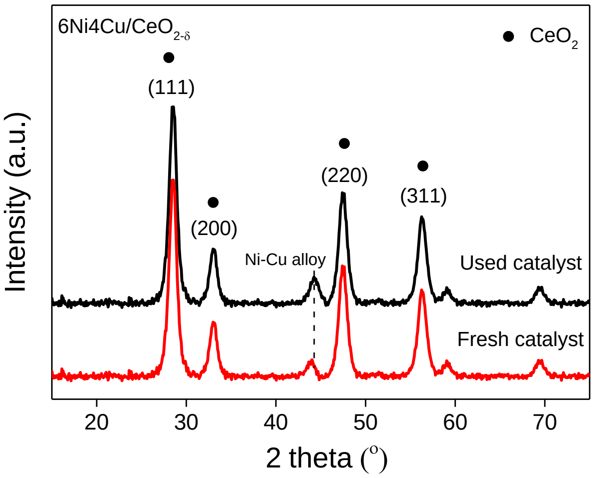

Figure 7.11 XRD patterns of fresh and used 6Ni4Cu/$CeO_{2-\delta}$ catalysts

Figure 7.11 shows the XRD patterns of the used and the fresh 6Ni4Cu/$CeO_{2-\delta}$ catalysts. One can see that the $CeO_{2-\delta}$ support of the used 6Ni4Cu/$CeO_{2-\delta}$ catalyst remains the fluorite structure though the characteristic XRD peak due to Ni-Cu alloy slightly shifts to a higher 2θ angle. The XRD peaks of both the support and alloy become stronger for the used 6Ni4Cu/$CeO_{2-\delta}$ catalyst as compared to those of fresh catalyst, which is due to the sintering of supported Ni-Cu alloy and $CeO_{2-\delta}$ support after the 20 cycles tests. The calculated lattice parameters and crystallite sizes, as listed in Table 7.3, confirm the significant sintering of the used catalyst.

Table 7.3 The structure parameters of fresh and used 6Ni4Cu/$CeO_{2-\delta}$ catalysts

Sample	2θ angle (°)	d-spacing [a] (nm)	Lattice parameter [b] (nm)	D [c] (nm)
Used catalyst	44.21	0.2048	0.3547	15.1
Fresh catalyst	43.99	0.2058	0.3564	10.1

Note: [a] The d-spacing of the Ni-Cu alloy was calculated using the equation: $2d\sin\theta = n\lambda$. [b] The lattice parameter of Ni-Cu alloy was estimated using the equation: $a = \sqrt{h^2 + k^2 + l^2} \times d$ based on the (111) crystal plane of cubic Ni-Cu alloy. [c] The crystallite size was calculated using the Scherrer equation.

The d-spacing and lattice parameter of the Ni-Cu alloy in the used 6Ni4Cu/$CeO_{2-\delta}$ catalyst are smaller than those of the fresh catalyst, closer to those of fresh 8Ni2Cu/$CeO_{2-\delta}$ catalyst (refer to Table 7.1). It is probably due to a fraction of Cu species diffusion out from the Ni-Cu alloy that leads to a decrease of d-spacing and lattice parameter.[142] However, the catalyst sintering should be responsible to the larger crystallite sizes and the increased lattice parameter, because the multiple cycles of thermal hydrogenation reactions can drive the growth of the Ni-Cu alloy and support of the used 6Ni4Cu/$CeO_{2-\delta}$ catalyst.

According to the XRD results and the mass loss of the used catalyst, we suppose that the structure change of Ni-Cu alloy, sintering and the catalyst loss contribute to the declined MA conversion on the 6Ni4Cu/$CeO_{2-\delta}$ catalyst. Nevertheless, the cycling tests demonstrate the outstanding catalytic activity, SA selectivity and excellent resistant to deactivation of the 6Ni4Cu/$CeO_{2-\delta}$ alloy catalyst, showing great potential for industrial MA hydrogenation processes.

7.4 Conclusion

In this work, Ni-Cu bimetallic catalysts supported on the $CeO_{2-\delta}$ support, with varying Ni/Cu ratios but remained metal loading of 10 wt%, were synthesised and evaluated for the hydrogenation of MA. In comparison with the monometallic 10Ni/$CeO_{2-\delta}$ and 10Cu/$CeO_{2-\delta}$ catalysts, the bimetallic xNiyCu/$CeO_{2-\delta}$ catalysts possessed smaller crystallite sizes, higher metal dispersion and higher MA→SA transformation activity. The Ni-Cu alloy can form in the Ni-rich regime of Ni/Cu ratios while the metallic Cu clusters exist besides of the alloy phase.

The detailed characterisation evidenced that there exists strong Cu-Ni electronic interaction in the bimetallic catalysts, namely, the electron transferring from Cu to Ni within the bimetallic particles owing to the different electronegativity of Ni and Cu. The strong Ni-Cu interaction resulted in the significant different properties for adsorption and activation behaviors for H_2 and MA, and eventually the different catalytic performance.

Alloying of Cu with Ni can greatly improve the MA conversion activity and, more significantly depress the production of GBL, namely extremely high selectivity of SA. The 6Ni4Cu/$CeO_{2-\delta}$ catalyst outperformed other bimetallic and monometallic catalysts, which was essentially due to uniform, smallest and highest dispersed Ni-Cu alloy particles and the appropriate electronic interaction within the Cu-Ni alloy particles.

Chapter 8 Effects of CeO_2 on MA hydrogenation on CeO_2@Ni/SiO_2 catalysts

8.1 Introduction

The metal-ceria interface of the M/ceria catalysts usually plays exceptional roles in determining their catalytic activity in various catalytic systems, such as water-gas shift reaction,[95, 106] CO_2 hydrogenation[241] as well as the methane and alcohol reforming.[110, 207] In the CO_2 hydrogenation to methanol, Cu-CeO_x interface at the CeO_x/Cu(111) model catalyst forces the CO_2 conversion to $CO_2^{\delta-}$ species rather than the conventional intermediate $HCCO^-$ on the Cu (111) surface, enabling CO_2 dissociation to adsorbed CO species on the surface of catalyst and sequential hydrogenation of carbonyl species to CH_3OH.[95, 241] In the catalytic reforming on the Ni/CeO_2 catalysts, the cleavages of O-H and C-H bonds predominantly occur at the Ni-CeO_2 interface, where the strong metal-support interaction (SMSI) can offer the active sites for the enhanced catalytic performance.[106, 110] In theory, the SMSI at the interface drives the formation of hybrid Ni-Ce-O or Ni-O-Ce geometric configurations that lead to strong electronic perturbation between Ni and Ce,[207] which is the origin of different catalytic activity in water-gas shift reaction and dry reforming of CH_4.[106, 110]

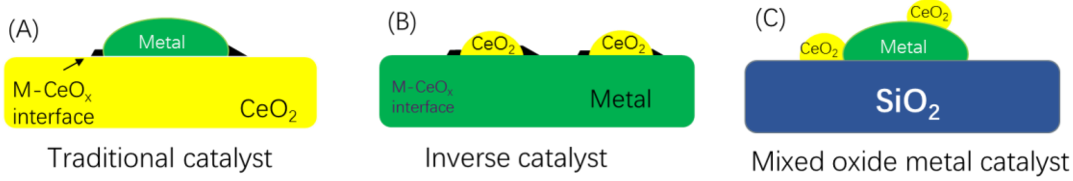

Traditional catalyst

Inverse catalyst

Mixed oxide metal catalyst

Figure 8.1 Typical metal–CeO_2 configurations of the CeO_2–containing catalysts

The M-CeO_2 geometric configurations can be various, though the three classes of M-CeO_2 configuration as illustrated in Figure 8.1 are relatively typical and facile to manufacture from material engineering point of view. Figure 8.1 (A) presents a traditional metal catalyst supported on CeO_2. Such type of configuration offers limited quantity of accessible interface active sites, because the accessible sites surround the metal particles resided on ceria. Therefore, the metal particle sizes and the surface area of support determine the number of active sites, hence relatively weak activity usually displays on catalysts with the large metal particles and bare CeO_2.[137] Figure 8.1 (B) shows an inverse catalyst configuration, where CeO_2 is deposited on the metal surface. This configuration offers an opportunity to tune the CeO_2 particle sizes yet ineffective to tune the metal particle sizes, which is desirable for the metal oxide sensitive reactions and fundamental investigation to the roles of CeO_2.[137] However, it is less common in technical application.

Figure 8.1 (C) displays the configuration of CeO_2 decorated metal catalyst supported on the porous support, such as SiO_2 or zeolite. This configuration benefits from the facile manufacturing: initially active metal species are highly dispersed and tightly laid down on the high-surface-area support like SiO_2, then decorated by CeO_2 at controlled extent. This type of catalyst combines the properties of nano-CeO_2 and metal nanoparticles, more importantly, offers abundant accessible metal-CeO_2 interfaces and thus profound impacts on the catalytic activity. This strategy has seldom been applied for develop Ni-based MA hydrogenation catalysts, although it has been successfully attempted in the decomposition of hydrous hydrazine to hydrogen[242], CO methanation[225] and dry reforming of CH_4[243] with high catalytic activity.

Owing to the important roles of the Ni-CeO_2 interface in C=O hydrogenolysis and the great advantages of the third configuration of Ni-CeO_2 interface, CeO_2 was adopted to modify Ni/SiO_2 to prepare CeO_2@Ni/SiO_2 catalysts for the liquid phase hydrogenation of MA at 210°C and 5 MPa of H_2 pressure. The CeO_2 loading was optimised and the contributions of CeO_2 were investigated through careful characterisation, in order to correlate the catalyst activity and product selectivity.

8.2 Experimental

8.2.1 Preparation of 15Ni/SiO_2 catalysts

The SiO_2 support (BET = 300 m^2/g, Sigma-Aldrich) was employed to prepare NiO/SiO_2 as the precursor of 15Ni/SiO_2 catalyst via a wet impregnation with $Ni(NO_3)_2\cdot 6H_2O$ solution. The concentration of $Ni(NO_3)_2\cdot 6H_2O$ solution can be tuned according to the targeted Ni loading. The hydrated precursor was dried at 120°C for 8 h, followed by calcination in air at 500°C for 3 h to produce NiO/SiO_2. Finally, the Ni/SiO_2 was finally obtained by H_2 reduction of the NiO/SiO_2 at 500°C for 3 h. In this research, the targeted Ni loading was 15 wt%, so the obtained catalyst is denoted as 15Ni/SiO_2 whose exact Ni loading was determined by ICP-OES.

8.2.2 Preparation of xCeO_2@15Ni/SiO_2 catalysts

The CeO_2 decorated 15Ni/SiO_2 catalysts were prepared by the impregnation method using the annealed NiO/SiO_2 precursors. The obtained NiO/SiO_2 precursor was wetted with a certain volume of $Ce(NO_3)_2\cdot 6H_2O$ solution in order to fabricate the theoretical CeO_2 loading of 1, 3, 5 wt%. The hydrated precursor was dried at 120°C for 8 h, followed by calcination in air at 500°C for 3 h to produce xCeO_2@15NiO/SiO_2 oxide precursors. The xCeO_2@15Ni/SiO_2 catalysts were obtained by reduction of their oxide precursors at 500°C for 3 h in a H_2/N_2 flow, denoted as 1CeO_2@15Ni/SiO_2, 3CeO_2@15Ni/SiO_2, and 5CeO_2@15Ni/SiO_2, where the number is in accordance with CeO_2 and Ni loading.

8.2.3 xCeO_2@15Ni/SiO_2 catalysts characterisation and evaluation

The as-prepared xCeO_2@15Ni/SiO_2 catalysts with different CeO_2 loading and their oxide precursors were characterised by XRD, TME, H_2-TPR, Raman and H_2-TPD techniques. The detailed procedures for the characterisation were described in *Chapter 2*. The catalytic performance of xCeO_2@15Ni/SiO_2 catalysts were evaluated at 210°C and 5 MPa hydrogen pressure in a batch reactor within 0.1 g catalyst, 4.9 g MA and 40 mL THF as a solvent, which was also detailed in *Chapter 2*.

8.3 Results and discussion

8.3.1 Structure and morphology of xCeO_2@15Ni/SiO_2 catalysts

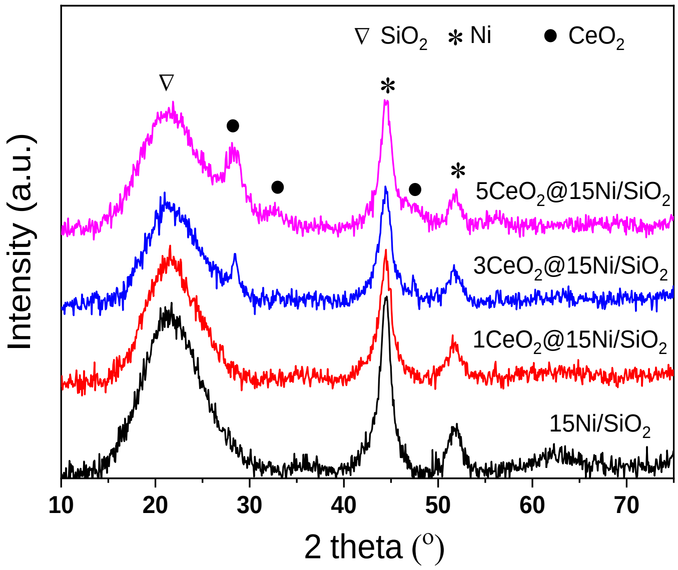

Figure 8.2 XRD patterns of reduced xCeO_2@15Ni/SiO_2 catalysts

Figure 8.2 shows the XRD patterns of the xCeO_2@15Ni/SiO_2 catalysts. The broad diffraction peaks in the 2θ between 15-30° are due to the amorphous silica.[244] The diffraction peaks of metallic Ni species are shown at 44.8° and 51.9°, which are due to the (111) and (200) planes of Ni^0, respectively. In addition, two new peaks at 28.3° and 32.7° in the 3CeO_2@15Ni/SiO_2 and 5CeO_2@15Ni/SiO_2 catalysts are respective to the (111) and (200) planes of crystalline CeO_2 (JCPDS 01-089-8436).

Such diffraction peaks due to CeO_2 are undiscernible for the $1CeO_2@15Ni/SiO_2$ catalyst, which is probably due to the low CeO_2 loading insensitive by XRD measurement or ultrahigh dispersion of CeO_2 with poor crystallinity.

The crystallite sizes of Ni particles are presented in Table 8.1, showing that the crystallite sizes of Ni particles slightly decrease as increasing CeO_2 loading, indicating that the presence of CeO_2 can prevent the sintering of Ni particles during the H_2 reduction treatment at the enhanced temperature.[242] The specific surface areas of the $xCeO_2@15Ni/SiO_2$ catalysts and the loading of Ni and CeO_2 are also summarised in Table 8.1. One can see that loading CeO_2 onto $15Ni/SiO_2$ did not decrease its surface area and the measured Ni and CeO_2 contents are very close to designed loading.

Table 8.1 The physical parameters of $xCeO_2@15Ni/SiO_2$ catalysts

Sample	Surface area [a] (m^2/g)	Ni content [b] (%)	CeO_2 (Ce) content [c] (%)	D(Ni) [d] (nm)
$15Ni/SiO_2$	150.8	14.89	0	12.7
$1CeO_2@15Ni/SiO_2$	153.6	14.88	0.87	10.2
$3CeO_2@15Ni/SiO_2$	157.6	14.89	3.15	9.8
$5CeO_2@15Ni/SiO_2$	151.6	14.89	5.05	9.4

Note: [a] The surface area of examined samples was measured by N_2 adsorption-desorption. [b,c] The Ni content and CeO_2 content were measured by ICP-OES. [d] The crystallite size of Ni species was estimated by the Scherrer equation.

Figure 8.3 shows the TEM and HRTEM images of the typical $15Ni/SiO_2$ and $3CeO_2@15Ni/SiO_2$ catalysts. As shown in Figure 8.3 (A), the metallic Ni particles are highly dispersed on the surface of the SiO_2 support with non-uniform particle size distribution between 5~20 nm. The HRTEM image of the $15Ni/SiO_2$ catalyst (Figure 8.3 (C)) shows the crystal fringe spacing of 0.20 nm, which corresponds to the (111) plane of metallic Ni crystal. The TEM image of the $3CeO_2@15Ni/SiO_2$ catalyst (Figure 8.3(B)) shows Ni is highly dispersed with particle size distribution of 3-18 nm. The HRTEM image of the $3CeO_2@15Ni/SiO_2$ catalyst (Figure 8.3(D)) reveals that most of the Ni particles (dark spots) are enveloped or closely contacted with small nanoparticles of CeO_2, which is verified by its inter-planar spacing of 0.31 nm, attributed to the (111) plane of CeO_2.

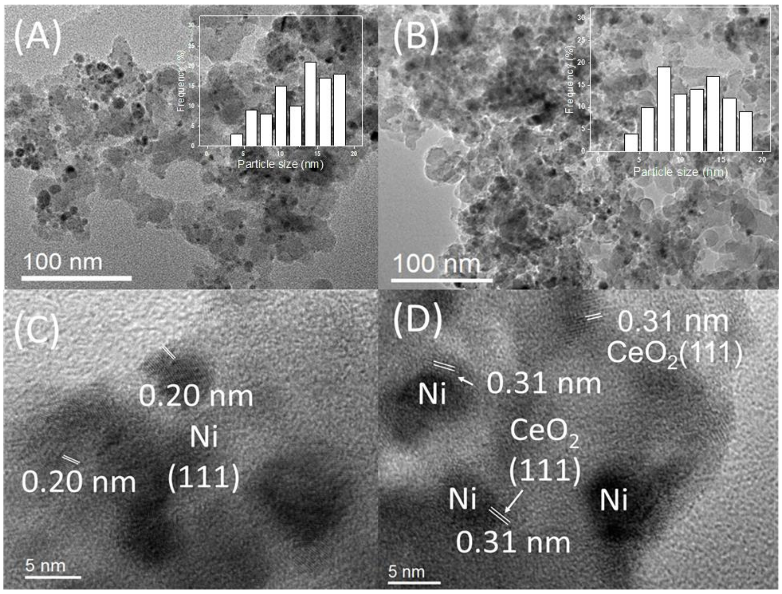
(A)
Frequency (%)
Particle size (nm)
100 nm
(B)
Frequency (%)
Particle size (nm)
100 nm
(C)
0.20 nm
Ni
0.20 nm
(111)
5 nm
(D)
0.31 nm
CeO2(111)
Ni
0.31 nm
CeO2
(111)
Ni
Ni
0.31 nm
5 nm

Figure 8.3 TEM and HRTEM images of reduced 15Ni/SiO_2 (A, C) and 3CeO_2@15Ni/SiO_2 catalysts (B, D)

8.3.2 Redox properties of xCeO_2@15Ni/SiO_2 catalysts

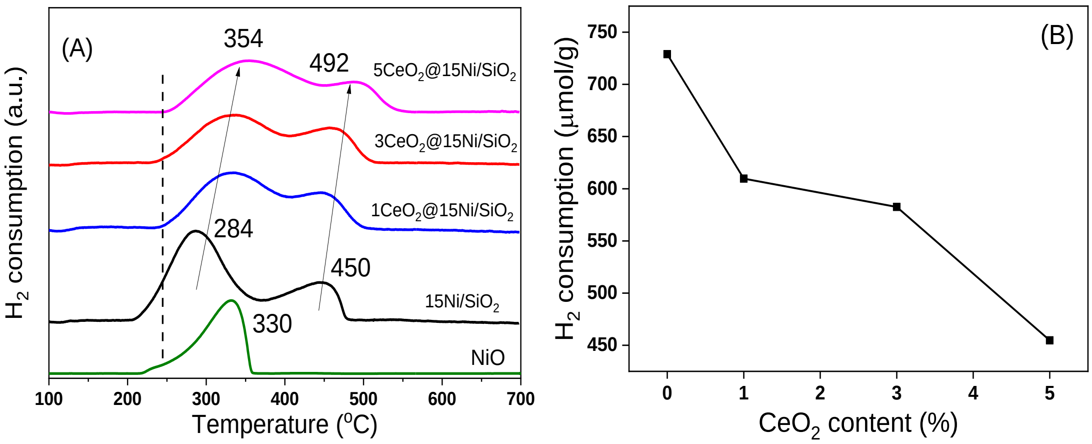

Figure 8.4 (A) H_2-TPR profiles of xCeO_2@15Ni/SiO_2 catalysts and (B) the dependence of hydrogen consumption against the Ce content

The H_2-TPR profiles of bare NiO and xCeO_2-15Ni/SiO_2 catalysts are shown in Figure 8.4. The maximum of hydrogen consumption for the NiO sample appears at 330 °C. There are two main hydrogen consumption peaks in the TPR of 15NiO/SiO_2 sample: the one at 284°C is due to the reduction of highly dispersed NiO species of weak interaction with the SiO_2, and the other at 450°C is due to the reduction of NiO species strongly bound to the SiO_2 surface.[245] When loading CeO_2 onto NiO/SiO_2, the reduction of NiO species occurs at a higher temperature and the maximum reduction systematically shifts to a higher temperature with gradual increase of CeO_2 loading. The result suggests that the deposition of CeO_2 on the NiO can retard NiO reduction, well consistent with the findings for the CeO_2 modified Ni/Al_2O_3

catalysts.[225] It was reported previously that the Ni-O bond confined in the CeO_2 lattice are more difficult to be reduced by H_2 because the strong interaction of Ni↔O↔Ce existing at the interface can stabilise the Ni-O bond, thus blocking the reduction of NiO species.[164] In addition, the CeO_2 species surrounding the NiO surface may can inhibit H_2 diffusion and thus retard reduction of the NiO.[225]

Figure 8.4(B) shows the dependence of the hydrogen consumption calculated from the TPR peaks on the CeO_2 loading. One can see that the15Ni/SiO_2 catalyst possesses the largest hydrogen consumption, while the hydrogen consumption declines as increasing CeO_2 loading. Because CeO_2 loading did not change Ni contents (as measured by ICP-OES), the enhanced reduction temperature for the xCeO_2@15Ni/SiO_2 samples can confirm that the coverage of CeO_2 on Ni can hinder the reduction of NiO to metallic Ni species. From the structure point of view, the Ni cations embedded in the CeO_2 matrix can coordinate with eight oxygen atoms, instead of six oxygen atoms in the NiO structure, so that the NiO species within the CeO_2 matrix are less reducible than the free NiO particles.

8.3.3 Surface defects of xCeO_2@15Ni/SiO_2 catalysts

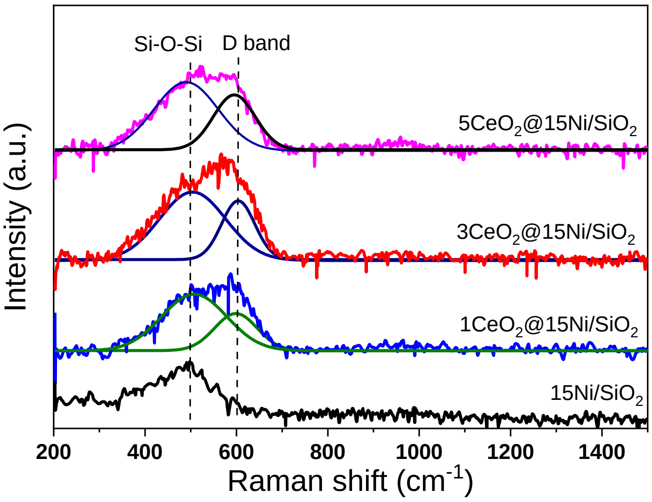

Figure 8.5 Raman spectra of xCeO_2@15Ni/SiO_2 catalysts

Figure 8.5 shows the Raman spectra of xCeO_2@15Ni/SiO_2 catalysts. The broad Raman bands at 490 cm^{-1} are attributed to the symmetric stretching of bridging oxygen in the six-membered SiO_4 rings which are predominantly existing in the amorphous SiO_2 support.[246] In comparison with the Raman spectra of the 15Ni/SiO_2 catalysts, the new vibration at 590 cm^{-1} is observed in the Raman spectra of the CeO_2 modified catalysts, which is associated with Ovac.[242] In this study, the direct reduction of Ce^{4+} to Ce^{3+} by hydrogen can lead to the formation of Ovac. Additionally, the Ni can incorporate into the CeO_2 lattice and generate hybrid Ni-O-Ce bonds, which can also create Ovac to compensate the doping-induced excess charge.[158] It is notable that the vibration at 460 cm^{-1} due to the fluorite phase of CeO_2 (F_{2g}) is not discernible because it may be masked or overlapped with the strong band of SiO_2. The Raman results indicate that the introduction of CeO_2 onto the 15Ni/SiO_2 catalysts brings in Ovac and the strong Ni-Ce interaction.

8.3.4 Hydrogen activation on the xCeO_2@15Ni/SiO_2 catalysts

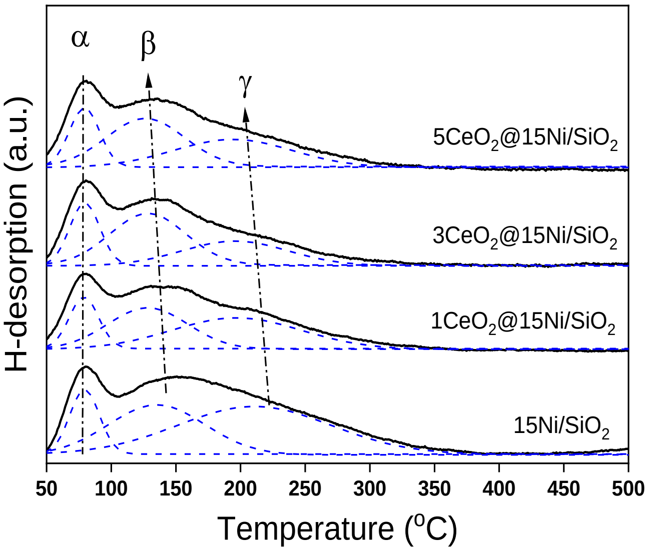

Figure 8.6 H_2-TPD profiles of reduced xCeO_2@15Ni/SiO_2 catalysts

Figure 8.6 shows the fitted H_2-TPD profiles of reduced xCeO_2-15Ni/SiO_2 catalysts. The three observable peaks (peak α , β and γ) at 80°C, 140 °C and 200°C are assigned to desorption of hydrogen molecules weakly adsorbed the surface of catalysts, strongly anchored at highly dispersed Ni^0 species[189] and the bulk Ni^0 species,[190] respectively. The increased CeO_2 content gradually decreases the maximum temperature of hydrogen desorption from the Ni^0 species, suggesting that CeO_2 weakens the binding energy of dissociative hydrogen on the Ni^0 surface due to, the strong Ni-CeO_2 interaction.[210, 247] Such strong Ni-CeO_2 interaction can redistribute the electronic configuration of Ni via chemical Ni-O-Ce bonds, leading to the formation of electronically perturbed Ni species ($Ni^{\delta+}$) at the interface,[242] so that it reduces the binding energy of H species on the metallic Ni species.

The quantitative analyses of the H_2 desorption are summarised in Table 8.2. It is found that there are comparable amounts of H_α for the four examined catalysts, indicating the amount of hydrogen weakly adsorbed on the catalysts is independent of the CeO_2 content. However, the CeO_2 amount significantly affects the population of hydrogen adsorbed on the Ni surface. As shown in Table 8.2, the 15Ni/SiO_2 catalyst possesses the largest H_β and H_γ, while the amount of H_β and H_γ gradually decreases with the Ce content up from the 1 to 5%. As expected, the estimated Ni dispersion based on the amount of hydrogen uptake at the metal surface also declines with the increasing Ce content, indicative of the masking effect of CeO_2 on the metallic Ni species. According to the H_2-TPD results, the strong Ni-CeO_2 interaction reduces the capacity of hydrogen uptake and weakens the binding energy of H adsorption on the metallic Ni surface.

Table 8.2 The quantitative analysis of H_2-TPD profiles of $xCeO_2$@15Ni/CeO_2 catalysts

Sample	H_α (μmol/g)	H_β (μmol/g)	H_γ (μmol/g)	$\sum(H_\beta + H_\gamma)$ (μmol/g)	Ni dispersion (%)
15Ni/SiO_2	34.25	53.35	81.12	134.47	10.7
1CeO_2@15Ni/SiO_2	33.26	44.84	43.68	88.52	7.0
3CeO_2@15Ni/SiO_2	32.25	41.89	35.68	77.57	6.1
5CeO_2@15Ni/SiO_2	34.89	35.53	27.99	63.52	5.0

Note: H_α, H_β and H_γ represent the estimated amount of adsorbed hydrogen, which were calculated based on the areas of α, β and γ peaks, respectively. Ni dispersion was calculated based on the hydrogen uptake at Ni species using the Equation 2.5 in *Chapter 2*.

8.3.5 Catalytic performance

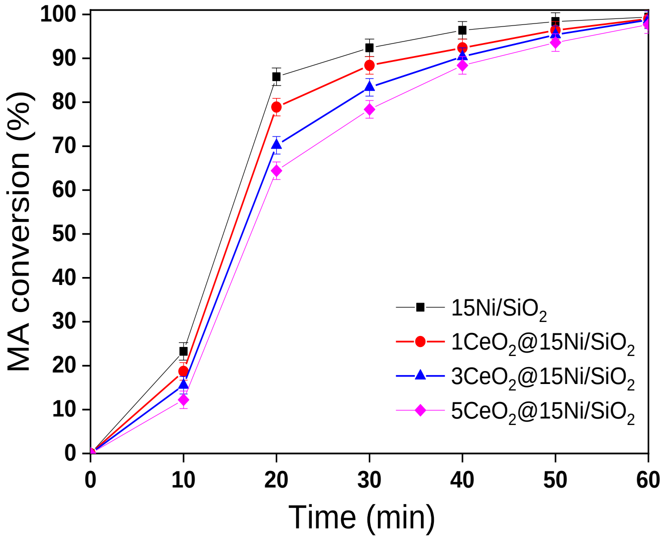

Figure 8.7 MA conversion over $xCeO_2$@15Ni/SiO_2 catalysts at 210°C and 5 MPa

Figure 8.7 shows MA conversion versus reaction time over $xCeO_2$@15Ni/SiO_2 catalysts. One can see MA completely converted to SA within an hour on all the catalyst though their MA conversion activity declined systematically with an increase of CeO_2 loading. As discussed in the previous Chapters (3~5), at appropriate Ni loading (<20 wt%), the metallic Ni species are the prominent active sites for MA hydrogenation to SA and Ovac favours the SA selectivity. All the samples possess almost identical Ovac density, so that their activity difference should not be due to Ovac density herein.

The turnover frequencies of MA → SA transformation ($\mathrm{TOF}_{MA\rightarrow SA}$) on the samples are estimated with respect to the exposed Ni^0, suggesting that 15Ni/SiO_2 and 1CeO_2@15Ni/SiO_2 have relatively similar values of $\mathrm{TOF}_{MA\rightarrow SA}$ (52.5 and 52.0 min^{-1}, respectively), slightly larger than that of 3CeO_2@15Ni/SiO_2 ($\mathrm{TOF}_{MA\rightarrow SA}$ = 50.1 min^{-1}) and 5CeO_2@15Ni/SiO_2 ($\mathrm{TOF}_{MA\rightarrow SA}$ = 48.2 min^{-1}). The slight decrease of the $\mathrm{TOF}_{MA\rightarrow SA}$ values suggests that the decoration of CeO_2 on Ni^0 species can diminish their activity in the MA→SA transformation, but the influence of CeO_2 is rather weak. Therefore, combined with the H_2-TPD results, we suppose that the difference in the apparent activities of the catalysts is primarily due to the exposed amount of Ni species and Ni dispersion.

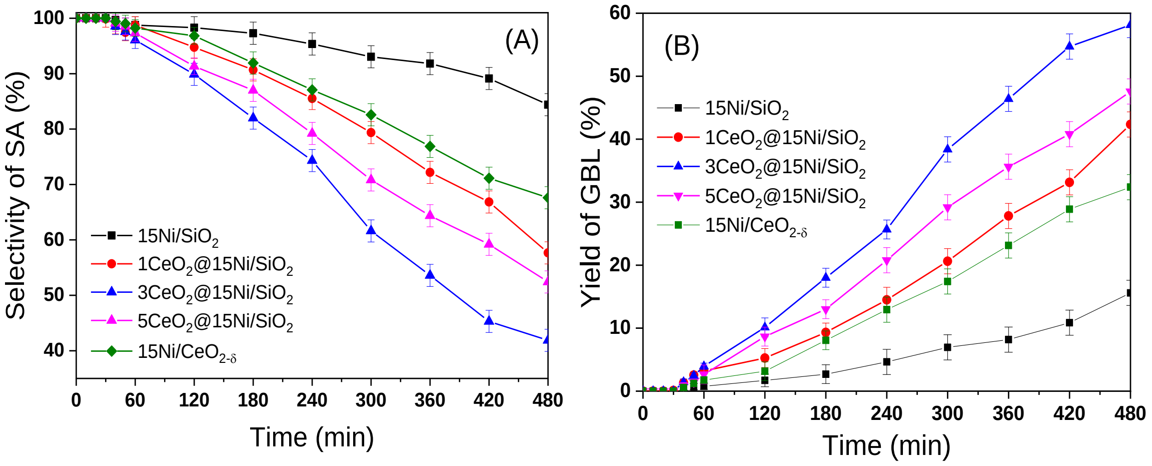

Figure 8.8 (A) Selectivity of SA and (B) yield of GBL over xCeO_2@15Ni/SiO_2 catalysts at 210°C and 5 MPa

As MA hydrogenation on Ni-based catalyst is a multi-step reaction in which GBL can only be produced from the hydrogenolysis of SA. The selectivity of SA remains about 100% in the initial 60 min, then SA slowly converts to GBL via the hydrogenolysis of SA. The selectivity of the four catalysts differs in the prolonged hydrogenation process of 8.0 h, revealing that they have distinct reactivity towards C=O hydrogenolysis. As shown in Figure 8.8 (B), the GBL yield is only 15% over 15Ni/SiO_2 catalyst in the 8 h hydrogenation course, though 42.3%, 58.1% and 47.5% GBL yields are achieved on the 1CeO_2@15Ni/SiO_2, 3CeO_2@15Ni/SiO_2 and 5CeO_2@15Ni/SiO_2 catalysts, respectively. The results suggest decorated 15Ni/SiO_2 with CeO_2 can significantly promote the SA→GBL transformation via C=O hydrogenolysis.

The $TOF_{SA\rightarrow GBL}$ value of $15Ni/SiO_2$ catalyst ($TOF_{SA\rightarrow GBL}$ = 0.29 min^{-1}) is much smaller than that of $1CeO_2@15Ni/SiO_2$ ($TOF_{SA\rightarrow GBL}$ = 0.56 min^{-1}), $3CeO_2@15Ni/SiO_2$ ($TOF_{SA\rightarrow GBL}$ = 1.65 min^{-1}) and $5CeO_2@15Ni/SiO_2$ ($TOF_{SA\rightarrow GBL}$ = 0.99 min^{-1}) catalysts. This result indicates that the introduction of CeO_2 into $15Ni/SiO_2$ catalyst can enhance the C=O hydrogenolysis on the Ni surface. As compared in Figure 8.8 (B), the $15Ni/CeO_{2-\delta}$ catalyst displays higher activity than $15Ni/SiO_2$ catalysts in GBL production, suggesting the enhanced role of CeO_2 in SA→GBL transformation. Additionally, it is interesting to note that the $xCeO_2@15Ni/SiO_2$ catalysts show superior catalytic activity to the $15Ni/CeO_{2-\delta}$ catalyst in SA→GBL transformation, verifying that the surface interplay between Ni and CeO_2 plays an paramount role in C=O hydrogenolysis.

Compared with the $15Ni/SiO_2$ catalyst, the decoration of CeO_2 can suppress the hydrogen adsorption at the surface of Ni species, which seems to be detrimental for the hydrogenolysis process. However, the superior SA→GBL activity on the $xCeO_2@15Ni/SiO_2$ catalysts suggests that the decoration of CeO_2 may enhance C=O activation despite that adverse the H_2 activation. To further unveil the roles of CeO_2 in C=O activation and hydrogenolysis, Fourier-transform infrared spectroscopy (FTIR) was employed to investigate the C=O adsorption behaviour on the surfaces of $3CeO_2$-Ni/SiO_2 and $15Ni/SiO_2$ catalysts using cyclohexanone as a probe molecule.

Figure 8.9 shows the IR spectra of cyclohexanone adsorption on the $3CeO_2@Ni/SiO_2$ and $15Ni/SiO_2$ catalysts, with FTIR scans of fresh catalysts as background, by temperature-programmed measurements. Figure 8.9 (A) shows the FTIR of the cyclohexanone adsorption on the $3CeO_2@Ni/SiO_2$ catalyst, where the peak at 1734 cm^{-1} is due to the vibration (νC=O) of C=O of the free or weakly adsorbed cyclohexanone molecule which can be easily removed by evacuation.

As the temperature rises to 210°C, the ν C=O at 1734 cm^{-1} is still dominant, though a new broad peak at 1590 cm^{-1} emerges in the $3CeO_2@15Ni/SiO_2$ catalyst due to the C=O group bound to the catalyst surface.[248, 249] The 1590 cm^{-1} band retains after evacuation, indicative of a strong adsorption of C=O on the surface of catalyst. Besides the display/disappear of the ν C=O, no IR signal at 1590 cm^{-1} is observable on the $15Ni/SiO_2$ catalyst (Figure 8.9 (B)). This result indicates that the strong chemsorption of C=O occurs onto CeO_2 rather than SiO or Ni.[118] The strong adsorption can polarise and weaken C=O bond, thus facilitate C=O hydrogenolysis over the $xCeO_2@15Ni/SiO_2$ catalysts. Similar results were also observed on the Ni/TiO_2 catalyst, where the authors found that Ni-TiO_x can strengthen C=O adsorption and improve the reactivity of C=O in the crotonaldehyde hydrogenation.[48]

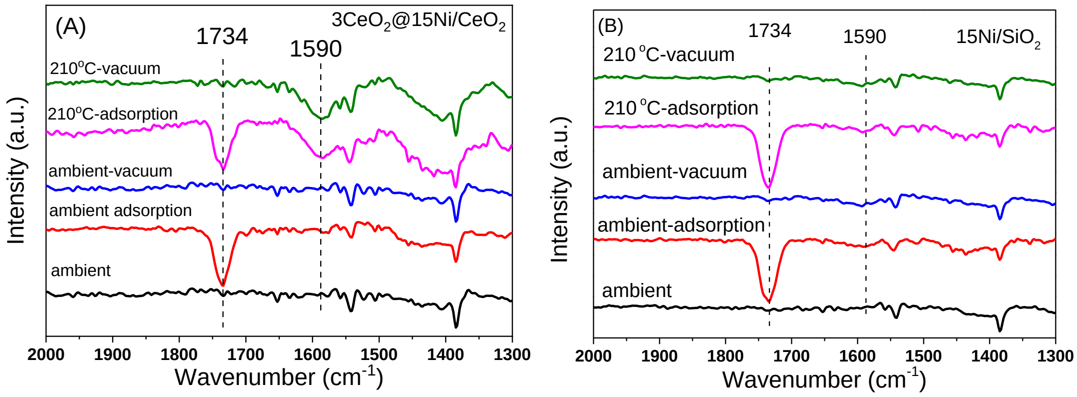

Figure 8.9 FT-IR spectra for cyclohexanone adsorption on $3CeO_2$@15Ni/SiO_2 and 15Ni/SiO_2 catalysts under ambient temperature and 210°C

The IR results suggest that a small amount of CeO_2 is responsible for the strong adsorption of C=O on the catalyst surface. It has been reported that the surface decorated CeO_2 strongly interacts with Ni species, leading to the formation of Ni-O-Ce bonds at the Ni-CeO_2 interface.[164] The Ni-O-Ce bond can cause the electron transfer from Ni to Ce, resulting in the formation of electron-deficient $Ni^{\delta+}$.[242] The $Ni^{\delta+}$ species weaken the adsorption of H_2[250], as proved by the H_2-TPD results, but strongly coordinate with the C=O group due to their strong electronic interaction. The $Ni^{\delta+}$ species serve as active sites for the C=O hydrogenolysis in the hydrogenation.[211, 251] Therefore, it is possible that the strong interaction between Ni and CeO_2 can electronically perturb the Ni species ($Ni^{\delta+}$), which contributes to the enhanced catalytic performance of SA → GBL.

Figure 8.7(B) shows there exists an optimal CeO_2 content in the xCeO_2@15Ni/SiO_2 for the SA→GBL transformation. In the given reaction duration, the GBL yield reaches the maximum when 3 wt% CeO_2 loaded, so does the $TOF_{SA\rightarrow GBL}$ value. As the CeO_2 loading excesses 3 wt%, for example, the $5CeO_2$@15Ni/SiO_2 catalyst, the catalytic hydrogenation of SA to GBL declines. As CeO_2 itself is not active for the C=O hydrogenolysis, the excess CeO_2 loading deposited on the $5CeO_2$@15Ni/SiO_2 catalyst surface may either mask some Ni^0 and/or the Ni-CeO_2 interface to expose, consequently reduce the accessible active sites at the catalyst surface and thus decrease the catalytic activity.

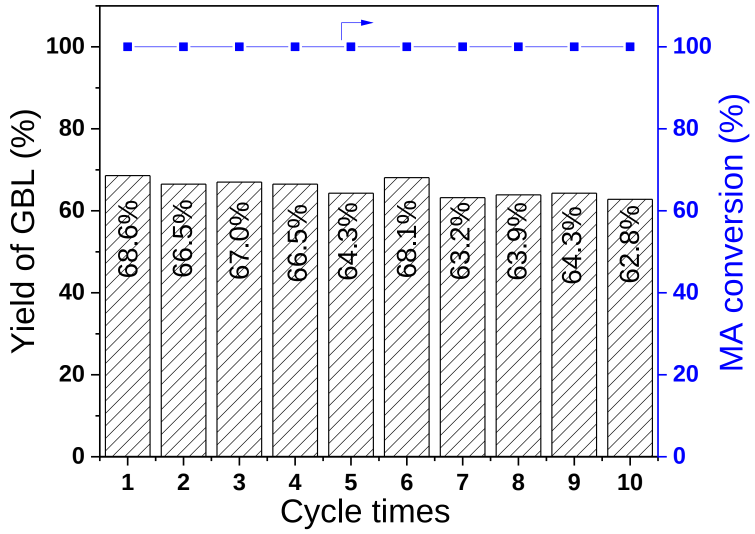

Figure 8.10 Stability of the $3CeO_2@15Ni/SiO_2$ catalyst in cycling MA hydrogenation

The stability test for the $3CeO_2@15Ni/SiO_2$ catalyst was conducted at 210°C and 5 MPa of hydrogen pressure in a batch reactor within 0.3 g catalyst, 4.9 g MA and 40 mL THF as the solvent. After each cycle, the catalyst was separated by centrifugation and then reused into the next cycle without any further treatment. After the stability test, the used catalyst was calcined at 500°C in a flow of N_2 to remove adsorbed organic species. The mass of the post-catalyst is 0.24 g, as weighed by electronic balance, indicating that 20 wt% of catalyst was lost during the catalyst recycle treatments. Figure 8.10 shows that the GBL yields are of the range of 62-68% with the maximum loss of 10% in the 10 cycling tests, which is insignificant and acceptable as consider the catalyst lost, suggesting that $3CeO_2@15Ni/SiO_2$ catalyst is very stable for MA hydrogenation to GBL.

8.4 Conclusion

The CeO_2 modified $xCeO_2@15Ni/SiO_2$ (x=0, 1, 3, 5 wt%) catalysts were prepared by a simple impregnation method, followed by H_2 reduction process at 500°C for 3 h. All the $xCeO_2@15Ni/SiO_2$ catalysts exhibited higher GBL yields in comparison with $15Ni/SiO_2$ catalyst, although the CeO_2 decorated catalysts slightly slugged the MA→SA transformation.

The results of the characterisation showed that the decorated CeO_2 was close contact with the metallic Ni species and brought in strong Ni-CeO_2 interaction. Such strong interaction between Ni and CeO_2 can perturb the electronic configuration of Ni that leads to formation of interface $Ni^{\delta+}$ species, which suppressed the hydrogen adsorption yet enhanced adsorption and activation of the carbonyl group on the catalysts surfaces.

The superior GBL yields on the xCeO_2@15Ni/SiO_2 catalysts are attributed to the surface modification of Ni by CeO_2 that brings about the strong Ni-CeO_2 interaction and offers more active sites to activate the C=O groups. Among the catalysts, 3CeO_2@15Ni/SiO_2 catalyst showed the highest MA→SA activity and GBL yield, which was attributed to its excellent balance between competition between H_2 and SA for adsorption and activation.

Chapter 9 Summary and outlook

9.1 Summary

Maleic anhydride is an important C_4 building block in the chemical industry, and its annual production will increase up to 2,987.2 kilotons in 2024 with a compound annual growth rate (CAGR) of 5.5%. The vast development of MA industries is driven by its high-value downstream hydrogenation products, such as SA, GBL and other C_4 compounds. However, MA is a cyclic anhydride, consisting of one olefinic bond conjugating with two acyl groups that bonded to the same oxygen atom, hence, its hydrogenation is prone to generate mixed products, because C=C hydrogenation and C=O hydrogenolysis can occur simultaneously or in the long-term continuous hydrogenation processes. On the other hand, the selective hydrogenation of C=C bonds and/or removal of C=O bonds are important fundamental topics but grand challenges in the industrial catalysis, which highly rely on the active, highly selective and stable catalysts. To produce high quality and value-added products, effective catalysts with high activity and selectivity are highly desirable for MA hydrogenation in the relevant chemical industries.

In principle, to achieve the selective hydrogenation, it is necessary to define the active sites for C=C and C=O hydrogenation and correlate the catalytic performance with the structure of catalysts, which in turn will facilitate the design and development of high-performance industrial catalysts. This thesis aims to design the efficient catalysts for MA hydrogenation and to define the active sites that dominate C=C hydrogenation and C=O hydrogenolysis. After a thorough literature review, the research challenges and methodologies were put forward in Chapters 1 and 2. Based on these, the PhD research project was carried out smoothly and its outcomes are presented in the thesis, as summarised below:

In Chapter 3, the properties of the $10Ni/CeO_{2-\delta}$ and the conventional $10Ni/Al_2O_3$ catalysts and their performance in the liquid phase MA hydrogenation were investigated. Although $10Ni/CeO_{2-\delta}$ possessed lower surface area than $10Ni/Al_2O_3$, we found the $10Ni/CeO_{2-\delta}$ catalyst exhibited nearly 12-fold higher initial specific activity in the hydrogenation of MA to SA and enhanced selectivity to GBL. The strong interaction between Ni and $CeO_{2-\delta}$ support was verified, which promoted Ni dispersion in small particle size. A portion of Ni species that incorporated into the CeO_2 matrix promoted to form Ovac on the $CeO_{2-\delta}$ support. The superior catalytic performance of $10Ni/CeO_{2-\delta}$ catalyst to the $10Ni/Al_2O_3$ catalyst in MA hydrogenation was due to the synergism of the enhanced dispersion of metallic Ni, oxygen vacancies on the CeO_2 support and the strong Ni-CeO_2 interaction.

In Chapter 4, the MA hydrogenation over various M/$CeO_{2-\delta}$ catalysts (M= Ni, Co, Cu) was studied to define the robust transition metal catalyst. We found that the 10Ni/$CeO_{2-\delta}$ catalyst was more active in MA hydrogenation and more selective to GBL yield than 10Co/$CeO_{2-\delta}$, while the 10Cu/$CeO_{2-\delta}$ catalyst was the least active in MA hydrogenation to SA and inert for SA hydrogenolysis to GBL. The MA hydrogenation to SA over 10Ni/$CeO_{2-\delta}$ and 10Co/$CeO_{2-\delta}$ catalysts followed quasi-first order kinetics, though complicated kinetics displayed on the 10Cu/$CeO_{2-\delta}$ catalyst. We convincingly assigned such different catalytic hydrogenation behaviour of the catalysts to the electronic nature of the active metals. The metallic Cu with fully filled d orbital (d^{10}) had weak capability of electron-donation to MA molecule, though the unpaired electrons of Co ($3d^7$) and Ni ($3d^8$) would favour the coordination and activation of MA, therefore, the latter displayed much higher activity. Compared with the 10Co/$CeO_{2-\delta}$ catalyst, the 10Ni/$CeO_{2-\delta}$ catalyst possessed higher metal dispersion and more Ovac that led to the higher activity in C=C hydrogenation and C=O hydrogenolysis.

According to obtained results in Chapter 3 and Chapter 4, Ovac density, nature of Ni species as well as Ni-$CeO_{2-\delta}$ interaction would play pivotal roles in catalysing MA hydrogenation over Ni-$CeO_{2-\delta}$ system. Therefore, in Chapter 5, a series of xNi/$CeO_{2-\delta}$ catalysts with a wide Ni loading ranged from 0 to 30 wt% were prepared and evaluated in MA hydrogenation to gain in-depth insight into Ovac, Ni nature and Ni-$CeO_{2-\delta}$ interaction in catalytic MA hydrogenation. We found that Ni loading can enhance Ovac formation, while excess Ni species would mask Ovac to expose on the $CeO_{2-\delta}$ surface. Compared to CeO_2, the defective $CeO_{2-\delta}$ support displayed higher activity in MA → SA transformation, proving that Ovac can catalyse C=C hydrogenation. The $TOF_{MA\rightarrow SA}$ declined with the decrease of Ovac amount in the xNi/$CeO_{2-\delta}$ catalysts, suggesting the significant roles of Ovac in the C=C hydrogenation. However, the Ni species is pivotal for MA → SA transformation since loading Ni on the $CeO_{2-\delta}$ support drastically improved the MA hydrogenation activity and determined the Ovac density. The 2Ni/$CeO_{2-\delta}$ displayed the largest $TOF_{MA\rightarrow SA}$, while the $TOF_{MA\rightarrow SA}$ over xNi/$CeO_{2-\delta}$ catalysts declined with increasing Ni content, which was due to the fact that the excess Ni species weakened the Ovac→Ni interaction and thus reduced their activity in C=C hydrogenation.

For C=O hydrogenolysis, metallic Ni species are indispensable for SA hydrogenolysis to GBL because reduced $CeO_{2-\delta}$ support was inactive for the reaction.

Furthermore, the specific activity of SA hydrogenolysis to GBL per Ni atom ($TOF_{SA \rightarrow GBL}$) showed a volcano-like relationship with Ni loading, and the optimal Ni loading was 17.5 wt%. Combined with characterisation results, highly dispersed Ni species and metallic Ni species governed the GBL yield. Due to the strong Ni-$CeO_{2-\delta}$ interaction, the highly dispersed Ni species can be cationised ($Ni^{\delta+}$) and promoted the formation of unsaturated CeO_x species with coordinative Ce cations, thus enhancing the activation of C=O and facilitating the hydrogenolysis of C=O on adjacent Ni^0. Such Ni^0-$Ni^{\delta+}$ synergism is a short-range interaction depending on the nickel loading on the xNi/$CeO_{2-\delta.}$ This finding well interprets the maximum GBL yield showed on the 17.5Ni/$CeO_{2-\delta}$ and the activity declines as further increase of Ni loading.

In Chapter 6, different shaped CeO_2 supports, nanorods (CeO_2-NR), nanocubes (CeO_2-NC) and nanoparticles (CeO_2-NP) were synthesised using a hydrothermal method and used as supports to prepare Ni-based catalysts for MA hydrogenation. We found that the rod-like CeO_2-NR support with abundant Ovac significantly enhanced Ni dispersion that improved hydrogen adsorption and activation on the Ni species. Compared with the 5Ni/$CeO_{2-\delta}$-NC and 5Ni/$CeO_{2-\delta}$-NP catalysts, the 5Ni/$CeO_{2-\delta}$-NR catalyst displayed the highest activity in C=C hydrogenation and the lowest apparent activation energy, revealing the pivotal roles of Ovac in MA→SA transformation. Furthermore, in the 8 h hydrogenation course, small amount of GBL was produced on the 5Ni/$CeO_{2-\delta}$-NC (5.24%) and 5Ni/$CeO_{2-\delta}$-NP (2.36%) catalysts but no GBL was produced on the 5Ni/$CeO_{2-\delta}$-NR catalyst, suggesting 5Ni/$CeO_{2-\delta}$-NR catalyst with highly dispersed Ni species and large amount of Ovac was not active for C=O hydrogenolysis.

The previous Chapters found that a short-range Ovac→Ni electronic interaction can enrich the surface electronic density of Ni catalyst and thus facilitate the C=C hydrogenation activity. This result indicates that negative Ni species are crucial for C=C hydrogenation. Accordingly, introducing a second metal, such as Cu, to Ni/$CeO_{2-\delta}$ catalyst would enable to modify electronic structure of Ni species and thus affect MA hydrogenation. In Chapter 7, the bimetallic Ni-Cu/$CeO_{2-\delta}$ catalysts with varying Ni/Cu ratios, prepared by an impregnation method, showed superior MA hydrogenation activity to monometallic Cu/$CeO_{2-\delta}$ and Ni/$CeO_{2-\delta}$ catalysts. The formation of Ni-Cu alloy improved the metal dispersion and strengthened the interaction between Ni and Cu, which led to the Ni→Cu electron transfer. Such electron interaction strengthened hydrogen adsorption on the metal surface and promoted MA hydrogenation. Moreover, the introduction of Cu to Ni significantly suppressed C=O hydrogenolysis, likely due to the repulsive effect between negative Ni species and electron-rich C=O group.

It is proposed that Ni-CeO_x interface that leads to cationic $Ni^{\delta+}$ formation due to the strong electronic perturbation of CeO_2 can enhance C=O hydrogenolysis. To confirm this, surface CeO_2 modified 15Ni/SiO_2 catalysts were prepared by the two-step impregnation method. The obtained xCeO_2@15Ni/SiO_2 catalysts showed higher activity for C=O hydrogenolysis than 15Ni/SiO_2 catalyst, even better than the 15Ni/$CeO_{2-\delta}$ catalyst. We supposed that surface strong interaction of Ni-$CeO_{2-\delta}$ played crucial roles in the C=O hydrogenolysis for the SA→GBL transformation. The characterisation results demonstrated that surface strong interaction between Ni and CeO_2 retarded NiO reduction and weakened the binding energy of atomic H adsorbed on Ni surface. The results suggested the strong metal-support electronic interaction due to the metal surface covered by reducible oxide, such as CeO_2, can reduce the interaction between catalyst and adsorbates. The cyclohexane adsorption spectra monitored by IR spectroscopy pointed out that introduction of CeO_2 to 15Ni/SiO_2 brought an additional strong chemical adsorption of the C=O group on the catalyst surface due to the strong electronic interaction between CeO_2 and Ni. Therefore, we concluded that the strong interaction between metallic Ni and CeO_2 can perturb the electronic configuration of Ni species and lead to formation of positive $Ni^{\delta+}$ species, resulting in enhanced C=O adsorption and consequently improved C=O hydrogenolysis.

In all, this thesis presented our new research findings for MA hydrogenation on Ni-based catalysts supported on $CeO_{2-\delta}$ supports. With solid characterisation and careful catalyst evaluation, we drew strong scientific findings as summarised below:

1.) The modified impregnation method developed by Dr Zheng Jiang team is an effective methodology to prepare high performance catalysts, by which high metal dispersion and strong metal-support can be realised.
2.) The structure defective $CeO_{2-\delta}$ is an active support for Ni-based MA hydrogenation catalysts, superior to those inert supports, such as Al_2O_3 and SiO_2. This is mainly because Ovac in $CeO_{2-\delta}$ is a kind of active site that adsorbs and activates H_2 as well as bring about the strong Ni-support interaction. The Ni-$CeO_{2-\delta}$ strong interaction is arisen from electron transfer from Ovac→Ni and Ni→Ce^{4+}, both occurring in the short range.
3.) Ni is an excellent transition metal catalyst superior to Co and Cu in MA hydrogenation, which is due to the valence electron configurations of the outermost 3*d* shell. The Cu with filled 3*d* electronic shell is not active for SA→GBL transformation because it is weak to activate H_2 and the C=O group.

4.) The Ovac density of $CeO_{2-\delta}$ supports is relevant to their morphologies. We found the $Ni/CeO_{2-\delta}$ nano-rod catalyst possessed higher Ovac density relative to the Ni catalysts supported on the nano-scaled $CeO_{2-\delta}$ supports with irregular morphology and nanocubes. The Ovac density and morphology-related $Ni-CeO_{2-\delta}$ interaction originate from the different atom configuration of the $CeO_{2-\delta}$ supports, which affect the adsorption/desorption, activation and hydrogenation of the reactants and products, eventually lead to different activity and selectivity.

5.) The electronic interaction between Ni-Cu and metal-$CeO_{2-\delta}$ brings in the superior performance on the $Ni-Cu/CeO_{2-\delta}$ bimetallic catalysts to the individual monometallic catalysts, in both the MA→SA and SA→GBL transformations. The electronic interaction within the catalysts involves electron transfers of Ni→Cu and metal→Ce^{4+} and Ovac→metal.

6.) Once CeO_2 used as a modifier rather than as the main support for Ni-based catalysts, there is an optimal CeO_2 loading to realise desirable MA hydrogenation performance. The loading of CeO_2 onto $15Ni/SiO_2$ catalysts led to dramatically enhanced GBL yield from SA hydrogenolysis but declined MA→SA transformation. The optimal CeO_2 loading was 3.0 wt%, whereas the further increase of CeO_2 loading led to masking the exposure of Ni species and reduced $Ni-CeO_2$ interface, which are the core hydrogenolysis active sites.

9.2 Outlook

Although the $Ni/CeO_{2-\delta}$ catalysts displayed high activity and selectivity in MA hydrogenation and their active sites for C=C hydrogenation and C=O hydrogenolysis have been preliminarily defined, there are still many aspects to be developed further. For the future work, the following suggestions may be useful for improving catalytic performance of Ni-based catalysts and in-depth understanding of the MA hydrogenation on Ni-based catalysts:

Firstly, to unveil the mechanism of MA hydrogenation is still unclear, especially for adsorption and activation of MA and the selective hydrogenolysis of C=O function group. Two plausible pathways for C=O hydrogenolysis are proposed: one is the direct hydrogenolysis of C=O by inserting two hydrogen molecules, and the other is first hydrogenation of C=O to form hydroxyl group prior to dehydration of the OH group to form the C=C bond which is finally hydrogenation to generate C-

C bond. To address this problem, the in-situ IR and in-situ XAS can be powerful tools to monitor the intermediates in the C=O hydrogenolysis process.

Secondly, to optimise the hydrogenation condition is required. In the thesis, the reaction pressure and temperature were fixed aiming to investigate the dependence of catalyst properties on the MA hydrogenation. It is necessary and highly desirable for the industrial application to optimise the reaction conditions, including defining the optimal solvent, H_2 pressure and hydrogenation temperature.

Thirdly, to expand the family of Ni-based bimetallic catalysts and to clarify the nature of the bimetallic interaction are required. Although our bimetallic Ni-Cu/$CeO_{2-\delta}$ catalysts displayed exceptional activity and selectivity in MA hydrogenation, showing great promise for industrial MA hydrogenation and other selective hydrogenation reactions, other bimetallic Ni-based systems with various second metals, such as Pd, Pt and Ru, may be explored to gain desirable performance. Furthermore, bimetallic catalysts can serve as excellent model catalysts to correlate the geometric and electronic structure with the catalytic activity and selectivity.

Fourthly, it is desirable to search cost-effective active supports to replace expensive ceria. As discussed in this thesis, the CeO_2 surface modified catalysts showed significant influences on the C=O hydrogenolysis, though the impacts of other reducible oxides such as ZnO and TiO_2 on C=O hydrogenolysis is unknown and worth investigating. The in-depth understanding of the roles of active oxide in C=O hydrogenoloysis is important and conducive to develop effective and economic catalysts for C=O hydrogenation.

Last but not the least, advanced techniques, especially in-situ characterisation to catalysts, are highly desirable to observe and understand the roles of the active sites in MA hydrogenation, the dynamic properties of the reaction intermediates. The acquired scientific insights will shed light on the structure-activity relationship for MA hydrogenation and guide the design of high quality industrial catalysts.

Appendix A The fundamental theory about characterisation

A.1 X-ray diffraction

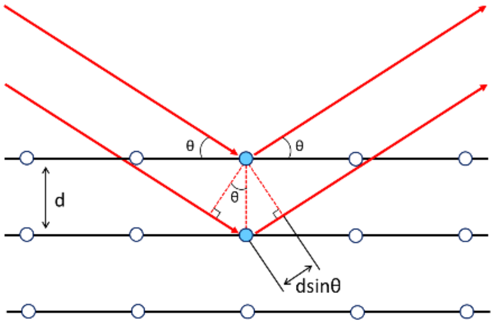

Figure A1 Simplified Illustration for Bragg diffraction

Powder X-ray Diffraction is a technique used to characterise the crystal structure and crystallite size in poly-crystalline or powder solid samples. In catalysis, XRD is also extensively employed to characterise heterogeneous solid catalysts and determine their crystal structure.

For a crystalline solid, the regular array of atoms in the structure can elastically scatter X-ray wave primarily through their electrons to many directions. Although these scattered waves can cancel one by another in most directions through destructive interference. However, some scattered waves can be coherent and enhance constructively in a few specific directions. In 1912, the Braggs, father and son, connected the observed scattering with reflections from evenly spaced planes within the crystal and described the condition that scattered waves can be enhance by the Bragg's law, as shown in Figure A1

$$\mathrm{n}\lambda = 2d_{hkl}\sin\theta$$

where d is the spacing between diffracting planes, θ is the incident angle, n is any integer, and λ is the wavelength of the beam. Based on the Bragg's Law, the position of a diffraction peak (2θ) is independent of the atoms within the crystal structure, but determined by the plane spacing. Thus, the spacing of planes can be calculated using the Bragg's Law with diffraction angle (2θ).

A.2 X-ray photoelectron spectroscopy

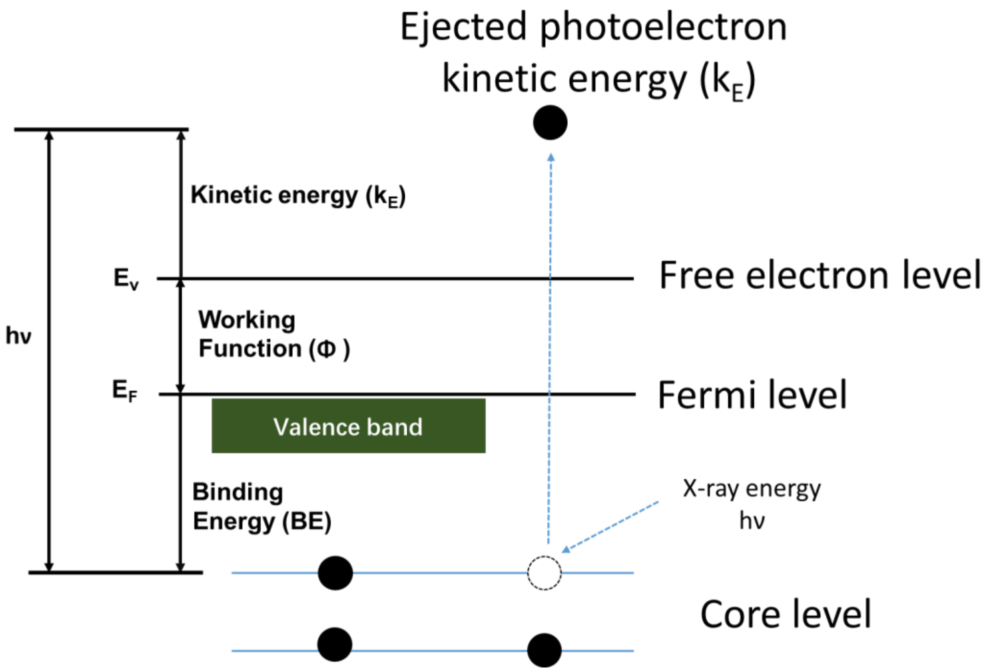
Ejected photoelectron
kinetic energy (k_E)
Kinetic energy (k_E)
E_v
Free electron level
hv
Working
Function (Φ)
E_F
Fermi level
Valence band
Binding
Energy (BE)
X-ray energy
hv
Core level

Figure A2 Typical illustration of the photoelectron emission from a model atom

X-ray photoelectron spectroscopy (XPS) is a quantitative spectroscopic technique that measures near-surface elemental composition as well as the chemical and electronic states of the elements. The fundamental theory of XPS is related to the photoelectric effect proposed by Einstein. As shown in Figure A2, a photon goes through a material and interacts with the electrons in the material. Adsorption of X-ray by an atom in a molecule or solid can result in ionisation with emission of a core (shell) electron. This process is described as:

$$\mathrm{A} + \mathrm{h\upsilon} \longrightarrow A^{+} + e^{-}$$

where A is the atom exposed to X-ray, hv represents the X-ray wave and A^+ is its ionised equivalent. Based on the law of conservation of energy, the process can be expressed as:

$$\mathrm{E(A)} + \mathrm{h\upsilon} = \mathrm{E}(A^{+}) + \mathrm{E}(e^{-})$$

where E(A), E(A^+) and E(e^-) represent the state energies of A, A^+ and e^-, respectively. Since the electron's energy is presented solely as kinetic energy (k_E), this equation can be adjusted to the following equation for the photoelectron k_E

$$k_E = \mathrm{h\upsilon} - [\mathrm{E}(A^{+}) - \mathrm{E(A)}]$$

As shown in Figure A2, the difference (E(A^+)-E(A)) is generally regarded as the binding energy (B.E.) of the electron plus working function (Φ), therefore, the energy formula can be arranged as following:

$$k_e = \mathrm{h\upsilon} - [\mathrm{BE} + \emptyset]$$

The binding energy can be regarded as the energy difference between the initial and final states after the photoelectron leaves from the atom. Because there are a variety of possibilities in the final states, various kinetic energies of the emitted electrons can be detected. However, each element has a unique set of binding energies, therefore XPS can be used to identify and determine the concentration of element on the surface of the material. Variations in the elemental binding energies, in particular the chemical shift, arise from differences in the chemical potential and polarizability of components, which is used to identify the chemical state of the analysed materials.

The final-state effect fundamentally consists of four types, which are described as follows:

Auger excitation: In terms of core ionisation by photoelectron emission, an outer shell electron can fill the created vacancy, whereby the electron moving to the lower energy level and releasing energy equal to the difference in orbital energies. The transition energy can be coupled to a second outer shell electron, which will be emitted from the atom if the transferred energy is greater than the orbital binding energy. The emitted electron is called as Auger electron and its kinetic energy can be descried as

$$E_{Aug} = E_{core\ state} - E_B - E_C$$

where $E_{core\ state}$, E_B and E_C are respectively the core level, first outer shell, and second outer shell electron binding energies, which can be measured from the vacuum level. This physical phenomenon that the filling of an inner-shell vacancy of an atom is accompanied by the emission of an electron from the same atom is the Auger process. The Auger process can affect the measured binding energy of the outgoing photoelectron.

Plasmon loss: Two types of plasma loss can occur during the photoelectron process. The bulk plasmon-loss happens when the outgoing photoelectron loses energy by interacting via collective oscillations in the bulk of materials. The surface plasmon-loss is related to the interaction of the outgoing photoelectron with surface plasmon state in the material. Generally, the energy of surface plasmon-loss is smaller than that for the bulk plasmon-loss. The effect of the plasmon-loss process is the generation of a new peaks or a series of peaks at higher apparent BE than the main XPS peak. The intensity of these peaks declines with distance from the primary peak and appears weaker than the primary XPS peaks. The position of a plasmon-loss peak relative to a primary peak depends on the type of materials.

Furthermore, the bulk and surface plasmon-loss peaks will be excluded for calculation of the total number of electrons emitted from the given orbital of an atom in the sample.

Relaxation: The relaxation process is to remove the partial charge from the valence band via a re-hybridisation of an atom. The magnitude of the decrease in BE due to relaxation can about several electron volts. The different chemical environment of atoms can vary the magnitude of the relaxation shift. It occurs to the same extent for all atoms in a material which stay in the same chemical and structural state. Therefore, it cannot result in a new peak in an XPS spectrum. It may be apparent in comparing of the position of a photoemission peaks from one sample to another.

Shake-up and shake-off: This process involves re-hybridisation of the ion to excite an electron in the valence band. In the shake-up process, the electronic excitation leads to promotion of a valence band electron. In the shake-off process, the electron is excited to a higher virtual state. Both shake-up and shift-off create a localised, occupied state above the initial E_F of the material which gives rise to a shift of the BE of the initial hole to higher value. The relaxation process leads to an overall increase in the background of a spectrum, by contrast, the shake-up and shake-off processes lead to the appearance of a new peak, called a satellite peak. The position of the satellite peak can be up to a few electron volts in BE above the primary photoelectron peak. The intensity of the satellite peak can be comparable to that of the main peak in some case [239].

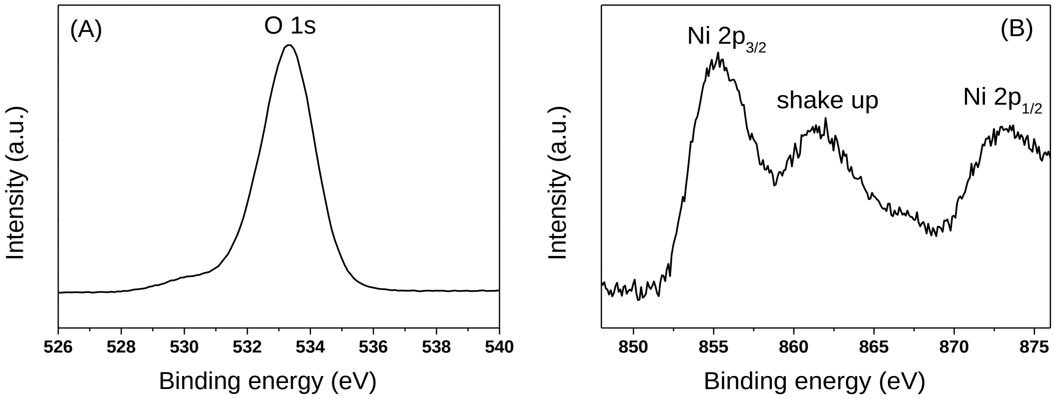

Figure A3 Typical XPS core level of O1s and Ni2p spectra

Figure A3 shows two typical XPS spectra of O1s and Ni2p. In the Ni2p XPS spectrum, the photoelectron peak related to 2p splits to two components $2p_{3/2}$ and $2p_{1/2}$. This phenomenon is commonly observed in the XPS spectrum for *p*, *d* and *f* peaks due to the interaction between the spins of the electron, *s* (up and down) and its orbital angular momentum, *l*. The values relative to spin-orbital splitting of a core level of an element in the different materials are nearly same, as well as the peak area ratios. However, the *s* orbitals do not split because their angular momentum is zero. For the *p* orbitals, vector coupling of spin-up and spin-down states with the ±1 orbital angular momentum vectors give total angular momentum of either $\frac{1}{2}$ (from |1-1/2| or |-1+1/2|) or $\frac{3}{2}$ (from |1+1/2| or |-1-1/2|). These two spin-orbital levels have different relative occupancies, roughly in proportion to the respective degeneracy of the levels, such as *p* 1:2, *d* 2:3 and *f* 3:4.

Besides the spin orbital splitting, another important phenomenon in the XPS spectrum is the chemical shift. For a specific element, different chemical bond can bring about different chemical environment, which can change the binding energy of a core electron of the atom, finally causing the chemical shift of XPS peaks. The core binding energies are determined by the electrostatic effect between the core level and the nucleus. The binding energy is also masked by the electrostatic shielding of the nuclear charge from all other electrons in the atoms. The increase or decrease in electronic charge will result in the chemical shift. In general, the removal of valence electron charge will cause an increase in binding energy while the addition of electron will give rise to a decrease in binding energy.

A.3 Raman spectroscopy

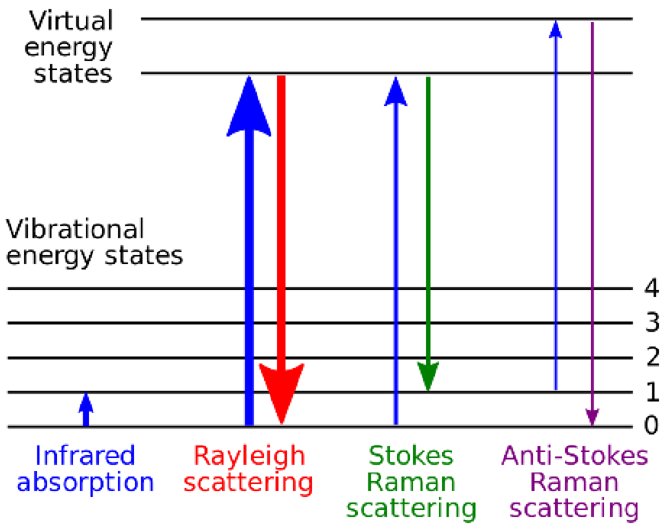

Figure A4 Working principle of Raman spectroscopy

Raman spectroscopy is a powerful tool for structural analysis, which was developed by Sir C. V. Raman and Kirishnan in 1928. Based on their theory, a laser light is incident on vibrating molecules, leading to the excitation of the photons to high-energy state. The exited molecules or atoms can return to different states. The excited molecule goes to a higher or lower frequency than the original state and this phenomenon is known as the Stokes Raman scattering or the anti-Stokes Raman scattering, respectively. A detailed description of the working principle is shown in Figure A4. Compared with Rayleigh scattering, Raman scattering displays 10^{-6} to 10^{-9} times less intensity. Hence, a laser with the high energy is required for the Raman scattering. It is found that Raman scattering is dependent on the chemical composition and structure of molecules and Raman shifts are characteristic of the compounds. Thus, Raman shift may be useful in distinguishing the structures of different constituents and molecules.

A.4 BET theory for surface area determination

The BET theory is applied to explain the physical multilayer adsorption of gas molecules on a solid surface, which was developed by Stephen Brunauer, Paul Hugh Emmett and Edward Teller in 1938.[252] The authors extended the Langmuir theory, which is used to address the monolayer molecule adsorption, to the multilayer gaseous adsorption with three hypotheses: (a) physical adsorption of gas molecule on the infinite surface of a solid; (b) the interaction of gas molecule being restricted to adjacent layers; (c) the Langmuir theory being applied for each layer. The BET equation can be expressed as:

$$\frac{P}{V(P_0-P)}=\frac{1}{V_mC}+\frac{(C-1)P}{V_mCP_0}$$

where P is the pressure of the adsorbate gas; P_0 is the saturated pressure of adsorbate gas; V is the volume of adsorbed gas; V_m is the volume of monolayer adsorbed gas; C is the BET constant.

Additionally, The BET content (C) can be described as

$$C=e^{(E_1-E_L)/RT}$$

where E_1 is the heat of adsorption on the first layer, E_L is the heat of liquefaction on second and subsequent layers, R is the ideal gas constant (8.314 J/(K • mol)) and T is the temperature.

Nowadays, the BET theory has been widely used as the fundamental theory for the measurement of the specific surface area of materials. The specific surface area can be determined by the volume of monolayer adsorbed gas (V_m). Based on the BET equation, several measurements of P/P_0 can be used to produce a linear plot of $1/V(P_0\text{-}P)$ against P/P_0 with a gradient equal to $(C\text{-}1)/V_mC$ (denoted as K) and a y-intercept equal to $1/V_mC$ (denoted as B). With the gradient and the intercept, a value of V_m can be calculated using the following method:

$$V_m = \frac{1}{K + B}$$

where K and B are the intercept and gradient respectively. The total surface area of the catalyst can be determined using the following equation:

$$S_{BET} = \frac{NV_M\sigma}{V}$$

where N is the Avogadro's constant (6.022×10^{23} mol^{-1}), V is the molar volume of adsorbed gas and σ is the cross-sectional area of adsorbed gas (0.162 nm^2/mol for N_2[253]). The specific surface area is obtained from the total surface area divided by the mass of the catalyst ($S = S_{total}/m$).

Appendix B The auxiliary results of MA conversion over Ni/CeO$_{2-\delta}$ catalyst

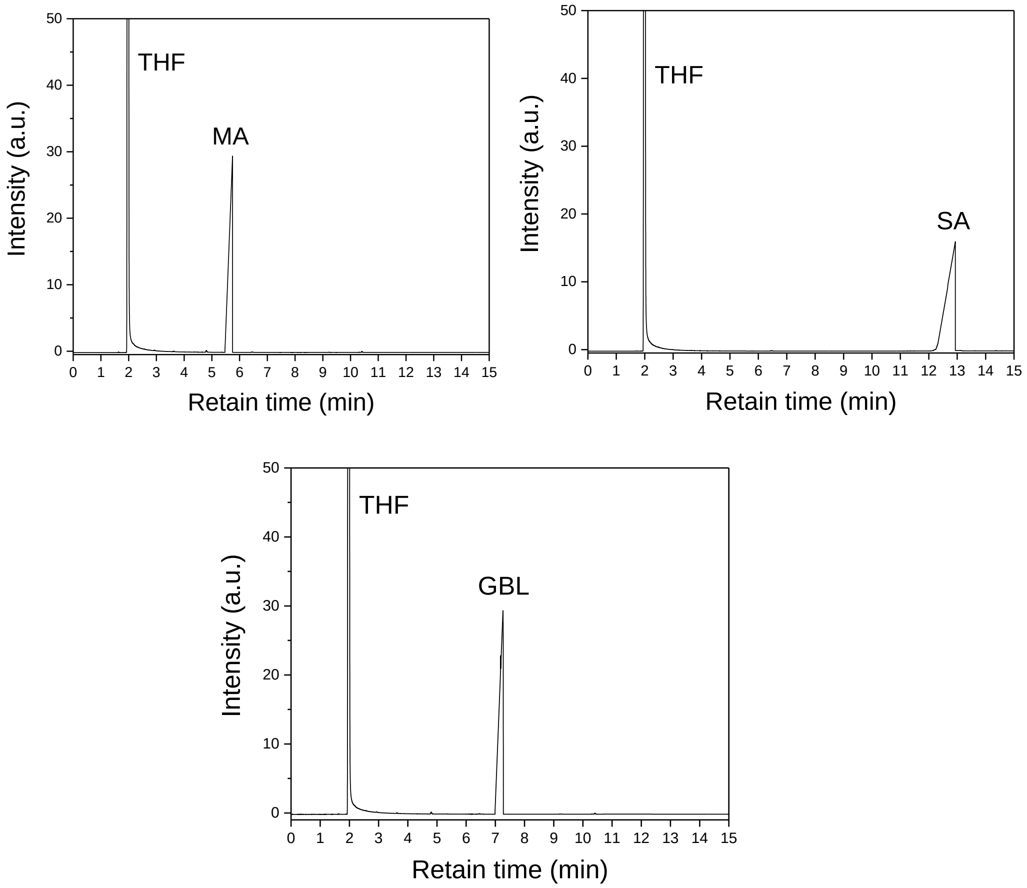

Figure B1 The typical GC spectra for the MA, SA and GBL dissolved in THF

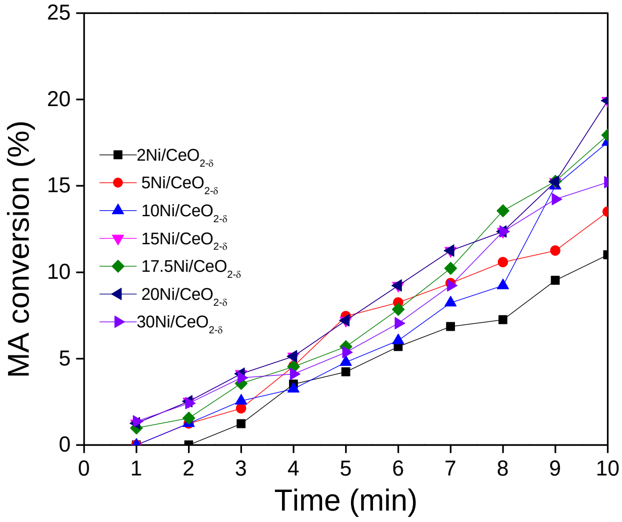

Figure B2 The MA conversion over xNi/CeO$_{2-\delta}$ catalysts at 210℃ and 5 MPa for 10 min (Chapter 5)

Table B1 The metal loading and dispersion of examined catalysts in the thesis

Sample	Metal loading	Metal dispersion (%)
Chapter 3		
10Ni/$CeO_{2-\delta}$	10.8	4.4
10Ni/Al_2O_3	10.5	3.8
Chapter 4		
10Co/$CeO_{2-\delta}$	10.3	3.9
10Ni/$CeO_{2-\delta}$	9.8	4.4
10Cu/$CeO_{2-\delta}$	9.7	2.9
Chapter 5		
2Ni/$CeO_{2-\delta}$	1.9	16.9
5Ni/$CeO_{2-\delta}$	4.8	9.3
10Ni/$CeO_{2-\delta}$	10.2	5.2
15Ni/$CeO_{2-\delta}$	15.3	4.7
17.5Ni/$CeO_{2-\delta}$	17.2	4.1
20Ni/$CeO_{2-\delta}$	20.5	3.2
30Ni/$CeO_{2-\delta}$	29.1	1.4
Chapter 6		
5Ni/$CeO_{2-\delta}$-NP	5.2	25.7
5Ni/$CeO_{2-\delta}$-NR	4.7	66.1
5Ni/$CeO_{2-\delta}$-NC	4.8	10.9
Chapter 8		
15Ni/SiO_2	14.89 (Ni), 0(Ce)	10.7
1CeO_2@15Ni/SiO_2	14.88 (Ni), 0.87(Ce)	7.0
3CeO_2@15Ni/SiO_2	14.89 (Ni), 3.15(Ce)	6.1
5CeO_2@15Ni/SiO_2	14.89 (Ni), 5.05(Ce)	5.0

Note: The metal loading is determined by ICP-OES and the percentage of Ni dispersion is calculated using the equation (2.5), which is described in Chapter 2.

Table B2 The MA conversion over the three 5Ni/$CeO_{2-\delta}$ catalysts with different morphologies at different temperature (Chapter 6)

Sample	T(°C)	Reaction time (min)						rate constant (k) (min^{-1})
		10	20	30	40	50	60	
5Ni/$CeO_{2-\delta}$-P	120	6.50	15.1	21.8	28.5	32.4	40.1	0.0082
	140	10.3	28.1	36.5	45.9	56.9	62.2	0.0161
	160	18.5	48.2	68.1	76.9	88.2	91.8	0.0393
	180	28.4	62.3	76.5	88.8	92.7	96.5	0.0534
5Ni/$CeO_{2-\delta}$-R	120	10.4	18.9	25.8	30.8	38.3	45.9	0.0099
	140	20.3	36.1	50.4	60.5	72.5	80.6	0.0255
	160	26.4	55.3	75.6	86.9	90.3	95.6	0.0461
	180	33.5	69.6	88.8	93.4	96.8	98.6	0.0693
5Ni/$CeO_{2-\delta}$-C	120	2.27	7.58	11.2	15.9	19.5	22.5	0.0042
	140	5.7	16.8	30.4	38.5	46.6	53.8	0.0123
	160	13.6	38.5	57.8	68.9	79.5	86.5	0.0311
	180	20.6	48.5	64.5	77.7	88.5	93.4	0.0415

Appendix C Bimetallic Ni-M/$CeO_{2-\delta}$ systems for MA hydrogenation

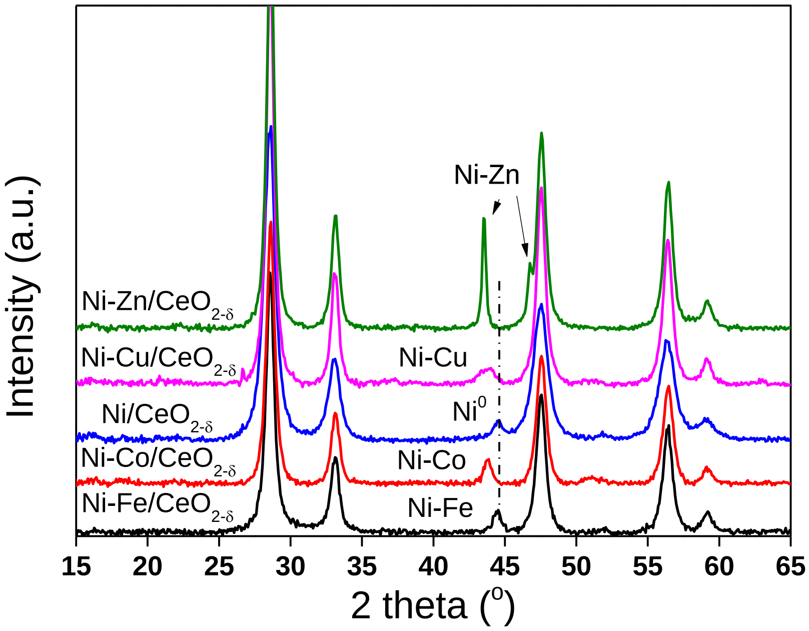

Figure C1 XRD patterns of various Ni-M/$CeO_{2-\delta}$ catalysts

The various Ni-M alloys are formed in the reduced Ni-M/$CeO_{2-\delta}$ catalysts due to the shift peaks relative to the metallic Ni phase.

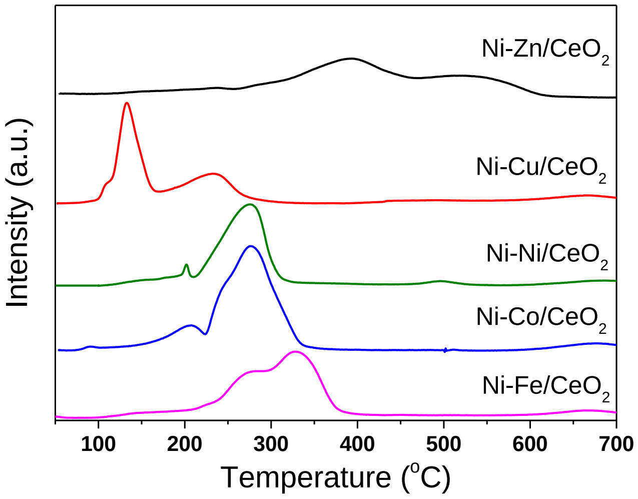

Figure C2 H_2-TPR profiles of Ni-M/CeO_2 precursors (M= Fe, Co, Cu and Zn)

The distinct reduction behaviours of various Ni-M/$CeO_{2-\delta}$ catalysts indicate that different interaction between Ni and induced metals.

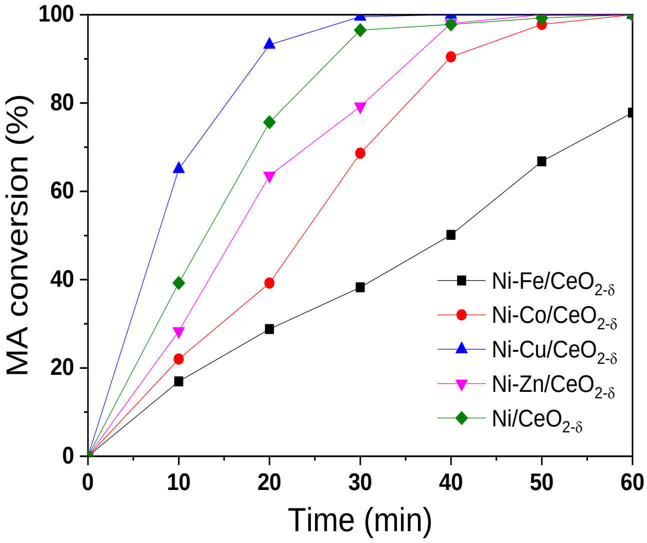

Figure C3 MA conversion over various Ni-M/$CeO_{2-\delta}$ catalysts at 210°C for 1 h

Various bimetallic Ni-M/$CeO_{2-\delta}$ catalysts display different activity in MA hydrogenation. In particular, bimetallic Ni-Cu/$CeO_{2-\delta}$ catalysts display the highest activity in the MA hydrogenation.

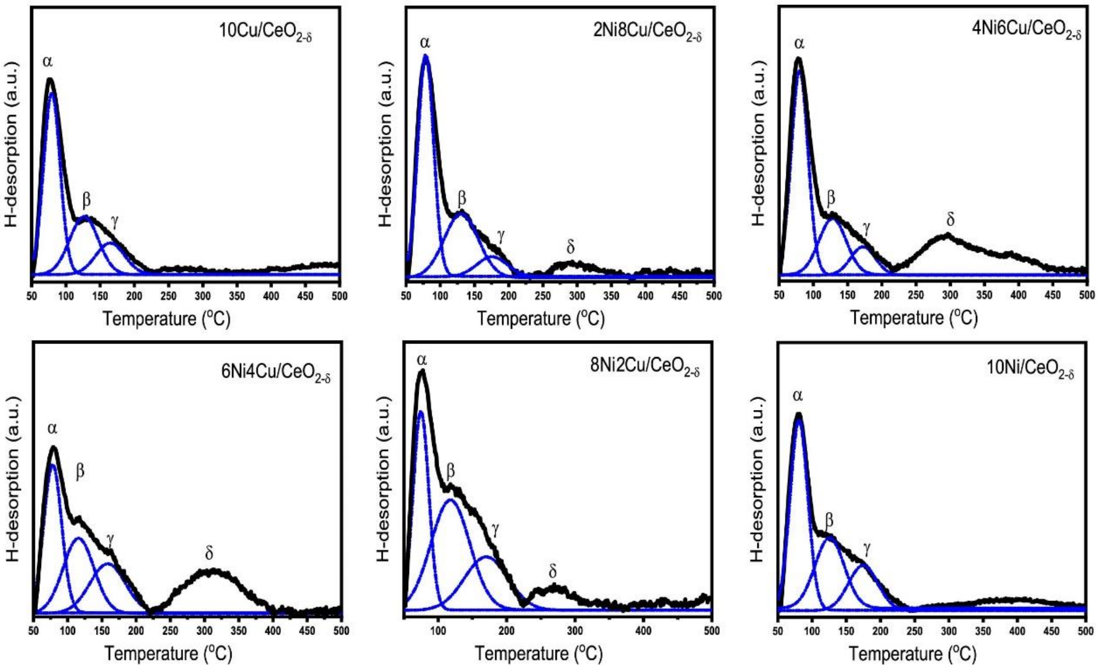

Figure C4 H_2-TPD profiles of xNiyCu/$CeO_{2-\delta}$ catalysts with fitting peaks

Publications

1. Xin Liao, Yin Zhang, Martyn Hill, Xin Xia, Yongxiang Zhao, and Zheng Jiang, Highly efficient Ni/CeO_2 catalyst for the liquid phase hydrogenation of maleic anhydride, *Applied Catalysis A, General*, 2014, 488: 256–264. DOI: 10.1016/j.apcata.2014.09.042

2. Xin Liao, Yin Zhang, Junqiu Guo, Lili Zhao, Martyn Hill, Zheng Jiang and Yongxiang Zhao, The catalytic hydrogenation of maleic anhydride on $CeO_{2-\delta}$-supported transition metal catalysts, Catalysts, 2017, 7,212-287. DOI: 10.3390/catal7090272

3. Xin Liao, Rihards Gerdts, Stewart F. Parker, Lina Chi, Yongxiang Zhao, Martyn Hill, Junqiu Guo, Martin O. Jones and Zheng Jiang, An in-depth understanding of the bimetallic effects and coked carbon species on an active bimetallic Ni(Co)/Al_2O_3 dry reforming catalyst. *Physical Chemistry Chemical Physics*, 2016, 18(26), 17311-17319. DOI: 10.1039/C6CP01089J

4. Zheng Jiang, Xin Liao, Yongxiang Zhao, Comparative study of the dry reforming of methane on fluidised aerogel and xerogel Ni/Al_2O_3 catalysts. *Applied Petrochemical Research*, 2013, 3(3-4), 91-99. DOI: 10.1007/s13203-013-0035-9

5. Selective Hydrogenation of Maleic Anhydride on Ni/$CeO_{2-\delta}$ Catalysts: Defining the Active Sites and their Roles in Hydrogenation，Journal of Catalyst, Manuscript number: JCAT-17-126

6. Junqiu Guo, Xin Liao, Ming-Hsien Lee, Geoff Hyett, Chung-Che Huang, Daniel W. Hewak, Sakellaris Mailis, Wei Zhou, Zheng Jiang. Experimental and DFT insights of the Zn-doping effects on the visible-light photocatalytic water splitting and dye decomposition over Zn-doped BiOBr photocatalysts, Applied Catalysis B, Environmental, in press, DOI: 10.1016/j.apcatb.2018.09.089

7. Xin Liao, Shape-dependent interaction between oxygen vacancies and Ni species in Ni/$CeO_{2-\delta}$ catalysts and their catalytic performance in the hydrogenation of maleic anhydride, in preparation

8. Xin Liao, Facile synthesis of Ni-CeO_2 heterojunction in the xCeO_2@Ni/SiO_2 catalysts and its enhancement in the hydrogenation of maleic anhydride, in preparation

Conference

1. Unusual alloy effects of bimetallic Ni-Cu/$CeO_{2-\delta}$ catalyst in catalytic hydrogenation of maleic anhydride, oral presentation in the 23rd Joint Annual Conference of the Chinese Society of Chemical Science and Technology in the UK and Society of Chemical Industry's Chinese UK Reginal Group (CSCST-SCI), 3rd September, 2016, Nottingham, UK

2. Clothing $CeO_{2-\delta}$ on Ni/SiO_2 catalyst: Exceptional activity in the hydrogenation of biomass-derived succinic anhydride, oral presentation in the 24th annual conference of CSCST-SCI, 23rd June, 2017, Newcastle upon Tyne, UK

3. Application of inelastic neutron scattering to studies of CO_2 reforming of methane over bimetallic Ni-Co/Al_2O_3catalyst, & A robust bimetallic Ni-Cu/$CeO_{2-\delta}$ catalyst for maleic anhydride hydrogenation, two posters in 16th international congress on catalysis,3rd-8th July, 2016, Beijing, China

4. Highly efficient Ni/CeO_2 catalyst for the liquid phase hydrogenation of maleic anhydride, oral presentation in EU-China workshop on resource recovery from biomass and green technology in waste/wastewater treatment, 8th-9th November, 2014, ShangHai, China.

Bibliography

[1] E. K. Rideal, Paul Sabatier. 1859-1941. *Obituary Notices of Fellows of the Royal Society*, 1942, **4,** 63-66.

[2] P. N. Rylander, Hydrogenation methods, Academic Pr, 1990.

[3] R. Augustine, L. Doyle, S. Malhotra, *et al.*, Heterogeneous catalysis in organic synthesis. *Catalysis of Organic Reactions*, 1994, **62,** 81.

[4] H. Pines, The chemistry of catalytic hydrocarbon conversions, Elsevier, 2012.

[5] V. Ponec, G. C. Bond, Catalysis by metals and alloys, Elsevier, 1995.

[6] P. Mäki-Arvela, J. Hájek, T. Salmi, *et al.*, Chemoselective hydrogenation of carbonyl compounds over heterogeneous catalysts. *Applied Catalysis A: General*, 2005, **292,** 1-49.

[7] U. K. Singh, M. A. Vannice, Kinetics of liquid-phase hydrogenation reactions over supported metal catalysts — a review. *Applied Catalysis A: General*, 2001, **213,** 1-24.

[8] W. Wang, S. Wang, X. Ma, *et al.*, Recent advances in catalytic hydrogenation of carbon dioxide. *Chemical Society Reviews*, 2011, **40,** 3703-3727.

[9] K. Weissermel, H.J. Arpe, Industrial Organic Chemistry, Fourth Edition, 2003.

[10] H.U. Blaser, C. Malan, B. Pugin, *et al.*, Selective Hydrogenation for Fine Chemicals: Recent Trends and New Developments. *Advanced Synthesis & Catalysis*, 2003, **345,** 103-151.

[11] S. De, J. Zhang, R. Luque, *et al.*, Ni-based bimetallic heterogeneous catalysts for energy and environmental applications. *Energy & Environmental Science*, 2016, **9,** 3314-3347.

[12] V. Ponec, On the role of promoters in hydrogenations on metals; α ,β - unsaturated aldehydes and ketones. *Applied Catalysis A: General*, 1997, **149,** 27-48.

[13] C. Milone, G. Neri, A. Donato, *et al.*, Selective Hydrogenation of Benzene to Cyclohexene on Ru/γ -Al_2O_3. *Journal of Catalysis*, 1996, **159,** 253-258.

[14] H. Li, X. Chen, M. Wang, *et al.*, Selective hydrogenation of cinnamaldehyde to cinnamyl alcohol over an ultrafine Co-B amorphous alloy catalyst. *Applied Catalysis A: General*, 2002, **225,** 117-130.

[15] H. Inoue, S. Sato, R. Takahashi, *et al.*, Dehydration of 1,4-butanediol over supported rare earth oxide catalysts. *Applied Catalysis A: General*, 2009, **352,** 66-73.

[16] B. Elvers, S. Hawkins, W. Russey, Ullmann's encyclopedia of industrial chemistry, Wiley Online Library, 1989.

[17] G. V. Research, Maleic Anhydride Market Size in, http://www.grandviewresearch.com/press-release/maleic-anhydride-market-report, 2016.

[18] J. R. Fernández, A. Vega, F. V. Díez, Partial oxidation of n-butane to maleic anhydride over VPO in a simulated circulating fluidized bed reactor. *Applied Catalysis A: General*, 2010, **376,** 76-82.

[19] N. Alonso-Fagúndez, M. L. Granados, R. Mariscal, *et al.*, Selective Conversion of Furfural to Maleic Anhydride and Furan with VO_x/Al_2O_3 Catalysts. *ChemSusChem*, 2012, **5,** 1984-1990.

[20] Z. Du, J. Ma, F. Wang, *et al.*, Oxidation of 5-hydroxymethylfurfural to maleic anhydride with molecular oxygen. *Green Chemistry*, 2011, **13,** 554.

[21] J. Lan, J. Lin, Z. Chen, *et al.*, Transformation of 5-Hydroxymethylfurfural (HMF) to Maleic Anhydride by Aerobic Oxidation with Heteropolyacid Catalysts. *ACS Catalysis*, 2015, **5,** 2035-2041.

[22] J. M. Pinazo, M. E. Domine, V. Parvulescu, *et al.*, Sustainability metrics for succinic acid production: A comparison between biomass-based and petrochemical routes. *Catalysis Today*, 2015, **239,** 17-24.

[23] C. Delhomme, D. Weuster-Botz, F. E. Kühn, Succinic acid from renewable resources as a C4 building-block chemical—a review of the catalytic possibilities in aqueous media. *Green Chemistry*, 2009, **11,** 13.

[24] J. J. Bozell, G. R. Petersen, Technology development for the production of biobased products from biorefinery carbohydrates—the US Department of Energy's "Top 10" revisited. *Green Chemistry*, 2010, **12,** 539.

[25] T. Jian Ping, J. Md Jahim, S. Harun, *et al.*, Overview of the Potential of Bio-Succinic Acid Production from Oil Palm Fronds. *Journal of Physical Science*, 2017, **28,** 53-72.

[26] X. Liao, Y. Zhang, M. Hill, *et al.*, Highly efficient Ni/CeO_2 catalyst for the liquid phase hydrogenation of maleic anhydride. *Applied Catalysis A: General*, 2014, **488,** 256-264.

[27] Y.S. Yoon, H. Khil Shin, B.S. Kwak, Ring conversion of γ -butyrolactone into N-methyl-2-pyrrolidone over modified zeolites. *Catalysis Communications*, 2002, **3,** 349-355.

[28] Y.L. Zhu, H.W. Xiang, G.S. Wu, *et al.*, A novel route for synthesis of γ -butyrolactone through the coupling of hydrogenation and dehydrogenation. *Chemical Communications*, 2002, 254-255.

[29] N. Wongittharom, C.H. Wang, Y.C. Wang, *et al.*, Charge-storage performance of Li/$LiFePO_4$ cells with additive-incorporated ionic liquid electrolytes at various temperatures. *Journal of Power Sources*, 2014, **260,** 268-275.

[30] S. S. Zhang, D. Foster, J. Read, A low temperature electrolyte for primary Li/CFx batteries. *Journal of Power Sources*, 2009, **188,** 532-537.

[31] Y. Matsuda, T. Fukushima, Y. Katoh, *et al.*, Characteristics of gel alkylene oxide polymer electrolytes containing γ -butyrolactone. *Journal of Power Sources*, 2003, **119–121,** 473-477.

[32] U. R. Pillai, E. Sahle-Demessie, D. Young, Maleic anhydride hydrogenation over Pd/Al_2O_3 catalyst under supercritical CO_2 medium. *Applied Catalysis B: Environmental*, 2003, **43,** 131-138.

[33] U. Herrmann, G. Emig, Liquid Phase Hydrogenation of Maleic Anhydride and Intermediates on Copper-Based and Noble Metal Catalysts. *Industrial & Engineering Chemistry Research*, 1997, **36,** 2885-2896.

[34] Y. Hara, H. Kusaka, H. Inagaki, *et al.*, A Novel Production of γ -Butyrolactone Catalyzed by Ruthenium Complexes. *Journal of Catalysis*, 2000, **194,** 188-197.

[35] L. Pu, L. Ye, Y. Yuanqi, Homogeneous hydrogenation of maleic anhydride to succinic anhydride catalyzed by Rh complex catalyst. *Journal of Molecular Catalysis A: Chemical*, 1999, **138,** 129-133.

[36] P. Fouilloux, The nature of raney nickel, its adsorbed hydrogen and its catalytic activity for hydrogenation reactions. *Applied Catalysis*, 1983, **8,** 1-42.

[37] Y. Feng, H. Yin, A. Wang, *et al.*, Selective hydrogenation of maleic anhydride to succinic anhydride catalyzed by metallic nickel catalysts. *Applied Catalysis A: General*, 2012, **425-426,** 205-212.

[38] P. Mäki-Arvela, L. P. Tiainen, M. Lindblad, *et al.*, Liquid-phase hydrogenation of citral for production of citronellol: catalyst selection. *Applied Catalysis A: General*, 2003, **241,** 271-288.

[39] A. J. Marchi, D. A. Gordo, A. F. Trasarti, *et al.*, Liquid phase hydrogenation of cinnamaldehyde on Cu-based catalysts. *Applied Catalysis A: General*, 2003, **249,** 53-67.

[40] C. I. Meyer, A. J. Marchi, A. Monzon, *et al.*, Deactivation and regeneration of Cu/SiO_2 catalyst in the hydrogenation of maleic anhydride. Kinetic modeling. *Applied Catalysis A: General*, 2009, **367,** 122-129.

[41] C. I. Meyer, S. A. Regenhardt, A. J. Marchi, *et al.*, Gas phase hydrogenation of maleic anhydride at low pressure over silica-supported cobalt and nickel catalysts. *Applied Catalysis A: General*, 2012, **417-418,** 59-65.

[42] S. H. Vaidya, C. V. Rode, R. V. Chaudhari, Bimetallic Pt–Sn/γ -alumina catalyst for highly selective liquid phase hydrogenation of diethyl succinate to γ -butyrolactone. *Catalysis Communications*, 2007, **8,** 340-344.

[43] J. Li, W. P. Tian, L. Shi, Hydrogenation of Maleic Anhydride to Succinic Anhydride over Ni/HY-Al_2O_3. *Industrial & Engineering Chemistry Research*, 2010, **49,** 11837-11840.

[44] R. I. Masel, Principles of adsorption and reaction on solid surfaces, John Wiley & Sons, 1996.

[45] M. Armbrüster, M. Behrens, F. Cinquini, *et al.*, How to Control the Selectivity of Palladium-based Catalysts in Hydrogenation Reactions: The Role of Subsurface Chemistry. *ChemCatChem*, 2012, **4,** 1048-1063.

[46] S. M. Jung, E. Godard, S. Y. Jung, *et al.*, Liquid-phase hydrogenation of maleic anhydride over Pd–Sn/SiO2. *Catalysis Today*, 2003, **87,** 171-177.

[47] B. Tapin, F. Epron, C. Especel, *et al.*, Study of Monometallic Pd/TiO_2 Catalysts for the Hydrogenation of Succinic Acid in Aqueous Phase. *ACS Catalysis*, 2013, **3,** 2327-2335.

[48] A. Dandekar, M. A. Vannice, Crotonaldehyde Hydrogenation on Pt/TiO_2 and Ni/TiO_2 SMSI Catalysts. *Journal of Catalysis*, 1999, **183,** 344-354.

[49] J. Xu, K. Sun, L. Zhang, *et al.*, A Novel Synthesis Route of Butyric Acid from Hydrogenation of Maleic Anhydride over Pd/TiO2 Catalysts. *Catalysis Letters*, 2006, **107,** 5-11.

[50] B. Tapin, F. Epron, C. Especel, *et al.*, Influence of the Re introduction method onto Pd/TiO_2 catalysts for the selective hydrogenation of succinic acid in aqueous-phase. *Catalysis Today*, 2014, **235,** 127-133.

[51] M. A. Mabry, W. W. Prichard, S. B. Ziemecki; Pd/Re hydrogenation catalyst for making tetrahydrofuran and 1,4-butanediol. US4609636 A, 1986.

[52] J. P. Lange; Process for hydrogenation. US20110112326, 2011.

[53] S. E. Pedersen, J. G. Frye, T. G. Attig, *et al.*; Catalysts for the hydrogenation of aqueous maleic acid to 1,4-butanediol. US5698749 A, 1997.

[54] M. Kitson, P. S. Williams; Catalyzed hydrogenation of carboxylic acids and their anhydrides to alcohols and/or esters. US4985572 A, 1991.

[55] S. M. Jung, E. Godard, S. Y. Jung, *et al.*, Liquid-phase hydrogenation of maleic anhydride over Pd/SiO_2: effect of tin on catalytic activity and deactivation. *Journal of Molecular Catalysis A: Chemical*, 2003, **198,** 297-302.

[56] H. Jeong, T. Hwan Kim, K. Ill Kim, *et al.*, The hydrogenation of maleic anhydride to γ -butyrolactone using mixed metal oxide catalysts in a batch-type reactor. *Fuel Processing Technology*, 2006, **87,** 497-503.

[57] U. R. Pillai, E. Sahle-Demessie, Selective hydrogenation of maleic anhydride to Î³-butyrolactone over Pd/Al_2O_3 catalyst using supercritical CO_2 as solvent. *Chemical Communications*, 2002, 422-423.

[58] W. Leitner, Supercritical Carbon Dioxide as a Green Reaction Medium for Catalysis. *Accounts of Chemical Research*, 2002, **35,** 746-756.

[59] Q. Wang, H. Cheng, R. Liu, *et al.*, Influence of metal particle size on the hydrogenation of maleic anhydride over Pd/C catalysts in $scCO_2$. *Catalysis Today*, 2009, **148,** 368-372.

[60] Y. Ma, Y. Huang, Y. Cheng, *et al.*, Selective liquid-phase hydrogenation of maleic anhydride to succinic anhydride on biosynthesized Ru-based catalysts. *Catalysis Communications*, 2014, **57,** 40-44.

[61] U. G. Hong, H. W. Park, J. Lee, *et al.*, Hydrogenation of succinic acid to γ -butyrolactone (GBL) over ruthenium catalyst supported on surfactant-templated mesoporous carbon. *Journal of Industrial and Engineering Chemistry*, 2012, **18,** 462-468.

[62] X. Di, C. Li, B. Zhang, *et al.*, Role of Re and Ru in Re–Ru/C Bimetallic Catalysts for the Aqueous Hydrogenation of Succinic Acid. *Industrial & Engineering Chemistry Research*, 2017, **56,** 4672-4683.

[63] J. A. T. Schwartz; Ru,Re/carbon catalyst for hydrogenation in aqueous solution. US5478952 A, 1995.

[64] P. A. Tooley, J. R. Black; Ru, Sn/oxide catalyst and process for hydrogenation in acidic aqueous solution. US5985789 A, 1999.

[65] D. Campos; Ruthenium-molybdenum catalyst for hydrogenation in aqueous solution. US20040122242 A1, 2004.

[66] S. A. Regenhardt, A. F. Trasarti, C. I. Meyer, *et al.*, Selective gas-phase conversion of maleic anhydride to propionic acid on Pt-based catalysts. *Catalysis Communications*, 2013, **35,** 59-63.

[67] G. Budroni, A. Corma, Gold and gold–platinum as active and selective catalyst for biomass conversion: Synthesis of γ -butyrolactone and one-pot synthesis of pyrrolidone. *Journal of Catalysis*, 2008, **257,** 403-408.

[68] U. Herrmann, G. Emig, Kinetics and Mechanism in the Liquid-Phase Hydrogenation of Maleic Anhydride and Intermediates. *Chemical Engineering & Technology*, 1998, **21,** 285-295.

[69] G. Castiglioni, A. Vaccari, G. Fierro, *et al.*, Structure and reactivity of copper-zinc-cadmium chromite catalysts. *Applied Catalysis A: General*, 1995, **123,** 123-144.

[70] G. L. Castiglioni, M. Ferrari, A. Guercio, *et al.*, Chromium-free catalysts for selective vapor phase hydrogenation of maleic anhydride to γ -butyrolactone. *Catalysis Today*, 1996, **27,** 181-186.

[71] D. Zhang, H. Yin, J. Xue, *et al.*, Selective Hydrogenation of Maleic Anhydride to Tetrahydrofuran over Cu−Zn−M (M = Al, Ti, Zr) Catalysts Using Ethanol As a Solvent. *Industrial & Engineering Chemistry Research*, 2009, **48,** 11220-11224.

[72] D. Zhang, H. Yin, R. Zhang, *et al.*, Gas Phase Hydrogenation of Maleic Anhydride to γ -Butyrolactone by Cu–Zn–Ce Catalyst in the Presence of n-Butanol. *Catalysis Letters*, 2007, **122,** 176-182.

[73] J. Li, L.-P. Qian, L.-Y. Hu, *et al.*, Low-temperature hydrogenation of maleic anhydride to succinic anhydride and γ -butyrolactone over pseudo-boehmite derived alumina supported metal (metal=Cu, Co and Ni) catalysts. *Chinese Chemical Letters*, 2016, **27,** 1004-1008.

[74] Y. Yu, Y. Guo, W. Zhan, *et al.*, Gas-phase hydrogenation of maleic anhydride to γ -butyrolactone at atmospheric pressure over Cu–CeO_2–Al_2O_3 catalyst. *Journal of Molecular Catalysis A: Chemical*, 2011, **337,** 77-81.

[75] S. Guo, W. Tian, L. Shi, Hydrogenation of maleic anhydride to succinic anhydride over nickel/clay catalysts. *Transition Metal Chemistry*, 2012, **37,** 757-763.

[76] M. E. Bertone, C. I. Meyer, S. A. Regenhardt, *et al.*, Highly selective conversion of maleic anhydride to γ -butyrolactone over Ni-supported catalysts prepared by precipitation–deposition method. *Applied Catalysis A: General*, 2015, **503,** 135-146.

[77] M. Englisch, A. Jentys, J. A. Lercher, Structure Sensitivity of the Hydrogenation of Crotonaldehyde over Pt/SiO_2 and Pt/TiO_2. *Journal of Catalysis*, 1997, **166,** 25-35.

[78] C.-g. Gao, Y.-x. Zhao, Y. Zhang, *et al.*, Synthesis characterization and catalytic evaluation of Ni/ZrO_2/SiO_2 aerogels catalysts. *Journal of Sol-Gel Science and Technology*, 2007, **44,** 145-151.

[79] C. I. Meyer, S. A. Regenhardt, M. E. Bertone, *et al.*, Gas-Phase Maleic Anhydride Hydrogenation Over Ni/SiO_2–Al_2O_3 Catalysts: Effect of Metal Loading. *Catalysis Letters*, 2013, **143,** 1067-1073.

[80] Y. Yang, Y. Zhang, C. Gao, *et al.*, Selective Hydrogenation of Maleic Anhydride to γ -Butyrolactone over TiO_x(x< 2) Surface-Modified Ni/TiO_2-SiO_2 in Liquid Phase *Chinese Journal of Catalysis*, 2011, **32,** 1768-1774.

[81] C.G. Gao, Y.X. Zhao, D.-s. Liu, Liquid phase hydrogenation of maleic anhydride over nickel catalyst supported on ZrO_2–SiO_2 composite aerogels. *Catalysis Letters*, 2007, **118,** 50-54.

[82] C. C. Torres, J. B. Alderete, C. Mella, *et al.*, Maleic anhydride hydrogenation to succinic anhydride over mesoporous Ni/TiO_2 catalysts: Effects of Ni loading and temperature. *Journal of Molecular Catalysis A: Chemical*, 2016, **423,** 441-448.

[83] S. A. Regenhardt, C. I. Meyer, T. F. Garetto, *et al.*, Selective gas phase hydrogenation of maleic anhydride over Ni-supported catalysts: Effect of support on the catalytic performance. *Applied Catalysis A: General*, 2012, **449,** 81-87.

[84] J. Li, W. P. Tian, X. Wang, *et al.*, Nickel and nickel–platinum as active and selective catalyst for the maleic anhydride hydrogenation to succinic anhydride. *Chemical Engineering Journal*, 2011, **175,** 417-422.

[85] M. E. Bertone, S. A. Regenhardt, C. I. Meyer, *et al.*, Highly Selective Cu-Modified Ni/SiO_2–Al_2O_3 Catalysts for the Conversion of Maleic Anhydride to γ -Butyrolactone in Gas Phase. *Topics in Catalysis*, 2015, **59,** 1-9.

[86] D. R. L. (Ed.), CRC Handbook of Chemistry and Physics, 74th ed., CRC Press, Baca Raton, 1993-1994.

[87] P. Atkins, J. de Paula, Atkins' Physical Chemistry, OUP Oxford, 2010.

[88] V. Pallassana, M. Neurock, First-Principles Periodic Density Functional Study of the Hydrogenation of Maleic Anhydride to Succinic Anhydride over Palladium(111). *The Journal of Physical Chemistry B*, 2000, **104,** 9449-9459.

[89] V. Pallassana, M. Neurock, G. W. Coulston, Theoretical Density Functional Analysis of Maleic Anhydride Chemisorption on Pd(111), Re(0001), and Bimetallic Pd_{ML}/Re(0001) and Pd_{ML}/Mo(110) Pseudomorphic Overlayers. *The Journal of Physical Chemistry B*, 1999, **103,** 8973-8983.

[90] V. Pallassana, M. Neurock, G. Coulston, Towards understanding the mechanism for the selective hydrogenation of maleic anhydride to tetrahydrofuran over palladium. *Catalysis Today*, 1999, **50,** 589-601.

[91] G. Sinha, O. Heikkinen, M. Vestberg, *et al.*, Adsorption of maleic anhydride on Pt(111). *Surface Science*, 2014, **620,** 9-16.

[92] S. Gil Girol, T. Strunskus, M. Muhler, *et al.*, Reactivity of ZnO Surfaces toward Maleic Anhydride. *The Journal of Physical Chemistry B*, 2004, **108,** 13736-13745.

[93] E. M. J. Johansson, S. Plogmaker, L. E. Walle, *et al.*, Comparing Surface Binding of the Maleic Anhydride Anchor Group on Single Crystalline Anatase TiO_2 (101), (100), and (001) Surfaces. *The Journal of Physical Chemistry C*, 2010, **114,** 15015-15020.

[94] F. Wang, S. He, H. Chen, *et al.*, Active Site Dependent Reaction Mechanism over Ru/CeO_2 Catalyst toward CO_2 Methanation. *Journal of the American Chemical Society*, 2016, **138,** 6298-6305.

[95] K. Mudiyanselage, S. D. Senanayake, L. Feria, *et al.*, Importance of the metal-oxide interface in catalysis: in situ studies of the water-gas shift reaction by ambient-pressure X-ray photoelectron spectroscopy. *Angewandte Chemie International Edition*, 2013, **52,** 5101-5105.

[96] Z. Wu, M. Li, J. Howe, *et al.*, Probing defect sites on CeO_2 nanocrystals with well-defined surface planes by Raman spectroscopy and O_2 adsorption. *Langmuir*, 2010, **26,** 16595-16606.

[97] T. Montini, M. Melchionna, M. Monai, *et al.*, Fundamentals and Catalytic Applications of CeO_2-Based Materials. *Chem Rev*, 2016, **116,** 5987-6041.

[98] T. Uchiyama, H. Yoshida, Y. Kuwauchi, *et al.*, Systematic morphology changes of gold nanoparticles supported on CeO_2 during CO oxidation. *Angewandte Chemie International Edition*, 2011, **50,** 10157-10160.

[99] L. Soler, A. Casanovas, A. Urrich, *et al.*, CO oxidation and COPrOx over preformed Au nanoparticles supported over nanoshaped CeO_2. *Applied Catalysis B: Environmental*, 2016, **197,** 47-55.

[100] H. Wu, L. Wang, Shape effect of microstructured CeO_2 with various morphologies on CO catalytic oxidation. *Catalysis Communications*, 2011, **12,** 1374-1379.

[101] M. Á. Centeno, C. Portales, I. Carrizosa, *et al.*, Gold supported CeO_2/Al_2O_3 catalysts for CO oxidation: influence of the ceria phase. *Catalysis Letters*, 2005, **102,** 289-297.

[102] X. Tang, B. Zhang, Y. Li, *et al.*, Carbon monoxide oxidation over CuO/CeO_2 catalysts. *Catalysis Today*, 2004, **93-95,** 191-198.

[103] E. Aneggi, J. Llorca, M. Boaro, *et al.*, Surface-structure sensitivity of CO oxidation over polycrystalline ceria powders. *Journal of Catalysis*, 2005, **234,** 88-95.

[104] Y. Liu, C. Wen, Y. Guo, *et al.*, Modulated CO Oxidation Activity of M-Doped Ceria (M = Cu, Ti, Zr, and Tb): Role of the Pauling Electronegativity of M. *The Journal of Physical Chemistry C*, 2010, **114,** 9889-9897.

[105] W. Gao, Z. Zhang, J. Li, *et al.*, Surface engineering on CeO_2 nanorods by chemical redox etching and their enhanced catalytic activity for CO oxidation. *Nanoscale*, 2015, **7,** 11686-11691.

[106] J. Carrasco, D. Lopez-Duran, Z. Liu, *et al.*, In situ and theoretical studies for the dissociation of water on an active Ni/CeO_2 catalyst: importance of strong metal-support interactions for the cleavage of O-H bonds. *Angewandte Chemie International Edition*, 2015, **54,** 3917-3921.

[107] R. K. Pati, I. C. Lee, S. Hou, *et al.*, Flame synthesis of nanosized Cu-Ce-O, Ni-Ce-O, and Fe-Ce-O catalysts for the water-gas shift (WGS) reaction. *ACS Appl Mater Interfaces*, 2009, **1,** 2624-2635.

[108] J. A. Rodriguez, J. C. Hanson, D. Stacchiola, *et al.*, In situ/operando studies for the production of hydrogen through the water-gas shift on metal oxide catalysts. *Physical Chemistry Chemical Physics*, 2013, **15,** 12004-12025.

[109] Q. Fu, H. Saltsburg, M. Flytzani-Stephanopoulos, Active nonmetallic Au and Pt species on ceria-based water-gas shift catalysts. *Science*, 2003, **301,** 935-938.

[110] Z. Liu, D. C. Grinter, P. G. Lustemberg, *et al.*, Dry Reforming of Methane on a Highly-Active Ni-CeO_2 Catalyst: Effects of Metal-Support Interactions on C-H Bond Breaking. *Angewandte Chemie International Edition*, 2016, **55,** 7455-7459.

[111] I. I. Soykal, H. Sohn, D. Singh, *et al.*, Reduction Characteristics of Ceria under Ethanol Steam Reforming Conditions: Effect of the Particle Size. *ACS Catalysis*, 2014, **4,** 585-592.

[112] R. Takahashi, I. Yamada, A. Iwata, *et al.*, Synthesis of 3-buten-1-ol from 1,4-butanediol over indium oxide. *Applied Catalysis A: General*, 2010, **383,** 134-140.

[113] N. Laosiripojana, S. Assabumrungrat, Conversion of poisonous methanethiol to hydrogen-rich gas by chemisorption/reforming over nano-scale CeO_2: The use of CeO_2 as catalyst coating material. *Applied Catalysis B: Environmental*, 2011, **102,** 267-275.

[114] A. Younis, D. Chu, S. Li, Cerium Oxide Nanostructures and their Applications, in, 2016.

[115] S. Sato, F. Sato, H. Gotoh, *et al.*, Selective Dehydration of Alkanediols into Unsaturated Alcohols over Rare Earth Oxide Catalysts. *ACS Catalysis*, 2013, **3,** 721-734.

[116] P. M. Albrecht, D. R. Mullins, Adsorption and reaction of methanol over CeO_x(100) thin films. *Langmuir*, 2013, **29,** 4559-4567.

[117] Z. Wu, M. Li, D. R. Mullins, *et al.*, Probing the Surface Sites of CeO_2 Nanocrystals with Well-Defined Surface Planes via Methanol Adsorption and Desorption. *ACS Catalysis*, 2012, **2,** 2224-2234.

[118] S. D. Senanayake, W. O. Gordon, S. H. Overbury, *et al.*, Adsorption and Reaction of Acetone over CeO_x (111) Thin Films. *The Journal of Physical Chemistry C*, 2009, **113,** 6208-6214.

[119] F. C. Calaza, T.-L. Chen, D. R. Mullins, *et al.*, Reactivity and reaction intermediates for acetic acid adsorbed on CeO_2 (1 1 1). *Catalysis Today*, 2015, **253,** 65-76.

[120] X. Liu, K. Zhou, L. Wang, *et al.*, Oxygen vacancy clusters promoting reducibility and activity of ceria nanorods. *Journal of the American Chemical Society*, 2009, **131,** 3140-3141.

[121] A. Laachir, V. Perrichon, A. Badri, *et al.*, Reduction of CeO_2 by hydrogen. Magnetic susceptibility and Fourier-transform infrared, ultraviolet and X-ray photoelectron spectroscopy measurements. *Journal of the Chemical Society, Faraday Transactions*, 1991, **87,** 1601-1609.

[122] G. Vicario, G. Balducci, S. Fabris, *et al.*, Interaction of hydrogen with cerium oxide surfaces: a quantum mechanical computational study. *The Journal of Physical Chemistry B*, 2006, **110,** 19380-19385.

[123] S. Bernal, J. J. Calvino, G. A. Cifredo, *et al.*, Hydrogen chemisorption on ceria: influence of the oxide surface area and degree of reduction. *Journal of the Chemical Society, Faraday Transactions*, 1993, **89,** 3499.

[124] B. Chen, Y. Ma, L. Ding, *et al.*, Reactivity of Hydroxyls and Water on a CeO_2(111) Thin Film Surface: The Role of Oxygen Vacancy. *The Journal of Physical Chemistry C*, 2013, **117,** 5800-5810.

[125] X. P. Wu, X. Q. Gong, G. Lu, Role of oxygen vacancies in the surface evolution of H at CeO_2(111): a charge modification effect. *Physical Chemistry Chemical Physics*, 2015, **17,** 3544-3549.

[126] Z. Wu, Y. Cheng, F. Tao, *et al.*, Direct Neutron Spectroscopy Observation of Cerium Hydride Species on a Cerium Oxide Catalyst. *Journal of the American Chemical Society*, 2017, **139,** 9721-9727.

[127] G. Vile, B. Bridier, J. Wichert, *et al.*, Ceria in hydrogenation catalysis: high selectivity in the conversion of alkynes to olefins. *Angewandte Chemie International Edition*, 2012, **51,** 8620-8623.

[128] J. Carrasco, G. Vilé, D. Fernández-Torre, *et al.*, Molecular-Level Understanding of CeO_2 as a Catalyst for Partial Alkyne Hydrogenation. *The Journal of Physical Chemistry C*, 2014, **118,** 5352-5360.

[129] H. Z. Zhu, Y. M. Lu, F. J. Fan, *et al.*, Selective hydrogenation of nitroaromatics by ceria nanorods. *Nanoscale*, 2013, **5,** 7219-7223.

[130] M. Cargnello, V. V. Doan-Nguyen, T. R. Gordon, *et al.*, Control of metal nanocrystal size reveals metal-support interface role for ceria catalysts. *Science*, 2013, **341,** 771-773.

[131] J. A. Farmer, C. T. Campbell, Ceria maintains smaller metal catalyst particles by strong metal-support bonding. *Science*, 2010, **329,** 933-936.

[132] M. Tamura, T. Kitanaka, Y. Nakagawa, *et al.*, Cu Sub-Nanoparticles on Cu/CeO_2 as an Effective Catalyst for Methanol Synthesis from Organic Carbonate by Hydrogenation. *ACS Catalysis*, 2016, **6,** 376-380.

[133] A. Bruix, J. A. Rodriguez, P. J. Ramirez, *et al.*, A new type of strong metal-support interaction and the production of H_2 through the transformation of water on Pt/CeO_2 (111) and Pt/CeO_x/TiO_2(110) catalysts. *Journal of the American Chemical Society*, 2012, **134,** 8968-8974.

[134] C. T. Campbell, Catalyst-support interactions: Electronic perturbations. *Nat Chem*, 2012, **4,** 597-598.

[135] H. P. Zhou, H. S. Wu, J. Shen, *et al.*, Thermally stable Pt/CeO_2 hetero-nanocomposites with high catalytic activity. *Journal of the American Chemical Society*, 2010, **132,** 4998-4999.

[136] N. Ta, J. J. Liu, S. Chenna, *et al.*, Stabilized gold nanoparticles on ceria nanorods by strong interfacial anchoring. *Journal of the American Chemical Society*, 2012, **134,** 20585-20588.

[137] J. A. Rodriguez, D. C. Grinter, Z. Liu, *et al.*, Ceria-based model catalysts: fundamental studies on the importance of the metal-ceria interface in CO oxidation, the water-gas shift, CO_2 hydrogenation, and methane and alcohol reforming. *Chemical Society Reviews*, 2017, **46,** 1824-1841.

[138] Z. Yang, Q. Wang, S. Wei, The synergistic effects of the Cu-CeO_2 (111) catalysts on the adsorption and dissociation of water molecules. *Physical Chemistry Chemical Physics*, 2011, **13,** 9363-9373.

[139] G. F. Santori, M. L. Casella, O. A. Ferretti, Hydrogenation of carbonyl compounds using tin-modified platinum-based catalysts prepared via surface organometallic chemistry on metals (SOMC/M). *Journal of Molecular Catalysis A: Chemical*, 2002, **186,** 223-239.

[140] K. Liberková, R. Touroude, Performance of Pt/SnO_2 catalyst in the gas phase hydrogenation of crotonaldehyde. *Journal of Molecular Catalysis A: Chemical*, 2002, **180,** 221-230.

[141] V. Ponec, Alloy catalysts: the concepts. *Applied Catalysis A: General*, 2001, **222,** 31-45.

[142] P. Li, J. Liu, N. Nag, *et al.*, In situ preparation of Ni–Cu/TiO_2 bimetallic catalysts. *Journal of Catalysis*, 2009, **262,** 73-82.

[143] S. Alayoglu, B. Eichhorn, Rh-Pt bimetallic catalysts: synthesis, characterization, and catalysis of core-shell, alloy, and monometallic nanoparticles. *Journal of the American Chemical Society*, 2008, **130,** 17479-17486.

[144] L. E. Murillo, A. M. Goda, J. G. Chen, Selective hydrogenation of the C=O bond in acrolein through the architecture of bimetallic surface structures. *Journal of the American Chemical Society*, 2007, **129,** 7101-7105.

[145] J. A. Schwarz, C. Contescu, A. Contescu, Methods for preparation of catalytic materials. *Chem Rev*, 1995, **95,** 477-510.

[146] K. P. de Jong, Synthesis of Solid Catalysts, Wiley, 2009.

[147] H. Knözinger, K. Kochloefl, Heterogeneous Catalysis and Solid Catalysts, 2003.

[148] J. D. Aiken, R. G. Finke, A review of modern transition-metal nanoclusters: their synthesis, characterization, and applications in catalysis. *Journal of Molecular Catalysis A: Chemical*, 1999, **145,** 1-44.

[149] R. Schlogl, Heterogeneous catalysis. *Angewandte Chemie International Edition*, 2015, **54,** 3465-3520.

[150] T. S. Moraes, R. C. R. Neto, M. C. Ribeiro, *et al.*, Effects of Ceria Morphology on Catalytic Performance of Ni/CeO_2 Catalysts for Low Temperature Steam Reforming of Ethanol. *Topics in Catalysis*, 2015, **58,** 281-294.

[151] N. Wang, W. Qian, W. Chu, *et al.*, Crystal-plane effect of nanoscale CeO_2 on the catalytic performance of Ni/CeO_2 catalysts for methane dry reforming. *Catalysis Science & Technology*, 2016, **6,** 3594-3605.

[152] R. Jenkins, R. L. Snyder, Introduction to X-ray powder diffractometry, Wiley, 1996.

[153] T. Ungár, Microstructural parameters from X-ray diffraction peak broadening. *Scripta Materialia*, 2004, **51,** 777-781.

[154] R. Guinebretière, X-Ray Diffraction by Polycrystalline Materials, Wiley, 2013.

[155] T. H. de Keijser, J. I. Langford, E. J. Mittemeijer, *et al.*, Use of the Voigt function in a single-line method for the analysis of X-ray diffraction line broadening. *Journal of Applied Crystallography*, 1982, **15,** 308-314.

[156] R. Si, M. Flytzani-Stephanopoulos, Shape and crystal-plane effects of nanoscale ceria on the activity of Au-CeO_2 catalysts for the water-gas shift reaction. *Angewandte Chemie International Edition*, 2008, **47,** 2884-2887.

[157] A. R. Denton, N. W. Ashcroft, Vegard's law. *Physical Review A*, 1991, **43,** 3161-3164.

[158] T. Taniguchi, T. Watanabe, N. Sugiyama, *et al.*, Identifying Defects in Ceria-Based Nanocrystals by UV Resonance Raman Spectroscopy. *The Journal of Physical Chemistry C*, 2009, **113,** 19789-19793.

[159] M. Guo, J. Lu, Y. Wu, *et al.*, UV and visible Raman studies of oxygen vacancies in rare-earth-doped ceria. *Langmuir*, 2011, **27,** 3872-3877.

[160] J. Deng, W. Chu, B. Wang, *et al.*, Mesoporous Ni/$Ce_{1-x}Ni_xO_{2-y}$ heterostructure as an efficient catalyst for converting greenhouse gas to H_2 and syngas. *Catalysis Science & Technology*, 2016, **6,** 851-862.

[161] K. Tang, W. Liu, J. Li, *et al.*, The Effect of Exposed Facets of Ceria to the Nickel Species in Nickel-Ceria Catalysts and Their Performance in a NO + CO Reaction. *ACS Appl Mater Interfaces*, 2015, **7,** 26839-26849.

[162] V. V. Ursaki, I. M. Tiginyanu, V. V. Zalamai, *et al.*, Multiphonon resonant Raman scattering in ZnO crystals and nanostructured layers. *Physical Review B*, 2004, **70,** 155204.

[163] J. Zhang, L. Li, X. Huang, *et al.*, Fabrication of Ag–CeO_2 core–shell nanospheres with enhanced catalytic performance due to strengthening of the interfacial interactions. *Journal of Materials Chemistry*, 2012, **22,** 10480.

[164] L. Barrio, A. Kubacka, G. Zhou, *et al.*, Unusual Physical and Chemical Properties of Ni in $Ce_{1-x}Ni_xO_{2-y}$ Oxides: Structural Characterization and Catalytic Activity for the Water Gas Shift Reaction. *The Journal of Physical Chemistry C*, 2010, **114,** 12689-12697.

[165] A. Knop-Gericke, X-ray Photoelectron Spectroscopy. An Introduction to Principles and Practices. *Angewandte Chemie International Edition*, 2012, **51,** 9218-9218.

[166] L. Liu, Z. Yao, Y. Deng, *et al.*, Morphology and Crystal-Plane Effects of Nanoscale Ceria on the Activity of CuO/CeO_2 for NO Reduction by CO. *ChemCatChem*, 2011, **3,** 978-989.

[167] H. Liu, Z. Huang, H. Kang, *et al.*, Efficient bimetallic NiCu-SiO_2 catalysts for selective hydrogenolysis of xylitol to ethylene glycol and propylene glycol. *Applied Catalysis B: Environmental*, 2018, **220,** 251-263.

[168] J. C. Fuggle, Z. Zoł nierek, The relationship between empty d-state density and XPS satellite intensities in nickel alloys. *Solid State Communications*, 1981, **38,** 799-802.

[169] K. Kishi, Y. Motoyoshi, S. Ikeda, Deposition of nickel from $Ni(CO)_4$ on palladium and iron surfaces studied by X-ray photoelectron spectroscopy. *Surface Science*, 1981, **105,** 313-324.

[170] S. E. Golunski, John Ward Jenkins. *Platinum Metals Review*, 2008, **52,** 249-250.

[171] J. L. Falconer, J. A. Schwarz, Temperature-Programmed Desorption and Reaction: Applications to Supported Catalysts. *Catalysis Reviews*, 2007, **25,** 141-227.

[172] V. P. Santos, S. A. C. Carabineiro, J. J. W. Bakker, *et al.*, Stabilized gold on cerium-modified cryptomelane: Highly active in low-temperature CO oxidation. *Journal of Catalysis*, 2014, **309,** 58-65.

[173] G. Jacobs, U. Graham, E. Chenu, *et al.*, Low-temperature water?gas shift: impact of Pt promoter loading on the partial reduction of ceria and consequences for catalyst design. *Journal of Catalysis*, 2005, **229,** 499-512.

[174] J. Kugai, J. T. Miller, N. Guo, *et al.*, Oxygen-enhanced water gas shift on ceria-supported Pd–Cu and Pt–Cu bimetallic catalysts. *Journal of Catalysis*, 2011, **277,** 46-53.

[175] J. Li, G. Lu, H. Li, *et al.*, Facile synthesis of 3D flowerlike CeO_2 microspheres under mild condition with high catalytic performance for CO oxidation. *J Colloid Interface Sci*, 2011, **360,** 93-99.

[176] T. Z. Ren, Z. Y. Yuan, B. L. Su, Microwave-Assisted Preparation of Hierarchical Mesoporous−Macroporous Boehmite AlOOH and γ -Al_2O_3. *Langmuir*, 2004, **20,** 1531-1534.

[177] M. P. Sohier, G. Wrobel, J. P. Bonnelle, *et al.*, Hydrogenation catalysts based on nickel and rare earths oxides. *Applied Catalysis A: General*, 1992, **84,** 169-186.

[178] N. M. Deraz, Effect of NiO content on structural, surface and catalytic characteristics of nano-crystalline NiO/CeO_2 system. *Ceramics International*, 2012, **38,** 747-753.

[179] T. C. Huang, E. Moran, A. I. Nazzal, *et al.*, Determination of the average ionic radius and effective valence of Ce in the $Nd_{2-x}Ce_xCuO_4$ electron superconductor system by X-ray diffraction. *Physica C: Superconductivity*, 1989, **159,** 625-628.

[180] S. Storck, H. Bretinger, W. F. Maier, Characterization of micro- and mesoporous solids by physisorption methods and pore-size analysis. *Applied Catalysis A: General*, 1998, **174,** 137-146.

[181] J. Sa, Y. Kayser, C. J. Milne, *et al.*, Temperature-programmed reduction of NiO nanoparticles followed by time-resolved RIXS. *Physical Chemistry Chemical Physics*, 2014, **16,** 7692-7696.

[182] W. Shan, Reduction property and catalytic activity of $Ce_{1-x}Ni_xO_2$ mixed oxide catalysts for CH_4 oxidation. *Applied Catalysis A: General*, 2003, **246,** 1-9.

[183] K. Sohlberg, S. T. Pantelides, S. J. Pennycook, Interactions of Hydrogen with CeO_2. *Journal of the American Chemical Society*, 2001, **123,** 6609-6611.

[184] T. Paryjczak, J. Rynkowski, K. Krzyzanowski, Temperature-programmed reduction of CuO−NiO/Al_2O_3 catalysts. *Reaction Kinetics and Catalysis Letters*, 1982, **21,** 295-298.

[185] P. Burroughs, A. Hamnett, A. F. Orchard, *et al.*, Satellite structure in the X-ray photoelectron spectra of some binary and mixed oxides of lanthanum and cerium. *Journal of the Chemical Society, Dalton Transactions*, 1976, 1686-1698.

[186] E. Bêche, P. Charvin, D. Perarnau, *et al.*, Ce 3d XPS investigation of cerium oxides and mixed cerium oxide (CexTiyOz). *Surface and Interface Analysis*, 2008, **40,** 264-267.

[187] L. Torrente-Murciano, A. Gilbank, B. Puertolas*, et al.*, Shape-dependency activity of nanostructured CeO_2 in the total oxidation of polycyclic aromatic hydrocarbons. *Applied Catalysis B: Environmental*, 2013, **132,** 116-122.

[188] B. Choudhury, P. Chetri, A. Choudhury, Oxygen defects and formation of Ce^{3+} affecting the photocatalytic performance of CeO_2 nanoparticles. *RSC Advances*, 2014, **4,** 4663-4671.

[189] J. Liu, C. Li, F. Wang*, et al.*, Enhanced low-temperature activity of CO_2 methanation over highly-dispersed Ni/TiO_2 catalyst. *Catalysis Science & Technology*, 2013, **3,** 2627.

[190] L. Znak, J. Zieliński, Effects of support on hydrogen adsorption/desorption on nickel. *Applied Catalysis A: General*, 2008, **334,** 268-276.

[191] S. S. Zumdahl, S. A. Zumdahl, Chemistry, Cengage Learning, 2006.

[192] M. A. M. W. W. P. S. B. Ziemecki; Process for making tetrahydrofuran and 1,4-butanediol using Pd/Re hydrogenation catalyst. US 4550185A, 1985.

[193] D. C. G. M. Sisler; Platinum-rhenium-tin catalyst for hydrogenation in aqueous solution. US10327795, 2003.

[194] W. Lu, G. Lu, Y. Guo*, et al.*, Gas-phase hydrogenation of maleic anhydride to butyric acid over $Cu/TiO_2/\gamma\text{-}Al_2O_3$ catalyst promoted by Pd. *Catalysis Communications*, 2003, **4,** 177-181.

[195] A. B. Kehoe, D. O. Scanlon, G. W. Watson, Role of Lattice Distortions in the Oxygen Storage Capacity of Divalently Doped CeO_2. *Chemistry of Materials*, 2011, **23,** 4464-4468.

[196] Y. Liu, K. Murata, M. Inaba, Steam Reforming of Bio-Ethanol to Produce Hydrogen over Co/CeO_2 Catalysts Derived from $Ce_{1-x}Co_xO_{2-y}$ Precursors. *Catalysts*, 2016, **6,** 26.

[197] Y. Cui, W.-L. Dai, Support morphology and crystal plane effect of Cu/CeO2 nanomaterial on the physicochemical and catalytic properties for carbonate hydrogenation. *Catalysis Science & Technology*, 2016, **6,** 7752-7762.

[198] M. Greluk, M. Rotko, A. Machocki, Conversion of Ethanol Over Co/CeO_2 and KCo/CeO_2 Catalysts for Hydrogen Production. *Catalysis Letters*, 2015, **146,** 163-173.

[199] L. P. Matte, A. S. Kilian, L. Luza*, et al.*, Influence of the CeO_2 Support on the Reduction Properties of Cu/CeO_2 and Ni/CeO_2 Nanoparticles. *The Journal of Physical Chemistry C*, 2015, **119,** 26459-26470.

[200] J. E. Spanier, R. D. Robinson, F. Zhang*, et al.*, Size-dependent properties of CeO_{2-y} nanoparticles as studied by Raman scattering. *Physical Review B*, 2001, **64.**

[201] B. Hammer, J. K. Nørskov, Electronic factors determining the reactivity of metal surfaces. *Surface Science*, 1995, **343,** 211-220.

[202] P. Claus, A. Brückner, C. Mohr*, et al.*, Supported Gold Nanoparticles from Quantum Dot to Mesoscopic Size Scale: Effect of Electronic and Structural Properties on Catalytic Hydrogenation of Conjugated Functional Groups. *Journal of the American Chemical Society*, 2000, **122,** 11430-11439.

[203] A. P. Grosvenor, M. C. Biesinger, R. S. C. Smart*, et al.*, New interpretations of XPS spectra of nickel metal and oxides. *Surface Science*, 2006, **600,** 1771-1779.

[204] M. a. M. Branda, N. C. Herna□ndez, J. F. Sanz*, et al.*, Density Functional Theory Study of the Interaction of Cu, Ag, and Au Atoms with the Regular $CeO_2(111)$ Surface. *The Journal of Physical Chemistry C*, 2010, **114,** 1934-1941.

[205] M. H. Weng, H.-T. Chen, Y.-C. Wang*, et al.*, Kinetics and Mechanisms for the Adsorption, Dissociation, and Diffusion of Hydrogen in Ni and Ni/YSZ Slabs: A DFT Study. *Langmuir*, 2012, **28,** 5596-5605.

[206] K. R. Hahn, A. P. Seitsonen, M. Iannuzzi*, et al.*, Functionalization of CeO_2 (1 1 1) by Deposition of Small Ni Clusters: Effects on CO_2 Adsorption and O Vacancy Formation. *ChemCatChem*, 2015, **7,** 625-634.

[207] J. Carrasco, L. Barrio, P. Liu*, et al.*, Theoretical Studies of the Adsorption of CO and C on Ni(111) and Ni/CeO_2(111): Evidence of a Strong Metal–Support Interaction. *The Journal of Physical Chemistry C*, 2013, **117,** 8241-8250.

[208] P. Winiarek, J. Kijenski, Hydrogenation of unsaturated hydrocarbons over alkali-metal-modified zinc oxide. *Journal of the Chemical Society, Faraday Transactions*, 1998, **94,** 167-172.

[209] S. Zhang, J. Li, Z. Xia*, et al.*, Towards highly active Pd/CeO_2 for alkene hydrogenation by tuning Pd dispersion and surface properties of the catalysts. *Nanoscale*, 2017, **9,** 3140-3149.

[210] S. J. Tauster, Strong metal-support interactions. *Accounts of Chemical Research*, 1987, **20,** 389-394.

[211] M. G. Prakash, R. Mahalakshmy, K. R. Krishnamurthy*, et al.*, Selective hydrogenation of cinnamaldehyde on nickel nanoparticles supported on titania: role of catalyst preparation methods. *Catalysis Science & Technology*, 2015, **5,** 3313-3321.

[212] C. Xu, D. W. Goodman, Adsorption and Reaction of Maleic Anhydride on Mo(110), Monolayer Pd(111)/Mo(110), and Multilayer Pd(111)/Mo(110). *Langmuir*, 1996, **12,** 1807-1816.

[213] W. Huang, Y. Gao, Morphology-dependent surface chemistry and catalysis of CeO_2 nanocrystals. *Catalysis Science & Technology*, 2014, **4,** 3772-3784.

[214] Z. G. Yan, C. H. Yan, Controlled synthesis of rare earth nanostructures. *Journal of Materials Chemistry*, 2008, **18,** 5046.

[215] K. Zhou, X. Wang, X. Sun*, et al.*, Enhanced catalytic activity of ceria nanorods from well-defined reactive crystal planes. *Journal of Catalysis*, 2005, **229,** 206-212.

[216] Tana, M. Zhang, J. Li*, et al.*, Morphology-dependent redox and catalytic properties of CeO2 nanostructures: Nanowires, nanorods and nanoparticles. *Catalysis Today*, 2009, **148,** 179-183.

[217] J. Conesa, Computer modeling of surfaces and defects on cerium dioxide. *Surface Science*, 1995, **339,** 337-352.

[218] M. Nolan, S. C. Parker, G. W. Watson, The electronic structure of oxygen vacancy defects at the low index surfaces of ceria. *Surface Science*, 2005, **595,** 223-232.

[219] H. X. Mai, L. D. Sun, Y. W. Zhang*, et al.*, Shape-selective synthesis and oxygen storage behavior of ceria nanopolyhedra, nanorods, and nanocubes. *The Journal of Physical Chemistry B*, 2005, **109,** 24380-24385.

[220] Y. Namai, K. Fukui, Y. Iwasawa, Atom-Resolved Noncontact Atomic Force Microscopic Observations of CeO_2 (111) Surfaces with Different Oxidation States: Surface Structure and Behavior of Surface Oxygen Atoms. *The Journal of Physical Chemistry B*, 2003, **107,** 11666-11673.

[221] H. Tan, J. Wang, S. Yu*, et al.*, Support Morphology-Dependent Catalytic Activity of Pd/CeO_2 for Formaldehyde Oxidation. *Environ Sci Technol*, 2015, **49,** 8675-8682.

[222] Z. L. Wang, X. Feng, Polyhedral Shapes of CeO_2 Nanoparticles. *The Journal of Physical Chemistry B*, 2003, **107,** 13563-13566.

[223] S. Aškrabić, Z. Dohčević-Mitrović, A. Kremenović, *et al.*, Oxygen vacancy-induced microstructural changes of annealed CeO_{2-x} nanocrystals. *Journal of Raman Spectroscopy*, 2012, **43,** 76-81.

[224] X. Du, D. Zhang, L. Shi, *et al.*, Morphology Dependence of Catalytic Properties of Ni/CeO_2 Nanostructures for Carbon Dioxide Reforming of Methane. *The Journal of Physical Chemistry C*, 2012, **116,** 10009-10016.

[225] Q. Liu, J. Gao, M. Zhang, *et al.*, Highly active and stable Ni/γ-Al_2O_3 catalysts selectively deposited with CeO_2 for CO methanation. *RSC Advances*, 2014, **4,** 16094-16103.

[226] L. Zaramello, B. L. Albuquerque, J. B. Domingos, *et al.*, Kinetic investigation into the chemoselective hydrogenation of alpha,beta-unsaturated carbonyl compounds catalyzed by Ni^0 nanoparticles. *Dalton Transactions*, 2017, **46,** 5082-5090.

[227] X. Yang, D. Chen, S. Liao, *et al.*, High-performance Pd–Au bimetallic catalyst with mesoporous silica nanoparticles as support and its catalysis of cinnamaldehyde hydrogenation. *Journal of Catalysis*, 2012, **291,** 36-43.

[228] K. Wu, L. D. Sun, C. H. Yan, Recent Progress in Well-Controlled Synthesis of Ceria-Based Nanocatalysts towards Enhanced Catalytic Performance. *Advanced Energy Materials*, 2016, **6,** 1600501-1600547.

[229] G. R. Rao, H. R. Sahu, B. G. Mishra, Surface and catalytic properties of Cu–Ce–O composite oxides prepared by combustion method. *Colloids and Surfaces A: Physicochemical and Engineering Aspects*, 2003, **220,** 261-269.

[230] J.-H. Lin, P. Biswas, V. V. Guliants, *et al.*, Hydrogen production by water–gas shift reaction over bimetallic Cu–Ni catalysts supported on La-doped mesoporous ceria. *Applied Catalysis A: General*, 2010, **387,** 87-94.

[231] E. T. Saw, U. Oemar, X. R. Tan, *et al.*, Bimetallic Ni–Cu catalyst supported on CeO_2 for high-temperature water–gas shift reaction: Methane suppression via enhanced CO adsorption. *Journal of Catalysis*, 2014, **314,** 32-46.

[232] A. Cox, M. J. L. Sangster, Vegard's rule and volumes of formation for impurity ions. *Journal of Physics C: Solid State Physics*, 1985, **18,** L1123.

[233] Q. Wu, L. D. L. Duchstein, G. L. Chiarello, *et al.*, In Situ Observation of Cu-Ni Alloy Nanoparticle Formation by X-Ray Diffraction, X-Ray Absorption Spectroscopy, and Transmission Electron Microscopy: Influence of Cu/Ni Ratio. *ChemCatChem*, 2014, **6,** 301-310.

[234] S. Lee, R. Hoffmann, Bcc and Fcc Transition Metals and Alloys: A Central Role for the Jahn−Teller Effect in Explaining Their Ideal and Distorted Structures. *Journal of the American Chemical Society*, 2002, **124,** 4811-4823.

[235] S. Robertson, Determination of reducibility and identification of alloying in copper-nickel-on-silica catalysts by temperature-programmed reduction. *Journal of Catalysis*, 1975, **37,** 424-431.

[236] S. A. Khromova, A. A. Smirnov, O. A. Bulavchenko, *et al.*, Anisole hydrodeoxygenation over Ni–Cu bimetallic catalysts: The effect of Ni/Cu ratio on selectivity. *Applied Catalysis A: General*, 2014, **470,** 261-270.

[237] A. R. Naghash, T. H. Etsell, S. Xu, XRD and XPS Study of Cu−Ni Interactions on Reduced Copper−Nickel−Aluminum Oxide Solid Solution Catalysts. *Chemistry of Materials*, 2006, **18,** 2480-2488.

[238] T. Ghodselahi, M. A. Vesaghi, A. Shafiekhani, *et al.*, XPS study of the Cu@Cu2O core-shell nanoparticles. *Applied Surface Science*, 2008, **255,** 2730-2734.

[239] J. F. Moulder, J. Chastain, Handbook of X-ray Photoelectron Spectroscopy: A Reference Book of Standard Spectra for Identification and Interpretation of XPS Data, Physical Electronics Division, Perkin-Elmer Corporation, 1992.

[240] A. Yin, C. Wen, X. Guo, *et al.*, Influence of Ni species on the structural evolution of Cu/SiO2 catalyst for the chemoselective hydrogenation of dimethyl oxalate. *Journal of Catalysis*, 2011, **280,** 77-88.

[241] J. Graciani, K. Mudiyanselage, F. Xu, *et al.*, Highly active copper-ceria and copper-ceria-titania catalysts for methanol synthesis from CO_2. *Science*, 2014, **345,** 546-550.

[242] L. He, B. Liang, L. Li, *et al.*, Cerium-Oxide-Modified Nickel as a Non-Noble Metal Catalyst for Selective Decomposition of Hydrous Hydrazine to Hydrogen. *ACS Catalysis*, 2015, **5,** 1623-1628.

[243] J. Xu, C. M. Y. Yeung, J. Ni, *et al.*, Methane steam reforming for hydrogen production using low water-ratios without carbon formation over ceria coated Ni catalysts. *Applied Catalysis A: General*, 2008, **345,** 119-127.

[244] Q. Yao, Z. H. Lu, Z. Zhang, *et al.*, One-pot synthesis of core-shell Cu@SiO_2 nanospheres and their catalysis for hydrolytic dehydrogenation of ammonia borane and hydrazine borane. *Sci Rep*, 2014, **4,** 7597.

[245] E. C. Lovell, J. Scott, R. Amal, Ni/SiO_2 catalysts for the carbon dioxide reforming of methane: varying support properties by flame spray pyrolysis. *Molecules*, 2015, **20,** 4594-4609.

[246] M. Leon, L. Giacomazzi, S. Girard, *et al.*, Neutron Irradiation Effects on the Structural Properties of KU1, KS-4V and I301 Silica Glasses. *IEEE Transactions on Nuclear Science*, 2014, **61,** 1522-1530.

[247] C. J. Pan, M. C. Tsai, W. N. Su, *et al.*, Tuning/exploiting Strong Metal-Support Interaction (SMSI) in Heterogeneous Catalysis. *Journal of the Taiwan Institute of Chemical Engineers*, 2017, **74,** 154-186.

[248] F. Zaera, The surface chemistry of hydrocarbon partial oxidation catalysis. *Catalysis Today*, 2003, **81,** 149-157.

[249] F. Zaera, New advances in the use of infrared absorption spectroscopy for the characterization of heterogeneous catalytic reactions. *Chemical Society Reviews*, 2014, **43,** 7624-7663.

[250] L. He, Y. Huang, A. Wang, *et al.*, Surface modification of Ni/Al_2O_3 with Pt: Highly efficient catalysts for H_2 generation via selective decomposition of hydrous hydrazine. *Journal of Catalysis*, 2013, **298,** 1-9.

[251] C. Rudolf, B. Dragoi, A. Ungureanu, *et al.*, NiAl and CoAl materials derived from takovite-like LDHs and related structures as efficient chemoselective hydrogenation catalysts. *Catalysis Science & Technology*, 2014, **4,** 179-189.

[252] S. Brunauer, P. H. Emmett, E. Teller, Adsorption of Gases in Multimolecular Layers. *Journal of the American Chemical Society*, 1938, **60,** 309-319.

[253] I. M. K. Ismail, Cross-sectional areas of adsorbed nitrogen, argon, krypton, and oxygen on carbons and fumed silicas at liquid nitrogen temperature. *Langmuir*, 1992, **8,** 360-365.